

Journal of
Mechanics of
Materials and Structures

Volume 3, N° 2

February 2008

 mathematical sciences publishers

JOURNAL OF MECHANICS OF MATERIALS AND STRUCTURES

<http://www.jomms.org>

EDITOR-IN-CHIEF Charles R. Steele
ASSOCIATE EDITOR Marie-Louise Steele
Division of Mechanics and Computation
Stanford University
Stanford, CA 94305
USA

BOARD OF EDITORS

D. BIGONI University of Trento, Italy
H. D. BUI École Polytechnique, France
J. P. CARTER University of Sydney, Australia
R. M. CHRISTENSEN Stanford University, U.S.A.
G. M. L. GLADWELL University of Waterloo, Canada
D. H. HODGES Georgia Institute of Technology, U.S.A.
J. HUTCHINSON Harvard University, U.S.A.
C. HWU National Cheng Kung University, R.O. China
IWONA JASIUK University of Illinois at Urbana-Champaign
B. L. KARIHALOO University of Wales, U.K.
Y. Y. KIM Seoul National University, Republic of Korea
Z. MROZ Academy of Science, Poland
D. PAMPLONA Universidade Católica do Rio de Janeiro, Brazil
M. B. RUBIN Technion, Haifa, Israel
Y. SHINDO Tohoku University, Japan
A. N. SHUPIKOV Ukrainian Academy of Sciences, Ukraine
T. TARNAI University Budapest, Hungary
F. Y. M. WAN University of California, Irvine, U.S.A.
P. WRIGGERS Universität Hannover, Germany
W. YANG Tsinghua University, P.R. China
F. ZIEGLER Technische Universität Wien, Austria

PRODUCTION


PAULO NEY DE SOUZA Production Manager
SHEILA NEWBERY Senior Production Editor
SILVIO LEVY Scientific Editor

See inside back cover or <http://www.jomms.org> for submission guidelines.

Regular subscription rate: \$500 a year.

Subscriptions, requests for back issues, and changes of address should be sent to Mathematical Sciences Publishers, 798 Evans Hall, Department of Mathematics, University of California, Berkeley, CA 94720-3840.

©Copyright 2008. Journal of Mechanics of Materials and Structures. All rights reserved.

 mathematical sciences publishers

ELASTIC CONSTANTS AND THERMAL EXPANSION AVERAGES OF A NONTEXTURED POLYCRYSTAL

ROLAND DEWIT

This paper gives expressions for the overall average elastic constants and thermal expansion coefficients of a polycrystal in terms of its single crystal components. The polycrystal is assumed to be statistically homogeneous, isotropic, and perfectly disordered. Upper and lower bounds for the averages are easily found by assuming a uniform strain or stress. The upper bound follows from Voigt's assumption that the total strain is uniform within the polycrystal while the lower bound follows from Reuss' original assumption that the stress is uniform. A self-consistent estimate for the averages can be found if it is assumed that the overall response of the polycrystal is the same as the average response of each crystallite. The derivation method is based on Eshelby's theory of inclusions and inhomogeneities. We define an equivalent inclusion, which gives an expression for the strain disturbance of the inhomogeneity when external fields are applied. The equivalent inclusion is then used to represent the crystallites. For the self-consistent model the average response of the grains has to be the same as the overall response of the material, or the average strain disturbance must vanish. The result is an implicit equation for the average polycrystal elastic constants and an explicit equation for the average thermal expansion coefficients. For the particular case of cubic symmetry the results can be reduced to a cubic equation for the self-consistent shear modulus. For lower symmetry crystals it is best to calculate the self-consistent bulk and shear modulus numerically.

Introduction

A polycrystal, whose properties vary in a complicated fashion from point to point over a small microscopic length scale, may appear on average to be uniform or perhaps, more generally, its properties appear to vary smoothly. The determination of such overall properties from the properties and geometrical arrangement of the constituent monocrystal grains is our aim. In the simplest case the polycrystal is assumed to be statistically homogeneous, isotropic, and perfectly disordered. General expressions for averages can then be derived. Many different properties can be averaged, such as dielectric constants, diffusivity, elastic constants, electrical conductivity, magnetic permeability, magnetostriction, piezoelectric constants, thermal conductivity, or thermal expansion. In this paper we treat the elastic constants, which have already received more attention than most other physical properties, and the thermal expansion.

Elastic constants are fundamental physical data needed for the characterization of materials. In addition to their fundamental importance, elastic constants and properties derived from them are used as the starting point for the mechanical design of almost all products. Theoretical averaging methods for the calculation of the isotropic elastic constants of a polycrystal from the single crystal constants of

Keywords: bulk modulus, compliance, cubic, disordered, effective medium, elastic constants, homogeneous, inclusion, inhomogeneity, isotropic, polycrystal, self-consistent, shear modulus, stiffness, thermal expansion.

its grains go back more than 100 years. Voigt [1887] assumed that the strain is constant throughout the polycrystal and he obtained a simple approximate solution. Many years later Reuss [1929] found a solution by assuming that the stress is constant. Hill [1952] showed that these two solutions provided upper and lower bounds of the possible average constants. In 1958 Kröner proposed a self-consistent theory and derived the self-consistent shear modulus of a cubic polycrystal, and Tomé [1998] showed how to incorporate the effect of thermal expansion into these models.

In this paper we develop a consistent intuitive notation to describe the concepts that have arisen in the field. The above developments are reviewed in this framework and additional results are presented. We try to keep the notation as clear as possible in the sometimes detailed calculations. Our major aim is to show how the relevant equations can be used to calculate explicit results; we give only selected results and refer to the literature for exhaustive listings. In this sense our paper has the character of a primer.

Relations for material properties are frequently expressed in terms of tensor equations, because tensors have clear rules for coordinate transformations and rotations. However, the relations are also frequently expressed in terms of matrices, because matrices allow straightforward mathematical calculations. The two methods can be used in parallel and are related to each other. We use both in this paper and represent them in symbolic form.

The analysis starts by defining the concept of an *effective medium*, which is a model that approximates the average state of the polycrystal and describes its average properties. In terms of this effective medium we can define *effective elastic constants*, which relate the average stress to the average strain in the effective medium. We can also define an *effective thermal expansion coefficient*. Various theories then derive effective properties as averages over crystallographic properties. The Voigt and Reuss models provide special cases of such an effective medium and the resulting effective properties give upper and lower bounds.

To get explicit scalar expressions for the effective properties from the symbolic equations we use the linear tensor invariants. The fundamental property of a tensor invariant is that it is independent of rotation in space and therefore isotropic. Hence the invariant is equal to its average. This method is used to derive explicit expressions for the effective elastic constants and thermal expansion coefficient in the simple theories.

Eshelby's theory of elastic inclusions and inhomogeneities is used to derive a self-consistent model. This is the method that was first used by Kröner [1958] to solve for the cubic polycrystal. There is, however, a more powerful and fundamental method to derive self-consistent estimates called *statistical continuum mechanics*, which we do not use in this paper. In an applied stress field, the inhomogeneity looks like an inclusion. We introduce the *equivalent inclusion* to determine the stress disturbance of the homogeneity by using the result of the inclusion. This allows us to solve for the strain disturbance of the inhomogeneity in an applied field.

The self-consistent model lets the equivalent inclusion represent a grain of the polycrystal. The strain disturbance then occurs because the local elastic and thermal properties of the grain differ from the average values for the polycrystal. The condition for self-consistency is that the average grain response is the same as the overall average of the polycrystal, or that the average disturbance vanishes. This leads to an implicit equation for the self-consistent effective elastic constants and an explicit equation for the self-consistent effective thermal expansion coefficient.

We next apply the results to crystals with cubic symmetry. For this case there are only three independent components of the single crystal elastic constants. The analysis can then be simplified considerably by using Walpole's notation for the decomposition of unity. This approach leads to the logical choice of the bulk modulus and shear modulus as the basic elastic constants to use in explicit calculations. When written out explicitly the equation for the self-consistent elastic constants is complicated but straightforward. The bulk modulus is isotropic. The equation for the self-consistent effective shear modulus can be reduced to a cubic equation, which was first obtained by Kröner [1958]. Finally, this equation can be solved explicitly in closed form. It is easy to calculate average numerical results for cubic crystals.

For lower crystal symmetries the solution of the implicit equation leads to high-order equations for the effective bulk and shear modulus. It is then best to continue the solution numerically. We present some results of these calculations.

Hooke's law

We start with a description of the elastic constants. For a single crystal, Hooke's law can be written as follows

$$\sigma_{ij} = c_{ijkl}e_{kl}, \quad (i, j, k, l = 1, 2, 3), \quad (1)$$

where repeated indices are summed, σ and e are the stress and strain, both second rank tensors, and c is the elastic stiffness, a fourth rank tensor. Hooke's law can also be written in matrix form as

$$\sigma_i = c_{ij}e_j, \quad (i, j = 1, \dots, 6), \quad (2)$$

where σ and e are the (6×1) stress and strain vectors and c is the (6×6) stiffness matrix. The two notations, tensors and matrices, are completely equivalent. The relation between them has been discussed in detail in [Nye 1960] and [Hearmon 1961]. The matrix form of the elastic stiffness or elastic moduli was introduced by Voigt [1887] and is frequently referred to as the Voigt notation or reduced notation. As in matrix theory, it is convenient to use the symbolic notation,

$$\sigma = ce, \quad (3)$$

to represent either of the foregoing equations. Equation (3) can be solved for the strain in terms of the stress:

$$e = \frac{\sigma}{c} = s\sigma,$$

where s , the elastic compliance, is the inverse of the stiffness c . We shall frequently use this divide notation, $1/c$, instead of the more common inverse notation, c^{-1} . The elastic properties of stiffness and compliance are usually referred to as the elastic constants of a material.

The effective medium

On a macroscopic scale a polycrystal may appear homogeneous or uniform, or perhaps, more generally, its properties appear to vary smoothly. Therefore we shall represent it by an effective medium, which is a model that approximately describes the overall average properties of the medium to some desired degree of accuracy. This then represents a gross description of the polycrystal. We also assume that in

the effective medium the average stress $\langle \sigma \rangle$ and average strain $\langle e \rangle$ are related by the same simple form as Hooke's law for the single crystal

$$\langle \sigma \rangle = C \langle e \rangle, \quad (4)$$

where C is the effective stiffness. So the effective medium is homogeneous. We also assume that it is isotropic and perfectly disordered. The latter means that there is no texture, no characteristic grain shapes, no characteristic grain boundary geometry, no correlations between regions of the medium, such as periodicity. The effective stiffness thus represents the average stiffness of the polycrystal. The bracket notation stands for volume averages,

$$\langle \sigma \rangle = \frac{1}{V} \int_V \sigma dV, \quad \langle e \rangle = \frac{1}{V} \int_V e dV,$$

and so the average stress or strain can almost be regarded as applied fields or boundary conditions. Equation (4) can now be solved for the average strain

$$\langle e \rangle = \frac{\langle \sigma \rangle}{C} = S \langle \sigma \rangle, \quad (5)$$

where S is the effective compliance. We have used the convention, suggested by Kröner [1958], that upper case letters are used for isotropic tensors or matrices that are material properties of the homogeneous effective medium. So upper case letters will represent the average properties of the polycrystal. Lower case letters are used for tensors or matrices that vary locally through the heterogeneous medium or the grains of the polycrystal and thus represent properties of the single crystal.

For an isotropic material there are only two independent elastic constants. Since the effective stiffness is isotropic, its tensor components can be expressed in terms of the two elastic constants as follows

$$C_{ijkl} = K \delta_{ij} \delta_{kl} + G \left(\delta_{ik} \delta_{jl} + \delta_{il} \delta_{jk} - \frac{2}{3} \delta_{ij} \delta_{kl} \right), \quad (6)$$

where K is the effective bulk modulus, G the effective shear modulus, and δ the Kronecker delta defined as follows

$$\delta_{ij} \equiv \begin{cases} 1 & \text{if } i = j \\ 0 & \text{if } i \neq j \end{cases},$$

$$\delta_{kk} \equiv 3.$$

We can solve Equation (6) for K and G . If we calculate the two linear invariants of C we get

$$\begin{cases} C_{iijj} = 9K \\ C_{ijij} = 3K + 10G \end{cases} \quad \text{or} \quad \begin{cases} K = \frac{1}{9} C_{iijj} \\ G = \frac{1}{10} \left(C_{ijij} - \frac{1}{3} C_{iijj} \right). \end{cases} \quad (7)$$

Thus we have expressed the two scalar elastic constants K and G in terms of the two linear invariants of the stiffness tensor C . We can do the same manipulations with the effective compliance tensor

$$S_{ijkl} = \frac{1}{9K} \delta_{ij} \delta_{kl} + \frac{1}{4G} \left(\delta_{ik} \delta_{jl} + \delta_{il} \delta_{jk} - \frac{2}{3} \delta_{ij} \delta_{kl} \right).$$

The linear invariants of S are

$$\begin{cases} S_{iijj} = \frac{1}{K} \\ S_{ijij} = \frac{1}{3K} + \frac{5}{2G} \end{cases} \quad \text{or} \quad \begin{cases} \frac{1}{K} = S_{iijj} \\ \frac{1}{G} = \frac{2}{5} \left(S_{ijij} - \frac{1}{3} S_{iijj} \right). \end{cases} \quad (8)$$

So now we have expressed the two elastic constants also in terms of the two linear invariants of the compliance tensor S .

The Voigt and Reuss models

To get actual expressions for the average elastic constants of a polycrystal in terms of the single crystal elastic constants, the [Voigt 1887] and [Reuss 1929] models are frequently invoked, because they provide an easy way to derive effective elastic constants. Furthermore, Hill [1952] showed that they provide bounds on those constants. Voigt assumed that there is a homogeneous or constant strain in the polycrystal, thus fulfilling compatibility, but not necessarily equilibrium. Reuss assumed a homogeneous or constant stress, thus fulfilling equilibrium, but not necessarily compatibility. For the Voigt model the actual strain is then equal to the average strain,

$$e = \langle e \rangle = \text{constant}, \quad (9)$$

and therefore we can decompose the average of the product of the stiffness and the strain into the product of the average stiffness and the average strain $\langle \sigma \rangle = \langle c \rangle \langle e \rangle$. Comparing with Equation (4) we find that for the Voigt model the effective stiffness is the average crystal stiffness,

$$C_V = \langle c \rangle, \quad (10)$$

which provides an upper bound on C . In the Reuss model we have

$$\sigma = \langle \sigma \rangle = \text{constant}, \quad (11)$$

and so $\langle e \rangle = \langle s \sigma \rangle = \langle s \rangle \langle \sigma \rangle$. Comparing with Equation (5) we find that for the Reuss model the effective compliance is the average crystal compliance,

$$S_R = \langle s \rangle \quad \text{or} \quad C_R = \langle c^{-1} \rangle^{-1}, \quad (12)$$

which provides an upper bound on S and a lower bound on C . To proceed further and get more explicit expressions for Equation (10) and Equation (12), we recall that fourth rank tensors have two linear invariants, and the fundamental property of invariants is that they are scalars and therefore do not depend on orientation in space. Therefore, each invariant is equal to its volume average. So we have

$$c_{iijj} = \langle c_{iijj} \rangle \quad \text{and} \quad c_{ijij} = \langle c_{ijij} \rangle. \quad (13)$$

Combining Equation (7), (10), and (13) we get for the Voigt model the result

$$\begin{aligned} K_V &= \frac{1}{9} c_{iijj}, \\ G_V &= \frac{1}{10} \left(c_{ijij} - \frac{1}{3} c_{iijj} \right). \end{aligned} \quad (14)$$

In detail, we have both in tensor and matrix notation

$$\begin{aligned} 9K_V &= (c_{1111} + c_{2222} + c_{3333}) + 2(c_{1122} + c_{1133} + c_{2233}) = (c_{11} + c_{22} + c_{33}) + 2(c_{12} + c_{13} + c_{23}), \\ 15G_V &= (c_{1111} + c_{2222} + c_{3333}) - (c_{1122} + c_{1133} + c_{2233}) + 3(c_{1212} + c_{1313} + c_{2323}) \\ &= (c_{11} + c_{22} + c_{33}) - (c_{12} + c_{13} + c_{23}) + 3(c_{44} + c_{55} + c_{66}). \end{aligned} \quad (15)$$

We also have for the compliance

$$s_{iijj} = \langle s_{iijj} \rangle \quad \text{and} \quad s_{ijij} = \langle s_{ijij} \rangle. \quad (16)$$

Combining Equation (8), (12), and (16) we get for the Reuss model the result

$$\frac{1}{K_R} = s_{iijj}, \quad \frac{1}{G_R} = \frac{2}{5} \left(s_{ijij} - \frac{1}{3} s_{iijj} \right). \quad (17)$$

In detail, we have

$$\begin{aligned} \frac{1}{K_R} &= (s_{1111} + s_{2222} + s_{3333}) + 2(s_{1122} + s_{1133} + s_{2233}) = (s_{11} + s_{22} + s_{33}) + 2(s_{12} + s_{13} + s_{23}), \\ \frac{15}{G_R} &= 4(s_{1111} + s_{2222} + s_{3333}) - 4(s_{1122} + s_{1133} + s_{2233}) + 3(s_{1212} + s_{1313} + s_{2323}) \\ &= 4(s_{11} + s_{22} + s_{33}) - 4(s_{12} + s_{13} + s_{23}) + 3(s_{44} + s_{55} + s_{66}). \end{aligned} \quad (18)$$

Hearmon [1961] has also derived these explicit equations, but by a different method. Hill [1952] showed that the Voigt and Reuss averages formed the least upper bound and the greatest lower bound, respectively, for the aggregate polycrystal.

Cubic polycrystal. For the special case of a cubic polycrystal, the Voigt relations (15) reduce to

$$3K_V = c_{11} + 2c_{12}, \quad 5G_V = c_{11} - c_{12} + 3c_{44}. \quad (19)$$

and the Reuss relations, Equation (18), become

$$\frac{1}{3K_R} = s_{11} + 2s_{12}, \quad \frac{5}{G_R} = 4(s_{11} - s_{12}) + 3s_{44}. \quad (20)$$

The Voigt and Reuss bulk moduli are identical in this case, $K_V = K_R$, and also equal to the single crystal and effective polycrystal bulk modulus. This is only true for cubic symmetry; for other crystal symmetries, the various estimates of the effective bulk modulus differ from each other.

Thermal expansion

Tomé [1998] showed how thermal expansion can be incorporated into the elastic equations. The stress in Hooke's law is related to the elastic strain, so in this case the total strain must be adjusted for the effects of the thermal expansion in order to get the elastic strain. Equation (3) for the single crystal is therefore modified to

$$\sigma = c(e - \alpha \delta T), \quad (21)$$

where α is the single crystal thermal expansion coefficient, a second rank tensor or a (6×1) vector, and δT is a small temperature change that takes place uniformly throughout material. Equation (4) for the effective medium is modified to

$$\langle \sigma \rangle = C(\langle e \rangle - A\delta T), \quad (22)$$

where A is the average thermal expansion coefficient of the effective medium. We emphasize the fact that α and A are tensors or (6×1) vectors by writing them **boldface** to distinguish them from the scalars below. Equation (21) can be solved for the local strain in the single crystal,

$$e = s\sigma + \alpha\delta T, \quad (23)$$

and Equation (22) for the average strain in the effective medium,

$$\langle e \rangle = S\langle \sigma \rangle + A\delta T. \quad (24)$$

The stress or strain and the temperature change in these equations can be applied arbitrarily and therefore these quantities will be treated as independent variables.

The Voigt model. With Voigt's assumption of constant strain, Equation (9), Equations (21) and (22) lead to $C_V\langle e \rangle - C_V A_V\delta T = \langle c \rangle\langle e \rangle - \langle c\alpha \rangle\delta T$. Since this equation holds for an arbitrary average strain $\langle e \rangle$ and an arbitrary temperature change δT , we can equate their coefficients. The first equality gives the relation Equation (10), which we already found without taking the influence of a temperature change into account. The second equality is

$$C_V A_V = \langle c\alpha \rangle \quad \text{or} \quad A_V = \frac{\langle c\alpha \rangle}{C_V} = S_V \langle c\alpha \rangle. \quad (25)$$

Tomé [1998] also found this result. Since the effective thermal expansion coefficient is isotropic, it can be expressed as $A_{ij} = A\delta_{ij}$, where A is the scalar effective thermal expansion coefficient. With the help of Equation (6), we can derive the relation

$$A = \frac{1}{9K} C_{iikl} A_{kl}. \quad (26)$$

We now take the linear invariant of Equation (25) and substitute it into Equation (26), remembering that the invariant is equal to its average, to get the effective thermal expansion coefficient for the Voigt model

$$A_V = \frac{1}{9K_V} c_{iikl} \alpha_{kl}. \quad (27)$$

In detail we have in both tensor and matrix notation

$$\begin{aligned} 9K_V A_V &= (c_{1111} + c_{1122} + c_{1133})\alpha_{11} + (c_{1122} + c_{2222} + c_{2233})\alpha_{22} \\ &\quad + (c_{1133} + c_{2233} + c_{3333})\alpha_{33} + 2(c_{1112} + c_{1222} + c_{1233})\alpha_{12} \\ &\quad + 2(c_{1113} + c_{1333} + c_{2213})\alpha_{13} + 2(c_{1123} + c_{2223} + c_{2333})\alpha_{23}, \\ &= (c_{11} + c_{12} + c_{13})\alpha_1 + (c_{12} + c_{22} + c_{23})\alpha_2 + (c_{13} + c_{23} + c_{33})\alpha_3 \\ &\quad + 2(c_{14} + c_{24} + c_{34})\alpha_4 + 2(c_{15} + c_{25} + c_{35})\alpha_5 + 2(c_{16} + c_{26} + c_{36})\alpha_6. \end{aligned} \quad (28)$$

Note that the effective thermal expansion coefficient of a polycrystal is coupled to the elastic constants in the Voigt model. For crystal structures where the off-diagonal terms of the elastic constant matrix vanish, such as cubic, hexagonal, tetragonal, and orthorhombic, the second line of Equation (28) vanishes and the equation simplifies considerably.

The Reuss model. With Reuss' assumption of constant stress, Equation (11), Equations (23) and (24) lead to $S_R\langle\sigma\rangle + A_R\delta T = \langle s\rangle\langle\sigma\rangle + \langle\alpha\rangle\delta T$. Since this equation holds for arbitrary average stress $\langle\sigma\rangle$ and arbitrary temperature change δT , we can equate their coefficients. The first equality gives the relation Equation (12), which we already found without the influence of temperature. The second equality is

$$A_R = \langle\alpha\rangle. \quad (29)$$

Tomé [1998] also found this result. The linear invariant of this equation is

$$A_R = \frac{1}{3}\alpha_{ii}. \quad (30)$$

In detail, we have the simple result

$$A_R = \frac{1}{3}(\alpha_{11} + \alpha_{22} + \alpha_{33}) = \frac{1}{3}(\alpha_1 + \alpha_2 + \alpha_3). \quad (31)$$

So in the Reuss model the overall thermal properties are independent of the elastic properties.

Eshelby's theory

To obtain a self-consistent estimate of the effective properties we use Eshelby's theory of elastic inclusions and inhomogeneities [Eshelby 1961]. That is the method Kröner [1958] first used to get a solution for the cubic polycrystal. Kröner [1972] later used statistical continuum mechanics to derive the same as well as additional results. The subject of inclusions, inhomogeneities, and the equivalent inclusion has been treated in detail by Mura [1982]. In the present treatment we also include Tomé's contribution for thermal expansion [Tomé 1998].

The inclusion. Consider an infinitely extended homogeneous material in domain D with elastic constants C everywhere, containing a domain Ω with a stress-free strain e^P , which is called the transformed inclusion. This inclusion causes a local stress σ' and strain e' , which are related by Hooke's law

$$\begin{aligned} \sigma' &= C(e' - e^P), & \text{in } \Omega, \\ \sigma' &= Ce', & \text{in } D - \Omega. \end{aligned}$$

If e^P is uniform and Ω is an ellipsoid, then the stress σ' and strain e' are also uniform in Ω and related to e^P by

$$e' = Ee^P, \quad \text{in } \Omega, \quad (32)$$

where E is the Eshelby tensor, which is a constant. Let us apply a stress $\bar{\sigma}$ at infinity with a corresponding strain \bar{e} , and a temperature change δT . The bar is used to denote that these quantities will be overall average values. They are related by Hooke's law $\bar{\sigma} = C(\bar{e} - A\delta T)$. The resulting total stress σ is then given by

$$\begin{aligned} \sigma &= \bar{\sigma} + \sigma' = C(\bar{e} + e' - e^P - A\delta T), & \text{in } \Omega, \\ \sigma &= \bar{\sigma} + \sigma' = C(\bar{e} + e' - A\delta T), & \text{in } D - \Omega. \end{aligned} \quad (33)$$

The prime represents deviations from the average value.

The inhomogeneity. Consider an infinitely extended material in domain D with the elastic constants C and thermal expansion A containing a domain Ω with the elastic constants c and thermal expansion α , which is called an inhomogeneity. We investigate the disturbance in an applied stress and temperature increment caused by the presence of this inhomogeneity. Let us again denote the applied stress at infinity by $\bar{\sigma}$ and the corresponding strain by \bar{e} , and the temperature increment by δT , while the stress disturbance and the strain disturbance are denoted by σ' and e' , respectively. The total stress (actual stress) is σ , and the total strain is e . Hooke's law is written as

$$\begin{aligned}\sigma &= \bar{\sigma} + \sigma' = c(e - \alpha\delta T) = c(\bar{e} + e' - \alpha\delta T), & \text{in } \Omega, \\ \sigma &= \bar{\sigma} + \sigma' = C(e - A\delta T) = C(\bar{e} + e' - A\delta T), & \text{in } D - \Omega.\end{aligned}\quad (34)$$

The equivalent inclusion. The equivalent inclusion is a method to determine the stress disturbance of the inhomogeneity using the result of the inclusion. So the inclusion has been introduced arbitrarily in order to simulate the inhomogeneity problem. In an applied stress or strain field, the inhomogeneity looks like an inclusion. The necessary and sufficient condition for the equivalency of the stresses and strains in the above two problems of inhomogeneity and inclusion is

$$c(\bar{e} + e' - \alpha\delta T) = C(\bar{e} + e' - e^P - A\delta T), \quad \text{in } \Omega. \quad (35)$$

This equation can be solved for e' when the transformed inclusion problem, Equation (32), in the homogeneous material is solved for E . After obtaining e' , the stress σ can be found from Equation (34) or Equation (33). If $\bar{\sigma}$ is a uniform stress and δT a uniform temperature change, e^P is also uniform in Ω and Eshelby's Equation (32) can be used. Substitution of Equation (32) into Equation (35) gives

$$c(\bar{e} + e' - \alpha\delta T) = C\left(\bar{e} + e' - \frac{e'}{E} - A\delta T\right), \quad \text{in } \Omega.$$

The solution of this equation for the strain disturbance is

$$e' = E \frac{-\delta c \bar{e} + (c\alpha - CA)\delta T}{\delta c E + C}, \quad (36)$$

where we have defined $\delta c \equiv c - C$. So Equation (36) represents the local strain disturbance at the inhomogeneity when a uniform strain \bar{e} and temperature change δT is applied to the domain.

The self-consistent model

We now take the equivalent inclusion to represent a grain in the polycrystal. The interpretation of Equation (36) is then as follows. The applied strain \bar{e} and temperature change δT cause a strain disturbance e' in the grain because the local elastic and thermal properties of the grain differ from the average elastic and thermal properties of the polycrystal. The condition for self-consistency is that the average grain response is the same as the overall average for the polycrystal, or that the average disturbance vanishes:

$\langle e' \rangle = \mathbf{0}$. Since \bar{e} and δT are independent and E is constant, we then get from Equation (36)

$$\left\langle \frac{\delta c}{\delta c E + C} \right\rangle = \mathbf{0}, \quad (37)$$

$$\left\langle \frac{c\alpha - CA}{\delta c E + C} \right\rangle = \mathbf{0}. \quad (38)$$

These equations are consistent with those of Tomé [1998]. Equation (37) is an implicit equation for the self-consistent effective elastic stiffness C . For cubic crystal symmetry it leads to a cubic equation for the self-consistent effective shear modulus, discussed below. It can also be solved for lower crystal symmetries, but then leads to a pair of high-order coupled equations for the effective bulk and shear modulus. For example, for hexagonal symmetry it leads to one equation that is quadratic in both K and G , and another equation that is quadratic in K and sixth order in G . In general, the simpler equation can be solved for K in terms of G and the result substituted into the other equation. It is then best to solve this latter equation numerically rather than symbolically. There are many solutions, but usually there is only one real positive one. The expression Equation (38) can be solved as

$$\mathbf{A} = \frac{\left\langle \frac{c\alpha}{\delta c E + C} \right\rangle}{\left\langle \frac{C}{\delta c E + C} \right\rangle}, \quad (39)$$

once the stiffness C has been obtained. For numerical purposes, this equation is rather tedious and lengthy. The calculation can be simplified as follows. If we define the (6×1) vector

$$\mathbf{v} = \frac{c\alpha}{\delta c E + C},$$

and the (6×6) matrix

$$\mathbf{M} = \left\langle \frac{C}{\delta c E + C} \right\rangle,$$

then the scalar effective thermal expansion coefficient is given by

$$A = \frac{v_1 + v_2 + v_3}{3(M_{11} + 2M_{12})}. \quad (40)$$

Upper limit. If we assume that the inhomogeneity is very soft, that is, $E = \mathbf{0}$, then Equations (37) and (39) reduce to

$$\langle c - C \rangle = \mathbf{0}, \quad \text{and} \quad \mathbf{A} = \left\langle \frac{c\alpha}{C} \right\rangle,$$

which reduce to the Voigt solutions, Equation (10) and Equation (25).

Lower limit. If we assume the inhomogeneity is very hard, $E = \mathbf{I}$, then Equation (37) and Equation (39) reduce to

$$\left\langle \frac{c - C}{c} \right\rangle = \mathbf{0}, \quad \mathbf{A} = \left\langle \frac{C}{c} \right\rangle^{-1} \langle \alpha \rangle, \quad (41)$$

which reduce to the Reuss solutions, Equation (12) and Equation (29), when we note that from Equation (41) we have

$$\left\langle \frac{C}{c} \right\rangle^{-1} = \mathbf{I}. \quad (42)$$

The Walpole notation

Walpole [1981] introduced a notation that greatly simplifies symbolic manipulations for isotropic and cubic materials. A fourth-order tensor will generally have a structure that reflects some underlying geometric symmetry, like that of a crystal. An appropriate decomposition of the structure of a tensor can reflect valuable physical insight while offering to simplify greatly the calculation of various inverses and inner products. Isotropic tensors are the principal ones to be prepared for in detailed calculations and there is a smaller role for anisotropic tensors that reflect the symmetry of cubic crystals.

Isotropic case. Walpole decomposed unity as $\mathbf{I} = \mathbf{J} + \mathbf{K}$. In terms of fourth rank tensors these symbols are defined as

$$I_{ijkl} \equiv \frac{1}{2}(\delta_{ik}\delta_{jl} + \delta_{il}\delta_{jk}), \quad J_{ijkl} \equiv \frac{1}{3}\delta_{ij}\delta_{kl},$$

$$K_{ijkl} \equiv \frac{1}{2}\left(\delta_{ik}\delta_{jl} + \delta_{il}\delta_{jk} - \frac{2}{3}\delta_{ij}\delta_{kl}\right).$$

In terms of (6×6) matrices we have the definitions

$$\mathbf{I} \equiv \begin{pmatrix} 1 & 0 & 0 & 0 & 0 & 0 \\ 0 & 1 & 0 & 0 & 0 & 0 \\ 0 & 0 & 1 & 0 & 0 & 0 \\ 0 & 0 & 0 & 1 & 0 & 0 \\ 0 & 0 & 0 & 0 & 1 & 0 \\ 0 & 0 & 0 & 0 & 0 & 1 \end{pmatrix}, \quad \mathbf{J} \equiv \begin{pmatrix} \frac{1}{3} & \frac{1}{3} & \frac{1}{3} & 0 & 0 & 0 \\ \frac{1}{3} & \frac{1}{3} & \frac{1}{3} & 0 & 0 & 0 \\ \frac{1}{3} & \frac{1}{3} & \frac{1}{3} & 0 & 0 & 0 \\ 0 & 0 & 0 & 0 & 0 & 0 \\ 0 & 0 & 0 & 0 & 0 & 0 \\ 0 & 0 & 0 & 0 & 0 & 0 \end{pmatrix}, \quad \mathbf{K} \equiv \begin{pmatrix} \frac{2}{3} & -\frac{1}{3} & -\frac{1}{3} & 0 & 0 & 0 \\ -\frac{1}{3} & \frac{2}{3} & -\frac{1}{3} & 0 & 0 & 0 \\ -\frac{1}{3} & -\frac{1}{3} & \frac{2}{3} & 0 & 0 & 0 \\ 0 & 0 & 0 & 1 & 0 & 0 \\ 0 & 0 & 0 & 0 & 1 & 0 \\ 0 & 0 & 0 & 0 & 0 & 1 \end{pmatrix}.$$

The decomposition is idempotent and orthogonal:

$$\mathbf{J}\mathbf{J} = \mathbf{J}, \quad \mathbf{K}\mathbf{K} = \mathbf{K}, \quad \mathbf{J}\mathbf{K} = \mathbf{K}\mathbf{J} = \mathbf{0}.$$

The linear invariants are

$$I_{iijj} = 3, \quad J_{iijj} = 3, \quad K_{iijj} = 0,$$

$$I_{ijij} = 6, \quad J_{ijij} = 1, \quad K_{ijij} = 5. \quad (43)$$

In the matrix notation the first invariant is the sum of all elements in the upper left quadrant, and the second invariant is the sum of all the diagonal elements. With this notation the effective stiffness, Equation (6), can now be written in symbolic notation

$$\mathbf{C} = 3\mathbf{K}\mathbf{J} + 2\mathbf{G}\mathbf{K}. \quad (44)$$

We see that decomposition reflects a split into an isotropic or dilatational part and a deviatoric or shear part. The Eshelby tensor for a spherical inclusion can be found in many texts [Kröner 1958; Eshelby 1961; Kröner 1972; Walpole 1981; Mura 1982; Tomé 1998] and in this notation it can be written

$$\mathbf{E} = \frac{3K}{4G + 3K}\mathbf{J} + \frac{6}{5}\frac{2G + K}{4G + 3K}\mathbf{K}.$$

Cubic symmetry. For a cubic crystal, Walpole further decomposed \mathbf{K} as $\mathbf{K} = \mathbf{K}' + \mathbf{K}''$. For the tensor definitions of these symbols see Walpole. In terms of (6×6) matrices,

$$\mathbf{K}' \equiv \begin{pmatrix} \frac{2}{3} & -\frac{1}{3} & -\frac{1}{3} & 0 & 0 & 0 \\ -\frac{1}{3} & \frac{2}{3} & -\frac{1}{3} & 0 & 0 & 0 \\ -\frac{1}{3} & -\frac{1}{3} & \frac{2}{3} & 0 & 0 & 0 \\ 0 & 0 & 0 & 0 & 0 & 0 \\ 0 & 0 & 0 & 0 & 0 & 0 \\ 0 & 0 & 0 & 0 & 0 & 0 \end{pmatrix}, \quad \mathbf{K}'' \equiv \begin{pmatrix} 0 & 0 & 0 & 0 & 0 & 0 \\ 0 & 0 & 0 & 0 & 0 & 0 \\ 0 & 0 & 0 & 0 & 0 & 0 \\ 0 & 0 & 0 & 1 & 0 & 0 \\ 0 & 0 & 0 & 0 & 1 & 0 \\ 0 & 0 & 0 & 0 & 0 & 1 \end{pmatrix}.$$

This decomposition is also idempotent and orthogonal:

$$\begin{aligned} \mathbf{K}' \mathbf{K}' &= \mathbf{K}', \\ \mathbf{K}'' \mathbf{K}'' &= \mathbf{K}'', \\ \mathbf{K}' \mathbf{K}'' &= \mathbf{K}'' \mathbf{K}' = \mathbf{0}, \\ \mathbf{J} \mathbf{K}' &= \mathbf{K}' \mathbf{J} = \mathbf{0}, \\ \mathbf{J} \mathbf{K}'' &= \mathbf{K}'' \mathbf{J} = \mathbf{0}. \end{aligned} \quad (45)$$

The linear invariants are

$$\begin{aligned} K'_{iijj} &= 0, & K''_{iijj} &= 0, \\ K'_{ijij} &= 2, & K''_{ijij} &= 3. \end{aligned} \quad (46)$$

With this notation the cubic crystal elastic stiffness can be written in a form that resembles the isotropic case

$$c = 3\kappa \mathbf{J} + 2\mu' \mathbf{K}' + 2\mu'' \mathbf{K}'', \quad (47)$$

where κ is the bulk modulus. Here μ' and μ'' are the $\{001\}\langle 110 \rangle$ and $\{001\}\langle 100 \rangle$ shear resistance of the crystal, respectively. For cubic crystals these moduli can be regarded as more fundamental elastic constants than the stiffness and compliance. They are related as follows

$$\begin{aligned} \kappa &= \frac{1}{3} (c_{11} + 2c_{12}) = \frac{1}{3(s_{11} + 2s_{12})}, \\ \mu' &= \frac{1}{2} (c_{11} - c_{12}) = \frac{1}{2(s_{11} - s_{12})}, \\ \mu'' &= c_{44} = \frac{1}{s_{44}}. \end{aligned} \quad (48)$$

The relations Equation (45) make it simple to calculate inverses, such as the elastic compliance

$$s = \frac{1}{c} = \frac{\mathbf{J}}{3\kappa} + \frac{\mathbf{K}'}{2\mu'} + \frac{\mathbf{K}''}{2\mu''}. \quad (49)$$

To prove this relation, take the matrix product of Equations (47) and (49) and show that it is unity.

Cubic crystal symmetry

We next apply some of the foregoing equations to the special case of cubic symmetry. For cubic symmetry, the results are much simpler than for all the lower crystal structures.

Voigt model. We illustrate the application of the concepts first to the Voigt model. From Equations (14), (47), (43), and (46) we have $K_V = \kappa$, and

$$G_V = \frac{2}{5} \mu' + \frac{3}{5} \mu'' \quad (50)$$

These results are the same as Equation (19). Furthermore, Equation (50) illustrates a general rule for averaging the cubic shear components, that is, take two fifths the coefficient of \mathbf{K}' plus three fifths the coefficient of \mathbf{K}'' .

Reuss model. For the Reuss model, we have from Equations (49), (43), and (46) $K_R = \kappa$ and

$$\frac{5}{G_R} = \frac{2}{\mu'} + \frac{3}{\mu''} \quad (51)$$

These results are the same as Equation (20). Equation (51) illustrates the general rule mentioned above.

Self-consistent model. In terms of the Walpole notation we have from Equation (44) and Equation (47)

$$\delta c \equiv c - C = 3(\kappa - K)\mathbf{J} + 2(\mu' - G)\mathbf{K}' + 2(\mu'' - G)\mathbf{K}''.$$

Using this we can also write

$$\frac{C}{\delta c} = \frac{K}{\kappa - K} \mathbf{J} + \frac{G}{\mu' - G} \mathbf{K}' + \frac{G}{\mu'' - G} \mathbf{K}''.$$

Therefore

$$\frac{\delta c}{\delta c E + C} = \frac{\mathbf{I}}{E + \frac{C}{\delta c}} = \frac{\mathbf{J}}{\frac{3K}{4G+3K} + \frac{K}{\kappa-K}} + \frac{\mathbf{K}'}{\frac{6}{5} \frac{2G+K}{4G+3K} + \frac{G}{\mu'-G}} + \frac{\mathbf{K}''}{\frac{6}{5} \frac{2G+K}{4G+3K} + \frac{G}{\mu''-G}} \quad (52)$$

Setting the average equal to zero, Equation (37), we have

$$\frac{\mathbf{J}}{\frac{3K}{4G+3K} + \frac{K}{\kappa-K}} + \frac{2}{5} \frac{\mathbf{K}}{\frac{6}{5} \frac{2G+K}{4G+3K} + \frac{G}{\mu'-G}} + \frac{3}{5} \frac{\mathbf{K}}{\frac{6}{5} \frac{2G+K}{4G+3K} + \frac{G}{\mu''-G}} = \mathbf{0}.$$

Since \mathbf{J} and \mathbf{K} are independent, their coefficients must vanish separately

$$\frac{1}{\frac{3K}{4G+3K} + \frac{K}{\kappa-K}} = 0, \quad \frac{2}{5} \frac{6}{5} \frac{2G+K}{4G+3K} + \frac{G}{\mu'-G} + \frac{3}{5} \frac{6}{5} \frac{2G+K}{4G+3K} + \frac{G}{\mu''-G} = 0.$$

The first equation can also be obtained by setting the first invariant of Equation (52) equal to zero, and has the solution

$$K = \kappa \quad (53)$$

The second equation can also be found by setting the second invariant of Equation (52) equal to zero, and can be reduced to the form

$$8G^3 + (9\kappa + 4\mu')G^2 - 3(\kappa + 4\mu')\mu''G - 6\kappa\mu'\mu'' = 0. \quad (54)$$

This is a cubic equation for the self-consistent effective shear modulus G of a cubic polycrystal that is statistically homogeneous, isotropic, and perfectly disordered. It was first obtained by Kröner [1958]. Hershey [1954] previously obtained a quartic equation that included Equation (54) as a factor.

The solution. There are general closed form solutions for cubic equations. If we write Equation (54) as follows

$$\gamma_3 G^3 + \gamma_2 G^2 + \gamma_1 G + \gamma_0 = 0, \quad (55)$$

with the coefficients

$$\begin{aligned} \gamma_3 &\equiv 8, & \gamma_2 &\equiv 9\kappa + 4\mu', \\ \gamma_1 &\equiv -3(\kappa + 4\mu')\mu'', & \gamma_0 &\equiv -6\kappa\mu'\mu'', \end{aligned} \quad (56)$$

and define

$$p \equiv \sqrt{\left(\frac{\gamma_2}{3}\right)^2 - \frac{\gamma_1\gamma_3}{3}}, \quad q \equiv -2\left(\frac{\gamma_2}{3}\right)^3 + \frac{\gamma_1\gamma_2\gamma_3}{3} - \gamma_0\gamma_3^2, \quad (57)$$

then the only nonnegative solution of Equation (55) for the effective self-consistent shear modulus of a cubic polycrystal is

$$G = 2\frac{p}{\gamma_3} \cos\left[\frac{1}{3} \arccos\left(\frac{q}{2p^3}\right)\right] - \frac{\gamma_2}{3\gamma_3}. \quad (58)$$

It is now straightforward to calculate the average cubic polycrystal shear modulus from the single crystal elastic constants. Ledbetter calls this approach the Hershey–Kröner–Eshelby model. He measured elastic constants for copper [Ledbetter 1981] and stainless steel [Ledbetter 1984] and found that among nine different averaging models this model works best.

Thermal expansion. For a cubic crystal the thermal expansion coefficient is isotropic: $\alpha_{ij} = \alpha\delta_{ij}$. Therefore all cases, that is the Voigt model Equation (27), the Reuss model Equation (30), and the self-consistent model Equation (38), reduce to $A = \alpha$. Since the thermal expansion is isotropic in cubic crystals there is no difference between the polycrystal and the single crystal.

Some numerical results for cubic crystals. Table 1 shows the single crystal elastic constants of several cubic crystals at room temperature. The values are obtained from the handbook by Simmons and Wang [1971] except that those for calcium are from [Ledbetter and Kim 2001].

We have chosen a set of materials covering a wide range of anisotropy, where the Zener anisotropy factor is given from the formula [Zener 1948]

$$A = \frac{\mu''}{\mu'} = \frac{2c_{44}}{c_{11} - c_{12}} = \frac{2(s_{11} - s_{12})}{s_{44}}.$$

Table 2 shows values of the average bulk and shear modulus for cubic polycrystals calculated from the data in Table 1, using Equations (48), (53), (50), (51), (56), (57), and (58). The Voigt and Reuss values

Material	c_{11}	c_{12}	c_{44}	Anisotropy
Aluminum	1.073	0.609	0.283	1.22
Calcium	1.076	0.125	0.5758	1.21
Calcium Fluoride	1.628	0.433	0.334	0.56
Copper	1.684	1.214	0.754	3.21
Diamond	9.5	3.9	4.3	1.54
Gold	1.7893	1.4863	0.4367	2.88
Lead	0.466	0.392	0.1441	3.89
Lithium	0.135	0.1144	0.0878	8.52
Silver	1.24	0.934	0.461	3.01
Silver Chloride	0.601	0.362	0.0625	0.52
Sodium	0.0526	0.0404	0.0426	6.98
Sodium Chloride	0.487	0.124	0.126	0.69

Table 1. Single crystal elastic constants for several cubic crystals in units of Mbar.

Material	K	G_V	G_R	G_{VRH}	G_S
Aluminum	0.764	0.263	0.260	0.261	0.261
Calcium	0.442	0.536	0.531	0.533	0.533
Calcium Fluoride	0.831	0.439	0.406	0.423	0.422
Copper	1.371	0.546	0.400	0.473	0.482
Diamond	5.767	3.700	3.541	3.621	3.625
Gold	1.587	0.323	0.249	0.286	0.292
Lead	0.416	0.101	0.067	0.084	0.087
Lithium	0.121	0.057	0.022	0.039	0.040
Silver	1.036	0.338	0.255	0.297	0.302
Silver Chloride	0.442	0.085	0.077	0.081	0.081
Sodium	0.045	0.028	0.013	0.020	0.021
Sodium Chloride	0.245	0.148	0.144	0.146	0.146

Table 2. Average elastic constants for several cubic polycrystals in units of Mbar. The bulk modulus is denoted by K and the shear modulus by G . The subscripts denote Voigt (V), Reuss (R), Hill (VRH), and self-consistent (S).

always bracket the self-consistent value. The Hill average is defined as the arithmetic mean of the Voigt and Reuss average [Hill 1952]:

$$G_{VRH} = \frac{1}{2} (G_V + G_R).$$

It is often close to the self-consistent value, G_S . More exhaustive listings are given in [Kröner 1972] and [Ledbetter and Kim 2001].

Other crystal symmetries

For symmetries lower than cubic, Equation (37) is better solved numerically. Tables 3 and 4 give the single crystal elastic constants and thermal expansion coefficients of several different crystal structures at room temperature [Simmons and Wang 1971; Krishnan et al. 1979].

The anisotropy factor for these crystal structures is a generalization of the Zener factor and is given by

$$AI = \frac{2(c_{44} + c_{55} + c_{66})}{c_{11} + c_{22} + c_{33} - c_{12} - c_{13} - c_{23}}.$$

To obtain the self-consistent values, Equation (37) is solved simultaneously for the bulk modulus, K , and the shear modulus, G , which are then denoted by K_S and G_S . The results are given in Table 5. The Voigt and Reuss values are given by Equations (15) and (18). As before, the Hill values are the arithmetic mean of the Voigt and Reuss averages, and lie close to the self-consistent values.

Material	Crystal	c_{11}	c_{12}	c_{13}	c_{23}	c_{14}	c_{22}
Titanium	hexagonal	1.624	0.92	0.69	0.69	0.0	1.624
Zirconium	hexagonal	1.434	0.728	0.653	0.653	0.0	1.434
Indium	tetragonal	0.445	0.395	0.405	0.405	0.0	0.445
Tin	tetragonal	0.86	0.35	0.3	0.3	0.0	0.86
Calcite	trigonal	1.4626	0.597	0.5076	0.5076	-0.2076	1.4626
Quartz	trigonal	0.8501	0.0696	0.1412	0.1412	0.1678	0.8501
Aragonite	orthorhombic	1.5958	0.3663	0.0197	0.1591	0.0	0.8697
Uranium	orthorhombic	2.148	0.465	0.218	1.076	0.0	1.986

Table 3. Single crystal elastic constants for several crystals in units of Mbar.

Material	c_{33}	c_{44}	c_{55}	c_{66}	Anisotropy	α_1	α_2	α_3
Titanium	1.807	0.467	0.467	0.352	0.93	9.55	9.55	10.65
Zirconium	1.648	0.32	0.32	0.353	0.80	5.7	5.7	11.4
Indium	0.444	0.0655	0.0655	0.122	3.92	1.2	1.3	-0.81
Tin	1.33	0.49	0.49	0.53	1.44	14.64	14.64	28.14
Calcite	0.8531	0.3405	0.3405	0.4328	1.03	-5.6	-5.6	25
Quartz	1.0535	0.5722	0.5722	0.39025	1.28	13	13	8
Aragonite	0.8503	0.4132	0.2564	0.4274	0.79	35	17	10
Uranium	2.671	1.244	0.734	0.743	1.08	25.41	0.65	20.65

Table 4. Single crystal elastic constants in units of Mbar and thermal expansion coefficients in units of $10^{-6}K^{-1}$ for several crystals.

Material	K_V	K_R	K_{VRH}	K_S	G_V	G_R	G_{VRH}	G_S
Titanium	1.073	1.073	1.073	1.073	0.441	0.426	0.434	0.434
Zirconium	0.954	0.952	0.953	0.953	0.364	0.356	0.360	0.360
Indium	0.416	0.416	0.416	0.416	0.0592	0.0372	0.0482	0.0491
Tin	0.550	0.535	0.543	0.542	0.442	0.410	0.426	0.428
Calcite	0.778	0.716	0.747	0.750	0.367	0.269	0.318	0.315
Quartz	0.384	0.377	0.381	0.381	0.467	0.405	0.436	0.433
Aragonite	0.490	0.447	0.468	0.464	0.404	0.367	0.385	0.383
Uranium	1.147	1.114	1.131	1.128	0.881	0.807	0.844	0.842

Table 5. Average elastic constants for several polycrystals in units of Mbar. The bulk modulus is denoted by K and the shear modulus by G . The subscripts denote Voigt (V), Reuss (R), Hill (VRH), and self-consistent (S).

Table 6 shows the effective thermal expansion coefficients calculated from Equations (28), (31), and (40).

Summary

The concept of effective medium and effective material properties has been described, in particular for elastic constants and thermal expansion. The effective properties are used to represent the overall average properties of a polycrystal. The concept is then applied to the particular cases of the Voigt, Reuss, and self-consistent models to obtain expressions for the overall average properties of a polycrystal in terms of the single crystal components. The self-consistent model is derived by invoking Eshelby's theory of inclusion and inhomogeneities. It gives an implicit equation for the self-consistent elastic constants and an explicit equation for the self-consistent thermal expansion coefficient. A brief description is given of the Walpole notation for isotropic and cubic materials. For the particular case of cubic symmetry the

Material	A_V	A_R	A_{VRH}	A_S	Crystal
Titanium	9.913	9.917	9.915	9.915	hexagonal
Zirconium	7.662	7.600	7.631	7.629	hexagonal
Indium	0.527	0.530	0.528	0.527	tetragonal
Tin	19.90	19.14	19.52	19.52	tetragonal
Calcite	2.564	4.60	3.582	3.440	trigonal
Quartz	11.07	11.33	11.20	11.20	trigonal
Aragonite	23.46	20.67	22.06	21.79	orthorhombic
Uranium	15.12	15.57	15.34	15.39	orthorhombic

Table 6. Average thermal expansion coefficients in units of $10^{-6}K^{-1}$ for several polycrystals of different crystal symmetries.

bulk modulus and thermal expansion are isotropic and the self-consistent shear modulus satisfies a cubic equation, which can be solved explicitly. Some numerical results calculated from the solution are listed. For lower crystal symmetries, the equations are solved numerically. Results are given for the average bulk modulus, shear modulus, and thermal expansion coefficients of various hexagonal, tetragonal, trigonal, and orthorhombic polycrystals. In general, it is found that the Hill average is close to the self-consistent value.

References

- [Eshelby 1961] J. D. Eshelby, “Elastic inclusions and inhomogeneities”, *Prog. Solid Mech.* **2** (1961), 87–140.
- [Hearmon 1961] R. F. S. Hearmon, *An introduction to applied anisotropic elasticity*, Oxford University Press, Oxford, 1961.
- [Hershey 1954] A. V. Hershey, “The elasticity of an isotropic aggregate of anisotropic cubic crystals”, *J. Appl. Mech.* **21** (1954), 236–240.
- [Hill 1952] R. Hill, “The elastic behavior of a crystalline aggregate”, pp. 349–354 in *Proceedings of the Physical society*, vol. A65, 1952.
- [Krishnan et al. 1979] R. S. Krishnan, R. Srinivasan, and S. Devanarayanan, *Thermal expansion of crystals*, Pergamon Press, Oxford, New York, Toronto, Sydney, Paris, Frankfurt, 1979.
- [Kröner 1958] E. Kröner, “Berechnung der elastischen Konstanten des Vielkristalls aus dem Konstanten des Einkristalls”, *Z. Phys.* **151** (1958), 504–518.
- [Kröner 1972] E. Kröner, *Statistical continuum mechanics*, Springer Verlag, New York, 1972. International Centre for Mechanical Sciences, Courses and Lectures No. 92, Course held at the Department of General Mechanics, October 1971, Udine.
- [Ledbetter 1981] H. M. Ledbetter, “Elastic constants of polycrystalline copper at low temperatures, relationship to single-crystal elastic constants”, *phys. status solidi A* **66** (1981), 477–484.
- [Ledbetter 1984] H. M. Ledbetter, “Monocrystal-polycrystal elastic constants of a stainless steel”, *phys. status solidi A* **85** (1984), 89–96.
- [Ledbetter and Kim 2001] H. Ledbetter and S. Kim, “Monocrystal elastic constants and derived properties of the cubic and the hexagonal elements”, Chapter 7, pp. 97–106 in *Properties of solids, liquids, and gases, volume II: elastic properties of solids: theory, elements and compounds, novel materials, technological materials, alloys, and building materials*, edited by M. Levy et al., Academic Press, New York, 2001.
- [Mura 1982] T. Mura, *Micromechanics of defects in solids*, Martinus Nijhoff Publishers, The Hague, Boston, London, 1982.
- [Nye 1960] J. F. Nye, *Physical properties of crystals*, Oxford University Press, Oxford, 1960.
- [Reuss 1929] A. Reuss, “Berechnung der Fließgrenze von Mischkristallen auf Grund der Plastizitätsbedingungen für Einkristalle”, *Z. ang. Math. und Mech.* **9** (1929), 49–58.
- [Simmons and Wang 1971] G. Simmons and H. Wang, *Single crystal elastic constants and calculated aggregate properties: A HANDBOOK*, 2nd ed., THE M.I.T. PRESS, Cambridge, Massachusetts, and London, England, 1971.
- [Tomé 1998] C. N. Tomé, “Tensor properties of textured polycrystals”, Chapter 7, pp. 282–324 in *Texture and anisotropy*, edited by U. F. Kocks et al., Cambridge University Press, 1998.
- [Voigt 1887] W. Voigt, “Theoretische Studien über die Elastizitätsverhältnisse der Kristalle”, *Abh. Kgl. Ges. Wis. Göttingen, Math. Kl.* **34**:1 (1887), 1–155.
- [Walpole 1981] L. J. Walpole, “Elastic behavior of composite materials: theoretical foundations”, *Adv. Appl. Mech.* **21** (1981), 169–242.
- [Zener 1948] C. Zener, *Elasticity and anelasticity of metals*, The University of Chicago Press, 1948.

Received 20 Jun 2007. Revised 6 Aug 2007. Accepted 6 Aug 2007.

ROLAND DEWIT: dewit@nist.gov

National Institute of Standards and Technology, 100 Bureau Drive, Stop 8553, Gaithersburg, MD 20899-8553, United States

ROBUSTNESS ANALYSIS OF STRUCTURES BASED ON PLASTIC LIMIT ANALYSIS WITH UNCERTAIN LOADS

YU MATSUDA AND YOSHIHIRO KANNO

This paper presents a method for computing an info-gap robustness function of structures, which is regarded as one measure of structural robustness, under uncertainties associated with the limit load factor. We assume that the external load in the plastic limit analysis is uncertain around its nominal value. Various uncertainties are considered for the live, dead, and reference disturbance loads based on the nonstochastic info-gap uncertainty model. Although the robustness function is originally defined by using the optimization problem with infinitely many constraints, we show that the robustness function is obtained as an optimal value of a linear programming (LP) problem. Hence, we can easily compute the info-gap robustness function associated with the limit load factor by solving an LP problem. As the second contribution, we show that the robust structural optimization problems of trusses and frames can also be reduced to LP problems. In numerical examples, the robustness functions, as well as the robust optimal designs, are computed for trusses and framed structures by solving LP problems.

1. Introduction

In designing civil, mechanical and aerospace structures, plastic limit analysis has been used widely for decades as a means of estimating the ultimate strength of structures. On the other hand, structural analysis considering the uncertainties have received fast-growing interest, because structures that are actually built will always have various uncertainties caused by manufacturing errors, limitation of knowledge of input disturbances, observation errors, simplification for modeling, etc. This paper discusses a solution technique for computing the measure of robustness of structures, where the applied loads are supposed to be uncertain. We assume that the dead, live, and/or the reference disturbance loads in limit analysis are uncertain around their nominal values. It should be emphasized that arbitrarily large uncertainty of these loads can be dealt with in our framework.

The limit analysis still receives much attention by numerous researchers from the viewpoint of solution techniques [Muralidhar and Jagannatha Rao 1997; Andersen et al. 1998; Cocchetti and Maier 2003; Krabbenhoft and Damkilde 2003]. Based on the probabilistic uncertainty models of structural systems, various approaches to stochastic limit analysis have also been proposed [Lloyd Smith et al. 1990; Rocho and Sonnenberg 2003; Staat and Heitzer 2003; Marti and Stoeckel 2004]. Recently, based on the non-probabilistic uncertainty model, Kanno and Takewaki [2007] has proposed a global optimization method for computing the smallest limit load factor of truss structures, in which the applied dead load is assumed to be uncertain but bounded.

Reliability-based structural design methods have been investigated extensively based on the framework of probabilistic uncertainty models [Kharmanda et al. 2004; Zang et al. 2005]. Nonprobabilistic

Keywords: data uncertainty, linear program, plastic limit analysis, robust optimization, info-gap analysis.

uncertainty models have also been developed for uncertain structural analysis. In such a nonprobabilistic uncertainty model, a mechanical system contains some unknown parameters which are assumed to be bounded. Ben-Haim and Elishakoff [1990] developed the well-known *convex model* approach, which has been applied to a robust truss optimization by Ganzerli and Pantelides [1999]. The interval linear algebra has been well developed for the so-called uncertain linear equations [Alefeld and Mayer 2000], which were employed in structural analysis considering various uncertainties [Qiu and Elishakoff 1998; Muhanna and Mullen 2001; Chen et al. 2002].

Recently, the *info-gap decision theory* has been proposed as a nonprobabilistic decision theory under uncertainties [Ben-Haim 2006], and has been applied to wide fields. In the info-gap decision theory, the *robustness function* plays a key role as a measure of robustness of systems having uncertainties [Ben-Haim 2006]. In structural engineering, the info-gap robustness function represents the greatest level of uncertainty at which any constraint on mechanical performance cannot be violated. The constraints on mechanical performance can be violated only at the large level of uncertainty in a structure with a large robustness function, while they can possibly be violated at a small level of uncertainty in a structure with a small robustness function. Thus, we can compare robustness of structures quantitatively in terms of the robustness function.

Unfortunately, in many practical situations it is difficult to compute the exact value of the robustness function of a structure. This is because the robustness function is defined as the optimal value of an optimization problem with infinitely many constraints. Kanno and Takewaki [2006a] proposed a method for computing a lower bound of the robustness function for trusses associated with stress and/or displacement constraints. Takewaki and Ben-Haim [2005] computed the robustness function of damped structures considering the dynamic response constraints. In the case of Takewaki and Ben-Haim [2005], the *worst case* of the uncertain parameters can be obtained analytically, which enables us to compute the exact value of the robustness function.

In this paper, we investigate the info-gap robustness function of structures associated with the lower bound constraint on the limit load factor. In the plastic limit analysis, we consider the uncertainties of the dead, live, and/or the reference disturbance loads, which obey the info-gap uncertainty models. As a main contribution, we show that the robustness function considering the limit load factor constraint can be obtained as an optimal value of a *linear programming* (LP) problem, which implies that the exact value of the robustness function can be computed easily. This is rather amazing, because it is not straightforward to find the worst case of the limit load factor under the uncertainty of dead load. Indeed, we have to find the global optimal solution of a nonlinear optimization problem in order to detect the worst-case limit load factor [Kanno and Takewaki 2007]. Thus, the results of this paper imply that computing the robustness function is much easier than finding the worst-case limit load factor. Consequently, there exists a class of constraints such that the robustness function can be computed easily while it is very difficult to find the worst case.

As the second contribution, we formulate the *robust counterpart* to the structural optimization associated with the limit load factor and present its tractable reformulation. For convex optimization problems, the notion and methodology of robust counterpart problem were developed by Ben-Tal and Nemirovski [2002], and were applied to robust compliance minimization of trusses [Ben-Tal and Nemirovski 1997]. As an alternative approach, robust optimization problems were formulated for structures based on the convex model analysis [Elishakoff et al. 1994; Ganzerli and Pantelides 1999], provided that the variations

of uncertain parameters are sufficiently small. The maximization problem of the robustness function of trusses associated with stress constraints was studied in [Kanno and Takewaki 2006b]. For a comprehensive survey on the robust structural design, the readers may refer to the review papers [Zang et al. 2005; Beyer and Sendhoff 2007].

For the limit load factor constraint, we formulate the minimization problem of the structural volume under the constraint such that the lower bound constraint on the limit load factor is always satisfied for the given level of uncertainty. In this problem, the major difficulty arises where the constraint includes the sublevel optimization problem even in the nominal case, because the limit load factor is defined as an optimal value of an optimization problem. It is shown that this robust optimization problem can be reformulated as an LP problem for trusses as well as frames with sandwich cross-sections.

This paper is organized as follows. In Section 2 we prepare the LP problem for the conventional limit analysis and introduce the definition of robustness function as well as the info-gap uncertainty model for structural analysis. For trusses, the robustness function associated with the lower bound constraint on the limit load factor is defined in Section 3 for various uncertainty models of external load, and for each model an LP problem is formulated which provides the robustness function. In Section 4, we show that the robustness function for a framed structure can be computed by solving an LP problem. Numerical experiments are presented in Section 5 for a truss and frames. The robust optimization problems associated with the limit load factor are formulated for trusses and frames in Sections 6.1 and 6.2, respectively, and they are reformulated into LP problems. Numerical experiments are presented in Section 6.3 for robust structural optimization, while conclusions are drawn in Section 7.

2. Preliminaries

2.1. Notation. The ℓ^p -norm of the vector $\mathbf{x} = (x_i) \in \Re^n$ for $1 \leq p < \infty$ is defined as

$$\|\mathbf{x}\|_p = \left(\sum_{i=1}^n |x_i|^p \right)^{1/p}.$$

In particular, the ℓ^1 - and ℓ^2 -norms are written as

$$\|\mathbf{p}\|_1 = \sum_{i=1}^n |p_i|, \quad \|\mathbf{p}\|_2 = (\mathbf{p}^\top \mathbf{p})^{1/2}.$$

The ℓ^∞ -norm is defined as $\|\mathbf{p}\|_\infty = \max_{i \in \{1, \dots, n\}} |p_i|$. For p satisfying $1 < p < \infty$, p^* is defined by

$$\frac{1}{p} + \frac{1}{p^*} = 1.$$

For $p = 1$ and $p = \infty$, we simply set $p^* = \infty$ and $p^* = 1$, respectively.

For column vectors $\mathbf{p} = (p_i) \in \Re^m$ and $\mathbf{q} = (q_i) \in \Re^n$, the $(m+n)$ -dimensional column vector $(\mathbf{p}^\top, \mathbf{q}^\top)^\top$ is often written simply as (\mathbf{p}, \mathbf{q}) . We write $\mathbf{p} \geq \mathbf{0}$ if $p_i \geq 0$ ($i = 1, \dots, m$). Define \Re_+^n and \Re_{++}^n by

$$\begin{aligned} \Re_+^n &= \{\mathbf{x} \in \Re^n \mid \mathbf{x} \geq \mathbf{0}\}, \\ \Re_{++}^n &= \{\mathbf{x} = (x_i) \in \Re^n \mid x_i > 0 \quad (i = 1, \dots, n)\}. \end{aligned}$$

The two sets $\mathcal{A} \subseteq \mathfrak{N}^m$ and $\mathcal{B} \subseteq \mathfrak{N}^n$ have Cartesian products defined by

$$\mathcal{A} \times \mathcal{B} = \{(\mathbf{a}^\top, \mathbf{b}^\top)^\top \in \mathfrak{N}^{m+n} \mid \mathbf{a} \in \mathcal{A}, \mathbf{b} \in \mathcal{B}\}.$$

In particular, we write $\mathfrak{N}^{m+n} = \mathfrak{N}^m \times \mathfrak{N}^n$. The empty set is denoted by \emptyset .

2.2. Robustness function associated with limit load factor. The robustness function was proposed as a measure of robustness for a general uncertain system, whose uncertainty is described by an info-gap uncertainty model [Ben-Haim 2006]. In this section, we formulate the robustness function of engineering structures for a particular case in which the limit load factor is chosen as a measure of structural performance.

Consider a finitely discretized structure. Small rotations and small strains are assumed. Let $\mathbf{f} \in \mathfrak{N}^{n^d}$ denote the vector of the external forces, where n^d denotes the number of degrees of freedom of displacements. Suppose that \mathbf{f} consists of the constant part \mathbf{f}_D and proportionally increasing part $\lambda \mathbf{f}_R$ as

$$\mathbf{f} = \lambda \mathbf{f}_R + \mathbf{f}_D. \quad (1)$$

Notice here that $\lambda \mathbf{f}_R$ is defined by the monotonically increasing load parameter $\lambda \in \mathfrak{N}_+$ and the constant reference load $\mathbf{f}_R \in \mathfrak{N}^{n^d} \setminus \{\mathbf{0}\}$. In civil engineering, \mathbf{f}_D consists of the dead load, live load, etc., while $\lambda \mathbf{f}_R$ is referred to as the live or disturbance load which may be a static approximation of dynamical loads caused by earthquakes, winds, etc. In this paper, \mathbf{f}_D is simply called the *dead load* and \mathbf{f}_R is called the *reference disturbance load* for simplicity of presentation.

For the given \mathbf{f}_R and \mathbf{f}_D , let $\lambda^*(\mathbf{f}_R, \mathbf{f}_D)$ denote the limit load factor. Throughout the paper, we assume $\lambda^*(\mathbf{0}, \mathbf{f}_D) > 0$, that is, the plastic collapse does not occur with the dead load \mathbf{f}_D only. Let $\underline{\lambda}$ denote the lower bound of the limit load factor, which is the performance requirement imposed by engineers. For the given $\underline{\lambda} \in \mathfrak{N}_{++}$, the conventional constraint on the limit load factor is written as

$$\lambda^*(\mathbf{f}_R, \mathbf{f}_D) \geq \underline{\lambda}. \quad (2)$$

We next suppose that \mathbf{f}_R and \mathbf{f}_D are known imprecisely. Let $\tilde{\mathbf{f}}_R \in \mathfrak{N}^{n^d}$ and $\tilde{\mathbf{f}}_D \in \mathfrak{N}^{n^d}$ denote the nominal values (or the best estimates) of \mathbf{f}_R and \mathbf{f}_D , respectively. For the given $\alpha \in \mathfrak{N}_+$, $\tilde{\mathbf{f}}_R$, and $\tilde{\mathbf{f}}_D$, let $\mathcal{R}_p(\alpha, \tilde{\mathbf{f}}_R) \subset \mathfrak{N}^{n^d}$ and $\mathcal{D}_p(\alpha, \tilde{\mathbf{f}}_D) \subset \mathfrak{N}^{n^d}$ be bounded sets. The rigorous and concrete definitions of \mathcal{R}_p and \mathcal{D}_p will be given in Section 3. The subscript p of \mathcal{R}_p and \mathcal{D}_p implies that the sets \mathcal{R}_p and \mathcal{D}_p are defined by using the ℓ^p -norm ($1 \leq p \leq +\infty$) as shown below. The parameter α represents the magnitude of the uncertainty, and hence α is referred to as the *uncertainty parameter* [Ben-Haim 2006].

The uncertainties of \mathbf{f}_R and \mathbf{f}_D are modeled as follows. For any \mathbf{f}_R and \mathbf{f}_D , assume that there exists an $\alpha \in \mathfrak{N}_+$ such that the conditions

$$\mathbf{f}_R \in \mathcal{R}_p(\alpha, \tilde{\mathbf{f}}_R), \quad \mathbf{f}_D \in \mathcal{D}_p(\alpha, \tilde{\mathbf{f}}_D), \quad (3)$$

are satisfied. We call \mathcal{R}_p and \mathcal{D}_p the uncertainty sets of \mathbf{f}_R and \mathbf{f}_D , respectively. We further assume that \mathcal{R}_p and \mathcal{D}_p satisfy the two basic axioms of the info-gap model [Ben-Haim 2006]:

- (i) Nesting: $0 \leq \alpha_1 < \alpha_2$ implies $\mathcal{R}_p(\alpha_1, \tilde{\mathbf{f}}_R) \times \mathcal{D}_p(\alpha_1, \tilde{\mathbf{f}}_D) \subset \mathcal{R}_p(\alpha_2, \tilde{\mathbf{f}}_R) \times \mathcal{D}_p(\alpha_2, \tilde{\mathbf{f}}_D)$,
- (ii) Contraction: $\mathcal{R}_p(0, \tilde{\mathbf{f}}_R) = \{\tilde{\mathbf{f}}_R\}$ and $\mathcal{D}_p(0, \tilde{\mathbf{f}}_D) = \{\tilde{\mathbf{f}}_D\}$.

From the nesting axiom we see that the uncertainty sets $\mathcal{R}_p(\alpha, \tilde{\mathbf{f}}_R)$ and $\mathcal{D}_p(\alpha, \tilde{\mathbf{f}}_D)$ become more inclusive as α becomes larger. The greater the value of α , the greater the ranges of possible variations of \mathbf{f}_R and \mathbf{f}_D . The contraction axiom guarantees that the estimates $\tilde{\mathbf{f}}_R$ and $\tilde{\mathbf{f}}_D$ are exact at $\alpha = 0$. Note that the value of α is usually unknown in actual structures. Throughout the following robustness analysis we do not use any knowledge of the actual range of uncertainty of loads, which is regarded as one of the advantages of using the info-gap theory.

For the fixed $\alpha \in \mathfrak{R}_+$, the robust counterpart of the constraint (2), is written as

$$\lambda^*(\mathbf{f}_R, \mathbf{f}_D) \geq \underline{\lambda}, \quad \text{for all } \mathbf{f}_R \in \mathcal{R}_p(\alpha, \tilde{\mathbf{f}}_R), \quad \text{for all } \mathbf{f}_D \in \mathcal{D}_p(\alpha, \tilde{\mathbf{f}}_D). \quad (4)$$

Throughout the paper, we assume $\lambda^*(\tilde{\mathbf{f}}_R, \tilde{\mathbf{f}}_D) \geq \underline{\lambda}$, that is, the robust constraint, Equation (4), is satisfied at the nominal situation. The robustness function represents the largest value of α with which the robust constraint, (4), is satisfied. More precisely, the robustness function $\hat{\alpha} : \mathfrak{R}_+ \rightarrow [0, +\infty]$ associated with the constraint of the limit load factor is defined as

$$\hat{\alpha}(\underline{\lambda}) = \max \left\{ \alpha \mid \lambda^*(\mathbf{f}_R, \mathbf{f}_D) \geq \underline{\lambda} \quad \left(\text{for all } (\mathbf{f}_R, \mathbf{f}_D) \in \mathcal{R}_p(\alpha, \tilde{\mathbf{f}}_R) \times \mathcal{D}_p(\alpha, \tilde{\mathbf{f}}_D) \right) \right\}. \quad (5)$$

Thus, $\hat{\alpha}$ is the function of the performance requirement $\underline{\lambda}$, as well as of the design variables of the structure. For the fixed $\underline{\lambda}$, the constraint, Equation (4), can be violated only at a large level of uncertainty if the structure has a large value of $\hat{\alpha}(\underline{\lambda})$. On the other hand, (4) can be violated at a small level of uncertainty if the structure has a small value of $\hat{\alpha}(\underline{\lambda})$. In this way, we can compare robustness of structures quantitatively in terms of the robustness function.

The problem (5), is classified to the semiinfinite programming, which means an optimization problem having a finite number of variables and infinitely many inequality constraints. Unfortunately, it is difficult to solve (5) directly, which motivates us to investigate a tractable reformulation in the following sections.

3. Robustness analysis of trusses

We investigate a tractable reformulation of the info-gap robustness function of trusses under various uncertainty models of external loads.

3.1. Basic problem of limit analysis of trusses. In this section, in order to make the paper self-contained, we prepare an LP problem for the conventional limit analysis of trusses. Consider an elastic/perfectly-plastic truss in the two- or three-dimensional space. Let n^m denote the number of members. We denote by $\mathbf{q} = (q_i) \in \mathfrak{R}^{n^m}$ the vector of member axial forces. The system of equilibrium equations between \mathbf{q} and the external load \mathbf{f} are written in the form of

$$H\mathbf{q} = \mathbf{f}, \quad (6)$$

where $H \in \mathfrak{R}^{n^d \times n^m}$ is a constant matrix. Recall that \mathbf{f} is divided into two parts as Equation (1).

Let $\bar{\sigma}_i > 0$ and $-\bar{\sigma}_i$ denote the yield stresses of the i th member in tension and compression, respectively. Here, we assume for simplicity that the yield stresses in tension and compression share a common absolute value. The member cross-sectional area is denoted by $a_i > 0$. Define \bar{q}_i by

$$\bar{q}_i = \bar{\sigma}_i a_i, \quad (7)$$

which is the absolute value of the admissible axial force. The admissible set $\mathcal{Q} \subset \mathfrak{N}^m$ of the axial forces is written as

$$\mathcal{Q} = \left\{ \mathbf{q} \in \mathfrak{N}^m \mid \bar{q}_i \geq |q_i| \quad (i = 1, \dots, m) \right\}. \quad (8)$$

From the static (or lower bound) principle [Hodge 1959], and by using Equation (1), (6), and (8), the limit load factor λ^* is obtained by solving the following LP problem:

$$\lambda^*(\mathbf{f}_R, \mathbf{f}_D) = \max_{\lambda, \mathbf{q}} \left\{ \lambda \mid H\mathbf{q} = \lambda \mathbf{f}_R + \mathbf{f}_D, \quad \mathbf{q} \in \mathcal{Q} \right\}, \quad (9)$$

where the variables are λ and \mathbf{q} . Note that the limit load factor λ^* is regarded as a function of \mathbf{f}_R and \mathbf{f}_D . Then the robustness function of the truss is defined as Equation (5). In the following discussion, we consider various models of the uncertainty sets $\mathcal{R}_p(\alpha, \tilde{\mathbf{f}}_R)$ and $\mathcal{D}_p(\alpha, \tilde{\mathbf{f}}_D)$, and discuss how to compute the robustness function $\hat{\alpha}(\underline{\lambda})$.

3.2. Uncertainty of dead load. In this section, we suppose that the dead load \mathbf{f}_D possesses uncertainty, while the reference disturbance load \mathbf{f}_R is assumed to be certain. Let $\boldsymbol{\zeta} \in \mathfrak{N}^{n^z}$ denote the vector of parameters that are considered to be unknown, or uncertain, where n^z denotes the number of such parameters. We describe the uncertainty of \mathbf{f}_D in terms of the unknown $\boldsymbol{\zeta}$. Suppose that \mathbf{f}_D depend on $\boldsymbol{\zeta}$ affinely so that the uncertainty set in Equation (3) is defined as

$$\mathcal{D}_p(\alpha, \tilde{\mathbf{f}}_D) = \left\{ \mathbf{f}_D \in \mathfrak{N}^{n^d} \mid \mathbf{f}_D = \tilde{\mathbf{f}}_D + F_0 \boldsymbol{\zeta}, \quad \alpha \geq \|\boldsymbol{\zeta}\|_p \right\}, \quad (10)$$

where $1 \leq p \leq +\infty$. Note that Equation (10) is the unified description of uncertainty models defined by using various norms, that is, the choice of p provides us with a variety of uncertainty models. In the uncertainty set, Equation (10), the constant matrix $F_0 \in \mathfrak{N}^{n^d \times n^z}$ represents the relative magnitude of the uncertainty of f_{Dj} and the correlation of the uncertainties among f_{D1}, \dots, f_{Dn^d} . Each component of F_0 has the unit of force. Hence, neither $\boldsymbol{\zeta}$ nor α has no physical unit. It is easy to verify that the uncertainty set \mathcal{D}_p defined by Equation (10) satisfies the axioms of the info-gap model introduced in Section 2.2.

An example of a truss is illustrated in Figure 1. To impose a nominal dead load $\tilde{\mathbf{f}}_D$, we suppose that external forces are applied at the nodes (f) and (g). The nominal reference disturbance load $\tilde{\mathbf{f}}_R$ is defined such that the proportionally increasing forces are applied at the nodes (c) and (d). In order to guarantee that \mathbf{f}_R is certain, F_0 is assumed to satisfy the condition that the components of $F_0 \boldsymbol{\zeta}$ corresponding to the external forces applied to the nodes (c) and (d) vanish for any $\boldsymbol{\zeta} \in \mathfrak{N}^{n^z}$.

According to Equation (5), the robustness function $\hat{\alpha}: \mathfrak{N}_+ \rightarrow [0, +\infty]$ with the uncertainty model $\mathbf{f}_D \in \mathcal{D}_p(\alpha, \tilde{\mathbf{f}}_D)$ is defined as

$$\hat{\alpha}(\underline{\lambda}) = \max_{\alpha} \left\{ \alpha \mid \lambda^*(\tilde{\mathbf{f}}_R, \mathbf{f}_D) \geq \underline{\lambda} \quad \left(\text{for all } \mathbf{f}_D \in \mathcal{D}_p(\alpha, \tilde{\mathbf{f}}_D) \right) \right\}. \quad (11)$$

For simplicity, we write $\mathbf{f}_R = \tilde{\mathbf{f}}_R$ in the remainder of this section.

For $r \in \mathfrak{N}_+$, we define the set $\mathcal{B}_p(r) \subset \mathfrak{N}^{n^z}$ by

$$\mathcal{B}_p(r) = \left\{ \boldsymbol{\zeta} \in \mathfrak{N}^{n^z} \mid r \geq \|\boldsymbol{\zeta}\|_p \right\}.$$

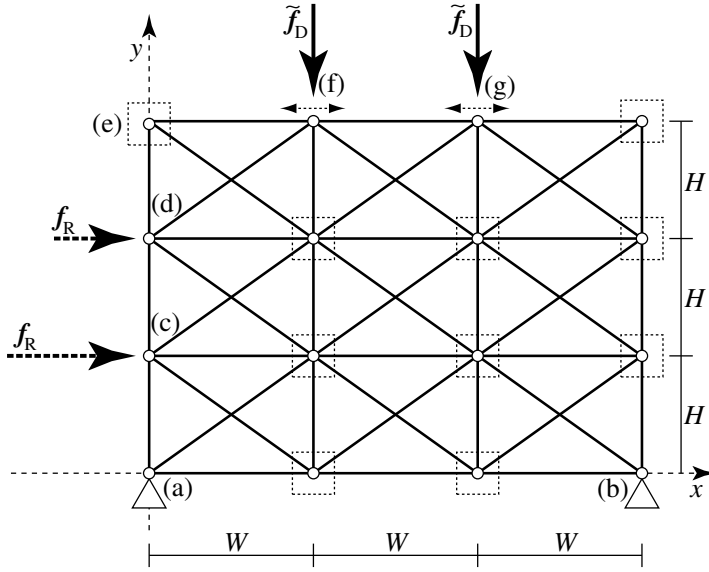


Figure 1. 3×3 truss.

The following proposition prepares the reformulation of the semiinfinite optimization problem (11) by eliminating λ^* .

Proposition 3.1. Define \hat{r} by

$$\hat{r} = \max_{r, q} \left\{ r \mid Hq = \underline{\lambda} f_R + \tilde{f}_D + F_0 \zeta, \quad q \in \mathcal{Q} \quad (\text{for all } \zeta \in \mathcal{B}_p(r)) \right\}. \quad (12)$$

Then the robustness function $\hat{\alpha}(\underline{\lambda})$ defined by Equation (10) and (11) satisfies $\hat{\alpha}(\underline{\lambda}) = \hat{r}$.

Proof. The constraint of (12) implies that the condition

$$\exists q' \in \mathfrak{N}^m: \quad Hq' = \underline{\lambda} f_R + \tilde{f}_D + F_0 \zeta, \quad q' \in \mathcal{Q} \quad (13)$$

is satisfied for any ζ satisfying $\hat{r} > \|\zeta\|_p$. For a fixed $\lambda \in \mathfrak{R}_+$, define the set $\mathcal{V}(\lambda) \subset \mathfrak{N}^m$ as

$$\mathcal{V}(\lambda) = \left\{ q \in \mathfrak{N}^m \mid Hq = \lambda f_R + \tilde{F}_D, \quad q \in \mathcal{Q} \right\}.$$

Note that $q \in \mathcal{V}(\lambda)$ if and only if (λ, q) is a feasible solution of the problem, Equation (9). Since (13) holds for $\zeta = \mathbf{0}$, we see that $q' \in \mathcal{V}(\underline{\lambda})$ is satisfied. From this observation and (9), we obtain

$$\lambda^*(f_R, f_D(\zeta)) \geq \underline{\lambda}, \quad (14)$$

where $f_D(\zeta) = \tilde{f}_D + F_0 \zeta$. Since we can show that Equation (14) holds for any ζ satisfying $\hat{r} > \|\zeta\|_p$, the definition (11) of $\hat{\alpha}$ implies

$$\hat{\alpha}(\underline{\lambda}) \geq \hat{r}. \quad (15)$$

On the other hand, choose ζ' satisfying $\hat{\alpha} > \zeta'$. It follows from Equation (11) that $\mathcal{V}(\lambda^*(\mathbf{f}_R, \mathbf{f}_D(\zeta'))) \neq \emptyset$ and $\mathcal{V}(0) \neq \emptyset$. Moreover, the set $\{(\lambda, \mathbf{q}) \in \mathfrak{R} \times \mathfrak{R}^{n^m} \mid \mathbf{q} \in \mathcal{V}(\lambda)\}$ is convex, from which it follows that for any $\underline{\lambda}$ satisfying $0 \leq \underline{\lambda} \leq \lambda^*(\mathbf{f}_R, \mathbf{f}_D(\zeta'))$, $\mathcal{V}(\underline{\lambda}) \neq \emptyset$ is satisfied, that is, Equation (13) is satisfied. Since this observation holds for any ζ' satisfying $\hat{\alpha} > \|\zeta'\|_p$, the definition (12) of \hat{r} implies

$$\hat{\alpha}(\underline{\lambda}) \leq \hat{r}. \quad (16)$$

Consequently, from Equation (15) and (16) we obtain $\hat{\alpha}(\underline{\lambda}) = \hat{r}$, which concludes the proof. \square

It is still difficult to solve Equation (12) because it requires that the constraints hold for infinitely many ζ satisfying $\zeta \in \mathcal{B}_p(r)$.

Let $H^\dagger \in \mathfrak{R}^{n^m \times n^d}$ denote the pseudoinverse of H . A basis for the null space of H is denoted by $H^\perp \in \mathfrak{R}^{n^m \times n^\xi}$, where $n^\xi = n^m - \text{rank}(H)$. Let \mathbf{h}_i^\dagger and \mathbf{h}_i^\perp the i th row vectors of H^\dagger and H^\perp , respectively, that is,

$$H^\dagger = \begin{pmatrix} \mathbf{h}_1^\dagger \\ \vdots \\ \mathbf{h}_{n^m}^\dagger \end{pmatrix}, \quad H^\perp = \begin{pmatrix} \mathbf{h}_1^\perp \\ \vdots \\ \mathbf{h}_{n^m}^\perp \end{pmatrix}.$$

Proposition 3.2. \hat{r} defined by Equation (12) is equal to the optimal value of the LP problem

$$\hat{r} = \max_{r, \xi} \left\{ r \mid \begin{aligned} &\mathbf{h}_i^\dagger(\underline{\lambda}\mathbf{f}_R + \tilde{\mathbf{f}}_D) + r\|\mathbf{h}_i^\dagger F_0\|_{p^*} + \mathbf{h}_i^\perp \xi \leq \bar{q}_i, \quad i = 1, \dots, n^m, \\ &-\mathbf{h}_i^\dagger(\underline{\lambda}\mathbf{f}_R + \tilde{\mathbf{f}}_D) + r\|\mathbf{h}_i^\dagger F_0\|_{p^*} - \mathbf{h}_i^\perp \xi \leq \bar{q}_i, \quad i = 1, \dots, n^m \end{aligned} \right\} \quad (17)$$

in the variables $r \in \mathfrak{R}$ and $\xi \in \mathfrak{R}^{n^\xi}$.

Proof. Observe that any $\mathbf{q} \in \mathfrak{R}^{n^m}$ satisfying the equilibrium equations

$$H\mathbf{q} = \underline{\lambda}\mathbf{f}_R + \tilde{\mathbf{f}}_D + F_0\xi,$$

can be represented as

$$\mathbf{q} = H^\dagger(\underline{\lambda}\mathbf{f}_R + \tilde{\mathbf{f}}_D + F_0\xi) + H^\perp \xi, \quad \xi \in \mathfrak{R}^{n^\xi}. \quad (18)$$

In Equation (18), we may regard q_i as a function of ξ , that is,

$$q_i(\xi) := \mathbf{h}_i^\dagger(\underline{\lambda}\mathbf{f}_R + \tilde{\mathbf{f}}_D) + \mathbf{h}_i^\dagger F_0\xi + \mathbf{h}_i^\perp \xi, \quad i = 1, \dots, n^m. \quad (19)$$

From the definition Equation (8) of \mathcal{Q} it follows that the constraints of (12) are equivalently rewritten as

$$q_i(\xi) \leq \bar{q}_i \quad (\text{for all } \xi \in \mathcal{B}_p(r)), \quad i = 1, \dots, n^m, \quad (20)$$

$$-q_i(\xi) \leq \bar{q}_i \quad (\text{for all } \xi \in \mathcal{B}_p(r)), \quad i = 1, \dots, n^m. \quad (21)$$

Moreover, Equation (20) and (21) are equivalent to

$$\begin{aligned} \max_{\xi} \{q_i(\xi) \mid r \geq \|\xi\|_p\} &\leq \bar{q}_i, \quad i = 1, \dots, n^m, \\ \max_{\xi} \{-q_i(\xi) \mid r \geq \|\xi\|_p\} &\leq \bar{q}_i, \quad i = 1, \dots, n^m. \end{aligned} \quad (22)$$

By using Equation (19) and the Hölder inequality [Michael Sttele 2004], we see that

$$\max_{\boldsymbol{\zeta}} \left\{ \mathbf{h}_i^\dagger F_0 \boldsymbol{\zeta} \mid r \geq \|\boldsymbol{\zeta}\|_p \right\} = r \|\mathbf{h}_i^\dagger F_0\|_{p^*}, \quad (23)$$

from which it follows that (22) is equivalently rewritten as

$$\begin{aligned} \mathbf{h}_i^\dagger (\underline{\lambda} \mathbf{f}_R + \tilde{\mathbf{f}}_D) + r \|\mathbf{h}_i^\dagger F_0\|_{p^*} + \mathbf{h}_i^\perp \boldsymbol{\xi} &\leq \bar{q}_i, \quad i = 1, \dots, n^m, \\ -\mathbf{h}_i^\dagger (\underline{\lambda} \mathbf{f}_R + \tilde{\mathbf{f}}_D) + r \|\mathbf{h}_i^\dagger F_0\|_{p^*} - \mathbf{h}_i^\perp \boldsymbol{\xi} &\leq \bar{q}_i, \quad i = 1, \dots, n^m. \end{aligned} \quad (24)$$

Consequently, the constraints of Equation (12) are equivalent to (24), which concludes the proof. \square

Proposition 3.2, together with Proposition 3.1, implies that the robustness function $\hat{\alpha}(\underline{\lambda})$ can be obtained easily by solving an LP problem (17), contradicting the fact that it is very difficult to solve the semiinfinite optimization problem (11).

3.3. Uncertainty of reference disturbance load. In this section, we investigate the uncertainty model of the reference disturbance load \mathbf{f}_R in Equation (1), while the dead load \mathbf{f}_D is assumed to be certain. For the given nominal value $\tilde{\mathbf{f}}_R$ and fixed $\alpha \in \mathfrak{N}_+$, let $\mathcal{R}_p(\alpha, \tilde{\mathbf{f}}_R)$ denote the uncertainty set of \mathbf{f}_R , which shall be rigorously defined below. According to Equation (5), the robustness function $\hat{\alpha} : \mathfrak{N}_+ \rightarrow [0, +\infty]$ in this case is defined as

$$\hat{\alpha}(\underline{\lambda}) = \max_{\alpha} \left\{ \alpha \mid \lambda^*(\mathbf{f}_R, \tilde{\mathbf{f}}_D) \geq \underline{\lambda} \left(\text{for all } \mathbf{f}_R \in \mathcal{R}_p(\alpha, \tilde{\mathbf{f}}_R) \right) \right\}. \quad (25)$$

For simplicity, we write $\mathbf{f}_D = \tilde{\mathbf{f}}_D$ in the remainder of this section .

3.3.1. Uncertainty of load distribution. Consider the uncertainty (or variations) of the distribution of the reference disturbance load.

Recall the example of a truss illustrated in Figure 1, which has been studied for the uncertainty model \mathcal{D}_p in Equation (10). At the nodes of the left side, the external forces are applied as the reference disturbance load. The nominal forces applied at the nodes (c) and (d) are illustrated in Figure 2 as $f_R^{(c)}$ and $f_R^{(d)}$. Suppose that the directions of these forces do not change, while the distribution is unknown as shown in Figure 2 as $f_R^{(c)}$ and $f_R^{(d)}$. The additional force may possibly be applied at the node (e), which is illustrated as $f_R^{(e)}$ in Figure 2. Such an uncertainty model can be written as $\mathbf{f}_R \in \mathcal{R}_p(\alpha, \tilde{\mathbf{f}}_R)$ with

$$\mathcal{R}_p(\alpha, \tilde{\mathbf{f}}_R) = \left\{ \mathbf{f}_R \in \mathfrak{N}^{n^d} \mid \mathbf{f}_R = \tilde{\mathbf{f}}_R + F_0 \boldsymbol{\zeta}, \quad \alpha \geq \|\boldsymbol{\zeta}\|_p, \quad \sum_{i=1}^{n^z} \zeta_i = 0 \right\}. \quad (26)$$

Here, F_0 is assumed to satisfy the condition that the components of the vector $F_0 \boldsymbol{\zeta}$ corresponding to the directions of $\tilde{\mathbf{f}}_R$ only are possibly not equal to zeros for any $\boldsymbol{\zeta} \in \mathfrak{N}^{n^z}$ as shown in Figure 2. Note that $n^z = 3$ and $\text{rank}(F_0) = 3$ in the example of Figure 2. The condition $\sum_{i=1}^{n^z} \zeta_i = 0$ in (26) is added in order to normalize the magnitude of \mathbf{f}_R . We can easily see that the uncertainty set \mathcal{D}_p defined by Equation (26) satisfies the nesting and contraction axioms of the info-gap uncertainty model introduced in Section 2.2.

Let $p = 2$ in the uncertainty model (26). Then the following proposition implies that the robustness function defined by (25) is obtained as the optimal value of an LP problem.

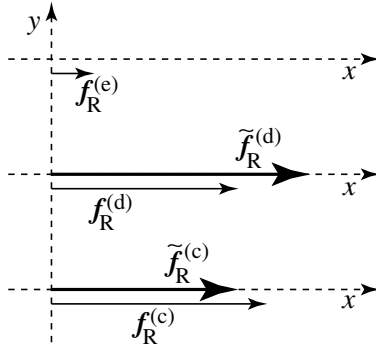


Figure 2. Uncertainty of distribution of the reference disturbance load f_R .

Proposition 3.3. Define $\mathbf{n} \in \mathfrak{R}^{n^z}$ by

$$\mathbf{n} = \frac{1}{\sqrt{n^z}}(1, 1, \dots, 1)^\top. \quad (27)$$

Then the robustness function, $\hat{\alpha}(\underline{\lambda})$ defined by (25) and (26) with $p = 2$, is obtained as the optimal value of the LP problem

$$\begin{aligned} \hat{\alpha}(\underline{\lambda}) = \max_{r, \xi} \left\{ r \mid \mathbf{h}_i^\dagger(\underline{\lambda} \tilde{\mathbf{f}}_R + \mathbf{f}_D) + r \sqrt{\|\mathbf{h}_i^\dagger F_0\|_2^2 - (\mathbf{h}_i^\dagger F_0 \mathbf{n})^2} + \mathbf{h}_i^\perp \xi \leq \bar{q}_i, \quad i = 1, \dots, n^m, \right. \\ \left. -\mathbf{h}_i^\dagger(\underline{\lambda} \tilde{\mathbf{f}}_R + \mathbf{f}_D) + r \sqrt{\|\mathbf{h}_i^\dagger F_0\|_2^2 - (\mathbf{h}_i^\dagger F_0 \mathbf{n})^2} - \mathbf{h}_i^\perp \xi \leq \bar{q}_i, \quad i = 1, \dots, n^m \right\} \quad (28) \end{aligned}$$

in the variables $r \in \mathfrak{R}$ and $\xi \in \mathfrak{R}^{n^\xi}$.

Proof. In a manner similar to Proposition 3.1, we can show that

$$\hat{\alpha}(\underline{\lambda}) = \max_{r, \mathbf{q}, \xi} \left\{ r \mid H\mathbf{q} = \underline{\lambda} \tilde{\mathbf{f}}_R + \mathbf{f}_D + \underline{\lambda} F_0 \xi, \quad \mathbf{q} \in \mathcal{Q} \quad (\text{for all } \xi \in \mathcal{B}_p(r)) \right\} \quad (29)$$

holds, because we may replace $F_0 \xi$ with $\underline{\lambda} F_0 \xi$ in the proof of Proposition 3.1. In a manner similar to Equation (22), we see that the constraints of the problem (29) are equivalently rewritten as

$$\mathbf{h}_i^\dagger(\underline{\lambda} \tilde{\mathbf{f}}_R + \mathbf{f}_D) + \mathbf{h}_i^\perp \xi + q_i^{\max} \leq \bar{q}_i, \quad i = 1, \dots, n^m, \quad (30)$$

$$\mathbf{h}_i^\dagger(\underline{\lambda} \tilde{\mathbf{f}}_R + \mathbf{f}_D) + \mathbf{h}_i^\perp \xi + q_i^{\min} \leq \bar{q}_i, \quad i = 1, \dots, n^m, \quad (31)$$

where

$$q_i^{\max} := \max_{\xi} \left\{ \mathbf{h}_i^\dagger F_0 \xi \mid r \geq \|\xi\|_2, \sum_{i=1}^{n^z} \zeta_i = 0 \right\}, \quad (32)$$

$$q_i^{\min} := \min_{\xi} \left\{ \mathbf{h}_i^\dagger F_0 \xi \mid r \geq \|\xi\|_2, \sum_{i=1}^{n^z} \zeta_i = 0 \right\} = -q_i^{\max}. \quad (33)$$

Analogous to the key equation, (23), in the proof of Proposition 3.2, we next evaluate q_i^{\max} defined by (32) analytically. Note that \mathbf{n} defined in Proposition 3.3 corresponds to the unit normal vector of the hyperplane

$$\pi = \left\{ \boldsymbol{\zeta} \in \mathfrak{R}^{n^z} \mid \sum_{i=1}^{n^z} \zeta_i = 0 \right\}.$$

Define $\mathbf{b}_i \in \mathfrak{R}^{n^z}$ by $\mathbf{b}_i = (\mathbf{h}_i^\dagger F_0)^\top$ for simplicity. Let $\mathbf{w}_i \in \mathfrak{R}^{n^z}$ denote the projection of the vector \mathbf{b}_i onto π , which is written as

$$\begin{aligned} \mathbf{w}_i &= \mathbf{b}_i - (\mathbf{b}_i^\top \mathbf{n}) \mathbf{n} \\ &= (\mathbf{h}_i^\dagger F_0)^\top - (\mathbf{h}_i^\dagger F_0 \mathbf{n}) \mathbf{n}. \end{aligned} \quad (34)$$

Since $\|\mathbf{n}\|_2 = 1$, we obtain

$$\|\mathbf{w}_i\|_2^2 = \|\mathbf{b}_i\|_2^2 - (\mathbf{b}_i^\top \mathbf{n})^2. \quad (35)$$

Then q_i^{\max} in Equation (32) is written as

$$q_i^{\max} = \max_{\boldsymbol{\zeta}} \left\{ \mathbf{b}_i^\top \boldsymbol{\zeta} \mid r \geq \|\boldsymbol{\zeta}\|_2, \sum_{i=1}^{n^z} \zeta_i = 0 \right\} = \max_{\boldsymbol{\zeta}} \left\{ \mathbf{w}_i^\top \boldsymbol{\zeta} \mid r \geq \|\boldsymbol{\zeta}\|_2, \boldsymbol{\zeta} \in \pi \right\}.$$

Since both \mathbf{w}_i and $\boldsymbol{\zeta}_i$ are on the hyperplane π , we obtain

$$q_i^{\max} = \max_{\boldsymbol{\zeta}} \{ \|\mathbf{w}_i\|_2 \|\boldsymbol{\zeta}\|_2 \mid r \geq \|\boldsymbol{\zeta}\|_2 \} = r \|\mathbf{w}_i\|_2. \quad (36)$$

By using Equation (35), we see that (36) is rewritten as

$$q_i^{\max} = r \sqrt{\|\mathbf{b}_i\|_2^2 - (\mathbf{b}_i^\top \mathbf{n})^2}. \quad (37)$$

By substituting Equation (37) into (30) and (31), and by using (29), we obtain (28). \square

The following proposition provides an LP problem to compute the robustness function (25) in the case of $p = \infty$ in Equation (26).

Proposition 3.4. Let l_i be

$$l_i = \max_{j \in \{1, \dots, n^z\}} |w_{ij}|, \quad i = 1, \dots, n^m,$$

where the vector $\mathbf{w}_i = (w_{ij}) \in \mathfrak{R}^{n^z}$ is defined by Equation (34). Then the robustness function $\hat{\alpha}(\underline{\lambda})$ defined by (25) and (26) with $p = \infty$ is obtained as the optimal value of the LP problem

$$\begin{aligned} \hat{\alpha}(\underline{\lambda}) = \max_{r, \boldsymbol{\xi}} \left\{ r \left[\mathbf{h}_i^\dagger (\underline{\lambda} \tilde{\mathbf{f}}_R + \mathbf{f}_D) + r \left[\|\mathbf{h}_i^\dagger F_0\|_2^2 - (\mathbf{h}_i^\dagger F_0 \mathbf{n})^2 \right] / l_i + \mathbf{h}_i^\perp \boldsymbol{\xi} \leq \bar{q}_i, \quad i = 1, \dots, n^m, \right. \right. \\ \left. \left. - \mathbf{h}_i^\dagger (\underline{\lambda} \tilde{\mathbf{f}}_R + \mathbf{f}_D) + r \left[\|\mathbf{h}_i^\dagger F_0\|_2^2 - (\mathbf{h}_i^\dagger F_0 \mathbf{n})^2 \right] / l_i - \mathbf{h}_i^\perp \boldsymbol{\xi} \leq \bar{q}_i, \quad i = 1, \dots, n^m \right\} \end{aligned} \quad (38)$$

in the variables $r \in \mathfrak{R}$ and $\boldsymbol{\xi} \in \mathfrak{R}^{n^k}$.

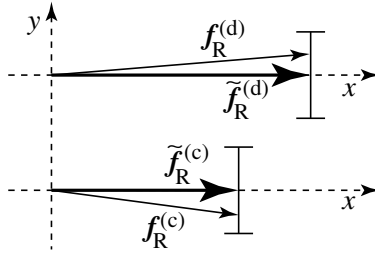


Figure 3. Uncertainty of direction of the reference disturbance load f_R .

Proof. The assertion can be shown in a manner similar to Proposition 3.3. Particularly, we should evaluate

$$q_i^{\max, \infty} := \max_{\zeta} \left\{ \mathbf{h}_i^\top F_0 \zeta \mid r \geq \|\zeta\|_\infty, \sum_{i=1}^{n^z} \zeta_i = 0 \right\} \quad (39)$$

instead of Equation (32). Observe that

$$\max_{\zeta, \beta} \{ \|\zeta\|_2 \mid r \geq \|\zeta\|_\infty, \zeta = \beta \mathbf{w}_i \} = \frac{1}{l_i} \|\mathbf{w}_i\|_2,$$

from which we see that Equation (39) is reduced to

$$\begin{aligned} q_i^{\max, \infty} &= \max_{\zeta} \left\{ \mathbf{b}_i^\top \zeta \mid r \geq \|\zeta\|_\infty, \sum_{i=1}^{n^z} \zeta_i = 0 \right\} \\ &= \max_{\zeta} \{ \mathbf{w}_i^\top \zeta \mid r \geq \|\zeta\|_\infty, \zeta \in \pi \} \\ &= \max_{\zeta, \beta} \{ \|\mathbf{w}_i\|_2 \|\zeta\|_2 \mid r \geq \|\zeta\|_\infty, \zeta = \beta \mathbf{w}_i \} \\ &= \frac{r}{l_i} \|\mathbf{w}_i\|_2^2. \end{aligned} \quad (40)$$

By substituting (34) and (40) into (30) and (31), we obtain the constraints of the problem (38), which concludes the proof. \square

3.3.2. Uncertainty of load direction. Recall the example of a truss illustrated in Figure 1. To apply the reference disturbance load f_R , external forces are applied at the nodes (c) and (d), which are denoted by $f_R^{(c)}$ and $f_R^{(d)}$, respectively. Suppose that the directions of $f_R^{(c)}$ and $f_R^{(d)}$ are uncertain as illustrated in Figure 3. Such an uncertainty model can be realized as $f_R \in \mathcal{R}_p(\alpha, \tilde{f}_R)$ with

$$\mathcal{R}_p(\alpha, \tilde{f}_R) = \left\{ f_R \in \mathfrak{N}^{n^d} \mid f_R = \tilde{f}_R + F_0 \zeta, \alpha \geq \|\zeta\|_p \right\}. \quad (41)$$

Here, F_0 is assumed to satisfy the condition that the components of $F_0 \zeta$ corresponding only to the directions orthogonal to the \tilde{f}_R are possibly not equal to zeros as illustrated in Figure 3. Note that $n^z = 2$ and $\text{rank}(F_0) = 2$ in the case of Figure 3.

In this section, we assume that the magnitude of uncertainty α in the uncertainty model (41) of \mathbf{f}_R is sufficiently small. This is because the magnitude of the reference load \mathbf{f}_R varies in (41). Obviously, formulations presented below are valid for arbitrary large value of α . However, from the engineering view point, we restrict ourselves to the case in which the variation of the magnitude of \mathbf{f}_R does not cause the ambiguity of the definition of the limit load factor when \mathbf{f}_R is running through $\mathcal{R}_p(\alpha, \tilde{\mathbf{f}}_R)$ defined by (41). Under this assumption, the definition (25) of the robustness function is guaranteed to be a proper measure of robustness. On the other hand, if this assumption is not satisfied, then the constraint $\lambda(\mathbf{f}_R, \tilde{\mathbf{f}}_D) \geq \underline{\lambda}$ does not have a proper meaning. To date, it is not clear whether the robustness function can be reformulated into a tractable form or not when we add the condition of normalization to the magnitude of \mathbf{f}_R in Equation (41). Instead, we can show that the robustness function is computed easily without a normalization condition, which is the contribution of this section. Note again that all results other than those in this section are valid for arbitrary large magnitude α of uncertainties. Particularly, in Section 3.3.1, it should be emphasized that we have considered the normalization condition of \mathbf{f}_R in (26).

The following proposition is obtained easily in a manner similar to Proposition 3.2.

Proposition 3.5. The robustness function $\hat{\alpha}(\underline{\lambda})$ defined by (25) and (41) is obtained as the optimal value of the LP problem

$$\hat{\alpha}(\underline{\lambda}) = \max_{r, \xi} \left\{ r \left| \begin{aligned} & \mathbf{h}_i^\dagger (\underline{\lambda} \tilde{\mathbf{f}}_R + \mathbf{f}_D) + r \underline{\lambda} \|\mathbf{h}_i^\dagger F_0\|_{p^*} + \mathbf{h}_i^\perp \xi \leq \bar{q}_i, \quad i = 1, \dots, n^m, \\ & -\mathbf{h}_i^\dagger (\underline{\lambda} \tilde{\mathbf{f}}_R + \mathbf{f}_D) + r \underline{\lambda} \|\mathbf{h}_i^\dagger F_0\|_{p^*} - \mathbf{h}_i^\perp \xi \leq \bar{q}_i, \quad i = 1, \dots, n^m \end{aligned} \right. \right\} \quad (42)$$

in the variables $r \in \Re$ and $\xi \in \Re^{n^{\xi}}$.

4. Robustness analysis of framed structures

4.1. Basic problem of limit analysis of frames. Consider a framed structure in the two-dimensional space that consists of a finite number of the conventional Euler–Bernoulli beam elements. The number of elements is denoted by n^m . Let q_i denote the axial force of the i th member. The moments acting on two endpoints are denoted by m_i^1 and m_i^2 . The shear force at the endpoint of the i th member is denoted by τ_i .

The equilibrium equations between the external force $(\lambda \mathbf{f}_R + \mathbf{f}_D)$ and the internal forces \mathbf{q} , \mathbf{m}^1 , \mathbf{m}^2 , and $\boldsymbol{\tau}$ can be written in the form of

$$H^q \mathbf{q} + H_1^m \mathbf{m}^1 + H_2^m \mathbf{m}^2 + H^\tau \boldsymbol{\tau} = \lambda \mathbf{f}_R + \mathbf{f}_D, \quad (43)$$

where $\mathbf{q} = (q_i) \in \Re^{n^m}$, $\mathbf{m}^1 = (m_i^1) \in \Re^{n^m}$, $\mathbf{m}^2 = (m_i^2) \in \Re^{n^m}$, and $\boldsymbol{\tau} = (\tau_i) \in \Re^{n^m}$. The matrices H^q , H_1^m , H_2^m , and $H^\tau \in \Re^{n^d \times n^m}$ are constant matrices, where n^d denotes the number of degrees of freedom of displacements of the frame. The moment equilibria of internal forces are written as

$$l_i \tau_i + m_i^1 + m_i^2 = 0, \quad i = 1, \dots, n^m. \quad (44)$$

By letting $\mathbf{y} = (\mathbf{q}, \mathbf{m}^1, \mathbf{m}^2, \boldsymbol{\tau}) \in \mathfrak{N}^{n^m} \times \mathfrak{N}^{n^m} \times \mathfrak{N}^{n^m} \times \mathfrak{N}^{n^m}$ for simplicity, the equilibrium equations (43) and (44) can be condensed in the form of

$$H\mathbf{y} = \lambda \mathbf{f}_R^0 + \mathbf{f}_D^0, \tag{45}$$

where H is a constant matrix. Here, the constant vector \mathbf{f}_R^0 consists of the components of \mathbf{f}_R and $\mathbf{0}$, while \mathbf{f}_D^0 consists of the components of \mathbf{f}_D and $\mathbf{0}$.

We next introduce the yielding condition of a beam element. Suppose that the members experience plastic deformations only at their two ends. Provided that the dependence of the yield condition on the shear force is negligible, the admissible set of internal forces is given as

$$\mathfrak{Y} = \left\{ \mathbf{y} = (\mathbf{q}, \mathbf{m}^1, \mathbf{m}^2, \boldsymbol{\tau}) \left| \frac{|q_i + q_i^p|}{\bar{q}_i} + \frac{|m_i^j|}{\bar{m}_i} \leq 1 \quad (\text{for all } i \in \{1, \dots, n^m\}, \text{ for all } j \in \{1, 2\}) \right. \right\}, \tag{46}$$

where the set \mathfrak{Y} is illustrated in Figure 4. Here, \bar{q}_i , \bar{m}_i , and q_i^p are given constants.

From (45) and (46), the limit load factor for the fixed \mathbf{f}_R and \mathbf{f}_D is obtained by solving the following LP problem:

$$\lambda^*(\mathbf{f}_R, \mathbf{f}_D) = \max_{\lambda, \mathbf{y}} \{ \lambda \mid H\mathbf{y} = \lambda \mathbf{f}_R^0 + \mathbf{f}_D^0, \quad \mathbf{y} \in \mathfrak{Y} \}. \tag{47}$$

4.2. Robustness function under uncertain dead load. In a manner similar to a truss investigated in Section 3, we can formulate LP problems providing the robustness function under various uncertainty models of the dead load \mathbf{f}_D and the reference disturbance load \mathbf{f}_R . For simplicity of the presentation, we pay attention only to the uncertainty model (10) of \mathbf{f}_D . It is straightforward to extend the result below to the other uncertainty models investigated in Section 3.3. The remainder of this section is devoted to reformulating the problem (11) for framed structures into a numerically tractable problem.

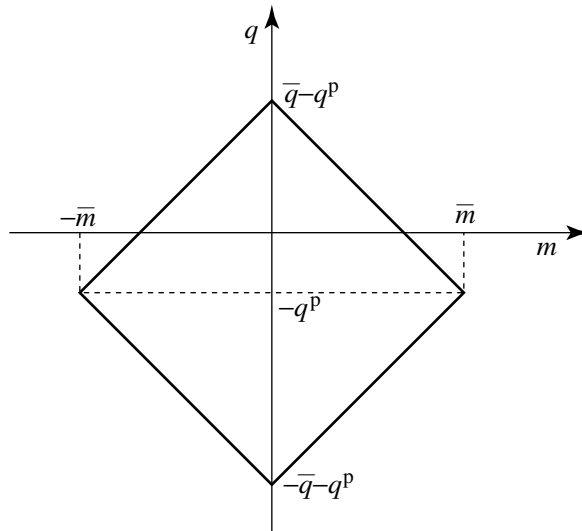


Figure 4. Yielding surface of the beam element.

Analogous to (18) in the proof of Proposition 3.2, any \mathbf{y} that solves the system of linear equations (45) can be written as

$$\mathbf{y} = H^\dagger(\lambda \mathbf{f}_R^0 + \tilde{\mathbf{f}}_D^0) + (H^\dagger F_0)\boldsymbol{\zeta} + H^\perp \boldsymbol{\xi}, \quad \boldsymbol{\xi} \in \mathfrak{R}^{n^\xi}. \quad (48)$$

For simplicity, we write Equation (48) component-wise as

$$q_i = \frac{1}{\bar{q}_i} \left[\mathbf{h}_i^q (\lambda \mathbf{f}_R^0 + \tilde{\mathbf{f}}_D^0) + (\mathbf{h}_i^q F_0)\boldsymbol{\zeta} + \bar{\mathbf{h}}_i^q \boldsymbol{\xi} \right], \quad i = 1, \dots, n^m, \quad (49)$$

$$m_i^1 = \frac{1}{\bar{m}_i} \left[\mathbf{h}_{i,1}^m (\lambda \mathbf{f}_R^0 + \tilde{\mathbf{f}}_D^0) + (\mathbf{h}_{i,1}^m F_0)\boldsymbol{\zeta} + \bar{\mathbf{h}}_{i,1}^m \boldsymbol{\xi} \right], \quad i = 1, \dots, n^m, \quad (50)$$

$$m_i^2 = \frac{1}{\bar{m}_i} \left[\mathbf{h}_{i,2}^m (\lambda \mathbf{f}_R^0 + \tilde{\mathbf{f}}_D^0) + (\mathbf{h}_{i,2}^m F_0)\boldsymbol{\zeta} + \bar{\mathbf{h}}_{i,2}^m \boldsymbol{\xi} \right], \quad i = 1, \dots, n^m, \quad (51)$$

where \mathbf{h}_i^q/\bar{q}_i , $\mathbf{h}_{i,1}^m/\bar{m}_i$, and $\mathbf{h}_{i,2}^m/\bar{m}_i$ denote appropriate row vectors of H^\dagger . Similarly, $\bar{\mathbf{h}}_i^q/\bar{q}_i$, $\bar{\mathbf{h}}_{i,1}^m/\bar{m}_i$, and $\bar{\mathbf{h}}_{i,2}^m/\bar{m}_i$ correspond to appropriate row vectors of H^\perp .

Proposition 4.1. For a framed structure with the yield condition (46), the robustness function $\hat{\alpha}(\lambda)$ defined by (10) and (11) is obtained as the optimal value of the LP problem

$$\begin{aligned} \hat{\alpha}(\lambda) = \max_{r, \boldsymbol{\xi}} \left\{ r \left| \left[(-1)^\mu \mathbf{h}_i^q / \bar{q}_i + (-1)^\nu \mathbf{h}_{i,j}^m / \bar{m}_i \right] (\lambda \mathbf{f}_R^0 + \tilde{\mathbf{f}}_D^0) + (-1)^\mu q_i^p / \bar{q}_i \right. \right. \\ \left. \left. + r \left\| \left[(-1)^\mu \mathbf{h}_i^q / \bar{q}_i + (-1)^\nu \mathbf{h}_{i,j}^m / \bar{m}_i \right] F_0 \right\|_{p^*} + \left[(-1)^\mu \bar{\mathbf{h}}_i^q / \bar{q}_i + (-1)^\nu \bar{\mathbf{h}}_{i,j}^m / \bar{m}_i \right] \boldsymbol{\xi} \leq 1, \right. \right. \\ \left. \left. i = 1, \dots, n^m, (j, \mu, \nu) \in \{1, 2\}^3 \right\} \quad (52) \end{aligned}$$

in the variables $r \in \mathfrak{R}$ and $\boldsymbol{\xi} \in \mathfrak{R}^{n^\xi}$.

Proof. In a manner similar to Proposition 3.1, we can show that $\hat{\alpha}(\lambda)$ is obtained as

$$\hat{\alpha}(\lambda) = \max_{r, \mathbf{y}} \left\{ r \left| H\mathbf{y} = \lambda \mathbf{f}_R^0 + \tilde{\mathbf{f}}_D^0 + F_0\boldsymbol{\zeta}, \quad \mathbf{y} \in \mathcal{O} \quad (\text{for all } \boldsymbol{\zeta} \in \mathcal{B}_p(r)) \right. \right\}. \quad (53)$$

Analogous to the proof of Proposition 3.2, we investigate the constraints of the problem (53). Since q_i , m_i^1 , and m_i^2 in (49)–(51) are regarded as linear functions of $\boldsymbol{\zeta}$, we write $q_i(\boldsymbol{\zeta})$, $m_i^1(\boldsymbol{\zeta})$, and $m_i^2(\boldsymbol{\zeta})$ for

simplicity. By using the definition (46) of \mathfrak{y} , the constraints of (53) can be rewritten as

$$\begin{aligned} \max_{\boldsymbol{\zeta}} \left\{ \frac{q_i(\boldsymbol{\zeta}) - q_i^p}{\bar{q}_i} + \frac{m_i^j(\boldsymbol{\zeta})}{\bar{m}_i} \mid \boldsymbol{\zeta} \in \mathcal{B}_p(r) \right\} &\leq 1, \\ \max_{\boldsymbol{\zeta}} \left\{ \frac{q_i(\boldsymbol{\zeta}) - q_i^p}{\bar{q}_i} - \frac{m_i^j(\boldsymbol{\zeta})}{\bar{m}_i} \mid \boldsymbol{\zeta} \in \mathcal{B}_p(r) \right\} &\leq 1, \\ \max_{\boldsymbol{\zeta}} \left\{ -\frac{q_i(\boldsymbol{\zeta}) - q_i^p}{\bar{q}_i} + \frac{m_i^j(\boldsymbol{\zeta})}{\bar{m}_i} \mid \boldsymbol{\zeta} \in \mathcal{B}_p(r) \right\} &\leq 1, \\ \max_{\boldsymbol{\zeta}} \left\{ -\frac{q_i(\boldsymbol{\zeta}) - q_i^p}{\bar{q}_i} - \frac{m_i^j(\boldsymbol{\zeta})}{\bar{m}_i} \mid \boldsymbol{\zeta} \in \mathcal{B}_p(r) \right\} &\leq 1, \quad \text{for all } i \in \{1, \dots, n^m\}, j \in \{1, 2\}, \end{aligned}$$

which are simply written as

$$\max_{\boldsymbol{\zeta}} \left\{ (-1)^\mu \frac{q_i(\boldsymbol{\zeta}) - q_i^p}{\bar{q}_i} + (-1)^\nu \frac{m_i^j(\boldsymbol{\zeta})}{\bar{m}_i} \mid r \geq \|\boldsymbol{\zeta}\|_p \right\} \leq 1, \quad (54)$$

$$\text{for all } i \in \{1, \dots, n^m\}, \quad j \in \{1, 2\}, \quad \mu \in \{1, 2\}, \quad \nu \in \{1, 2\}. \quad (55)$$

From the Hölder inequality [Michael Sttele 2004], the equation

$$\max_{\boldsymbol{\zeta}} \{ \mathbf{b}^\top \boldsymbol{\zeta} \mid r \geq \|\boldsymbol{\zeta}\|_p \} = r \|\mathbf{b}\|_{p^*}$$

holds for any constant $\mathbf{b} \in \mathfrak{N}^k$, from which it follows that Equation (55) is equivalent to

$$\begin{aligned} &\left[(-1)^\mu \mathbf{h}_i^q / \bar{q}_i + (-1)^\nu \mathbf{h}_{i,j}^m / \bar{m}_i \right] (\underline{\lambda} \mathbf{f}_R^0 + \tilde{\mathbf{f}}_D^0) + (-1)^\mu q_i^p / \bar{q}_i \\ &+ r \left\| \left[(-1)^\mu \mathbf{h}_i^q / \bar{q}_i + (-1)^\nu \mathbf{h}_{i,j}^m / \bar{m}_i \right] F_0 \right\|_{p^*} + \left[(-1)^\mu \bar{\mathbf{h}}_i^q / \bar{q}_i + (-1)^\nu \bar{\mathbf{h}}_{i,j}^m / \bar{m}_i \right] \\ &\boldsymbol{\xi} \leq 1, \text{ for all } i \in \{1, \dots, n^m\}, \quad j \in \{1, 2\}, \quad \mu \in \{1, 2\}, \quad \nu \in \{1, 2\}. \quad (56) \end{aligned}$$

Substitution of Equation (56) into (53) results in (52), which concludes the proof. \square

Proposition 4.1 is important, because it implies that the robustness function of a framed structure can be obtained easily by solving the LP problem (52). Similarly, it can be shown that the robustness function with respect to the uncertain reference disturbance load \mathbf{f}_R is also obtained as the optimal value of an LP problem, provided that \mathbf{f}_R obeys the uncertainty model introduced in Section 3.3.

5. Numerical experiments

In the following examples, computation was carried out on a Pentium M (1.7 GHz with 512 MB memory) with MATLAB V. 7.3 [MatLab 2006]. We solve an LP problem by using the MATLAB built-in function `linprog`. In the following examples, we mainly consider the uncertainty (10) of the dead load \mathbf{f}_D with $p = 2$ in order to avoid the redundancy of presentation. However, it should be emphasized that our major

contribution of this paper is to present the LP reformulation of the info-gap robustness function under various uncertainty models of f_D and f_R .

5.1. 3 × 3 truss. Consider a plane truss illustrated in Figure 1, where $W = 70.0$ cm, $H = 50.0$ cm, $n^d = 28$, and $n^m = 42$. The nodes (a) and (b) are pin-supported.

As the nominal dead load \tilde{f}_D , we apply the external forces (0, −300.0) kN at the nodes (f) and (g) as shown in Figure 1. Note again that f_D represents the sum of conventional live load and dead load in civil engineering. The nominal reference disturbance load \tilde{f}_R is defined such that (100.0, 0) kN and (50.0, 0) kN, respectively, are applied at the nodes (c) and (d). For each member, the yield stress is $\sigma_i^y = 400$ MPa and cross-sectional area is $a_i = 25.0$ cm² in Equation (7). Note that this example is similar to the example investigated in [Kanno and Takewaki 2007] for computing the worst-case limit load factor under the uncertainty of dead load.

The limit load factor under the nominal load is computed as $\lambda^*(\tilde{f}_R, \tilde{f}_D) = 24.18$ by employing the usual limit analysis, that is, by solving the LP problem (9). The collapse mode corresponds to the sway-type with horizontal displacements of the joints as shown in Figure 5.

Firstly, suppose that the dead load f_D obeys the uncertainty model (10), while f_R is assumed to be certain. Consider the following two cases:

Case 1: $p = 2$ in Equation (10);

Case 2: $p = \infty$ in Equation (10).

The uncertain dead load $F_0 \zeta$ is assumed to exist possibly at all free nodes except for the nodes (c) and (d). At the nodes (f) and (g), the uncertain load is supposed to exist in the directions orthogonal to \tilde{f}_D . Hence, the reference disturbance load is guaranteed to be unchanged as discussed in Section 3.2, where $n^z = 22$ in Equation (10). The coefficient matrix F_0 is defined so that the uncertainties of components of the vector $F_0 \zeta$ have no correlation, and each nonzero component of F_0 is equal to 100.0 kN. Accordingly, in Case 2, the uncertain load $F_0 \zeta$ runs through the squares and arrows depicted with the dotted lines in Figure 1. We set $\underline{\lambda} = 23.0$ in Equation (11). By solving the LP problem (17), we obtain $\hat{\alpha}(\underline{\lambda}) = 0.4170$ in Case 1 and $\hat{\alpha}(\underline{\lambda}) = 0.1000$ in Case 2.

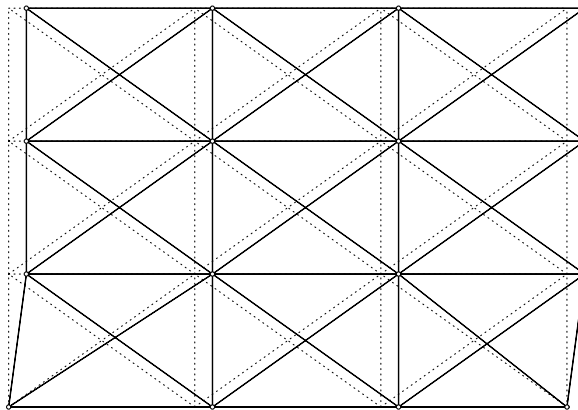


Figure 5. Collapse mode of 3 × 3 truss with the nominal external load.

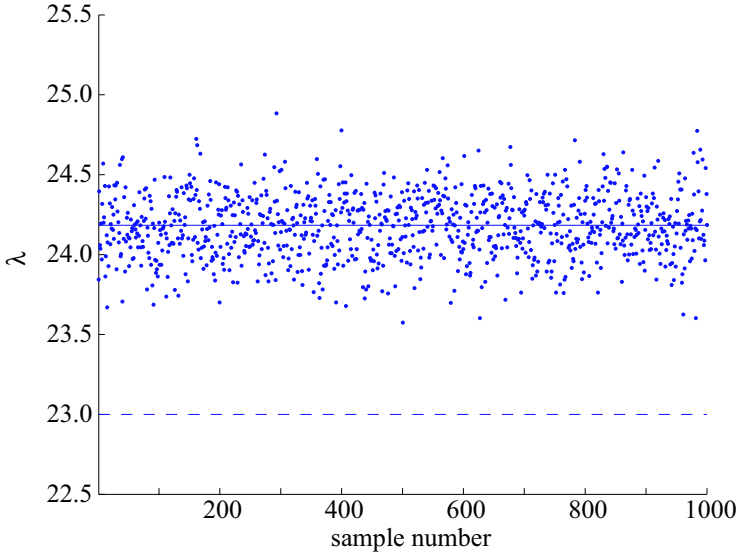


Figure 6. Limit load factor of the 3×3 truss in Case 1 for the uncertain f_D corresponding to randomly generated ζ (— nominal limit load factor $\lambda^*(\tilde{f}_R, \tilde{f}_D)$; -- performance requirement $\underline{\lambda}$).

For Case 1, we randomly generate a number of ζ satisfying $\|\zeta\|_2 = \hat{\alpha} = 0.4170$, and perform the limit analysis. The limit load factors $\lambda^*(\tilde{f}_R, f_D(\zeta))$ obtained are shown in Figure 6 as many points. It is observed from Figure 6 that all generated limit load factors are larger than the lower bound $\underline{\lambda}$, which supports the assertion that the constraint $\lambda^*(\tilde{f}_R, f_D) \geq \underline{\lambda}$ is guaranteed to be satisfied for any $f_D \in \mathcal{D}_2(\hat{\alpha}, \tilde{f}_D)$. Note that the actual worst-case dead load cannot be exactly predicted, in general, by taking a rather small number of random samples of ζ . Hence, in Figure 6 we cannot find the case in which the limit load factor coincides with $\underline{\lambda}$.

Figure 7 depicts the variation of the robustness function $\hat{\alpha}$ with respect to the performance requirement $\underline{\lambda}$. It is observed from Figure 7 that $\hat{\alpha} = 0$ corresponds to $\underline{\lambda} = \lambda^*(\tilde{f}_R, \tilde{f}_D)$, that is, the robustness function vanishes if $\underline{\lambda}$ is equal to the nominal limit load factor. The variation of $\hat{\alpha}$ possesses an angular point. This is because the worst-case dead load as well as the collapse mode in the worst case depends on the magnitude of uncertainty as observed in [Kanno and Takewaki 2007, section 6.1].

We next investigate robustness of the truss against the uncertain reference disturbance load f_R as discussed in Section 3.3. The dead load f_D is supposed to be certain. Consider the following three cases:

- Case 3: $p = 2$ in Equation (26);
- Case 4: $p = \infty$ in Equation (26);
- Case 5: $p = 2$ in Equation (41).

Note that $n^z = 3$ in Case 3 and Case 4 as illustrated in Figure 2, while $n^z = 2$ in Case 5 as illustrated in Figure 3. Each nonzero component of F_0 is equal to 100.0 kN. We set $\underline{\lambda} = 23.0$ in Equation (25). The

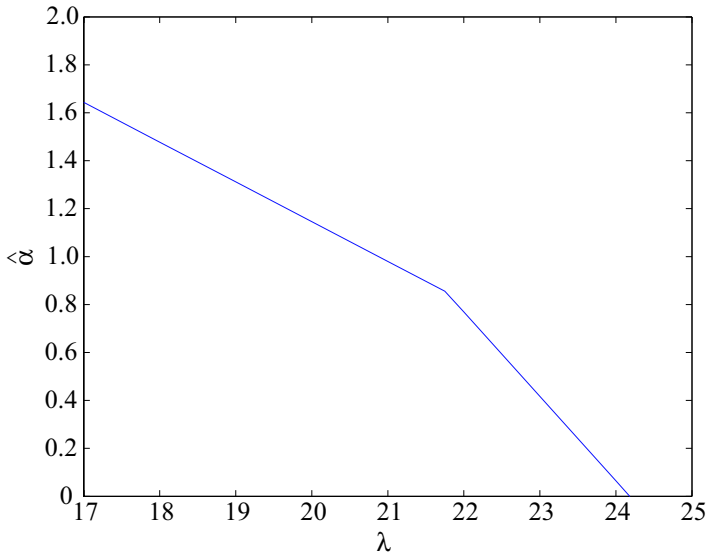


Figure 7. Variation of the robustness function $\hat{\alpha}$ of the 3×3 truss in Case 1 with respect to the performance requirement $\underline{\lambda}$.

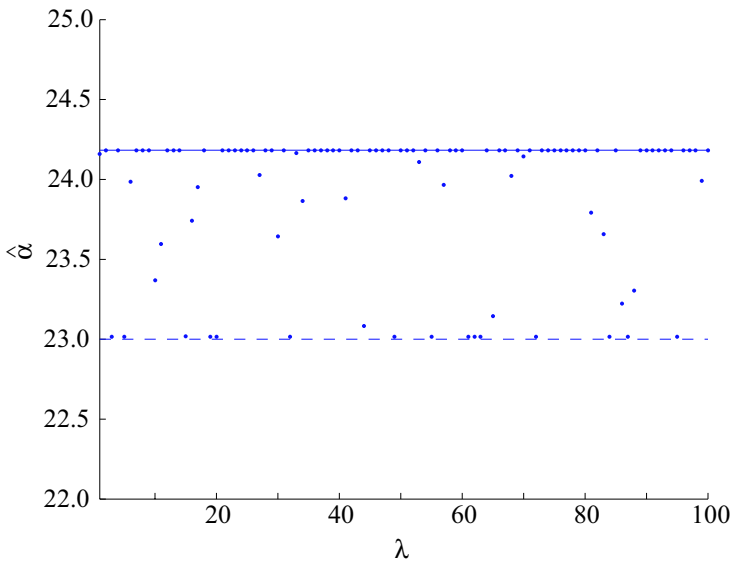


Figure 8. Limit load factor of the 3×3 truss in Case 4 for the uncertain f_R corresponding to randomly generated ζ (— nominal limit load factor $\lambda^*(\tilde{f}_R, \tilde{f}_D)$; -- performance requirement $\underline{\lambda}$).

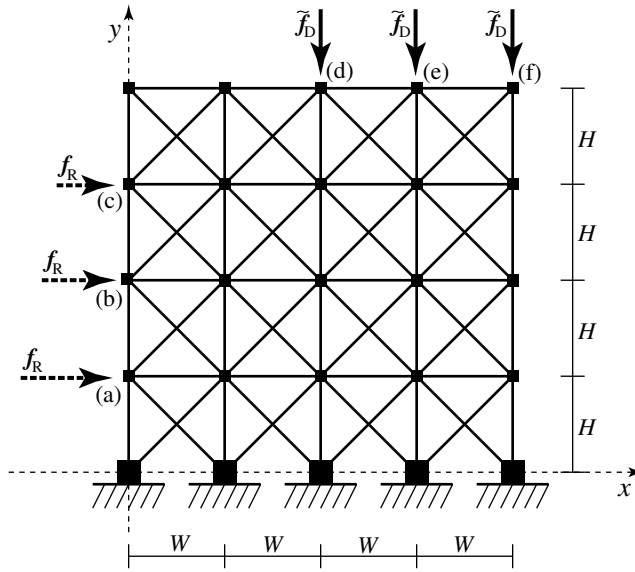


Figure 9. 68-member frame.

robustness functions are computed by solving the LP problems (28), (38), and (42) as $\hat{\alpha}(\underline{\lambda}) = 0.1739$, 0.1424, and 0.1207, respectively, in Case 3, Case 4, and Case 5. For Case 4, we randomly generate a number of ζ satisfying $\|\zeta\|_\infty = \hat{\alpha} = 0.1424$. The corresponding limit load factors $\lambda^*(\mathbf{f}_R(\zeta), \tilde{\mathbf{f}}_D)$ are depicted in Figure 8. It is observed from Figure 8 that all generated limit load factors are not smaller than the performance requirement $\underline{\lambda}$. Moreover, there exists the case in which the limit load factor coincides with $\underline{\lambda}$.

5.2. 68-member frame. Consider a plane frame illustrated in Figure 9, where $W = 200.0$ cm and $H = 200.0$ cm. The intersecting pair of diagonals is not connected at their center. All lowest nodes are the fixed supports, that is, $n^d = 60$ and $n^m = 68$.

As the nominal dead load $\tilde{\mathbf{f}}_D$, we apply the external forces $(0, -300.0)$ kN at the nodes (d)–(f) as shown in Figure 9. The nominal reference disturbance load $\tilde{\mathbf{f}}_R$ is defined such that $(100.0, 0)$ kN, $(70.0, 0)$ kN, and $(40.0, 0)$ kN are applied at the nodes (a)–(c), respectively.

For each member, the yield criterion is defined by (46) with $\bar{q}_i = 1000.0$ kN, $\bar{M}_i = 1000.0$ kN · m, and $N_i^p = 250.0$ kN. The limit load factor under the nominal dead load is computed as $\lambda^*(\tilde{\mathbf{f}}_R, \tilde{\mathbf{f}}_D) = 28.58$ by employing the usual limit analysis, that is, by solving the LP problem (47).

Suppose that the dead load \mathbf{f}_D has uncertainty and runs through the uncertainty set, Equation (10), while the reference disturbance load \mathbf{f}_R is assumed to be certain. The uncertain dead load $F_0 \zeta$ is assumed to exist possibly at all free nodes except for the nodes (a)–(c). At the nodes (d)–(f), the uncertain dead load is supposed to exist in the direction of the x -axis. Note that the uncertain external moment is not considered, and hence $n^z = 31$ in Equation (10). The coefficient matrix F_0 is defined so that the uncertainties of components of $F_0 \zeta$ have no correlation, and each nonzero component of F_0 is equal to 100.0 kN.

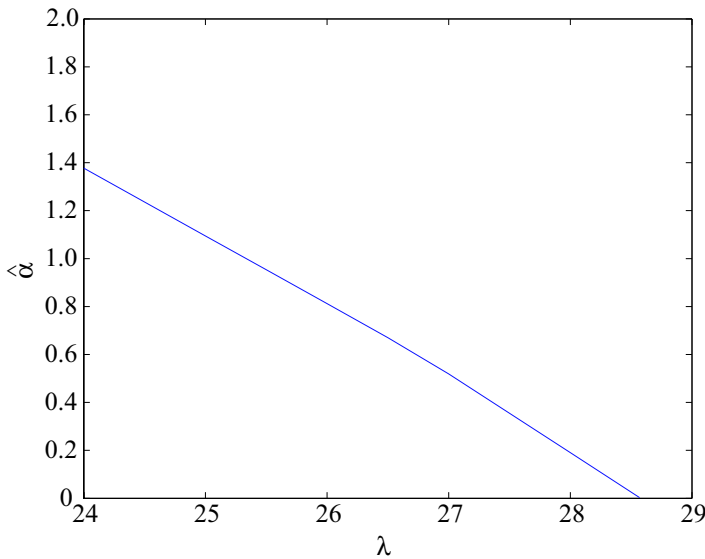


Figure 10. Variation of the robustness function $\hat{\alpha}$ of the 68-member frame with respect to the performance requirement $\underline{\lambda}$.

For a fixed $\underline{\lambda}$ and $p = 2$, the robustness function $\hat{\alpha}(\underline{\lambda})$ is computed by solving the LP problem (52). Figure 10 depicts the variation of the robustness function $\hat{\alpha}$ with respect to the performance requirement $\underline{\lambda}$. It is observed from Figure 10 that $\hat{\alpha}$ is a nonlinear function of $\underline{\lambda}$, since the collapse mode in the worst case depends on the magnitude of uncertainty of the dead load.

5.3. 36-member frame. Consider a plane frame illustrated in Figure 11, where

$$\begin{aligned}
 W &= 200.0 \text{ cm}, & H &= 200.0 \text{ cm}, \\
 n^d &= 60, & n^m &= 36.
 \end{aligned}$$

As the nominal dead load \tilde{f}_D , we apply the external forces (0, -300.0) kN at the nodes (d)–(h) as shown in Figure 11. The nominal reference disturbance load \tilde{f}_R is defined such that (100.0, 0) kN, (30.0, 0) kN, and (20.0, 0) kN, respectively, are applied at the nodes (a), (c), and (d), respectively. The nominal limit load factor is computed as $\lambda^*(\tilde{f}_R, \tilde{f}_D) = 15.00$.

Suppose that the dead load f_D has uncertainty such that $f_D \in \mathcal{D}_2(\alpha, \tilde{f}_D)$, while the reference disturbance load f_R is assumed to be certain. The uncertain dead load $F_0 \zeta$ is assumed to exist possibly at all free nodes except for the nodes (a)–(d). At the nodes (e)–(h), the uncertain dead forces are supposed to exist in the direction of the x -axis. Note that the uncertain external moment is not considered, and hence $n^z = 28$ in Equation (10). The coefficient matrix F_0 is defined so that the uncertainties of components of $F_0 \zeta$ have no correlation, and each nonzero component of F_0 is equal to 100.0 kN. Figure 12 depicts the variation of the robustness function $\hat{\alpha}$ with respect to the performance requirement $\underline{\lambda}$. It is observed from Figure 12 that $\hat{\alpha}$ is a nonlinear function of $\underline{\lambda}$.

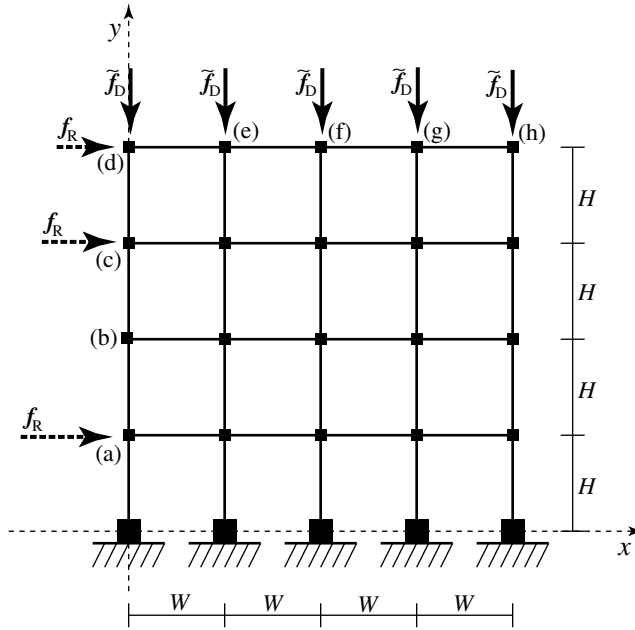


Figure 11. 36-member frame.

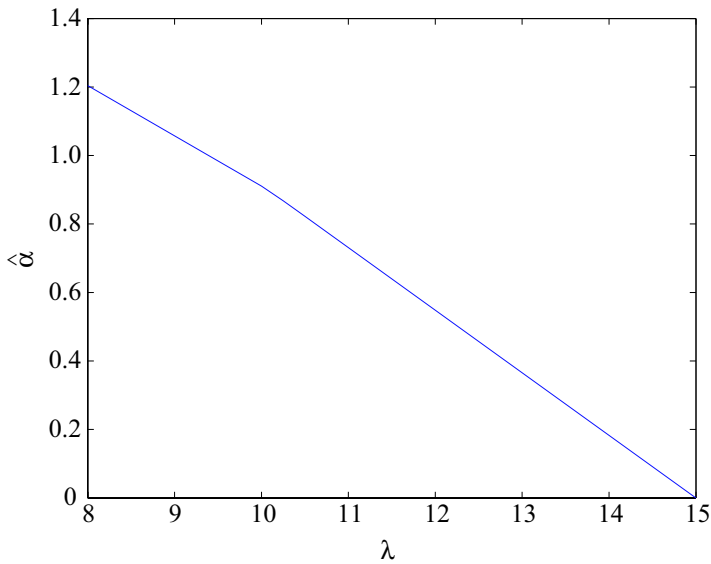


Figure 12. Variation of the robustness function $\hat{\alpha}$ of the 36-member frame with respect to the performance requirement λ .

6. Robust optimization and level of uncertainty

The robust optimization problem is investigated under the limit load factor constraint with the uncertain dead load. The level α of the uncertainty is fixed throughout this section.

6.1. Robust optimization of trusses. In this section, we formulate the robust optimization problem of trusses associated with the limit load factor by utilizing the theoretical results in Section 3. The notation introduced in Section 3 are used in this section again.

Let l_i denote the length of the i th member. The vector of member cross-sectional areas is denoted by $\mathbf{a} = (a_i) \in \mathfrak{R}^m$, which is regarded as a design variable vector. Without uncertainty of the external load, we first consider the minimization problem of the structural volume over the lower bound constraint of the limit load factor, which is formulated as

$$\min_{\mathbf{a}} \mathbf{l}^\top \mathbf{a} \quad \text{such that} \quad \begin{cases} \lambda^*(\mathbf{f}_R, \mathbf{f}_D) \geq \underline{\lambda}, \\ \mathbf{a} \geq \mathbf{0}, \end{cases} \quad (57)$$

Note that the limit load factor $\lambda^*(\mathbf{f}_R, \mathbf{f}_D)$ depends on \mathbf{a} implicitly in (57), because the absolute value of admissible axial force \bar{q}_i in (8) depends on a_i as (7). We can regard (57) as the nominal (or conventional) structural optimization problem associated with the limit load factor.

Suppose that \mathbf{f}_D is uncertain obeying the uncertainty model (10) for the fixed $\alpha \in \mathfrak{R}_{++}$, while \mathbf{f}_R is assumed to be certain. For simplicity, we write $\mathbf{f}_R = \tilde{\mathbf{f}}_R$ in the remainder of this section. The robust counterpart problem [Ben-Tal and Nemirovski 2002] of (57) is formulated as

$$\min_{\mathbf{a}} \mathbf{l}^\top \mathbf{a} \quad \text{such that} \quad \begin{cases} \lambda^*(\mathbf{f}_R, \mathbf{f}_D) \geq \underline{\lambda} & (\text{for all } \mathbf{f}_D \in \mathcal{D}_p(\alpha, \tilde{\mathbf{f}}_D)), \\ \mathbf{a} \geq \mathbf{0}. \end{cases} \quad (58)$$

Note again that α is fixed in Equation (58), while α has been regarded as a variable in (11). Observe that the constraint

$$\lambda^*(\mathbf{f}_R, \mathbf{f}_D) \geq \underline{\lambda} \quad (\text{for all } \mathbf{f}_D \in \mathcal{D}_p(\alpha, \tilde{\mathbf{f}}_D)) \quad (59)$$

becomes active at an optimal solution of (58). Hence, the robustness function of the optimal solution of (58) is given by

$$\hat{\alpha}(\underline{\lambda}) = \alpha. \quad (60)$$

It follows from the result of Proposition 3.2 that the robust constraint (59) of (58) is equivalently rewritten as

$$\begin{aligned} \mathbf{h}_i^\dagger(\underline{\lambda} \mathbf{f}_R + \tilde{\mathbf{f}}_D) + \alpha \|\mathbf{h}_i^\dagger F_0\|_{p^*} + \mathbf{h}_i^\perp \boldsymbol{\xi} &\leq \bar{q}_i, \quad i = 1, \dots, n^m, \\ -\mathbf{h}_i^\dagger(\underline{\lambda} \mathbf{f}_R + \tilde{\mathbf{f}}_D) + \alpha \|\mathbf{h}_i^\dagger F_i\|_{p^*} - \mathbf{h}_i^\perp \boldsymbol{\xi} &\leq \bar{q}_i, \quad i = 1, \dots, n^m. \end{aligned}$$

Consequently, by using Equation (7), the problem (58) is equivalent to the following LP problem in the variables \mathbf{a} and $\boldsymbol{\xi}$:

$$\min_{\mathbf{a}, \boldsymbol{\xi}} \mathbf{l}^\top \mathbf{a} \text{ such that } \begin{cases} \mathbf{h}_i^\dagger (\underline{\lambda} \mathbf{f}_R + \tilde{\mathbf{f}}_D) + \alpha \|\mathbf{h}_i^\dagger F_0\|_{p^*} + \mathbf{h}_i^\perp \boldsymbol{\xi} \leq \bar{\sigma}_i a_i, & i = 1, \dots, n^m, \\ -\mathbf{h}_i^\dagger (\underline{\lambda} \mathbf{f}_R + \tilde{\mathbf{f}}_D) + \alpha \|\mathbf{h}_i^\dagger F_i\|_{p^*} - \mathbf{h}_i^\perp \boldsymbol{\xi} \leq \bar{\sigma}_i a_i, & i = 1, \dots, n^m, \\ \mathbf{a} \geq \mathbf{0}. \end{cases} \quad (61)$$

It is rather amazing that the robust optimization problem (58) can be reformulated into the LP problem (61).

Similarly, it can be shown that the robust optimization problem under the uncertain reference disturbance load \mathbf{f}_R is also reformulated into an LP problem, if \mathbf{f}_R obeys the uncertainty model introduced in Section 3.3.

6.2. Robust optimization of framed structures. In this section, we show that a robust optimization problem of frames associated with the limit load factor can be reformulated as an LP problem. The notation introduced in Section 4 are used in this section again.

Let l_i and a_i denote the length and cross-sectional area of the i th member, respectively. Consider the sandwich cross-section with the radius d_i , the moment of inertia of which is written as $t_i = d_i^2 a_i$. Then \bar{q}_i and \bar{m}_i in (46) are written as

$$\bar{q}_i = \bar{\sigma}_i a_i, \quad \bar{m}_i = \bar{\sigma}_i d_i a_i. \quad (62)$$

Provided that d_i is fixed, we can assume that only \mathbf{a} is the design variables vector. Hence, the nominal optimization problem of frames can be formulated in the form of (57).

Suppose that \mathbf{f}_D is uncertain and obeys the uncertainty model (10) for the fixed $\alpha \in \Re_{++}$. The robust counterpart of the optimization problem is formulated in the form of (58). In a manner similar to Section 6.1, it follows from the result of Proposition 4.1 that the robust constraint (59) for frames is equivalently rewritten into the constraints of (52). Consequently, by using (62), the problem (58) for frames is equivalent to the following LP problem in the variables \mathbf{a} and $\boldsymbol{\xi}$:

$$\min_{\mathbf{a}, \boldsymbol{\xi}} \mathbf{l}^\top \mathbf{a} \text{ such that } \begin{aligned} & \left[(-1)^\mu \mathbf{h}_i^q + (-1)^\nu \mathbf{h}_{i,j}^m / d_i \right] (\underline{\lambda} \mathbf{f}_R^0 + \tilde{\mathbf{f}}_D^0) + (-1)^\mu q_i^p + \alpha \left\| \left[(-1)^\mu \mathbf{h}_i^q + (-1)^\nu \mathbf{h}_{i,j}^m / d_i \right] F_0 \right\|_{p^*} \\ & + \left[(-1)^\mu \bar{\mathbf{h}}_i^q + (-1)^\nu \bar{\mathbf{h}}_{i,j}^m / d_i \right] \boldsymbol{\xi} \leq \bar{\sigma}_i a_i, \quad i = 1, \dots, n^m, (j, \mu, \nu) \in \{1, 2\}^3, \quad \mathbf{a} \geq \mathbf{0}. \end{aligned} \quad (63)$$

6.3. Level of uncertainty and optimal structural volume. By using the LP formulations (61) and (62), we investigate the relation between the level of uncertainty α and the structural volume $\mathbf{l}^\top \mathbf{a}$ at the optimal design of the robust optimization problem.

6.3.1. Truss example. Recall the 3×3 truss illustrated in Figure 1, the loading condition of which has been defined in Section 5.1. Consider the robust optimization problem (58) with $\underline{\lambda} = 23.0$ and $\alpha = 0.4$. The robust optimal design found by solving (61) is shown in Figure 13, where the width of each member

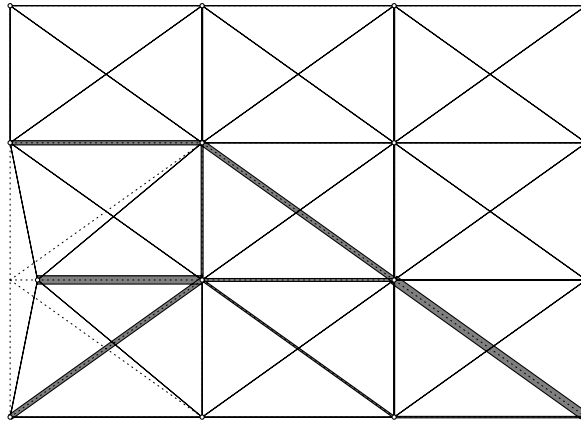


Figure 13. Robust optimal design of the 3×3 truss at $(\hat{\alpha}, \underline{\lambda}) = (0.4, 23.0)$ and the collapse mode with the nominal external load.

is proportional to its cross-sectional area. The limit load factor of this design under the nominal dead load is $\lambda^*(\tilde{\mathbf{f}}_R, \tilde{\mathbf{f}}_D) = 23.57$. The corresponding collapse mode is also illustrated in Figure 13.

Figure 14 depicts the relation between the structural volume and the robustness function at the optimal design. Note again that (60) holds at an optimal solution of (61). Moreover, the optimal solution of (61) at $\alpha = 0$ coincides with the optimal solution of the nominal optimization problem (57). It is of interest to note that, from the definition of the robustness function, any truss design satisfying the constraint (59) with $\underline{\lambda} = 24.0$ is plotted in (or on the boundary of) the domain \mathcal{F} in Figure 14. Thus, engineers may be able to make decisions incorporating the tradeoff between the robustness and the structural volume by using Figure 14. Note that the optimal value of the problem (61) depends linearly on α if the active set of constraints does not change when α increases. Hence, the optimal structural volume is a piecewise linear function of α in this example.

6.3.2. Frame example. Recall the 68-member frame illustrated in Figure 9, the loading condition of which has been defined in Section 5.2. The cross-section of each member is assumed to be sandwich, where $d_i = 1.0$ for simplicity. Supposing that \mathbf{f}_D is uncertain, consider the robust optimization problem (58), where $\underline{\lambda} = 27.0$ and $\alpha = 0.5$.

The robust optimal design found by solving Equation (62) is shown in Figure 15, where the width of each member is proportional to its cross-sectional area. The limit load factor of this design under the nominal dead load is $\lambda^*(\mathbf{f}_R, \tilde{\mathbf{f}}_D) = 28.47$. Figure 16 depicts the relation between the optimal structural volume and the robustness function for various values of $\underline{\lambda}$.

7. Conclusions

In this paper, we have proposed tractable numerical methods for robustness analysis of structures associated with the limit load factor under the load uncertainties. Particularly, it has been shown that the info-gap robustness function can be obtained by solving a linear programming (LP) problem. The effective method for computing the robustness function may permit us to apply the info-gap decision theory

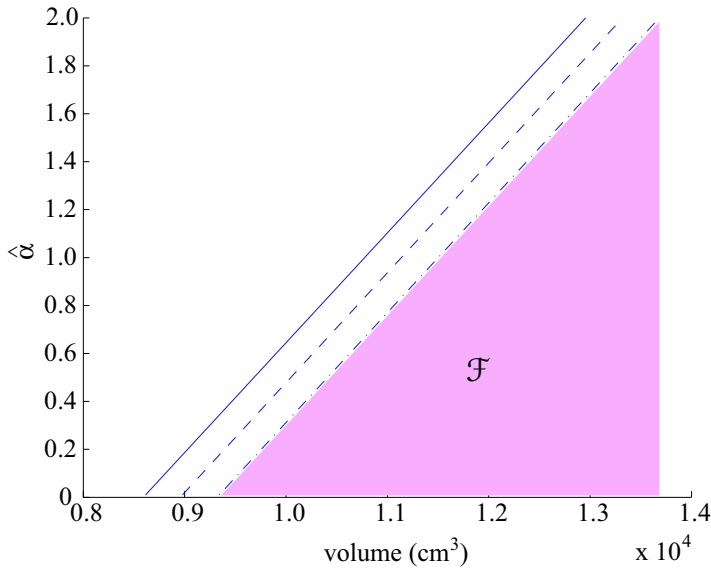


Figure 14. Relation between the robustness function $\hat{\alpha}$ and the optimal structural volume of the 3×3 truss (— $\lambda = 22.0$; -- $\lambda = 23.0$; - · - $\lambda = 24.0$).

[Ben-Haim 2006] to designing structures which never encounter violation of mechanical performance constraints under the uncertainty considered.

A main contribution of this paper is to show that the robustness function associated with the constraint on the limit load factor can be obtained as the optimal value of an LP problem. It is rather amazing that the robustness function can be computed easily by solving an LP problem, because the robustness function is originally defined in terms of the optimization problem over the infinitely many constraints. Moreover, for the given magnitude of uncertainty, detecting the worst-case limit load factor corresponds to finding a

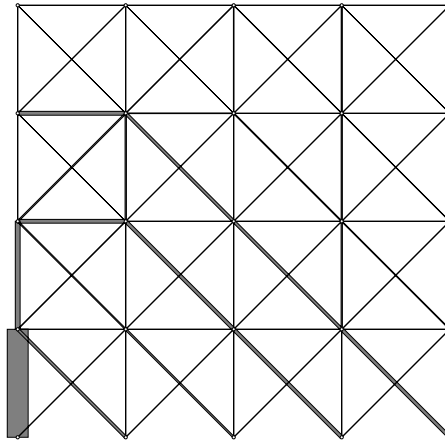


Figure 15. Robust optimal solution of the 68-member frame at $(\hat{\alpha}, \lambda) = (0.5, 27.0)$.

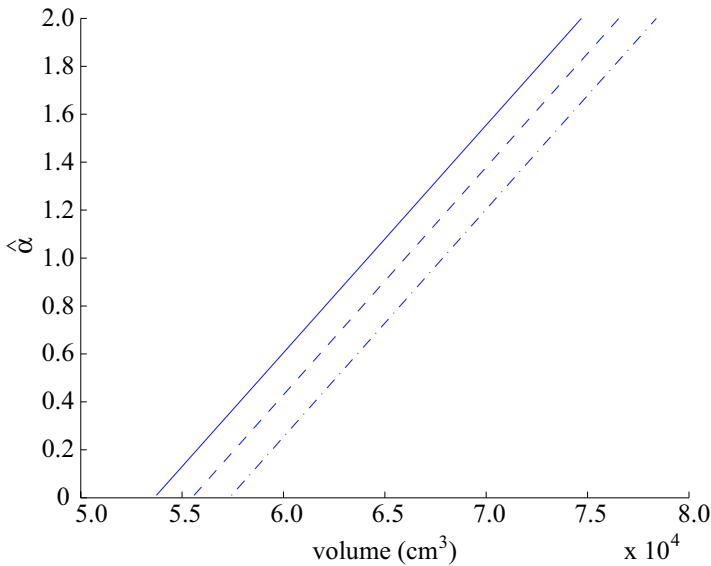


Figure 16. Relation between the robustness function $\hat{\alpha}$ and the optimal structural volume of the 68-member frame (— $\underline{\lambda} = 26.0$; -- $\underline{\lambda} = 27.0$; -·- $\underline{\lambda} = 28.0$).

global optimal solution of a nonlinear optimization problem as discussed in [Kanno and Takewaki 2007], that is, the results of this paper imply that computation of the robustness function is much easier than finding the worst case. Thus, we have shown that the constraint on the limit load factor is regarded as a tractable class of problems for computing the robustness function, although it is very difficult to compute the exact value of the robustness function in general.

We can compare the robustness of structures quantitatively by using the robustness function. In the numerical examples, the robustness function has been computed for uncertain trusses and framed structures by solving LP problems. The nonlinear relation between the robustness function and the performance requirement has been observed. It should be emphasized that most convex model approaches for robustness and/or uncertainty analysis have been developed based on first-order perturbation, while the proposed method does not use any approximation. Hence, the method presented is valid even for a large magnitude of uncertainty.

As a second contribution, the robust structural optimization associated with the limit load factor has been formulated for a given magnitude of uncertainty. It has been shown that this robust optimization problem can be reformulated as an LP problem for trusses as well as frames with sandwich cross-sections. In the numerical examples, robust optimal designs of a truss and frame are computed by solving LP problems. The relation between the robustness function and the optimal structural volume has been investigated by solving the robust optimization problems for various magnitudes of uncertainty.

Acknowledgment

The authors are grateful to Izuru Takewaki for his helpful comments. They are also grateful to anonymous referees for valuable comments and suggestions.

References

- [Alefeld and Mayer 2000] G. Alefeld and G. Mayer, “Interval analysis: theory and applications”, *J. Comput. Appl. Math.* **121** (2000), 421–464.
- [Andersen et al. 1998] K. Andersen, E. Christiansen, and M. L. Overton, “Computing limit loads by minimizing a sum of norms”, *SIAM J. Sci. Comput.* **19** (1998), 1046–1062.
- [Ben-Haim 2006] Y. Ben-Haim, *Information-gap decision theory: decisions under severe uncertainty*, 2nd ed., Academic Press, London, UK, 2006.
- [Ben-Haim and Elishakoff 1990] Y. Ben-Haim and I. Elishakoff, *Convex models of uncertainty in applied mechanics*, Elsevier, Amsterdam, The Netherlands, 1990.
- [Ben-Tal and Nemirovski 1997] A. Ben-Tal and A. Nemirovski, “Robust truss topology optimization via semidefinite programming”, *SIAM J. Optimiz.* **7** (1997), 991–1016.
- [Ben-Tal and Nemirovski 2002] A. Ben-Tal and A. Nemirovski, “Robust optimization—methodology and applications”, *Math. Program.* **B92** (2002), 453–480.
- [Beyer and Sendhoff 2007] H.-G. Beyer and S. Sendhoff, “Robust optimization—a comprehensive survey”, *Comput. Methods Appl. Mech. Eng.* **196** (2007), 3190–3218.
- [Chen et al. 2002] S. Chen, H. Lian, and X. Yang, “Interval static displacement analysis for structures with interval parameters”, *Int. J. Numer. Methods Eng.* **53** (2002), 393–407.
- [Cocchetti and Maier 2003] G. Cocchetti and G. Maier, “Elastic-plastic and limit-state analyses of frames with softening plastic-hinge models by mathematical programming”, *Int. J. Solids Struct.* **40** (2003), 7219–7244.
- [Elishakoff et al. 1994] I. Elishakoff, R. T. Haftka, and J. Fang, “Structural design under bounded uncertainty—optimization with anti-optimization”, *Comput. Struct.* **53** (1994), 1401–1405.
- [Ganzerli and Pantelides 1999] S. Ganzerli and C. P. Pantelides, “Load and resistance convex models for optimum design”, *Struct. Optimization* **17** (1999), 259–268.
- [Hodge 1959] P. G. Hodge, *Plastic analysis of structures*, McGraw-Hill, New York, 1959.
- [Kanno and Takewaki 2006a] Y. Kanno and I. Takewaki, “Robustness analysis of trusses with separable load and structural uncertainties”, *Int. J. Solids Struct.* **43** (2006), 2646–2669.
- [Kanno and Takewaki 2006b] Y. Kanno and I. Takewaki, “Sequential semidefinite program for robust truss optimization based on robustness functions associated with stress constraints”, *J. Optim. Theory Appl.* **130** (2006), 265–287.
- [Kanno and Takewaki 2007] Y. Kanno and I. Takewaki, “Worst-case plastic limit analysis of trusses under uncertain loads via mixed 0-1 programming”, *J. Mech. Mater. Struct.* **2** (2007), 245–273.
- [Kharmanda et al. 2004] G. Kharmanda, N. Olhoff, A. Mohamed, and M. Lemaire, “Reliability-based topology optimization”, *Struct. Multidiscip. Optimiz.* **26** (2004), 295–307.
- [Krabbenhoft and Damkilde 2003] K. Krabbenhoft and L. Damkilde, “A general non-linear optimization algorithm for lower bound limit analysis”, *Int. J. Numer. Methods Eng.* **56** (2003), 165–184.
- [Llyoyd Smith et al. 1990] D. Llyoyd Smith, P.-H. Chuang, and J. Munro, “Fuzzy linear programming in plastic limit design”, pp. 425–435 in *Mathematical Programming Methods in Structural Plasticity*, edited by D. Lloyd Smith, Springer-Verlag, Wien, Austria, 1990.
- [Marti and Stoeckel 2004] K. Marti and G. Stoeckel, “Stochastic linear programming methods in limit load analysis and optimal plastic design under stochastic uncertainty”, *ZAMM* **10** (2004), 666–677.
- [MatLab 2006] The MathWorks, *Using MATLAB*, Natick, MA: The MathWorks, 2006.
- [Michael Stele 2004] J. Michael Stele, *The Cauchy-Schwarz master class*, Cambridge University Press, New York, NY, 2004.
- [Muhanna and Mullen 2001] R. L. Muhanna and R. L. Mullen, “Uncertainty in mechanics problems—interval-based approach”, *J. Eng. Mech. (ASCE)* **127** (2001), 557–566.
- [Muralidhar and Jagannatha Rao 1997] R. Muralidhar and J. R. Jagannatha Rao, “New models for optimal truss topology in limit design based on unified elastic/plastic analysis”, *Comput. Methods Appl. Mech. Eng.* **140** (1997), 109–138.

- [Qiu and Elishakoff 1998] Z. Qiu and I. Elishakoff, “Antioptimization of structures with large uncertain-but-non-random parameters via interval analysis”, *Comput. Methods Appl. Mech. Eng.* **152** (1998), 361–372.
- [Rocho and Sonnenberg 2003] P. Rocho and S. Sonnenberg, “Limit analysis of frames—application to structural reliability”, pp. 269–282 in *Numerical methods for limit and shakedown analysis* (John von Neumann Institute for Computing), edited by M. Staat and M. Heitzer, Jülich, Germany, 2003.
- [Staat and Heitzer 2003] M. Staat and M. Heitzer, “Probabilistic limit and shakedown problems”, pp. 217–268 in *Numerical methods for limit and shakedown analysis* (John von Neumann Institute for Computing), edited by M. Staat and M. Heitzer, Jülich, Germany, 2003.
- [Takewaki and Ben-Haim 2005] I. Takewaki and Y. Ben-Haim, “Info-gap robust design with load and model uncertainties”, *J. Sound Vib.* **288** (2005), 551–570.
- [Zang et al. 2005] C. Zang, M. I. Friswell, and J. E. Mottershead, “A review of robust optimal design and its application in dynamics”, *Comput. Struct.* **83** (2005), 315–326.

Received 25 Jun 2007. Revised 7 Aug 2007. Accepted 8 Aug 2007.

YU MATSUDA: y-matsuda@ipl.t.u-tokyo.ac.jp

Department of Mathematical Informatics, Graduate School of Information Science and Technology, University of Tokyo, Tokyo 113-8656, Japan

YOSHIHIRO KANNO: kanno@mist.i.u-tokyo.ac.jp

Department of Mathematical Informatics, Graduate School of Information Science and Technology, University of Tokyo, Tokyo 113-8656, Japan

<http://www.simplex.t.u-tokyo.ac.jp/>

EULERIAN CONJUGATE STRESS AND STRAIN

ANDREW N. NORRIS

New results are presented for the stress conjugate to arbitrary Eulerian strain measures. The conjugate stress depends on two arbitrary quantities: the strain measure $f(\mathbf{V})$ and the corotational rate defined by the spin $\mathbf{\Omega}$. It is shown that for every choice of f there is a unique spin, called the f -spin, which makes the conjugate stress as close as possible to the Cauchy stress. The f -spin reduces to the logarithmic spin when the strain measure is the Hencky strain $\ln \mathbf{V}$. The formulation and the results emphasize the similarities in form of the Eulerian and Lagrangian stresses conjugate to the strains $f(\mathbf{V})$ and $f(\mathbf{U})$, respectively. Many of the results involve the solution to the equation $\mathbf{A}\mathbf{X} - \mathbf{X}\mathbf{A} = \mathbf{Y}$, which is presented in a succinct format.

1. Introduction

The notion of stress and strain are interlinked, regardless of the existence of a strain energy function. At the most basic level they are related by mechanical power, the rate of work per unit current volume of material,

$$\text{tr}(\boldsymbol{\sigma}\mathbf{D}) = \dot{w}. \quad (1-1)$$

Here $\boldsymbol{\sigma}$ is the Cauchy stress and \mathbf{D} the stretching tensor. This work-conjugate relation is independent of any notion of a reference configuration, although it is useful to introduce one. Let \mathbf{F} be the deformation gradient between the current and reference states, and let \mathbf{T} and \mathbf{E} be the stress and strain associated with the reference state, respectively. \mathbf{T} and \mathbf{E} are mutually conjugate if they satisfy

$$\text{tr}(\mathbf{T}\dot{\mathbf{E}}) = \dot{w} \det \mathbf{F}, \quad (1-2)$$

where the factor $\det \mathbf{F}$ arises from the change in volume between the current and reference descriptions. In fact, Equation (1-2) is usually taken as the starting point for determining stress. The choice of the strain \mathbf{E} is not unique, but once chosen it fixes the definition of \mathbf{T} through the work conjugacy of Equation (1-2). It is strange but true that the same simple connection does not apply to the relation between current or Eulerian strain and the Cauchy stress. The difficulty is in the definition of strain, say \mathbf{e} . What \mathbf{e} is such that $\dot{\mathbf{e}} = \mathbf{D}$? It turns out that this question is incomplete and that we must broaden it and seek the strain for which $\dot{\mathbf{e}} = \mathbf{D}$, where \circ signifies a corotational rate. Actually, the corotational rate itself also has to be found. Fortunately, both the strain and the rate have been determined: Xiao et al. [1998a] showed that the unique solution is obtained by using the Hencky strain $\ln \mathbf{V}$ in combination with the logarithmic rate. But we are getting ahead of ourselves.

It is evident that work-conjugacy is simpler for reference or Lagrangian stress and strain than for their counterparts in the current or Eulerian configuration. Note that the distinction between Lagrangian and

Keywords: conjugate, Eulerian, stress, logarithmic strain rate, Hencky, corotational.

Eulerian is made explicit by the polar decomposition $\mathbf{F} = \mathbf{R}\mathbf{U} = \mathbf{V}\mathbf{R}$; quantities associated with or defined by \mathbf{U} and \mathbf{V} will be called Lagrangian and Eulerian, respectively.

It is instructive to review work-conjugacy for Lagrangian stress and strain. The starting point is the fact that the stretching tensor \mathbf{D} is the symmetric part of $\dot{\mathbf{F}}\mathbf{F}^{-1}$. Let the strain be chosen, quite generally, as $\mathbf{E} = f(\mathbf{U})$, where the function f is sufficiently smooth, then Equations (1–1) and (1–2) imply

$$\text{tr}(\mathbf{T}[\nabla f(\mathbf{U})]\dot{\mathbf{U}}) = \text{tr}(\boldsymbol{\sigma}\mathbf{D}) \det \mathbf{F}. \tag{1-3}$$

The gradient $\nabla f(\mathbf{U})$ is a fourth order tensor function which will be described later. At the same time the kinematic quantities, strain rate $\dot{\mathbf{U}}$ and stretching \mathbf{D} , may be related quite easily (see Appendix A)

$$\dot{\mathbf{U}} = 2(\mathbf{U} \boxtimes \mathbf{I} + \mathbf{I} \boxtimes \mathbf{U})^{-1}(\mathbf{U} \boxtimes \mathbf{U}) \mathbf{R}'\mathbf{D}\mathbf{R}. \tag{1-4}$$

Using the independence of \mathbf{D} , Equations (1–3) and (1–4) imply, formally at least, that the stress conjugate to the Lagrangian strain $f(\mathbf{U})$ is

$$\mathbf{T} = (\nabla f(\mathbf{U}))^{-1} \mathbf{T}^{(1)}, \tag{1-5}$$

where $\mathbf{T}^{(1)}$, sometimes called the Biot stress or the Jaumann stress, and \mathbf{S} , the second Piola–Kirchhoff stress tensor, are

$$\begin{aligned} \mathbf{T}^{(1)} &= \frac{1}{2}(\mathbf{U} \boxtimes \mathbf{I} + \mathbf{I} \boxtimes \mathbf{U}) \mathbf{S}, \\ \mathbf{S} &= \mathbf{F}^{-1} \boldsymbol{\sigma} \mathbf{F}^{-t} \det \mathbf{F}. \end{aligned} \tag{1-6}$$

We have used the symmetry of \mathbf{T} and certain commutative properties to express the stress in Equation (1–5) as a fourth order tensor acting on $\mathbf{T}^{(1)}$. The tensor product notation, \boxtimes , explained in the next section, is used throughout as we find it makes results more transparent. Equations (1–5) and (1–6) embody work-conjugacy for arbitrary Lagrangian strain $f(\mathbf{U})$.

Although the notation in Equation (1–5) might be unfamiliar, the result is not (see [Ogden 1984, eq. (3.5.31)]). The fourth order gradient tensor $\nabla f(\mathbf{U})$ is discussed in detail by Norris [2007]. In particular, it is positive definite, symmetric, and invertible for any strain measure function [Hill 1978]. Examples will be presented for the Seth–Hill strain measure functions,

$$f^{(m)}(x) = m^{-1}(x^m - 1).$$

For instance, the stress $\mathbf{T}^{(m)}$ associated with $f^{(m)}(\mathbf{U})$ is

$$\mathbf{T}^{(0)} = (\nabla \ln \mathbf{U})^{-1} \mathbf{T}^{(1)} = \int_0^1 dx \mathbf{U}^x \boxtimes \mathbf{U}^{1-x} \mathbf{T}^{(1)}, \tag{1-7a}$$

$$\mathbf{T}^{(\frac{1}{3})} = \frac{1}{3}(\mathbf{U}^{2/3} \boxtimes \mathbf{I} + \mathbf{U}^{1/3} \boxtimes \mathbf{U}^{1/3} + \mathbf{I} \boxtimes \mathbf{U}^{2/3}) \mathbf{T}^{(1)}, \tag{1-7b}$$

$$\mathbf{T}^{(\frac{1}{2})} = \frac{1}{2}(\sqrt{\mathbf{U}} \boxtimes \mathbf{I} + \mathbf{I} \boxtimes \sqrt{\mathbf{U}}) \mathbf{T}^{(1)}, \tag{1-7c}$$

$$\mathbf{T}^{(2)} = \mathbf{S}, \tag{1-7d}$$

$$\mathbf{T}^{(-m)} = (\mathbf{U}^m \boxtimes \mathbf{U}^m) \mathbf{T}^{(m)}. \tag{1-7e}$$

Some of the conjugate stresses listed are well known, for instance $m = 1, 2, -2$ [Hill 1978; Ogden 1984], and Equation (1–7e) follows from [Ogden 1984, p. 158]. Identities Equation (1–7a)–(1–7c) and

the others will become evident later. The second identity in Equation (1–7a) follows from [Norris 2007]. We note that the Piola–Kirchhoff stress is conjugate to $\mathbf{E} = \frac{1}{2}(\mathbf{U}^2 - 1)$, the Green strain, which is typically used in applications.

A principal objective of this paper is to find analogous expressions for the Eulerian stress $\boldsymbol{\tau}$ conjugate to the strain $\mathbf{e} = f(\mathbf{V})$, where \mathbf{V} is the right stretch tensor, and the function f is again arbitrary. We also require that the Cauchy stress be included among the Eulerian stresses, just as the Piola–Kirchhoff stress appears naturally for the Green strain.

Unlike the Lagrangian strains, $\dot{f}(\mathbf{V})$ is not an objective tensor [Dill 2006], and it is known that this strain rate does not, in general, possess a conjugate stress [MacVean 1968]. This difficulty can be avoided by defining conjugacy in terms of corotational strain rates. The corotational rate of a symmetric second order tensor $\mathbf{A}(t)$ is

$$\overset{\circ}{\mathbf{A}} \equiv \dot{\mathbf{A}} + \mathbf{A}\boldsymbol{\Omega} - \boldsymbol{\Omega}\mathbf{A},$$

where the skew symmetric tensor $\boldsymbol{\Omega}$ is called the spin. Xiao et al. [1998c; 1998b] showed that an objective spin has the general form

$$\boldsymbol{\Omega} = \mathbf{W} + \mathbb{P}(\mathbf{V}) \mathbf{D}, \tag{1–8}$$

where \mathbf{W} is the skew symmetric part of $\dot{\mathbf{F}}\mathbf{F}^{-1}$ and \mathbb{P} is an isotropic fourth order tensor-valued function of \mathbf{V} . Lehmann and Liang [1993] showed that using the rate associated with \mathbf{R} , a corotational spin equal to the “twirl” $\boldsymbol{\Omega}^R = \dot{\mathbf{R}}\mathbf{R}^t$, the Eulerian and Lagrangian stresses conjugate to $f(\mathbf{V})$ and $f(\mathbf{U})$ are related by $\boldsymbol{\tau} = \mathbf{R}\mathbf{T}\mathbf{R}^t$. This relationship simply rotates the Lagrangian stress, but does not reproduce the Cauchy stress for any choice of f .

The fundamental relation for Eulerian conjugate stress is based on the finding of Xiao et al. [1997] that

$$\ln(\mathbf{V}) \overset{\circ}{=} \mathbf{D}, \tag{1–9}$$

where $\overset{\circ}{\ln}$ denotes an objective corotational rate defined by the logarithmic spin $\boldsymbol{\Omega}^{\log}$ [Xiao et al. 1997]. We will discuss $\boldsymbol{\Omega}^{\log}$ in detail, providing a new derivation and representation, and comparison with $\boldsymbol{\Omega}^R$. Equation (1–9) allows us to define a class of work-conjugate Eulerian stress-strain pairs for all $f(\mathbf{V})$ that includes the Cauchy stress. However, it should be borne in mind that the logarithmic rate is but one of a continuum of possibilities.

A second objective of this paper is a generalization of Equation (1–9) to arbitrary strain measure $f(\mathbf{V})$. Xiao et al. [1997] proved that \mathbf{D} is recovered only from the Hencky strain $\ln(\mathbf{V})$ combined with the logarithmic spin; no other strain measure can yield \mathbf{D} , no matter what spin is used. Here we will show that for a given strain measure $f(\mathbf{V})$, there is a unique spin which provides the best *approximation* of \mathbf{D} , and the corresponding conjugate stress is the best approximation of the Cauchy stress.

1.1. Summary of principal results. Our first main result is:

Theorem 1. The stress conjugate to the Eulerian strain $f(\mathbf{V})$ is

$$\boldsymbol{\tau} = (\nabla f(\mathbf{V}))^{-1} \boldsymbol{\tau}^{(1)}(\boldsymbol{\Omega}), \tag{1–10}$$

where $\boldsymbol{\tau}^{(1)}$ depends on the corotational rate used as

$$\boldsymbol{\tau}^{(1)}(\boldsymbol{\Omega}) = [\mathbf{V}^2 \boxtimes \mathbf{I} + \mathbf{I} \boxtimes \mathbf{V}^2 + (\mathbf{V}^2 \boxtimes \mathbf{I} - \mathbf{I} \boxtimes \mathbf{V}^2)\mathbb{P}(\mathbf{V})]^{-1} (\mathbf{V} \boxtimes \mathbf{I} + \mathbf{I} \boxtimes \mathbf{V}) \boldsymbol{\sigma}.$$

We will explain this result in detail, and provide alternative representations for Equation (1–10). We note at this stage the similarity in form between Equations (1–5) and (1–10). In particular, the stress $\boldsymbol{\tau}^{(m)}$ conjugate to the strain $f^{(m)}(\mathbf{V})$ is

$$\begin{aligned} \boldsymbol{\tau}^{(0)} &= (\nabla \ln \mathbf{V})^{-1} \boldsymbol{\tau}^{(1)} = \int_0^1 dx \mathbf{V}^x \boxtimes \mathbf{V}^{1-x} \boldsymbol{\tau}^{(1)}, \\ \boldsymbol{\tau}^{(\frac{1}{3})} &= \frac{1}{3}(\mathbf{V}^{2/3} \boxtimes \mathbf{I} + \mathbf{V}^{1/3} \boxtimes \mathbf{V}^{1/3} + \mathbf{I} \boxtimes \mathbf{V}^{2/3}) \boldsymbol{\tau}^{(1)}, \\ \boldsymbol{\tau}^{(\frac{1}{2})} &= \frac{1}{2}(\sqrt{\mathbf{V}} \boxtimes \mathbf{I} + \mathbf{I} \boxtimes \sqrt{\mathbf{V}}) \boldsymbol{\tau}^{(1)}, \\ \boldsymbol{\tau}^{(2)} &= 2(\mathbf{V} \boxtimes \mathbf{I} + \mathbf{I} \boxtimes \mathbf{V})^{-1} \boldsymbol{\tau}^{(1)}, \\ \boldsymbol{\tau}^{(-m)} &= (\mathbf{V}^m \boxtimes \mathbf{V}^m) \boldsymbol{\tau}^{(m)}. \end{aligned}$$

The second principal result introduces a new spin defined by the Eulerian strain measure.

Theorem 2. For every Eulerian strain measure $f(\mathbf{V})$ there is a unique corotational rate which minimizes the difference between the conjugate stress and the Cauchy stress. The rate is defined by the f-spin $\boldsymbol{\Omega}^f = \mathbf{W} + \mathbb{P}^f \mathbf{D}$ which depends upon the function f via the fourth order projection tensor

$$\mathbb{P}^f = (\mathbf{V} \boxtimes \mathbf{I} - \mathbf{I} \boxtimes \mathbf{V})^* [(\nabla f(\mathbf{V}))^{-1} - (\mathbf{V} \boxtimes \mathbf{I} + \mathbf{I} \boxtimes \mathbf{V})^{-1} (\mathbf{V}^2 \boxtimes \mathbf{I} + \mathbf{I} \boxtimes \mathbf{V}^2)],$$

and \mathbb{A}^* denotes the pseudo-inverse (or Moore–Penrose inverse) of the tensor \mathbb{A} . The conjugate stress using the f-spin is

$$\boldsymbol{\tau} = \boldsymbol{\sigma}^f \equiv \boldsymbol{\sigma} + \sum_{i=1}^n \left(\frac{1}{\lambda_i f'(\lambda_i)} - 1 \right) \mathbf{V}_i \boxtimes \mathbf{V}_i \boldsymbol{\sigma}, \tag{1–11}$$

where λ_i are the principal stretches, \mathbf{V}_i the principal dyads, that is, the eigenvalues and eigentensors of \mathbf{V} , and the eigen-index $n \in \{1, 2, 3\}$ is the number of distinct eigenvalues. The conjugate stress is minimal in the sense that $|\boldsymbol{\tau} - \boldsymbol{\sigma}| > |\boldsymbol{\sigma}^f - \boldsymbol{\sigma}|$ for any other corotational rate.

The pseudo-inverse is a unique quantity and will be defined in detail later.

The logarithmic spin [Xiao et al. 1998a] is a very special case of the f-spin. It is clear from Equation (1–11) that when $f(x) = \ln x$ and the f-spin is used then the conjugate stress is simply the Cauchy stress, so $\boldsymbol{\sigma}^{\ln} = \boldsymbol{\sigma}$. Note that $\boldsymbol{\sigma}$ is recovered as $\boldsymbol{\tau}^{(0)}$, the stress conjugate to the Hencky strain $\ln(\mathbf{V})$. No other spin reproduces the Cauchy stress as the conjugate of any strain [Xiao et al. 1997]. This emphasizes the mutual relation between the Hencky strain and the logarithmic spin.

1.2. Review and plan of the paper. No attempt is made to summarize the considerable literature on work-conjugacy, strain measures and associated stresses, although two introductory reviews are worthy of mention. Curnier and Rakotomanana [1991] provide an instructive overview of strain measures and conjugate stresses, with extensive references to the literature prior to 1990. A more concise but in-depth description of work conjugacy and its implications is given by Ogden [1984]. These reviews and most of the work prior to 1991 dealt with stress conjugate to Lagrangian strain measures, although there had been some relevant work on quantities related to $\ln(\mathbf{V})$. For instance, Fitzgerald [1980] considered the

stress conjugate to $\ln(\mathbf{V})$ in the context of hyperelasticity. Hoger [1987] derived expressions for the rate of change of \mathbf{U} , which subsequently proved useful for Lehmann et al. [1991; 1993] when they considered \mathbf{V} specifically. The focus here is on Eulerian strain and its work-conjugate stress, and builds upon developments in the 1990s. Lehmann and Liang [1993] introduced a clear procedure to extend the idea of work-conjugacy to strains whose rates are not objective in a fixed frame (see also [Lehmann and Guo 1991]). The idea, reviewed in Section 4, permits the use of corotational rates. This is especially important for Eulerian strain measures since Xiao et al. [1997] proved that the only way to obtain \mathbf{D} with Eulerian strain is as the logarithmic rate of $\ln(\mathbf{V})$. We emphasize that the pointwise rate of working \dot{w} is the focus as we consider its implications for pointwise stress based on different definitions of strain. No assumptions of material homogeneity, isotropy, or otherwise is assumed or required.

In a series of groundbreaking papers, Xiao et al. [1997; 1998b; 1998c] provide the most complete and thorough analysis of Eulerian conjugate stress and strain. Culminating with [Xiao et al. 1998a], these authors showed that the notion of conjugate stress is just as relevant to Eulerian strain as it is for Lagrangian strain. Because the role of the rate, or spin, is central to the Eulerian problem but is absent from Lagrangian work-conjugacy, it is essential to have a thorough understanding of the possible spin tensors and their dependence on quantities such as \mathbf{D} , \mathbf{W} , and \mathbf{V} . Once this is understood then the form of the conjugate stress becomes apparent. Xiao et al. [1998a] derived expressions for the Eulerian conjugate stress for arbitrary strain measures f and for arbitrary permissible corotational strain rate. Their subsequent work has highlighted the role of the logarithmic rate and the Hencky strain in applications to hyperelasticity and other constitutive theories; see [Xiao et al. 2006] for a thorough review.

This paper presents new results which extend the work of Xiao et al. in several directions. The introduction and discovery of the role of the f-spin shows that there is a certain unique conjugate stress associated with every Eulerian strain measure. The dual formulation for the Eulerian and Lagrangian conjugate stresses in Equations (1–5) and (1–10) further emphasizes the similarities in the two descriptions. The formulation throughout is in direct tensor notation, which we believe makes the results more transparent.

The plan of the paper is as follows. The notation is introduced in Section 2, where the gradient and the pseudo-inverse of a tensor are defined. Corotational strain rates are discussed in Section 3 and some basic results for Eulerian strain measures are derived. The f-spin is introduced and discussed in Section 4. It is shown that the corotational rate defined by the f-spin, or f-rate, has certain unique and desirable properties. The main results for conjugate stress-strain pairs are deduced in Section 5.

2. Tensors functions and the pseudo-inverse.

2.1. Preliminaries. We will be dealing with tensors of second and fourth order. Second order tensors act on vectors in a three dimensional inner product space, $\mathbf{x} \rightarrow \mathbf{A}\mathbf{x}$ with transpose \mathbf{A}^t such that $\mathbf{y} \cdot \mathbf{A}\mathbf{x} = \mathbf{x} \cdot \mathbf{A}^t\mathbf{y}$. Spaces of symmetric and skew-symmetric tensors are distinguished, $\text{Lin} = \text{Sym} \oplus \text{Skw}$ where $\mathbf{A} \in \text{Sym}$ (Skw) if and only if $\mathbf{A}^t = \mathbf{A}$ ($\mathbf{A}^t = -\mathbf{A}$). The inner product on Lin is defined by $\mathbf{A} \cdot \mathbf{B} = \text{tr}(\mathbf{A}\mathbf{B}^t)$. The product $\mathbf{A}\mathbf{B} \in \text{Lin}$ is defined by $\mathbf{y} \cdot \mathbf{A}\mathbf{B}\mathbf{x} = (\mathbf{A}^t\mathbf{y}) \cdot \mathbf{B}\mathbf{x}$.

Psym is the space of positive definite second order tensors. When dealing with functions of a symmetric tensor it is often useful to rephrase the functional form in terms of the spectral decomposition:

$$\mathbf{A} = \sum_{i=1}^n \alpha_i \mathbf{A}_i, \quad \mathbf{I} = \sum_{i=1}^n \mathbf{A}_i, \quad \mathbf{A}_i \mathbf{A}_j = \begin{cases} \mathbf{A}_i, & i = j, \\ 0, & i \neq j, \end{cases}$$

where $\mathbf{A}_i \in \text{Psym}$, and $n \leq 3$ is the eigen-index. Thus,

$$f(\mathbf{A}) = \sum_{i=1}^n f(\alpha_i) \mathbf{A}_i.$$

The Poisson bracket of two second order tensors is

$$\{\mathbf{A}, \mathbf{B}\} = \mathbf{AB} - \mathbf{BA}.$$

$\mathbb{L}\text{in}$ is the space of fourth order tensors acting on Lin , $\mathbf{X} \rightarrow \mathbb{A}\mathbf{X}$ with transpose \mathbb{A}^t such that

$$\mathbf{Y} \cdot \mathbb{A}\mathbf{X} = \mathbf{X} \cdot \mathbb{A}^t \mathbf{Y}$$

for all $\mathbf{X}, \mathbf{Y} \in \text{Lin}$. The vector space may be decomposed $\mathbb{L}\text{in} = \text{Sym} \oplus \text{Skw}$ where Sym and Skw denote the spaces of symmetric ($\mathbb{A}^t = \mathbb{A}$) and skew-symmetric ($\mathbb{A}^t = -\mathbb{A}$) tensors, respectively. Any $\mathbb{A} \in \mathbb{L}\text{in}$ can be uniquely partitioned into symmetric and skew parts: $\mathbb{A} = \mathbb{A}^{(+)} + \mathbb{A}^{(-)}$, where $\mathbb{A}^{(\pm)} = (\mathbb{A} \pm \mathbb{A}^t)/2$. The identity $\mathbb{1}$ satisfies $\mathbb{1}\mathbf{X} = \mathbf{X}$ for all $\mathbf{X} \in \text{Lin}$. The product $\mathbb{A}\mathbb{B} \in \mathbb{L}\text{in}$ is defined by $\mathbf{Y} \cdot \mathbb{A}\mathbb{B}\mathbf{X} = (\mathbb{A}^t \mathbf{Y}) \cdot \mathbb{B}\mathbf{X}$. $\mathbb{P}\text{sym}$ is the space of positive definite fourth order tensors: $\mathbb{A} \in \mathbb{P}\text{sym}$ if and only if $\mathbf{X} \cdot \mathbb{A}\mathbf{X} > 0$, for all nonzero $\mathbf{X} \in \text{Sym}$.

The square tensor product $\mathbf{X} \boxtimes \mathbf{Y}$, $\text{Lin} \times \text{Lin} \rightarrow \mathbb{L}\text{in}$, is defined by [Rosati 2000]

$$(\mathbf{X} \boxtimes \mathbf{Y}) \mathbf{Z} = \mathbf{X}\mathbf{Z}\mathbf{Y}^t, \quad \text{for all } \mathbf{Z} \in \text{Lin}.$$

In particular, we note the property $(\mathbf{A} \boxtimes \mathbf{B})(\mathbf{X} \boxtimes \mathbf{Y}) = (\mathbf{A}\mathbf{X}) \boxtimes (\mathbf{B}\mathbf{Y})$.

2.1.1. The tensor gradient function and its inverse. The gradient of a tensor function $f(\mathbf{A})$ is a fourth order tensor $\nabla f \in \mathbb{L}\text{in}$ defined by

$$\nabla f(\mathbf{A}) \mathbf{X} = \lim_{\epsilon \rightarrow 0} \frac{1}{\epsilon} [f(\mathbf{A} + \epsilon \mathbf{X}) - f(\mathbf{A})]. \tag{2-1}$$

We make extensive use of the following representation, which uses the spectral form of \mathbf{A} ,

$$\nabla f(\mathbf{A}) = \sum_{i,j=1}^n \frac{f(\alpha_i) - f(\alpha_j)}{\alpha_i - \alpha_j} \mathbf{A}_i \boxtimes \mathbf{A}_j,$$

where the ratio becomes $f'(\alpha_i)$ for $i = j$. Equation (2-1) for the first derivative is well known [Ogden 1984; Xiao 1995]. Norris [2007] provides formulas for the n^{th} derivative of a tensor valued-function. We define the inverse tensor function $\Delta f(\mathbf{A}) \in \mathbb{L}\text{in}$ by

$$\Delta f(\mathbf{A}) \equiv (\nabla f(\mathbf{A}))^{-1} = \sum_{i,j=1}^n \frac{\alpha_i - \alpha_j}{f(\alpha_i) - f(\alpha_j)} \mathbf{A}_i \boxtimes \mathbf{A}_j,$$

where the ratio is $1/f'(\alpha_i)$ for $i = j$. The definition of $\Delta f(\mathbf{A})$ is problematic if $f'(\alpha_i)$ vanishes, but we preclude this possibility next by restricting consideration to strictly monotonic functions: strain measure functions.

2.2. Strain measure functions. The function f is a *strain measure* [Hill 1978; Scheidler 1991] if it is a smooth function $f : \mathbb{R}^+ \rightarrow \mathbb{R}$ which satisfies

$$f(1) = 0, \quad f'(1) = 1, \quad f' > 0.$$

It may be shown [Norris 2007] that the gradient of a strain measure function and its inverse are positive definite fourth order tensors, for instance, $\nabla f(\mathbf{A}), \Delta f(\mathbf{A}) \in \mathbb{P}\text{sym}$. We restrict attention to strain measure functions for the remainder of the paper.

2.3. The pseudo-inverse. For $\mathbf{A} \in \text{Psym}$ consider the equation

$$\{\mathbf{A}, \mathbf{X}\} = \mathbf{Y}, \tag{2-2}$$

for the unknown \mathbf{X} in terms of \mathbf{Y} . It is assumed that \mathbf{Y} is either symmetric or skew and that \mathbf{X} is of the opposite parity [Dui 2006]. The equation can be written $\mathbf{A}\mathbf{X} - \mathbf{X}\mathbf{A} = \mathbf{Y}$, or

$$\mathbb{J}(\mathbf{A})\mathbf{X} = \mathbf{Y}, \tag{2-3}$$

where $\mathbb{J}(\mathbf{A}) \equiv \mathbf{A} \boxtimes \mathbf{I} - \mathbf{I} \boxtimes \mathbf{A}$. We will only consider $\mathbb{J}(\mathbf{A})$ for symmetric \mathbf{A} , implying $\mathbb{J} \in \text{Sym}$ and \mathbb{J} maps $\text{Sym} \rightarrow \text{Skw}$ and $\text{Skw} \rightarrow \text{Sym}$. Therefore, \mathbb{J} does not possess eigenvalues, eigenvectors or an inverse in the usual sense.

The unique solution of the tensorial Equation (2-2) is [Norris 2007]

$$\mathbf{X} = \mathbb{J}^*(\mathbf{A})\mathbf{Y} = (\mathbf{A} \boxtimes \mathbf{I} - \mathbf{I} \boxtimes \mathbf{A})^*\mathbf{Y}. \tag{2-4}$$

The pseudo-inverse, or equivalently the Moore–Penrose inverse, \mathbb{J}^* , is defined such that

$$\mathbb{J}\mathbb{J}^*\mathbb{J} = \mathbb{J}, \quad \mathbb{J}^*\mathbb{J}\mathbb{J}^* = \mathbb{J}^*. \tag{2-5}$$

The spectral forms of $\mathbb{J}(\mathbf{A})$ and its pseudo-inverse are

$$\mathbb{J}(\mathbf{A}) = \sum_{i,j=1}^n (\alpha_i - \alpha_j) \mathbf{A}_i \boxtimes \mathbf{A}_j, \quad \mathbb{J}^*(\mathbf{A}) = \sum_{\substack{i,j=1 \\ i \neq j}}^n (\alpha_i - \alpha_j)^{-1} \mathbf{A}_i \boxtimes \mathbf{A}_j,$$

which clearly satisfy Equation (2-5).

Further insight into the pseudo-inverse is gained by introducing the set of $N \leq 6$ fourth order tensors associated with $\mathbf{A} \in \text{Sym}$,

$$\mathbb{A}_I = \begin{cases} \mathbf{A}_I \boxtimes \mathbf{A}_I, & I = 1, \dots, n, \\ \mathbf{A}_i \boxtimes \mathbf{A}_j + \mathbf{A}_j \boxtimes \mathbf{A}_i, & I = n + 1, \dots, N. \end{cases} \tag{2-6}$$

$N = 6$ for $n = 3$, and the indices $I = 4, 5, 6$ correspond to $(i, j) = (2, 3), (3, 1), (1, 2)$, respectively. Similarly $N = 3$ if $n = 2$ and $N = 1$ if $n = 1$. Note that

$$\mathbb{I} = \sum_{I=1}^N \mathbb{A}_I, \tag{2-7}$$

and

$$\mathbb{A}_I \mathbb{A}_J = \begin{cases} \mathbb{A}_I & I = J, \\ 0, & I \neq J. \end{cases} \tag{2-8}$$

The identity $\mathbb{I} = \mathbf{I} \boxtimes \mathbf{I}$ implies the partition of unity in Equation (2-7), and it may be readily checked that the \mathbb{A}_I satisfy the orthogonality conditions of Equation (2-8).

The pseudo-inverse satisfies

$$\mathbb{J}^* \mathbb{J} = \mathbb{J} \mathbb{J}^* = \mathbb{I} - \sum_{I=1}^n \mathbb{A}_I = \sum_{I=n+1}^N \mathbb{A}_I. \tag{2-9}$$

This is never equal to the identity \mathbb{I} , which is the property that distinguishes the pseudo-inverse from the standard notion of inverse. Further properties of the pseudo-inverse are presented in [Norris 2007]. The explicit solution of Equation (2-3) can be expressed in a variety of ways without the use of fourth order tensors. Perhaps the simplest is the recently discovered solution of Dui et al. [2007]:

$$\mathbf{X} = (3\mathbf{A}'^2 - \frac{1}{2}(\text{tr } \mathbf{A}'^2) \mathbf{I})^{-1} (2\mathbf{A}'\mathbf{Y} + \mathbf{Y}\mathbf{A}'),$$

where \mathbf{A}' is the deviatoric part of \mathbf{A} .

3. Kinematics

3.1. Basics. The polar decomposition of the deformation gradient is $\mathbf{F} = \mathbf{R}\mathbf{U} = \mathbf{V}\mathbf{R}$ where $\mathbf{R} \in \text{SO}(3)$ satisfies $\mathbf{R}\mathbf{R}^t = \mathbf{R}^t\mathbf{R} = \mathbf{I}$ and the right and left stretch tensors \mathbf{U} and \mathbf{V} are positive definite and related by $\mathbf{V} = (\mathbf{R} \boxtimes \mathbf{R})\mathbf{U}$. The fundamental Eulerian strain can be taken as either \mathbf{V} or its square, $\mathbf{B} = \mathbf{V}^2 = \mathbf{F}\mathbf{F}^t$. The spectral representations of \mathbf{V} and \mathbf{B} are

$$\mathbf{V} = \sum_{i=1}^n \lambda_i \mathbf{V}_i, \quad \mathbf{B} = \sum_{i=1}^n \beta_i \mathbf{V}_i, \quad \mathbf{V}_i \mathbf{V}_j = \begin{cases} \mathbf{V}_i, & i = j, \\ 0, & i \neq j, \end{cases} \tag{3-1}$$

where $\lambda_i > 0$ and $\beta_i = \lambda_i^2$.

The rate of change of \mathbf{B} is $\dot{\mathbf{B}} = \mathbf{L}\mathbf{B} + \mathbf{B}\mathbf{L}^t$ where $\mathbf{L} = \dot{\mathbf{F}}\mathbf{F}^{-1}$. Let $\mathbf{D} \in \text{Sym}$ and $\mathbf{W} \in \text{Skw}$ be the symmetric and skew-symmetric parts of \mathbf{L} , respectively. Thus, $\mathbf{L} = \mathbf{D} + \mathbf{W}$ and $\dot{\mathbf{B}}$ can be expressed

$$\dot{\mathbf{B}} = (\mathbf{I} \boxtimes \mathbf{B} - \mathbf{B} \boxtimes \mathbf{I}) \mathbf{W} + (\mathbf{I} \boxtimes \mathbf{B} + \mathbf{B} \boxtimes \mathbf{I}) \mathbf{D}. \tag{3-2}$$

We will find this form useful for deriving more general strain rates.

3.2. Corotational rates. Let $\mathbf{A}(t)$ be a symmetric second order tensor, and $\mathbf{\Omega}$ is skew and arbitrary. Define the corotational rate

$$\overset{\circ}{\mathbf{A}} \equiv \dot{\mathbf{A}} + \{\mathbf{A}, \mathbf{\Omega}\}, \quad \mathbf{\Omega} \in \text{Skw}. \quad (3-3)$$

For any $\mathbf{\Omega}(t) \in \text{Skw}$ we can identify a rotation $\mathbf{Q}(t) \in \text{SO}(3)$ such that

$$\overline{\dot{\mathbf{A}}\mathbf{Q}^t} = \mathbf{Q}\overset{\circ}{\mathbf{A}}\mathbf{Q}^t.$$

Differentiating the left member and using Equation (3-3) for the right member implies that $\mathbf{\Omega} = -\mathbf{Q}^t\dot{\mathbf{Q}}$. Hence, \mathbf{Q} must satisfy $\dot{\mathbf{Q}} = -\mathbf{Q}\mathbf{\Omega}$, with solution unique up to a rigid body rotation. The corotational rate may therefore be interpreted as the Lie derivative with respect to spatial rotation defined by $\mathbf{Q}(t)$. Thus, let ϕ define the mapping (rotation) $\mathbf{x} \rightarrow \mathbf{Q}\mathbf{x}$, then the corotational rate is $\phi[\frac{d}{dt}\phi^{-1}(\cdot)]$.

The Jaumann rate $\overset{\circ}{\mathbf{A}}$ defined by $\mathbf{\Omega} = \mathbf{W}$ corresponds to $\mathbb{P} = 0$ in Equation (1-8). Using the latter formula to parameterize the spin $\mathbf{\Omega}$ allows us to express the general corotational rate of \mathbf{A} as

$$\overset{\circ}{\mathbf{A}} = \overset{\circ}{\mathbf{A}} + (\mathbf{A} \boxtimes \mathbf{I} - \mathbf{I} \boxtimes \mathbf{A})\mathbb{P}(\mathbf{V})\mathbf{D}. \quad (3-4)$$

Equation (3-2) implies that the Jaumann rate of \mathbf{B} is $\overset{\circ}{\mathbf{B}} = (\mathbf{I} \boxtimes \mathbf{B} + \mathbf{B} \boxtimes \mathbf{I})\mathbf{D}$. The general rate $\overset{\circ}{\mathbf{B}}$ then follows from Equation (3-4), and $\overset{\circ}{\mathbf{V}}$ can be determined from the identity $\overset{\circ}{\mathbf{B}} = (\mathbf{V} \boxtimes \mathbf{I} + \mathbf{I} \boxtimes \mathbf{V})\overset{\circ}{\mathbf{V}}$. In summary, the general form of the corotational rate of the fundamental Eulerian strains are

$$\overset{\circ}{\mathbf{B}} = [\mathbf{B} \boxtimes \mathbf{I} + \mathbf{I} \boxtimes \mathbf{B} + (\mathbf{B} \boxtimes \mathbf{I} - \mathbf{I} \boxtimes \mathbf{B})\mathbb{P}(\mathbf{V})]\mathbf{D}, \quad (3-5a)$$

$$\overset{\circ}{\mathbf{V}} = [(\mathbf{V} \boxtimes \mathbf{I} + \mathbf{I} \boxtimes \mathbf{V})^{-1}(\mathbf{V}^2 \boxtimes \mathbf{I} + \mathbf{I} \boxtimes \mathbf{V}^2) + (\mathbf{V} \boxtimes \mathbf{I} - \mathbf{I} \boxtimes \mathbf{V})\mathbb{P}(\mathbf{V})]\mathbf{D}. \quad (3-5b)$$

3.3. Spins. Many candidates have been considered from the infinity of possible spins [Dill 2006]. For instance, the polar spin

$$\mathbf{\Omega}^R = \dot{\mathbf{R}}\mathbf{R}^t, \quad (3-6)$$

corresponding to $\mathbf{Q} = \mathbf{R}^t$, is useful as a comparison spin. Other common spins [Xiao et al. 1998c] are $\mathbf{\Omega}^E$ defined by the *twirl* of the Eulerian principal axes and $\mathbf{\Omega}^L$ related to the Lagrangian principal axes. It is shown in Appendix A that $\mathbf{\Omega}^\alpha = \mathbf{W} + \mathbb{P}^\alpha\mathbf{D}$, $\alpha = R, E, L$, where

$$\mathbb{P}^R = (\mathbf{I} \boxtimes \mathbf{V} - \mathbf{V} \boxtimes \mathbf{I})(\mathbf{I} \boxtimes \mathbf{V} + \mathbf{V} \boxtimes \mathbf{I})^{-1}, \quad (3-7a)$$

$$\mathbb{P}^E = (\mathbf{I} \boxtimes \mathbf{V}^2 - \mathbf{V}^2 \boxtimes \mathbf{I})^*(\mathbf{I} \boxtimes \mathbf{V}^2 + \mathbf{V}^2 \boxtimes \mathbf{I}), \quad (3-7b)$$

$$\mathbb{P}^L = (\mathbf{I} \boxtimes \mathbf{V}^2 - \mathbf{V}^2 \boxtimes \mathbf{I})^* 2\mathbf{V} \boxtimes \mathbf{V}. \quad (3-7c)$$

The three spins $\mathbf{\Omega}^R$, $\mathbf{\Omega}^E$ and $\mathbf{\Omega}^L$ are related by $\mathbf{\Omega}^E - \mathbf{\Omega}^R = \mathbf{\Omega}^L - \mathbf{W}$ (see Appendix A). The fourth order projection tensors are therefore connected by $\mathbb{P}^E - \mathbb{P}^L = \mathbb{P}^R$, and we note the additional relation $\mathbb{P}^E + \mathbb{P}^L = \mathbb{P}^{R*}$, which is readily verified.

The most general form of the isotropic tensor-valued function $\mathbb{P} \in \text{Sym}$ involves three isotropic scalar functions ν_1, ν_2, ν_3 [Xiao et al. 1998c],

$$\mathbb{P}(\mathbf{V}) = (\mathbf{V} \boxtimes \mathbf{I} - \mathbf{I} \boxtimes \mathbf{V})[\nu_1 \mathbb{I} + \nu_2(\mathbf{V} \boxtimes \mathbf{I} + \mathbf{I} \boxtimes \mathbf{V}) + \nu_3 \mathbf{V} \boxtimes \mathbf{V}] = \sum_{\substack{i,j=1 \\ i \neq j}}^n p_{ij} \mathbf{V}_i \boxtimes \mathbf{V}_j, \quad (3-8)$$

where

$$p_{ij} = (\lambda_i - \lambda_j) [v_1 + (\lambda_i + \lambda_j)v_2 + \lambda_i\lambda_jv_3], \quad v_k = v_k(I_1, I_2, I_3), \quad k = 1, 2, 3.$$

Here, I_1, I_2, I_3 are the invariants of \mathbf{V} : $I_1 = \text{tr}(\mathbf{V})$, $I_2 = \frac{1}{2} I_1^2 - \frac{1}{2} \text{tr}(\mathbf{V}^2)$, $I_3 = \det \mathbf{V}$.

The corotational rate of \mathbf{V} can now be written

$$\overset{\circ}{\mathbf{V}} = \mathbb{Q}\mathbf{D}, \tag{3-9}$$

where the fourth order tensor $\mathbb{Q} \in \text{Sym}$ follows from Equation (3-5b),

$$\mathbb{Q} = (\mathbf{V} \boxtimes \mathbf{I} + \mathbf{I} \boxtimes \mathbf{V})^{-1} (\mathbf{V}^2 \boxtimes \mathbf{I} + \mathbf{I} \boxtimes \mathbf{V}^2) + (\mathbf{V} \boxtimes \mathbf{I} - \mathbf{I} \boxtimes \mathbf{V}) \mathbb{P}(\mathbf{V}) = \sum_{i,j=1}^n q_{ij} \mathbf{V}_i \boxtimes \mathbf{V}_j,$$

and

$$q_{ij} = (\lambda_i - \lambda_j) p_{ij} + \frac{\lambda_i^2 + \lambda_j^2}{\lambda_i + \lambda_j}. \tag{3-10}$$

3.4. Eulerian strain measures. The Lagrangian Seth–Hill strain $\mathbf{E}^{(m)} = m^{-1}(\mathbf{U}^m - \mathbf{I})$ corresponds to $f(x) = f^{(m)}(x)$. We define the analogous Eulerian strain

$$\mathbf{e}^{(m)} = f^{(m)}(\mathbf{V}) = m^{-1}(\mathbf{V}^m - \mathbf{I}),$$

and note in particular the Hencky strain $\mathbf{e}^{(0)} = \ln \mathbf{V}$. Other examples include

$$\mathbf{e}^{(1)} = \mathbf{V} - \mathbf{I}, \quad \mathbf{e}^{(2)} = \frac{1}{2}(\mathbf{B} - \mathbf{I}), \quad \mathbf{e}^{(-1)} = \mathbf{I} - \mathbf{V}^{-1}, \quad \mathbf{e}^{(-2)} = \frac{1}{2}(\mathbf{I} - \mathbf{B}^{-1}).$$

3.5. Eulerian strain rates. We now present some identities for the corotational rates of Eulerian strains. These will prove useful later in deriving conjugate Eulerian stresses. The first identity applies to arbitrary strain measures:

Lemma 1. The corotational rate of any Eulerian strain measure $f(\mathbf{V})$ is

$$f(\overset{\circ}{\mathbf{V}}) = [\nabla f(\mathbf{V})] \mathbb{Q}(\mathbf{V}) \mathbf{D}.$$

The proof is a simple application of the chain rule, using Equation (3-9) for $\overset{\circ}{\mathbf{V}}$. This separates the dependence on the strain measure f from the dependence on the particular corotational rate used, which determines \mathbb{Q} .

The second identity connects the strain rate with the Hencky strain:

Lemma 2. The strain rate of any Eulerian strain measure $f(\mathbf{V})$ can be expressed in terms of the Hencky strain rate as

$$f(\overset{\circ}{\mathbf{V}}) = [\nabla f(\mathbf{V})](\Delta \ln \mathbf{V}) \overset{\circ}{\ln \mathbf{V}}.$$

The proof is a straightforward generalization of the chain rule of differentiation [Xiao et al. 1998c, Theorem 2]. Let $\mathbf{M} = \ln \mathbf{V}$ and $f(\mathbf{V}) = \hat{f}(\mathbf{M})$ then,

$$\hat{f}(\overset{\circ}{\mathbf{M}}) = \nabla_{\mathbf{M}} \hat{f}(\mathbf{M}) \overset{\circ}{\mathbf{M}} = \nabla f(\mathbf{V}) (\nabla_{\mathbf{M}} \mathbf{V}) \overset{\circ}{\mathbf{M}}.$$

But the fourth order tensor $\nabla_{\mathbf{M}} \mathbf{V}$ is just the inverse of $\nabla_{\mathbf{V}} \mathbf{M}$ since $\nabla_{\mathbf{V}} \mathbf{V} = \mathbb{I}$.

4. The f-spin and the logarithmic spin

4.1. Strain rate and the stretching tensor. In order to make the connection between the kinematics and the power \dot{w} we must relate some strain rate to the stretching tensor \mathbf{D} . A general connection can be found by starting with the rate of change of an arbitrary tensor valued function of \mathbf{B} . Thus,

$$\dot{\tilde{f}}(\mathbf{B}) = [\nabla \tilde{f}(\mathbf{B})] \dot{\mathbf{B}} = \sum_{i,j=1}^n \frac{\tilde{f}(\beta_i) - \tilde{f}(\beta_j)}{\beta_i - \beta_j} \mathbf{V}_i \otimes \mathbf{V}_j \dot{\mathbf{B}},$$

where the temporary definition $\tilde{f}(x) = f(x^2)$ is used, so that $f(\mathbf{V}) = \tilde{f}(\mathbf{B})$. Reverting to $f(\mathbf{V})$ and using $\beta_i = \lambda_i^2$, the rate of change of the associated function of \mathbf{V} is

$$\dot{f}(\mathbf{V}) = \sum_{i,j=1}^n \frac{f(\lambda_i) - f(\lambda_j)}{\lambda_i^2 - \lambda_j^2} \mathbf{V}_i \otimes \mathbf{V}_j \dot{\mathbf{B}}, \tag{4-1}$$

where the ratio becomes $f'(\lambda_i)/(2\lambda_i)$ for $i = j$. Substituting $\dot{\mathbf{B}}$ into Equation (4-1) and using the filtering properties of \mathbf{V}_i , such as $(\mathbf{V}_i \otimes \mathbf{V}_j)(\mathbf{I} \otimes \mathbf{B}) = \beta_j \mathbf{V}_i \otimes \mathbf{V}_j$, gives

$$\begin{aligned} \dot{f}(\mathbf{V}) &= \sum_{i,j=1}^n (f(\lambda_j) - f(\lambda_i)) \mathbf{V}_i \otimes \mathbf{V}_j \mathbf{W} + \sum_{i,j=1}^n \frac{f(\lambda_i) - f(\lambda_j)}{\beta_i - \beta_j} (\beta_i + \beta_j) \mathbf{V}_i \otimes \mathbf{V}_j \mathbf{D} \\ &= \{\mathbf{W}, f(\mathbf{V})\} + \sum_{i,j=1}^n \frac{\lambda_i^2 + \lambda_j^2}{\lambda_i^2 - \lambda_j^2} (f(\lambda_i) - f(\lambda_j)) \mathbf{V}_i \otimes \mathbf{V}_j \mathbf{D}. \end{aligned}$$

Adding and subtracting terms, this becomes

$$\dot{f}(\mathbf{V}) = \widehat{\mathbf{D}} + \{\mathbf{W}, f(\mathbf{V})\} + \sum_{\substack{i,j=1 \\ i \neq j}}^n \left[\frac{\lambda_i^2 + \lambda_j^2}{\lambda_i^2 - \lambda_j^2} - \frac{1}{f(\lambda_i) - f(\lambda_j)} \right] (f(\lambda_i) - f(\lambda_j)) \mathbf{V}_i \otimes \mathbf{V}_j \mathbf{D}, \tag{4-2}$$

where $\widehat{\mathbf{D}}$ is a modified version of the stretching tensor,

$$\widehat{\mathbf{D}} = \mathbf{D} + \sum_{i=1}^n [\lambda_i f'(\lambda_i) - 1] \mathbf{V}_i \otimes \mathbf{V}_i \mathbf{D}. \tag{4-3}$$

Note that the double sum in Equation (4-2) excludes the $i = j$ terms. We can therefore rewrite it in a form suggestive of a new corotational rate,

$$\dot{f}(\mathbf{V}) = \widehat{\mathbf{D}} + \{\boldsymbol{\Omega}^f, f(\mathbf{V})\}, \quad \boldsymbol{\Omega}^f = \mathbf{W} + \mathbb{P}^f \mathbf{D}, \tag{4-4}$$

where $\boldsymbol{\Omega}^f \in \text{Skw}$ is called the f-spin, and its fourth order projection tensor is

$$\mathbb{P}^f = (\mathbf{V} \otimes \mathbf{I} - \mathbf{I} \otimes \mathbf{V})^* [\Delta f(\mathbf{V}) - (\mathbf{V} \otimes \mathbf{I} + \mathbf{I} \otimes \mathbf{V})^{-1} (\mathbf{V}^2 \otimes \mathbf{I} + \mathbf{I} \otimes \mathbf{V}^2)]. \tag{4-5}$$

Alternatively, \mathbb{P}^f can be expressed in the form Equation (3–8) with matrix elements

$$p_{ij}^f = \frac{1}{f(\lambda_i) - f(\lambda_j)} - \frac{\lambda_i^2 + \lambda_j^2}{\lambda_i^2 - \lambda_j^2}.$$

Note that $\boldsymbol{\Omega}^f$ can blow up, but the action $\{\boldsymbol{\Omega}^f, g(\mathbf{V})\}$ remains finite for any differentiable function g , including f . In particular, the f-spin is an objective material spin in the sense defined by [Xiao et al. 1998c].

The corotational rate associated with the f-spin is defined in the usual manner as

$$g^{\circ f}(\mathbf{V}) = \dot{g}(\mathbf{V}) + \{g(\mathbf{V}), \boldsymbol{\Omega}^f\}.$$

The reason for introducing this new rate is $f^{\circ f}(\mathbf{V}) = \widehat{\mathbf{D}}$, which follows from Equation (4–4). This shows that for a particular choice of spin the corotational rate of an arbitrary strain measure $f(\mathbf{V})$ is related to the modified stretching tensor $\widehat{\mathbf{D}}$. The important point is that this is the closest, in a sense to be defined, the strain rate can get to the actual stretching tensor \mathbf{D} . These ideas are made concrete through:

Lemma 3. For any objective corotational rate

$$|f^{\circ}(\mathbf{V}) - \mathbf{D}|^2 = |f^{\circ}(\mathbf{V}) - \widehat{\mathbf{D}}|^2 + |\widehat{\mathbf{D}} - \mathbf{D}|^2, \tag{4-6}$$

where $\widehat{\mathbf{D}}$ is the modified stretching tensor defined by Equation (4–3).

The proof follows by writing

$$\begin{aligned} f^{\circ}(\mathbf{V}) - \mathbf{D} &= f^{\circ}(\mathbf{V}) - \widehat{\mathbf{D}} + (\widehat{\mathbf{D}} - \mathbf{D}) = f^{\circ}(\mathbf{V}) - f^{\circ f}(\mathbf{V}) + (\widehat{\mathbf{D}} - \mathbf{D}) \\ &= \sum_{\substack{i,j=1 \\ i \neq j}}^n (p_{ij} - p_{ij}^f)(f(\lambda_i) - f(\lambda_j))\mathbf{V}_i \otimes \mathbf{V}_j + \sum_{i=1}^n [\lambda_i f'(\lambda_i) - 1]\mathbf{V}_i \otimes \mathbf{V}_i. \end{aligned} \tag{4-7}$$

Hence,

$$|f^{\circ}(\mathbf{V}) - \mathbf{D}|^2 = \sum_{\substack{i,j=1 \\ i \neq j}}^n [(p_{ij} - p_{ij}^f)(f(\lambda_i) - f(\lambda_j))\text{tr}(\mathbf{V}_i \mathbf{D} \mathbf{V}_j)]^2 + \sum_{i=1}^n [(\lambda_i f'(\lambda_i) - 1)\text{tr}(\mathbf{V}_i \mathbf{D})]^2,$$

where the two sums on the right hand side are the corresponding terms in Equation (4–6).

Therefore, we get:

Lemma 4. For every Eulerian strain measure f there is a unique spin which minimizes the difference between $f^{\circ}(\mathbf{V})$ and \mathbf{D} , and that spin is $\boldsymbol{\Omega}^f$. The minimal difference is

$$|f^{\circ f}(\mathbf{V}) - \mathbf{D}|^2 = \sum_{i=1}^n [(\lambda_i f'(\lambda_i) - 1)\text{tr}(\mathbf{V}_i \mathbf{D})]^2.$$

The proof follows using Lemma 3 in the form

$$|f(\mathbf{V}) - \mathbf{D}|^2 \geq |\hat{\mathbf{D}} - \mathbf{D}|^2,$$

with equality if and only if $\mathbf{\Omega} = \mathbf{\Omega}^f$.

4.2. The logarithmic spin. Lemma 4 implies that the corotational rate of strain equals \mathbf{D} if the strain measure has the property $xf'(x) - 1 = 0$. The only solution that satisfies the condition $f(1) = 0$ is $f(x) = \ln x$, and the associated spin follows from Equation (4–5) as $\mathbf{\Omega}^{\log} = \mathbf{W} + \mathbb{P}^{\log}\mathbf{D}$ where

$$p_{ij}^{\log} = \frac{1}{\ln \lambda_i - \ln \lambda_j} - \frac{\lambda_i^2 + \lambda_j^2}{\lambda_i^2 - \lambda_j^2}.$$

$\mathbf{\Omega}^{\log}$ is the well known logarithmic spin [Xiao et al. 1997]. Hence, of all possible rates and of all possible Eulerian strain measures only the combination of the Hencky strain and the rate defined by the logarithmic spin together yield the strain rate \mathbf{D} . This is the unique relationship between $\ln \mathbf{V}$, \mathbf{D} , and $\mathbf{\Omega}^{\log}$ which makes both the Hencky strain and the logarithmic spin special. This result was first derived by Xiao et al. [1997], and may be summarized as:

Lemma 5. The strain rate \mathbf{D} is recovered only as the corotational rate of the Eulerian strain $\mathbf{e}^{(0)} = \ln \mathbf{V}$ with spin $\mathbf{\Omega}^{\log}$ where the fourth order projection tensor \mathbb{P}^{\log} is given by Equation (4–5) with $f = \ln$. That is,

$$\overset{\circ}{\ln} \mathbf{V} = \mathbf{D}.$$

4.2.1. Some properties of the logarithmic spin. An instructive alternative form for \mathbb{P}^{\log} is obtained by introducing

$$\mathbb{P}^{\ln} \equiv (\mathbf{V} \boxtimes \mathbf{I} - \mathbf{I} \boxtimes \mathbf{V})^* \Delta \ln(\mathbf{V}),$$

so that

$$\mathbb{P}^{\log} = \mathbb{P}^{\ln} + \mathbb{P}^E = \mathbb{P}^{\ln} + \mathbb{P}^L + \mathbb{P}^R.$$

Each of the projection tensors may be expressed in terms of matrix elements $p_{ij} = -p_{ji}$ according to Equation (3–8) as

$$p_{ij}^R = -\frac{\lambda_i - \lambda_j}{\lambda_i + \lambda_j}, \quad p_{ij}^E = -\frac{\lambda_i^2 + \lambda_j^2}{\lambda_i^2 - \lambda_j^2}, \quad p_{ij}^L = -\frac{2\lambda_i\lambda_j}{\lambda_i^2 - \lambda_j^2}, \quad p_{ij}^{\ln} = \frac{1}{\ln \lambda_i - \ln \lambda_j}.$$

The form of p_{ij}^{\log} agrees with the formula for \mathbb{P}^{\log} derived by Xiao et al. [1997, Equation (41)]. Note that

$$\text{sgn} p_{ij}^{\log} = \text{sgn} p_{ij}^R = -\text{sgn}(p_{ij}^{\log} - p_{ij}^R).$$

The implications are twofold. The first equalities indicate that the spin induced by both $\mathbf{\Omega}^{\log}$ and by $\mathbf{\Omega}^R$ are in the same sense relative to the underlying spin \mathbf{W} . The latter equalities imply that the relative spin induced by $\mathbf{\Omega}^{\log}$ is of smaller magnitude than that of $\mathbf{\Omega}^R$.

The f-spin, which is uniquely defined by the strain measure f , defines the skew matrix elements p_{ij}^f . Consider the reverse problem: given some objective corotational rate defined by elements p_{ij} , is there a function f such that $p_{ij}^f = p_{ij}$? There is no such function for the spins $\mathbf{\Omega}^R$, $\mathbf{\Omega}^E$ and $\mathbf{\Omega}^L$, as the reader can

readily verify. Obviously, $f = \ln$ for $\mathbf{\Omega} = \mathbf{\Omega}^{\log}$, but it remains an open question for general $\mathbf{\Omega}$ whether a strain measure function exists such that $\mathbf{\Omega} = \mathbf{\Omega}^f$.

5. Eulerian conjugate stress-strain pairs

5.1. Arbitrary strain and corotational rate. It was noted in Section 1 that the concept of work-conjugate stress-strain pairs is more complicated for Eulerian quantities owing to the fact that the connection between the strain rate and the stretching tensor is not evident a priori. This issue was resolved by Lehmann and Liang [1993], who introduced the notion that the Eulerian pair $\boldsymbol{\tau}$ and \mathbf{e} are defined to be conjugate if

$$\dot{w} = \text{tr}(\mathbf{Q}\boldsymbol{\tau}\mathbf{Q}'\overline{\mathbf{Q}\mathbf{e}\mathbf{Q}'}) \tag{5-1}$$

for some rotation \mathbf{Q} . This clearly generalizes the Lagrangian work-conjugacy condition Equation (1-2), but it is necessary because of the fact that Eulerian rates are not as restricted. The definition in Equation (5-1) is equivalent to

$$\dot{w} = \text{tr}(\boldsymbol{\tau}\overset{\circ}{\mathbf{e}}) \tag{5-2}$$

where $\overset{\circ}{\mathbf{e}} = \dot{\mathbf{e}} + \{\mathbf{e}, \mathbf{\Omega}\}$ and $\mathbf{\Omega} = -\mathbf{Q}'\dot{\mathbf{Q}}$. Equation (5-2) is taken as the starting point, since it depends only on the corotational rate through the spin $\mathbf{\Omega}$, therefore \mathbf{Q} is not required.

For a given strain measure $\mathbf{e} = f(\mathbf{V})$ and corotational rate $\mathbf{\Omega} = \mathbf{W} + \mathbb{P}\mathbf{D}$ the strain rate $\overset{\circ}{\mathbf{e}}$ follows from Equation (3-3). The stress $\boldsymbol{\tau}$ is therefore conjugate to \mathbf{e} if the following holds for all stretching tensors \mathbf{D} :

$$\text{tr}(\boldsymbol{\tau}[\nabla f(\mathbf{V})]\mathbb{Q}(\mathbf{V})\mathbf{D}) = \text{tr}(\boldsymbol{\sigma}\mathbf{D}).$$

The fourth order tensor $\nabla f(\mathbf{V})$ is invertible for all strain measures. The necessary and sufficient condition required to determine $\boldsymbol{\tau}$ is therefore that the fourth order tensor \mathbb{Q} is invertible. This requirement was obtained by Xiao et al. [1997] in a slightly different manner; basically, that the six elements q_{ij} of Equation (3-10) are all nonzero. Hence, q_{ij}^{-1} are bounded, and \mathbb{Q}^{-1} exists. We refer the reader to [Xiao et al. 1997] for further details.

In summary, the conjugate stress is

$$\boldsymbol{\tau} = [\Delta f(\mathbf{V})]\mathbb{Q}^{-1}\boldsymbol{\sigma},$$

where the order of $[\Delta f(\mathbf{V})]$ and \mathbb{Q}^{-1} are arbitrary since they commute. This is Theorem 1.

5.2. Conjugate stress and the f-rate. An alternative approach is suggested by Equation (4-7). Let $\overset{\circ}{\mathbf{e}} = \mathbb{F}\mathbf{D}$, then the fourth order tensor \mathbb{F} is by assumption invertible and the conjugate stress is simply $\boldsymbol{\tau} = \mathbb{F}^{-1}\boldsymbol{\sigma}$. The tensor \mathbb{F} can be obtained directly in spectral form from Equation (4-7) and easily inverted, to give

Lemma 6. For arbitrary strain measure and rate the conjugate stress can be expressed

$$\boldsymbol{\tau} = \boldsymbol{\sigma}^f - \sum_{\substack{i,j=1 \\ i \neq j}}^n \frac{1}{1 + [(p_{ij} - p_{ij}^f)(f(\lambda_i) - f(\lambda_j))]} \mathbf{V}_i \boxtimes \mathbf{V}_j \boldsymbol{\sigma}. \tag{5-3}$$

The conjugate stress satisfies

$$|\boldsymbol{\tau} - \boldsymbol{\sigma}|^2 = |\boldsymbol{\tau} - \boldsymbol{\sigma}^f|^2 + |\boldsymbol{\sigma}^f - \boldsymbol{\sigma}|^2, \tag{5-4}$$

where the modified stress tensor $\boldsymbol{\sigma}^f$ is

$$\boldsymbol{\sigma}^f = \boldsymbol{\sigma} + \sum_{i=1}^n \left[\frac{1}{\lambda_i f'(\lambda_i)} - 1 \right] \mathbf{V}_i \boxtimes \mathbf{V}_i \boldsymbol{\sigma}.$$

The proof follows from Equation (5-3) by analogy with the proof of Lemma 3. Hence,

$$|\boldsymbol{\tau} - \boldsymbol{\sigma}|^2 \geq |\boldsymbol{\sigma}^f - \boldsymbol{\sigma}|^2$$

with equality if and only if $\boldsymbol{\Omega} = \boldsymbol{\Omega}^f$, and we deduce the following.

Lemma 7. For every Eulerian strain measure $f(\mathbf{V})$ the corotational rate of the f-spin $\boldsymbol{\Omega}^f$ minimizes the difference between the conjugate stress and the Cauchy stress. The conjugate stress is then $\boldsymbol{\tau} = \boldsymbol{\sigma}^f$ and the minimal difference is

$$|\boldsymbol{\tau} - \boldsymbol{\sigma}|^2 = \sum_{i=1}^n \left[\left(\frac{1}{\lambda_i f'(\lambda_i)} - 1 \right) \text{tr}(\mathbf{V}_i \boldsymbol{\sigma}) \right]^2.$$

This proves Theorem 2.

In general $\boldsymbol{\sigma}^f$ is not equal to the Cauchy stress for any strain measure, with the exception of $f = \ln$, discussed below. It is, however, possible for $\boldsymbol{\sigma}^f$ and $\boldsymbol{\sigma}$ to coincide under special circumstances: if the three elements $\text{tr}(\mathbf{V}_i \boldsymbol{\sigma})$ simultaneously vanish. This is by definition a state of pure shear [Norris 2006]. Hence, we have the following statement.

Lemma 8. If the Cauchy stress is a state of pure shear with $\text{diag}(\boldsymbol{\sigma}) = 0$ in the principal axes of \mathbf{V} , then

$$\boldsymbol{\sigma}^f = \boldsymbol{\sigma}.$$

The stress conjugate to $f(\mathbf{V})$ equals the Cauchy stress if the f-rate is used.

If the material is isotropic then the stress and strain share the same triad of principal axes. In that case $\text{diag}(\boldsymbol{\sigma})$ expressed in the principal axes of \mathbf{V} is simply the principle stresses, which vanishes only in the absence of stress. Hence the circumstances under which Lemma 8 applies cannot occur for isotropic materials. If the material is not isotropic, but we restrict attention to linear anisotropic elasticity, then $\text{diag}(\boldsymbol{\sigma})$ expressed in the principal axes of strain \mathbf{e} will vanish only if both stress and strain are zero. This follows from the assumed positive definite property of the strain energy, equal to $\frac{1}{2} \text{tr}(\boldsymbol{\sigma} \mathbf{e})$. In summary, the circumstances under which Lemma 8 apply require nonlinear and anisotropic elasticity. This does not eliminate its possibility but it makes it difficult to envision a situation when Lemma 8 would occur.

5.3. Logarithmic rate. The logarithmic rate, as noted before, is a special case of the f-rate. We conclude by examining the conjugate stress for arbitrary strain measure using the logarithmic rate. Xiao et al. [1997] showed that the logarithmic rate is the only one with the property of Lemma 5, which is that among all strains and all rates, only $\ln \mathbf{V}$ and $\boldsymbol{\Omega}^{\log}$ correspond to the stretching tensor \mathbf{D} . This fundamental result for $\ln(\mathbf{V})$ is generalized to arbitrary Eulerian strain measure $\mathbf{e} = f(\mathbf{V})$ by

$$\mathbf{e}^{\circ \log} = (\nabla f(\mathbf{V})) (\Delta \ln \mathbf{V}) \mathbf{D},$$

which follows from Lemmas 2 and 5. Now require that the work-conjugacy identity $\text{tr}(\boldsymbol{\tau} \mathbf{e}^{\text{olog}}) = \text{tr}(\boldsymbol{\sigma} \mathbf{D})$ holds for all \mathbf{D} , and use the invertibility of the fourth order tensors $\nabla f(\mathbf{V})$ and $\Delta \ln \mathbf{V}$ plus the property that they commute. This implies that the stress conjugate to the Eulerian strain $\mathbf{e} = f(\mathbf{V})$ is

$$\boldsymbol{\tau} = (\Delta f(\mathbf{V})) (\nabla \ln \mathbf{V}) \boldsymbol{\sigma},$$

for $\boldsymbol{\Omega} = \boldsymbol{\Omega}^{\text{olog}}$. It is straightforward to show that this can be expressed in spectral form as

$$\boldsymbol{\tau} = \boldsymbol{\sigma}^f + \sum_{i,j=1}^n \left(\frac{\ln \lambda_i - \ln \lambda_j}{f(\lambda_i) - f(\lambda_j)} - 1 \right) \mathbf{V}_i \boxtimes \mathbf{V}_j \boldsymbol{\sigma}, \tag{5-5}$$

again for $\boldsymbol{\Omega} = \boldsymbol{\Omega}^{\text{olog}}$. This identity, although valid only for the logarithmic rate, shows how the conjugate stress in that case is related to the modified stress $\boldsymbol{\sigma}^f$. The latter depends upon the strain measure f , and is optimal in the sense of best for all possible strain rates. Equation (5-5) shows that the logarithmic rate is not optimal since $\boldsymbol{\tau}$ satisfies Equation (5-4) with both terms on the RHS of the latter nonzero. However, when the strain measure f reduces to \ln then $\boldsymbol{\sigma}^f \rightarrow \boldsymbol{\sigma}$ and the sum in Equation (5-5) vanishes. This again shows the combined properties of the Hencky strain and the logarithmic rate as being doubly optimal for all strain measures and spins.

6. Conclusion

We have examined the implications of work-conjugacy with emphasis on Eulerian stress-strain pairs. There is, however, remarkable similarity in the form of the dual conjugate stresses for both Lagrangian and Eulerian strains. The similarity is evident from the identical format of Equations (1-5) and (1-10), which involve fundamental stresses $\mathbf{T}^{(1)}$ and $\boldsymbol{\tau}^{(1)}$ defined by the strains $f(\mathbf{U})$ and $f(\mathbf{V})$, respectively. The Lagrangian stress $\mathbf{T}^{(1)}$ is called Biot stress or Jaumann stress, but there does not appear to be a common term for its Eulerian counterpart $\boldsymbol{\tau}^{(1)}$.

The major distinction between Lagrangian and Eulerian work-conjugacy is that the latter requires the introduction of the corotational rate, which itself is quite arbitrary. We have shown that every permissible Eulerian strain measure $f(\mathbf{V})$ has associated with it a unique corotational rate, the f -rate. The conjugate stress obtained using the f -rate is optimal in the sense that it is the closest possible to the Cauchy stress $\boldsymbol{\sigma}$. The optimal stress, $\boldsymbol{\sigma}^f$, is defined by f and $\boldsymbol{\sigma}$ through Lemma 6, and it reduces to the Cauchy stress if and only if $f = \ln$. This reinforces the results of Xiao et al. [1998a] for the logarithmic rate and the Hencky strain, while generalizing the notion of the logarithmic rate to arbitrary strain functions through the strain dependent spin $\boldsymbol{\Omega}^f$.

Appendix A: The spins $\boldsymbol{\Omega}^R$, $\boldsymbol{\Omega}^E$ and $\boldsymbol{\Omega}^L$

From the definition of $\boldsymbol{\Omega}^R$ in Equation (3-6), and using $\mathbf{F} = \mathbf{R}\mathbf{U}$, we have

$$\mathbf{L} = \dot{\mathbf{F}}\mathbf{F}^{-1} = \boldsymbol{\Omega}^R + \mathbf{R}\dot{\mathbf{U}}\mathbf{U}^{-1}\mathbf{R}^t.$$

The symmetric and skew parts of this relation yield [Truesdell and Noll 1965]

$$\mathbf{D} = \frac{1}{2} \mathbf{R} (\dot{\mathbf{U}}\mathbf{U}^{-1} + \mathbf{U}^{-1}\dot{\mathbf{U}}) \mathbf{R}^t, \tag{A.1}$$

and

$$\mathbf{W} = \boldsymbol{\Omega}^R + \frac{1}{2}\mathbf{R}(\dot{\mathbf{U}}\mathbf{U}^{-1} - \mathbf{U}^{-1}\dot{\mathbf{U}})\mathbf{R}^t. \tag{A.2}$$

Equation (A.1) may be solved for $\dot{\mathbf{U}}$ in the form given by Equation (1–4). Substituting $\dot{\mathbf{U}}$ in Equation (A.2) gives

$$\boldsymbol{\Omega}^R = \mathbf{W} + (\mathbf{I} \boxtimes \mathbf{V} - \mathbf{V} \boxtimes \mathbf{I})(\mathbf{I} \boxtimes \mathbf{V} + \mathbf{V} \boxtimes \mathbf{I})^{-1}\mathbf{D}.$$

Let $\mathbf{v}_i, i = 1, \dots, n \leq 3$, be the principal axes of \mathbf{B} and \mathbf{V} . The twirl $\boldsymbol{\Omega}^E$ defines the rate of rotation of this triad by $\dot{\mathbf{v}}_i = \boldsymbol{\Omega}^E \mathbf{v}_i$. The rate of change of the eigentensors of \mathbf{B} follows from $\mathbf{V}_i = \mathbf{v}_i \otimes \mathbf{v}_i$ as $\dot{\mathbf{V}}_i = \{\boldsymbol{\Omega}^E, \mathbf{V}_i\}$. The second portion of Equation (3–1) then gives

$$\dot{\mathbf{B}} = \sum_{i=1}^n \dot{\beta}_i \mathbf{V}_i + \{\boldsymbol{\Omega}^E, \mathbf{B}\}, \tag{A.3}$$

which can be considered as an equation for $\boldsymbol{\Omega}^E$, similar to Equation (2–2). The solution follows from Equations (2–4) and (3–2) as

$$\boldsymbol{\Omega}^E = (\mathbf{I} \boxtimes \mathbf{B} - \mathbf{B} \boxtimes \mathbf{I})^* \left(\dot{\mathbf{B}} - \sum_{i=1}^n \dot{\beta}_i \mathbf{V}_i \right) = \mathbf{W} + (\mathbf{I} \boxtimes \mathbf{B} - \mathbf{B} \boxtimes \mathbf{I})^* (\mathbf{I} \boxtimes \mathbf{B} + \mathbf{B} \boxtimes \mathbf{I})\mathbf{D}.$$

Hence $\boldsymbol{\Omega}^E = \mathbf{W} + \mathbb{P}^E \mathbf{D}$ where \mathbb{P}^E is given by Equation (3–7b). The rate of change of the principal stretches are obtained by substituting $\boldsymbol{\Omega}^E$ into Equation (A.3), as

$$\sum_{i=1}^n \dot{\beta}_i \mathbf{V}_i = \left[\mathbb{1} - (\mathbf{I} \boxtimes \mathbf{B} - \mathbf{B} \boxtimes \mathbf{I})^* (\mathbf{I} \boxtimes \mathbf{B} - \mathbf{B} \boxtimes \mathbf{I}) \right] (\mathbf{I} \boxtimes \mathbf{B} + \mathbf{B} \boxtimes \mathbf{I})\mathbf{D}.$$

Then using Equations (2–6) and (2–9), we obtain the well known result

$$\sum_{i=1}^n \dot{\beta}_i \mathbf{V}_i = 2 \sum_{i=1}^n \beta_i \mathbf{V}_i \boxtimes \mathbf{V}_i \mathbf{D} \quad \Leftrightarrow \quad \dot{\lambda}_i = \lambda_i \operatorname{tr}(\mathbf{V}_i \mathbf{D}).$$

The twirl $\tilde{\boldsymbol{\Omega}}^L$ defines the rate of rotation of the Lagrangian principal axes $\mathbf{u}_i, i = 1, \dots, n$ as $\dot{\mathbf{u}}_i = \tilde{\boldsymbol{\Omega}}^L \mathbf{u}_i$. Hence, $\dot{\mathbf{U}}_i = \{\tilde{\boldsymbol{\Omega}}^L, \mathbf{U}_i\}$, where $\mathbf{U}_i = \mathbf{u}_i \otimes \mathbf{u}_i$, are the eigentensors of \mathbf{U} . Taking the rate of change of the identity $\mathbf{V}_i = (\mathbf{R} \boxtimes \mathbf{R})\mathbf{U}_i$, linking the Eulerian and Lagrangian eigentensors, gives

$$\dot{\mathbf{U}}_i = (\mathbf{R} \boxtimes \mathbf{R})^{-1} \{ \boldsymbol{\Omega}^E - \boldsymbol{\Omega}^R, \mathbf{V}_i \}.$$

The Lagrangian twirl is therefore

$$\tilde{\boldsymbol{\Omega}}^L = (\mathbf{R} \boxtimes \mathbf{R})^{-1} (\boldsymbol{\Omega}^E - \boldsymbol{\Omega}^R) = (\mathbf{I} \boxtimes \mathbf{U}^2 - \mathbf{U}^2 \boxtimes \mathbf{I})^* 2(\mathbf{U} \boxtimes \mathbf{U})(\mathbf{R} \boxtimes \mathbf{R})^{-1} \mathbf{D}.$$

This is related to the spin $\boldsymbol{\Omega}^L = \mathbf{W} + \mathbb{P}^L \mathbf{D}$ defined via \mathbb{P}^L of Equation (3–7c) by $\tilde{\boldsymbol{\Omega}}^L = (\mathbf{R} \boxtimes \mathbf{R})^{-1} (\boldsymbol{\Omega}^L - \mathbf{W})$.

Acknowledgment

Advice given by Ellis Dill is gratefully appreciated.

References

- [Curnier and Rakotomanana 1991] A. Curnier and L. Rakotomanana, “Generalized strain and stress measures: critical survey and new results”, *Engineering Transactions (Polish Academy of Sciences)* **39**:3-4 (1991), 461–538.
- [Dill 2006] E. H. Dill, *Continuum Mechanics: Elasticity, Plasticity, Viscoelasticity*, CRC Press, 2006.
- [Dui 2006] G.-S. Dui, “Some Basis-Free Formulae for the Time Rate and Conjugate Stress of Logarithmic Strain Tensor”, *J. Elasticity* **83**:2 (May 2006), 113–151.
- [Dui et al. 2007] G.-S. Dui, Z. Wang, and Q. Ren, “Explicit formulations of tangent stiffness tensors for isotropic materials”, *Int. J. Num. Meth. Engin.* **69**:4 (2007), 665–675.
- [Fitzgerald 1980] E. J. Fitzgerald, “A tensorial Hencky measure of strain and strain rate for finite deformations”, *J. Appl. Phys.* **51**:10 (1980), 5111–5115.
- [Hill 1978] R. Hill, “Aspects of invariance in solid mechanics”, *Adv. Appl. Mech.* **18** (1978), 1–75.
- [Hoger 1987] A. Hoger, “The stress conjugate to logarithmic strain”, *Int. J. Solids Struct.* **23**:12 (1987), 1645–1656.
- [Lehmann and Guo 1991] T. H. Lehmann and Z. Guo, “The conjugacy between Cauchy stress and logarithm of the left stretch tensor”, *Eur. J. Mech. A* **10**:4 (1991), 395–404.
- [Lehmann and Liang 1993] T. Lehmann and H. Liang, “The stress conjugate to logarithmic strain In V”, *Z. Angew. Math. Mech.* **73**:12 (1993), 357–363.
- [MacVean 1968] D. B. MacVean, “The elementary work in a continuum and the correlation of stress and strain tensors”, *Z. Angew. Math. Phys.* **19** (1968), 157–185.
- [Norris 2006] A. N. Norris, “Pure shear axes and elastic strain energy”, *Q. J. Mech. Appl. Math.* **59** (2006), 551–562.
- [Norris 2007] A. N. Norris, “Higher derivatives and the inverse derivative of a tensor-valued function of a tensor”, *Q. Appl. Math.* (**accepted**) (2007), 1–1.
- [Ogden 1984] R. W. Ogden, *Non-Linear Elastic Deformations*, Ellis Horwood, 1984.
- [Rosati 2000] L. Rosati, “A novel approach to the solution of the tensor equation $AX+XA=H$ ”, *Int. J. Solids Struct.* **37**:25 (June 2000), 3457–3477.
- [Scheidler 1991] M. Scheidler, “Time rates of generalized strain tensors. Part I: Component formulas”, *Mech. Materials* **11** (1991), 199–210.
- [Truesdell and Noll 1965] C. Truesdell and W. Noll, *The non-linear field theories of mechanics*, vol. III, edited by S. Flugge, Encyclopedia of Physics **3**, Springer-Verlag, Berlin, 1965.
- [Xiao 1995] H. Xiao, “Invariant characteristic representations for classical and micropolar anisotropic elasticity tensors”, *J. Elasticity* **40** (1995), 239 – 265.
- [Xiao et al. 1997] H. Xiao, O. T. Bruhns, and A. Meyers, “Logarithmic strain, logarithmic spin and logarithmic rate”, *Acta Mech.* **124**:1 (1997), 89–105.
- [Xiao et al. 1998a] H. Xiao, O. T. Bruhns, and A. Meyers, “Objective corotational rates and unified work-conjugacy relation between Eulerian and Lagrangean strain and stress measures”, *Arch. Mech.* **50**:6 (1998), 1015–1045.
- [Xiao et al. 1998b] H. Xiao, O. T. Bruhns, and A. Meyers, “On objective corotational rates and their defining spin tensors”, *Int. J. Solids Struct.* **35**:30 (October 1998), 4001–4014.
- [Xiao et al. 1998c] H. Xiao, O. T. Bruhns, and A. Meyers, “Strain Rates and Material Spins”, *J. Elasticity* **52**:1 (July 1998), 1–41.
- [Xiao et al. 2006] H. Xiao, O. Bruhns, and A. Meyers, “Elastoplasticity beyond small deformations”, *Acta Mech.* **182**:1 (March 2006), 31–111.

Received 20 Aug 2007. Revised 18 Sep 2007. Accepted 16 Sep 2007.

ANDREW N. NORRIS: norris@rutgers.edu

Mechanical and Aerospace Engineering, Rutgers University, 98 Brett Road, Piscataway NJ 08854-8058, United States

<http://mechanical.rutgers.edu/norris>

OUT-OF-PLANE STRESS AND DISPLACEMENT FOR THROUGH-THE-THICKNESS CRACKS IN PLATES OF FINITE THICKNESS

JOHN CODRINGTON, ANDREI KOTOUSOV AND SOOK YING HO

The out-of-plane stress and displacement fields are investigated analytically for mode I through-the-thickness cracks in an infinite plate of finite thickness within the first-order plate theory. The developed method is based on the distributed dislocation approach and an earlier derived three-dimensional solution for an edge dislocation. Numerical results are obtained through application of Gauss–Chebyshev quadrature for both finite length and semiinfinite crack cases. The calculated stress and displacement fields are found to be in good agreement with already published experimental and finite element studies. Further results for the averaged through-the-thickness stress intensity factor are given and again found to be in good agreement with previous finite element values. The developed solutions can therefore be used in experimental techniques for the assessment of the stress intensity factor using the out-of-plane displacement measurements, for example by the interferometry method.

1. Introduction

The investigation of geometric singularities like edges or cracks in engineering structures requires an understanding of the complicated three-dimensional stress field surrounding the singularity. Over the past fifty years, analytical and numerical investigations in fracture mechanics have mainly focused on two-dimensional or axisymmetric geometries. This is due to the much needed simplifications that the classic two-dimensional theories of elasticity bring to the mathematical analysis. Three-dimensional effects are often acknowledged in these studies as the true crack tip stress field is always triaxial. However, the relationship between the actual three-dimensional distribution and the results obtained within the two-dimensional theories is still not completely understood. For that reason, three-dimensional crack problems have been identified as a critical area where further research is needed [Erdogan 2000].

The three-dimensional crack-front stress and displacement fields have been investigated by many researchers including Cruse [1970], Burton et al. [1984], Yang and Freund [1985], Nakamura and Parks [1988], Leung and Su [1995] and Nevalainen and Dodds [1995], to name only a few. In particular, Hartranft and Sih [1970] proposed an approximate three-dimensional theory and studied the effects of plate thickness on the stress intensity factor. A comprehensive literature review on the earlier investigations of three-dimensional crack problems is provided by Kwon and Sun [2000].

The triaxial stress state in the vicinity of a crack tip in a sufficiently brittle material has been found to have a significant influence on fracture behavior [Kong et al. 1995]. Yang and Freund [1985] and Yuan

Keywords: distributed dislocation technique, edge dislocation, out-of-plane constraint factor, out-of-plane displacement, plate thickness effect, through-the-thickness crack.

The work described herein was supported by the Australian Research Council (ARC) through research grant no. DP0557124. The support is gratefully acknowledged.

and Brocks [1998] have shown that the specimen thickness significantly effects the crack tip stress and displacement fields, which play a crucial role in the initiation and propagation of cracks [Guo 2000].

A number of experimental investigations have been undertaken to determine the three-dimensional stress and displacement fields in the vicinity of the crack tip for a range of cracked geometries. In an experimental study by Rosakis and Ravi-Chandar [1986], the method of caustics by transmission and reflection was employed to determine the extent of the three-dimensional crack tip region. They found that plane stress conditions are recovered at a radial distance of around half the plate thickness, which confirms the analytical results of Yang and Freund [1985]. Similar conclusions were made by Pfaff et al. [1994] and Humbert et al. [2000] who utilized interferometry to determine the out-of-plane displacement field surrounding a mode I crack.

Theoretical investigations of three-dimensional crack tip stress and displacement fields have mainly utilized finite element (FE) techniques. Several researchers, including Nakamura and Parks [1988] and She and Guo [2007b], have provided detailed analyzes of the crack tip region for mode I and mixed mode (I-II) semiinfinite cracks, respectively. It was shown that the out-of-plane stress and displacement fields exhibit significant three-dimensional effects within a radial distance from the crack tip of about half the plate thickness and converge with the plane stress solutions at around 1.5 times the plate thickness. The FE results of Nakamura and Parks [1988] were found to be in reasonable agreement with the experimental study by Pfaff et al. [1994].

The purpose of this paper is to present an analytical method for calculating the stress and displacement fields at the tip of a through-the-thickness crack using the first order plate theory. This theory was previously utilized by Yang and Freund [1985] for investigating three-dimensional effects for a semiinfinite crack though only qualitative comparison with experimental results was provided in their work. The methods developed in the current paper are based on the distributed dislocation technique (DDT) and the solution for an edge dislocation in a plate of arbitrary thickness [Kotousov and Wang 2002]. Both semiinfinite and finite length cracks are investigated covering almost all geometries considered in the previous studies. The calculated results compare well with the previously published data. These solutions can therefore be used in experimental techniques for the assessment of the stress intensity factor using the out-of-plane displacement measurements, for example by the interferometry method.

In this paper, a brief review of the DDT for semiinfinite cracks is first given followed by the results for the out-of-plane constraint factor. In the next section, the formulation of the finite length crack problem is presented along with the results for the out-of-plane displacement.

2. Semiinfinite crack in a finite thickness plate

We will begin by providing an outline of the DDT as applied to a straight semiinfinite crack in a plate of thickness $2h$. A full description of the technique has already been given by Codrington and Kotousov [2007]; however, a brief review will be presented here for completeness. It is assumed that a through-the-thickness crack lies along the x axis ($-\infty < x < 1$) in an infinite plane and is subjected to a remotely applied mode I stress intensity factor K . If the crack is replaced with a continuous distribution of dislocations along the x axis then the y -stress field is given by the superposition principle as the singular

integral equation [Hills et al. 1996]

$$\sigma_{yy}(x, y) = \frac{1}{\pi} \int_{-\infty}^1 B_y(\xi) G_{yy}(x - \xi, y) d\xi. \tag{1}$$

In Equation (1), $B_y(\xi)$ is the unknown dislocation density function; it is related to the separation of the crack faces $g(\xi)$ by $B_y(\xi) = -dg(\xi)/d\xi$. The function $G_{yy}(x, y)$ is the dislocation influence function, which forms the singular kernel of the system. The influence functions depend on the geometry of the problem under investigation and various solutions are available in the literature. A comprehensive review is provided by Hills et al. [1996]. In the case of a plane stress or plane strain analysis, the y direction influence function for a dislocation in an infinite plane is given by Hills et al. [1996] as

$$G_{yy}(x, y) = \frac{2\mu}{(\kappa + 1)} \frac{x}{\rho^4} (x^2 + 3y^2), \tag{2}$$

where μ is the shear modulus, κ is Kolosov’s constant being either $(3 - \nu)/(1 + \nu)$ for plane stress or $3 - 4\nu$ for plane strain, with ν being Poisson’s ratio, and $\rho^2 = x^2 + y^2$.

Three-dimensional geometry effects will be considered for the case of a finite thickness plate by applying the solution for an edge dislocation in an infinite plate of thickness $2h$ [Kotousov and Wang 2002]. The developed influence functions are based on first-order plate theory [Kane and Mindlin 1956] whereby it is assumed that the out-of-plane strain is uniform in the thickness direction. Namely, generalized plane strain conditions are assumed to exist. In addition, the simplification is made that the dislocation Burgers vector and each of the triaxial stress components are uniform across the thickness of the plate and are equal to the average through-the-thickness values. Results obtained from this theory have been shown to be in good agreement with the through-the-thickness averages from careful three-dimensional FE studies [Berto et al. 2004; Kačianauskas et al. 2005; She and Guo 2007a]. The y direction influence function for the case of a finite thickness plate is determined by Kotousov and Wang [2002] as

$$G_{yy}(x, y) = -\frac{E}{4(1 - \nu^2)} \frac{x}{\rho^2} \left[-(1 - \nu^2) + \frac{4\nu^2}{(\lambda\rho)^2} - 2\nu^2 K_0(\lambda\rho) - \frac{2\nu^2 (2 + (\lambda\rho)^2) K_1(\lambda\rho)}{\lambda\rho} \right], \tag{3}$$

where E is Young’s modulus, $K_0(\cdot)$ and $K_1(\cdot)$ are the modified Bessel functions of the second kind of order 0 and 1, respectively, and the parameter λ is given by

$$\lambda = \frac{1}{h} \sqrt{\frac{6}{1 - \nu}}.$$

To solve the integral equation (1) via Gauss–Chebyshev quadrature, we need first to introduce the coordinate transformations

$$x = \frac{2t}{t + 1}, \quad \xi = \frac{2s}{s + 1}, \tag{4}$$

which give rise to the transformed integral equation

$$\bar{\sigma}_{yy}(t, y) = \frac{2}{\pi} \int_{-1}^1 \bar{B}_y(s) \bar{G}_{yy}(t - s, y) \frac{ds}{(s + 1)^2}. \tag{5}$$

By applying Gauss–Chebyshev quadrature to (5), the integral is reduced to a linear series in n unknowns, $\bar{\phi}(s_i)$, such that

$$\bar{\sigma}_{yy}(t, y) = \frac{2}{n} \sum_{i=1}^n \frac{1}{s_i + 1} \bar{\phi}(s_i) \bar{G}_{yy}(t - s_i, y), \tag{6}$$

where n is the number of integration points and

$$s_i = \cos\left(\frac{2i - 1}{2n} \pi\right), \quad i = 1 \dots n.$$

Along the length of the crack, where $x < 1$ and $y = 0$, the summation (6) is only valid at the discrete collocation points, which are

$$t_k = \cos\left(\frac{k}{n} \pi\right), \quad k = 1 \dots n - 1.$$

Outside of the crack interval, where $x > 1$ or $y \neq 0$, Equation (6) may be evaluated at any point.

The nonsingular function $\bar{\phi}(s)$ is related to the dislocation density by

$$\bar{B}_y(s) = \bar{\phi}(s)(1 + s)^{1/2}(1 - s)^{-1/2}. \tag{7}$$

It is assumed in Equation (7) that the stress field and, similarly, the gradient of the crack opening displacement are square root singular at the crack tip, where $x = s = 1$. Furthermore, the singularity is taken as being uniform across the entire thickness of the plate. This is due to the averaging nature of the first-order plate theory employed in the dislocation solution, which assumes a constant Burgers vector and uniform stresses across the plate thickness. Other singularities that are associated with three-dimensional geometry are, as a result, unable to be described in the analysis, for example the corner singularity found at the intersection of the crack front and the free surface of the plate [Benthem 1980]. As $x \rightarrow -\infty$ or $s \rightarrow -1$, the gradient of the crack opening displacement approaches zero and this has also been incorporated into Equation (7).

The through-the-thickness average crack tip stress intensity factor can be determined directly from an asymptotic analysis of the crack tip opening displacement or stress field near the crack tip. In the case of the plane stress or plane strain analysis, this gives

$$K_{\text{tip}} = \lim_{r \rightarrow 0} \sqrt{2\pi r} \frac{2\mu}{\kappa + 1} \frac{\partial \hat{g}(r)}{\partial r} = \sqrt{2\pi} \frac{2\mu}{\kappa + 1} \bar{\phi}(1), \quad (\theta = \pi) \tag{8}$$

and for the case of a finite thickness plate

$$K_{\text{tip}} = \lim_{r \rightarrow 0} \sqrt{2\pi r} \hat{\sigma}_{yy}(r, 0) = \frac{\sqrt{2\pi} E}{4(1 - \nu^2)} \bar{\phi}(1). \tag{9}$$

Here, $\hat{g}(r) = g(x)$ for $\theta = \pi$ or 0, $\hat{\sigma}_{yy}(r, \theta) = \sigma_{yy}(x, y)$ and the conversion between Cartesian and polar coordinates can be made via the transformations $x = r \cos(\theta) + 1$ and $y = r \sin(\theta)$. From inspection of Equation (9), it can be seen that the stress intensity factor for the finite thickness plate is simply the plane strain form of (8). However, it should be noted that the stress state is actually generalized plane strain, in accordance with the first-order plate theory, not plane strain as (9) suggests. The function $\bar{\phi}$ has only been defined at each of the integration points; therefore, $\bar{\phi}(1)$ may be found using the extrapolation formula obtained by Krenk [1975] and Hills et al. [1996]. In most cases it is generally sufficient to approximate

$\bar{\phi}(1)$ by $\bar{\phi}(s_1)$, since the computations for the exact value of $\bar{\phi}(1)$ are quite lengthy. In a similar manner, the side condition of a stress intensity factor, K_{far} , applied remotely from the crack tip can be written as

$$\bar{\phi}(S_n) = \frac{K_{\text{far}}}{\sqrt{2\pi}} \frac{\kappa + 1}{2\mu} \tag{10}$$

for the cases of plane stress and strain. In the finite thickness plate analysis, it is assumed that plane stress conditions will prevail remotely from the crack tip [Yang and Freund 1985] and therefore the plane stress form of (10) is employed.

Use is now made of the requirement that the crack faces must remain traction free, which means that $\sigma_{yy}(x, 0) = 0$ along the crack length or simply $\bar{\sigma}_{yy}(t_k, 0) = 0$. This constraint, together with Equation (6), provides a system of $n - 1$ linear equations in n unknowns $\bar{\phi}(s_i)$. Depending on whether a plane stress/strain analysis or a finite thickness plate analysis is undertaken, the choice of the kernel function $G_{yy}(x, y)$ as either (2) or (3) respectively is made. The n th equation which completes the set of linear equations is given by the condition of the remotely applied stress intensity factor (10). The set of n linear equations in n unknowns can now be solved via any standard method.

3. Results for the out-of-plane stress

In this section, results for the out-of-plane stress field are presented for a semiinfinite crack in a plate of finite thickness. The effect of the out-of-plane stresses are commonly described in the literature by the out-of-plane constraint factor

$$\widehat{T}_z(r, \theta) = T_z(x, y) = \frac{\sigma_{zz}(x, y)}{\nu[\sigma_{xx}(x, y) + \sigma_{yy}(x, y)]}$$

where the stress components $\sigma_{xx}(x, y)$ and $\sigma_{zz}(x, y)$ are found in a similar manner to (6) by replacing the kernel with

$$G_{xx}(x, y) = \frac{E}{4(1 - \nu^2)} \frac{x}{\rho^2} \left[(1 - \nu^2) + \frac{4\nu^2}{(\lambda\rho)^2} - 2\nu^2 K_0(\lambda\rho) - \frac{4\nu^2 K_1(\lambda\rho)}{\lambda\rho} \right],$$

$$G_{zz}(x, y) = \frac{E\nu}{2(1 - \nu^2)} \frac{\lambda x}{\rho} K_1(\lambda\rho),$$

respectively [Kotousov and Wang 2002].

Results for the out-of-plane constraint factor crack are shown in Figure 1, for a semiinfinite, as a function of the radial distance from the crack tip to plate thickness ratio $r/2h$ with $\theta = 0$. FE results by Nakamura and Parks [1988] and She and Guo [2007b] for semiinfinite cracks are also provided as a comparison. Both the mid-thickness (MT) and through-the-thickness average (AV) FE values are given. It can be seen that the mid-thickness results are in better agreement with the present values than the average results are. This is due to the different modeling assumptions made in each of the studies. Namely, the current investigation makes the simplification of generalized plane strain conditions in the vicinity of the crack tip. Furthermore, FE techniques are limited by the finite mesh size in representing the singular stress field near the crack tip. Figure 1 shows that at the crack tip the conditions reach near plane strain while at approximately $r/2h = 1.5$ the plane stress solution is recovered. In these and all

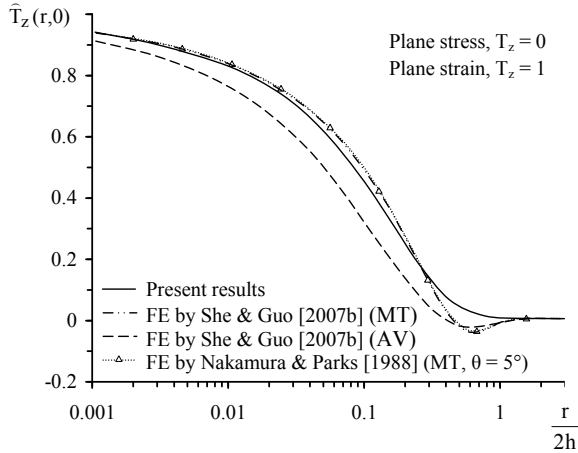


Figure 1. Out-of-plane constraint factor as a function of the ratio $r/2h$ for a semiinfinite crack ($\theta = 0^\circ$).

subsequent calculations, Poisson’s ratio is taken as $\nu = 0.3$ though any variation of ν has minimal effect on the constraint factor. Approximately 250 integration points are required to reach a convergence in the solution.

Figure 2 shows the results for the out-of-plane constraint factor as a function of θ for various $r/2h$. Again a semiinfinite crack model has been used. The mid-thickness FE results by She and Guo [2007b] are given and they show a good agreement with the present results. Results for the ratio of the average crack tip stress intensity factor to the far-field stress intensity factor are shown in Figure 3 as a function of Poisson’s ratio. The crack tip stress intensity factor for the case of a finite thickness plate is determined by Equation (9). The present results are identical to the through-the-thickness average of the values presented by She and Guo [2007b] and Nakamura and Parks [1988] for semiinfinite cracks.

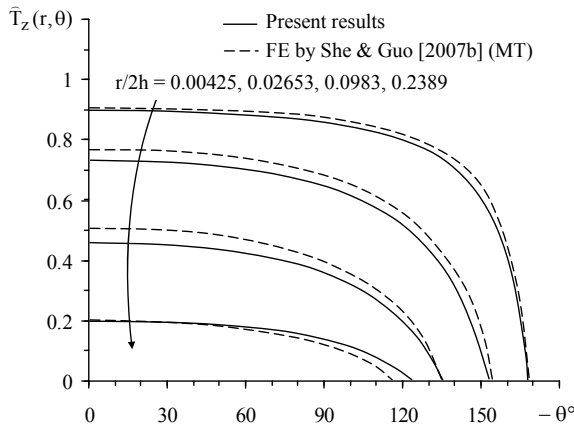


Figure 2. Out-of-plane constraint factor as a function of θ for various $r/2h$ for a semiinfinite crack.

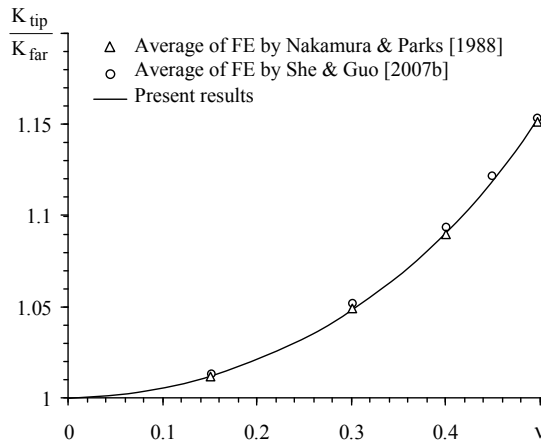


Figure 3. Ratio of the average crack tip stress intensity factor to the far-field stress intensity factor as a function of Poisson’s ratio for a semiinfinite crack.

4. Results for the out-of-plane displacement

The out-of-plane displacement for the case of a semiinfinite crack can be determined at any point within the plate by the function

$$\widehat{u}_z(r, \theta, z) = u_z(x, y, z) = \frac{z}{\pi h} \int_{-\infty}^1 B_y(\xi) G_{uz}(x - \xi, y) d\xi,$$

where the plate mid-thickness is at $z = 0$ and the plate surfaces are at $z = \pm h$. The displacement kernel for the finite thickness plate analysis is given by Kotousov and Wang [2002] as

$$G_{uz}(x, y) = -\frac{vh\lambda}{2} \frac{x}{\rho} \left[\frac{1}{\lambda\rho} - K_1(\lambda\rho) \right]$$

and in the case of plane stress is

$$G_{uz}(x, y) = -\frac{vh}{2} \frac{x}{\rho^2}.$$

The formulation of the finite length crack problem is very similar to that of the semiinfinite crack as outlined in Section 2 and thus most details are omitted. It is assumed that a through-the-thickness crack of length $2a$ lies within $-a < x < a$ on the x axis in an infinite plane and is subjected to remotely applied stress, $\sigma_{yy}^\infty(x)$. The governing singular integral equation therefore becomes [Hills et al. 1996]

$$\sigma_{yy}(x, y) = \frac{1}{\pi} \int_{-a}^a B_y(\xi) G_{yy}(x - \xi, y) d\xi + \sigma_{yy}^\infty(x). \tag{11}$$

Solution to the integral equation (11) follows via application of Gauss–Chebyshev quadrature in a similar manner as for the semiinfinite crack case. The transformations (4), however, are replaced with the new transformations:

$$x = at, \quad \xi = as,$$

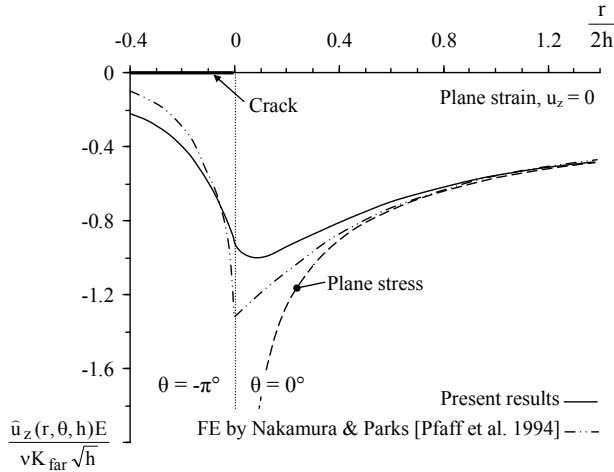


Figure 4. Normalized out-of-plane surface displacement as a function of $r/2h$ in the case of a semiinfinite crack.

and the nonsingular function $\bar{\phi}(s)$ is now related to the dislocation density by

$$\bar{B}_y(s) = \bar{\phi}(s)(1 + s)^{-1/2} (1 - s)^{-1/2}.$$

Here it is assumed that the dislocation density function is square root singular at both $s = -1$ and $s = 1$ since there is a singularity in the displacement gradient and stress fields at each of the crack tips.

The out-of-plane displacement for the finite length crack may be determined by

$$\hat{u}_z(r, \theta, z) = u_z(x, y, z) = \frac{z}{\pi h} \int_{-a}^a B_y(\xi) G_{u_z}(x - \xi, y) d\xi - \frac{\nu}{E} z \sigma_{yy}^\infty(x),$$

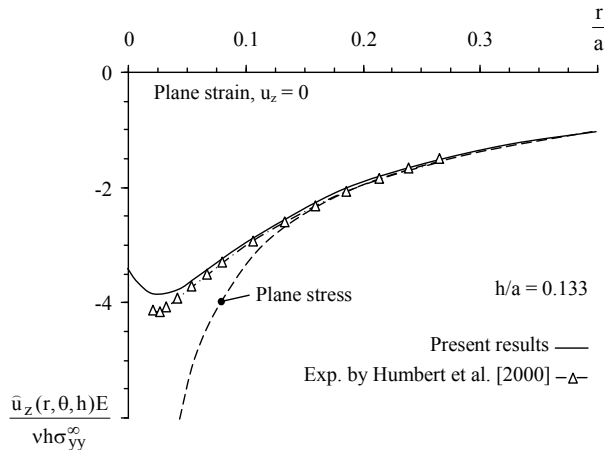


Figure 5. Normalized out-of-plane surface displacement as a function of r/a in the case of a finite length crack ($\theta = 0^\circ$).

where the extra term is due to the uniform lateral contraction of the infinite plate loaded by the remote tensile stress $\sigma_{yy}^{\infty}(x)$. The conversion between Cartesian and polar coordinates is then made by $y = r \sin \theta$ and $x = r \cos \theta + a$.

Results for normalized out-of-plane surface displacement along the line of the crack are presented in Figure 4 in the case of a semiinfinite crack. The empirical fit by Pfaff et al. [1994] to the FE results by Nakamura and Parks [1988] is also given as a comparison. The difference between the finite element results and the present ones could be explained by the mesh refinement issues at the crack tip in the FE model. Figure 5 displays the results for the normalized out-of-plane displacement ahead of the crack tip for the case of a finite length crack. The present results are in good agreement with the experimental values of Humbert et al. [2000]. The difference is less than 10% and can be partially explained by the presence of the process zone at the crack tip where the material is subjected to inelastic deformations.

5. Conclusion

An analytical method is presented for calculating the out-of-plane stress and displacement fields in plates of finite thickness. The developed method is based on the DDT and the three-dimensional solution for an edge dislocation in plates of arbitrary thickness. Numerical results are obtained for both finite length and semiinfinite crack models through application of Gauss–Chebyshev quadrature. Results for the normalized out-of-plane constraint factor and the out-of-plane surface displacement are presented. The present values are compared with finite element and experimental results and found to be consistent. Further results for the ratio of the crack tip stress intensity factor to the applied stress intensity factor are given. A comparison with the through-the-thickness average values from previous finite element studies shows a very good agreement. These solutions can therefore be used in the experimental techniques for the assessment of the stress intensity factor using the out-of-plane displacement measurements.

References

- [Benthem 1980] J. P. Benthem, “The quarter-infinite crack in a half space; alternative and additional solutions”, *Int. J. Solids Struct.* **16** (1980), 119–130.
- [Berto et al. 2004] F. Berto, P. Lazzarin, and C. H. Wang, “Three-dimensional linear elastic distributions of stress and strain energy density ahead of V-shaped notches in plates of arbitrary thickness”, *Int. J. Fract.* **127** (2004), 265–282.
- [Burton et al. 1984] W. S. Burton, G. B. Sinclair, J. S. Solecki, and J. L. Swedlow, “On the implications for LEFM of the three-dimensional aspects in some crack/surface intersection problems”, *Int. J. Fract.* **25** (1984), 3–32.
- [Codrington and Kotousov 2007] J. Codrington and A. Kotousov, “Application of the distributed dislocation technique for calculating crack tip plasticity effects”, *Fatigue Fract. Eng. Mater. Struct.* **30**:12 (2007), 1182–1193.
- [Cruse 1970] T. A. Cruse, “Lateral constraint in a cracked, three dimensional elastic body”, *Int. J. Fract.* **6** (1970), 326–328.
- [Erdogan 2000] F. Erdogan, “Fracture mechanics”, *Int. J. Solids Struct.* **37** (2000), 171–183.
- [Guo 2000] W. Guo, “Recent advances in three-dimensional fracture mechanics”, *Key Eng. Mater.* **183** (2000), 193–198.
- [Hartranft and Sih 1970] R. J. Hartranft and G. C. Sih, “An approximate three-dimensional theory of plates with application to crack problems”, *Int. J. Eng. Sci.* **8** (1970), 711–729.
- [Hills et al. 1996] D. A. Hills, P. A. Kelly, D. N. Dai, and A. M. Korsunsky, *Solution of crack problems—the distributed dislocation technique*, Kluwer Academic Publishers, Dordrecht, 1996.
- [Humbert et al. 2000] L. Humbert, V. Valle, and M. Cottron, “Experimental determination and empirical representation of out-of-plane displacements in a cracked elastic plate loaded in mode I”, *Int. J. Solids Struct.* **37** (2000), 5493–5504.

- [Kane and Mindlin 1956] T. R. Kane and R. D. Mindlin, “High frequency extensional vibrations of plates”, *J. Appl. Mech.* **23** (1956), 277–283.
- [Kačianauskas et al. 2005] R. Kačianauskas, M. Zenon, V. Žarnovskij, and E. Stupak, “Three-dimensional correction of the stress intensity factor for a plate with a notch”, *Int. J. Fract.* **136** (2005), 75–98.
- [Kong et al. 1995] X. M. Kong, N. Schluter, and W. Dahl, “Effect of triaxial stress on mixed-mode fracture”, *Eng. Fract. Mech.* **52** (1995), 379–388.
- [Kotousov and Wang 2002] A. Kotousov and C. H. Wang, “Fundamental solutions for the generalised plane strain theory”, *Int. J. Eng. Sci.* **40** (2002), 1775–1790.
- [Krenk 1975] S. Krenk, “On the use of the interpolation polynomial for solutions of singular equations”, *Quart. Appl. Math* **32** (1975), 479–484.
- [Kwon and Sun 2000] S. W. Kwon and C. T. Sun, “Characteristics of three-dimensional stress fields in plates with a through-the-thickness crack”, *Int. J. Fract.* **104** (2000), 291–315.
- [Leung and Su 1995] A. Y. T. Leung and R. K. L. Su, “A numerical study of singular stress field of 3D cracks”, *Finite Elem. Anal. Des.* **18** (1995), 389–401.
- [Nakamura and Parks 1988] T. Nakamura and D. M. Parks, “Three-dimensional stress field near the crack front of a thin elastic plate”, *J. Appl. Mech.* **55** (1988), 805–813.
- [Nevalainen and Dodds 1995] M. Nevalainen and R. H. Dodds, “Numerical investigation of 3-D constraint effects on brittle fracture in Se(b) and C(T) specimens”, *Int. J. Fract.* **74** (1995), 131–161.
- [Pfaff et al. 1994] R. D. Pfaff, P. D. Washabaugh, and W. G. Knauss, “An interpretation of Twyman-Green interferograms from static and dynamic fracture experiments”, *Int. J. Solids Struct.* **32** (1994), 939–955.
- [Rosakis and Ravi-Chandar 1986] A. J. Rosakis and K. R. Ravi-Chandar, “On crack-tip stress state: an experimental evaluation of three-dimensional effects”, *Int. J. Solids Struct.* **22** (1986), 121–134.
- [She and Guo 2007a] C. She and W. Guo, “Three-dimensional stress concentrations at elliptical holes in elastic isotropic plates subjected to tensile stress”, *Int. J. Fatigue* **29** (2007a), 330–335.
- [She and Guo 2007b] C. She and W. Guo, “The out-of-plane constraint of mixed-mode cracks in thin elastic plates”, *Int. J. Solids Struct.* **44** (2007b), 3021–3034.
- [Yang and Freund 1985] W. Yang and L. B. Freund, “Transverse shear effects for through cracks in an elastic plate”, *Int. J. Solids Struct.* **21** (1985), 977–994.
- [Yuan and Brocks 1998] H. Yuan and W. Brocks, “Quantification of constraint effects in elastic-plastic crack front fields”, *J. Mech. Phys. Solids* **46** (1998), 219–241.

Received 2 Apr 2007. Revised 23 Sep 2007. Accepted 1 Oct 2007.

JOHN CODRINGTON: john.codrington@adelaide.edu.au
School of Mechanical Engineering, The University of Adelaide, SA 5005, Australia

ANDREI KOTOUSOV: andrei.kotousov@mecheng.adelaide.edu.au
School of Mechanical Engineering, The University of Adelaide, SA 5005, Australia

SOOK YING HO: sookying.ho@adelaide.edu.au
School of Mechanical Engineering, The University of Adelaide, SA 5005, Australia

INVESTIGATION OF MODE II CRACK GROWTH FOLLOWING A VERY HIGH SPEED IMPACT

WEI MA AND ZHUPING DUAN

A recoverable plate impact testing technology has been developed for studying fracture mechanisms of mode II crack. With this technology, a single duration stress pulse with submicrosecond duration and high loading rates, up to $10^8 \text{ MPa m}^{1/2} \text{ s}^{-1}$, can be produced. Dynamic failure tests of Hard-C 60# steel were carried out under asymmetrical impacting conditions with short stress-pulse loading. Experimental results show that the nucleation and growth of several microcracks ahead of the crack tip, and the interactions between them, induce unsteady crack growth. Failure mode transitions during crack growth, both from mode I crack to mode II and from brittle to ductile fracture, were observed. Based on experimental observations, a discontinuous crack growth model was established. Analysis of the crack growth mechanisms using our model shows that the shear crack extension is unsteady when the extending speed is between the Rayleigh wave speed c_R and the shear wave speed c_s . However, when the crack advancing speed is beyond c_s , the crack grows at a steady intersonic speed approaching $\sqrt{2}c_s$. It also shows that the transient mechanisms, such as nucleation, growth, interaction and coalescence among microcracks, make the main crack speed jump from subsonic to intersonic and the steady growth of all the subcracks causes the main crack to grow at a stable intersonic speed.

1. Introduction

During the past several decades, researchers have made great progress in experiments on dynamic failure mechanisms [Erdogan and Sih 1963; Kalthoff 1987; 1988; Ravichandran and Clifton 1989; Kalthoff 1990; Prakash and Clifton 1992; Ravi-Chandar 1995; Zhou et al. 1996; Needleman 1999; Rosakis et al. 1999; Abraham and Gao 2000; Ravi-Chandar et al. 2000; Rosakis et al. 2000; Geubelle and Kubair 2001; Samudrala et al. 2002; Cox et al. 2005]. Usually, experiments on how cracks start and grow are conducted with apparatus such as the Hopkinson bar; however, it produces relatively low loading rates from 10^1 to $10^6 \text{ MPa m}^{1/2} \text{ s}^{-1}$. Hence, these experiments do not clearly reveal the transients of crack initiation.

Recently, Ravichandran and Clifton [1989] and Prakash and Clifton [1992] developed a plate impact technique with a high loading rate for understanding the essential fracture dynamics. This technique can produce a plane strain mode I crack using a square tensile pulse lasting less than a microsecond. It raises the loading rates by two orders of magnitude over the Hopkinson bar technique and is a noteworthy advance for the study of the transient mechanisms of material failure. However, for investigating the

Keywords: plate impact tests, dynamic fracture, failure mode transition, intersonic crack extension, discontinuous crack growth model.

The authors gratefully acknowledge the support of the National Science Foundation of China (grant nos. 10275085 and 10672166).

fracture mechanisms of mode II cracks, the technique needs to be improved. We address some aspects of this problem.

So far, restrictions in current testing technology have prevented complete understanding of the failure mechanisms in mode II fractures, notwithstanding a great number of investigations and the observation of many interesting phenomena [Kalthoff 1987; 1988; 1990; Ravi-Chandar 1995; Ravi-Chandar et al. 2000]. Kalthoff [1987; 1988] has studied the failure of high strength steel loading including dynamic mode II cracks and have shown that low speed impact induces cleavage fracture. The cracks extend at an angle of about 70° with respect to the original crack line, which shows that the maximum hoop stress criterion [Erdogan and Sih 1963] governs the crack initiation and growth. When the impact speed exceeds a critical value, the failure mode changes from crack fracture to shear band failure, and microscope images of the fracture surface revealed that the failure mechanism had also changed from cleavage fracture to ductile shear failure.

In similar investigations, Ravi-Chandar [1995] and Ravi-Chandar et al. [2000] demonstrated that at low loading rates, the crack tip formed a plastic zone around it, but no crack started; at moderate loading rates, a brittle crack began and the failure mode changed from ductile to brittle; and at high loading rates, the crack formed and advanced along the original crack line but was arrested in the specimen. Postmortem microstructural examination of the failure surface indicated that the maximum shear stress criterion governed the fracture process.

Elsewhere, Zhou et al. [1996] studied the initiation and propagation of shear bands by applying asymmetric mode II crack impact loading to a prenotched plate specimen. Results show that, when the impact velocity exceeds a critical value, a shear band advances throughout the specimen. When the impact velocity falls below this critical value, a shear band arrests first inside the specimen, and then a crack starts from the arrested shear band tip and grows along the propagating shear band. Under a microscope, the fracture surfaces show that a ductile mode shear failure occurs inside the shear band, and the crack fails in an opening mode. The coexistence of shear band failure and crack fracture implies that the mode II crack loading changes the failure mode from shear band failure to crack fracture.

Recently, much attention focuses on shear-dominated intersonic crack extension mechanisms. Inter-sonic cracking has been directly observed in asymmetrical impact tests on a specimen consisting of a homogeneous and isotropic solid with an artificial weak band plane [Rosakis et al. 1999, 2000], in which the shear cracks propagated initially with a speed just above the shear wave speed c_s , accelerated sharply to the longitudinal wave speed c_l , and finally approached a steady intersonic speed $\sqrt{2}c_s$.

Motivated by the experimental observations, many researchers have paid great attention to intersonic cracking [Needleman 1999; Abraham and Gao 2000; Geubelle and Kubair 2001; Samudrala et al. 2002]. The studies, based on continuum elastodynamics and molecular dynamics [Abraham and Gao 2000], show that when a shear crack propagates along a weak plane, a daughter crack first initiates in front of the crack tip, and then joins with the mother crack, and, as a result, the crack propagates with intersonic speeds. This conclusion has been confirmed by the fact that when a daughter crack growing at intersonic speed nucleates just ahead of the mother crack tip, the Mach cone angles at the daughter crack tip show that its velocity is consistent with the longitudinal wave speed.

The simulation study also shows that a finite peak stress ahead of the mother crack is the only possible mechanism of daughter crack nucleation. Therefore, the interaction of the “mother-daughter” crack causes a subsonic shear crack to jump over the forbidden velocity zone between the Rayleigh wave

speed c_R and shear wave speed c_s . Identical results followed from numerical calculations [Needleman 1999].

Samudrala et al. [2002] found analytical results for the subsonic and intersonic mode II crack propagation with a rate-dependent cohesive zone, indicating that the subsonic regime is inherently unstable for mode II crack propagation, but, with increasing rate sensitivity, stable mode II crack growth prevails at low subsonic speeds. At intersonic speeds, the mode II crack growth is unstable up to a critical speed higher than $\sqrt{2}c_s$, above which it becomes stable.

Samudrala et al. [2002] also investigated the effect on crack propagation of a dimensionless rate parameter and of shear strength of the crack plane. In the cohesive zone model, they found that fracture energy is finite at intersonic crack speeds and that more energy is dissipated when intersonic speeds are close to c_1 . Furthermore, the fracture energy is sensitive to a rate parameter describing the influence of shear stress on the local sliding rate in the cohesive zone. By decreasing the crack plane strength, they found that an intersonic mode II crack would accelerate all the way up to c_1 , whereas increasing it seems to favor steady crack growth with an intersonic speed close to $\sqrt{2}c_s$. These results agree with the crack speed characteristics observed in the experiments of Rosakis et al. [1999; 2000].

Numerical calculations by Geubelle and Kubair [2001] show an extension speed transition of a shear dominated crack from subsonic to intersonic. Usually, a rapid acceleration of the primary cohesive zone at the crack tip induces the transition. Occasionally, a secondary failure zone or perhaps a microcrack generated ahead of the crack, which quickly coalesces with the primary failure zone, can induce the transition as well. The calculations reveal that intersonic crack propagation is possible for a wide range of loading conditions, as long as the shear-dominated loading intensity is a major fraction of the strength of the fracture plane. Moreover, under mixed-mode loading conditions when the shear component of the external loading is sufficiently large, cracks can propagate intersonically. When the crack grows steadily at an intersonic speed, cohesive failure is mainly induced by shear stresses, even though the remote loading is of mixed mode.

To understand the mechanisms of mode II crack growth under high-speed impact loading, we have developed an improved plate impact testing technique and conducted dynamic failure tests of Hard-C 60[#] steel. The technique can generate a compressive stress pulse lasting less than a microsecond with a loading rate as high as $10^8 \text{ MPa m}^{1/2}\text{s}^{-1}$. During an asymmetrical impact, an edge crack plate specimen develops a plane strain deformation state at the crack tip. Experimental results demonstrate that the nucleation and growth of microcracks ahead of a main crack result in unstable crack propagation with nonuniform extension speeds increasing from subsonic to intersonic.

In addition, failure mode transitions, both from mode I to mode II crack and from brittle to ductile failure, were observed during the crack growth. Based on these observations, we propose a discontinuous transient crack growth model. We discuss the relevant dynamic mechanisms of crack initiation and growth, using the energy principle of dynamic fracture mechanics.

The article is organized as follows. In Section 2, we give the relevant theory for describing the crack dynamics in an asymmetrical plate. Then, in Sections 3 and 5, we describe the experimental details, including material properties, specimen configurations, the experimental setup, and the testing approach. In Section 5, we analyze under a microscope the crack growth mechanisms. Finally, we propose a discontinuous transient crack growth model for describing of intersonic crack growth qualitatively and discuss the results.

2. Theoretical background

The dynamic fracture process displays many complex features, such as the response of material crystal and atomic structures, inelastic properties, microdefects, strain rate sensitivities, and so on; however, moving crack tips in a variety of materials all exhibit the phenomena of crack initiation, kinking, and bifurcation, all of which are assumed to occur in continuous media. Thus, we can still effectively use continuum mechanics for describing the essential dynamic failure mechanisms. Here, we present the elastic wave theory [Achenbach 1973] as the theoretical basis for improving the plate impacting technique. Then, we use the energy methods of elastodynamic fracture theory [Freund 1990] and the analytic results of the linear elastodynamic problem [Ma 1998] to interpret the failure mechanisms of materials and investigate the behaviors of crack growth.

With the asymmetrical plate impact technique, it is easy to produce a mode II crack deformation field in an edge crack plate specimen. Such a specimen is effectively simulated as semiinfinite crack tip field in an infinite elastic body. It is reasonable to assume that one-dimensional stress waves propagate during the collision. Furthermore, we assume that no incident stress pulses reflect from the component interfaces because all collision components have the same impedance and they are joined without gaps. Figure 1 illustrates a distance-time (x, t) diagram of the stress wave fronts prevailing in the collision and the smaller velocity-stress (v, σ) diagram characterizing each region in the (x, t) diagram. The figure shows that at time t_3 two unloading stress pulses meet in the momentum trap, and create a tension stress pulse. At time t_4 , when the pulse reaches the interface between the specimen and the momentum trap, the interface splits and the momentum trap separates from the specimen. Because the momentum trap is thicker than the flyer, it can trap the entire tensile pulse. Thus, the flyer transfers its momentum to the momentum trap, and, in the collision process, the specimen feels only the impact of a single duration compressive stress pulse. In addition, the diameter-to-thickness ratio of the specimens is chosen larger

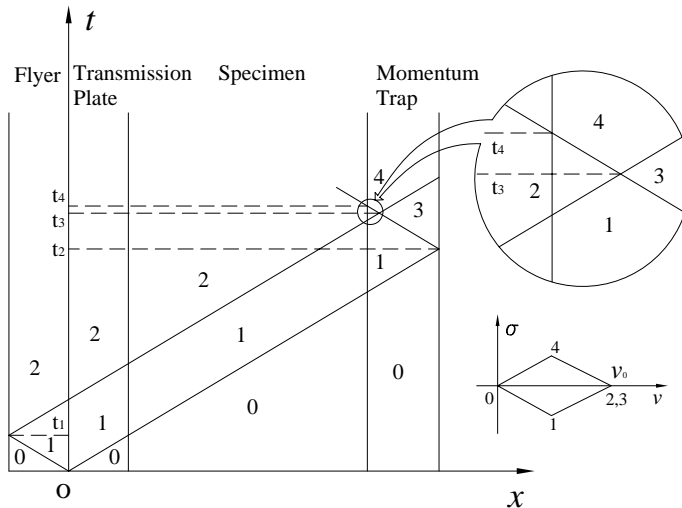


Figure 1. Distance-time (x, t) diagram in the asymmetrical plate impact procedure, with velocity-stress (v, σ) illustrated in the inset.

than four, effectively reducing the effect of their boundaries on crack growth. These measures ensure that a plane strain mode II crack deformation field develops in the central region of the edge crack plate specimen, which can be confirmed in the microscope images of the fracture surface described below.

In asymmetrical impact loading, strictly speaking, a transient mixed-mode deformation field develops at the crack tip, in which the mode II crack deformation field predominates because of the shear effects produced by the high strength compressive stress pulses; however, a time-dependent mode I deformation weak field also forms [Freund 1990]. Figure 2 illustrates the wavefront for the stress pulse scattered by the crack tip when the impact is shorter than $2l/c_1$. Generally, a longitudinal plane pulse (1) induces a mode II crack deformation field; the competition between the inertial resistance and Poisson's effect creates a mode I deformation weak field, and the cylindrical waves (2)–(8) generate a mixed-mode deformation field. In this study, we directly measure variations of the compressive stress pulses using the Mn-Cu gauge technique [Raiser et al. 1990; Fowles et al. 1970]. To validate the measurements, we compare the amplitudes of stress pulses with the calculated values based on the measured impact speeds V_0 and the elastodynamic relation, $\sigma_0 = \rho c_1 V_0/2$.

The energetics relevant to dynamic fracture are briefly described below; more details can be found in [Freund 1990]. For mixed-mode crack growth at nonuniform speed v , the dynamic energy release rate is given by

$$G = \frac{1 - \mu^2}{E} [A_I(v)K_I^2 + A_{II}(v)K_{II}^2], \tag{2-1}$$

where

$$A_I(v) = \frac{v^2 \alpha_d}{(1 - \mu)c_s^2 D}, \quad A_{II}(v) = \frac{v^2 \alpha_s}{(1 - \mu)c_s^2 D},$$

$$D = 4\alpha_d \alpha_s - (1 + \alpha_s^2)^2, \quad \alpha_d^2 = 1 - v^2/c_l^2, \quad \alpha_s^2 = 1 - v^2/c_s^2.$$

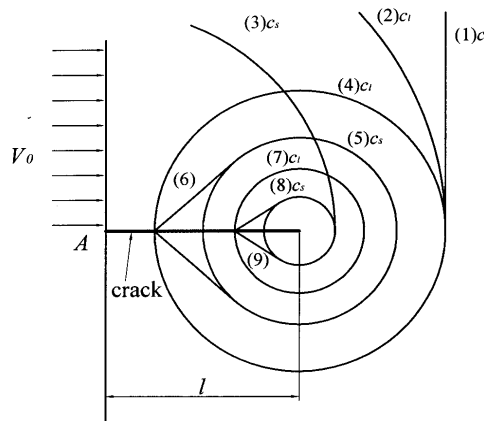


Figure 2. The wave fronts of the stress pulses scattering by the crack tip in the asymmetrical impact procedure.

The dimensionless functions $A_I(v)$ and $A_{II}(v)$ are universal functions of the crack speed v and the properties of the materials. They do not depend on the load or the crack body configuration. E and μ are the Young's modulus and Poisson's ratio. K_I and K_{II} are the time-dependent stress intensity factors of mode I and II with the instantaneous crack length vt . According to Griffith's critical energy release rate criterion, a crack must extend so that the crack tip releases energy at a rate equal to the dynamic fracture energy of the material. Hence, under isothermal conditions, the growth criterion is $G = \Gamma$, where G is the energy release rate and Γ is the special fracture energy of arbitrary crack growth at nonuniform speed. (These standard descriptions of G and Γ are more intuitive than precise, as they have dimensions of energy per area or force per length.) Generally, G is a property of the local mechanical field of the crack tip; it represents the effect of applied loading, the body configuration, and bulk material parameters. Γ characterizes resistance to crack extension and is related to the current crack length and speed.

A theoretical study by Lee and Freund [1990] analyzed the two-dimensional elastodynamic problem of a semiinfinite plate containing a static edge crack under asymmetrical impact loading with a normal velocity imposed suddenly on one side of the edge cracked plate. By using a universal function of the crack growth speed and the static stress intensity factor, the time-dependent stress intensity factors K_I and K_{II} are expressed as

$$K_I(t, l, v) = k_I(v)K_c(t, l, 0), \quad K_{II}(t, l, v) = k_{II}(v)K_c(t, l, 0)$$

in which $K_c(t, l, 0) = \lambda/(2\pi l)^{1/2}$, $k_I(v)$ and $k_{II}(v)$ can be found in [Lee and Freund 1990; Ravi-Chandar et al. 2000], and λ is proportional to the stress pulse amplitude. Here, it is assumed that the results can generalize for the situation of dynamic crack growth. That is, the stress intensity factor is a function of crack length and time, as well as the crack speeds. Thus, we use the time-dependent intensity factors K_I and K_{II} of Equation (2-1) to evaluate the crack growth speeds and dynamic stress intensity factors.

3. Experimental details

3.1. Materials. We test Hard-C 60[#] steel. Because its behavior reveals clear rate-dependent characteristics in dynamic loading, it is a suitable material for examining how loading rates affect macroscopic and microscopic failure. The material properties of Hard-C 60[#] steel are given in reference [Ma and Duan 2000]. Before testing, the material was normalized at 880° C, quenched rapidly in oil, and then tempered at 200° C for 3 hours. The treatment created a relatively homogeneous martensitic microstructure, significantly increasing the yield limit. Uniaxial tensile tests, under loading at a strain rate of 10^{-1} s^{-1} , show that the yield stress increases from 420 MPa to about 580 MPa. Quasistatic three-point bending tests show that the fracture toughness is about $55.2 \text{ MPa m}^{1/2}$. Figure 3 shows a SEM image of the quasistatic fracture surface. It clearly reveals cleavage fracture traits. Measurements indicate that the average hardness has reached 54 HRC, which is brittle enough for our purposes. Hence, we can assume that the plastic deformation region, if it even exists at the dynamic crack tip, is negligibly small, and that the results of impacting experiments can be interpreted using elastodynamic fracture theory outlined in the previous section.

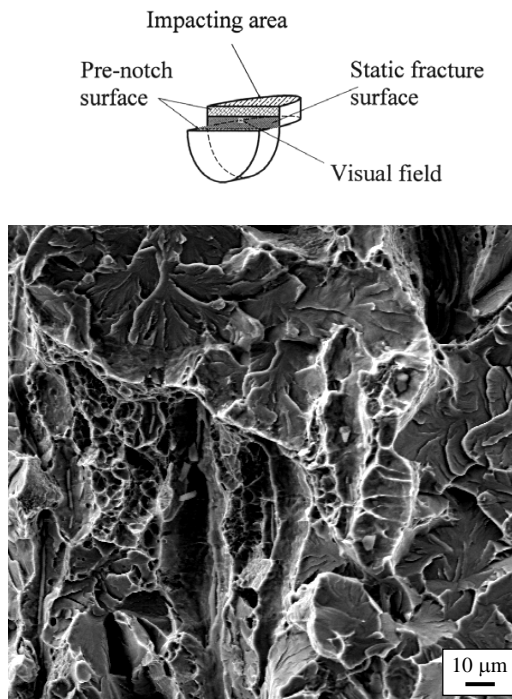


Figure 3. The SEM picture of the brittle fracture surface of the opening mode cracks under the quasistatic three-point bending loading conditions. The inset shows the corresponding visual field.

4. Components in the collision system

To create a plane strain state at the crack tip in the edge crack plate specimen, we employ a special impact system consisting of the flyer, specimen, transmission plate, and momentum trap. The geometry of the impact components is shown in Figure 4. The single edge-notched specimen is a round disc 50 mm in diameter and 10 mm thick. The initial notch about 5 mm long and $150\ \mu\text{m}$ wide is cut by electric discharge machining; see Figure 4a. The other components are half round discs with same material and radius, but with different thickness (see again Figure 4). Before the impact tests, all component surfaces were machine-lapped flat using 3–15 μm diamond powder papers and then polished on Texmeth cloth over a flat plate using a 0.1–0.3 μm diamond paste. The process ensured the surfaces were flattened to an accuracy better than one Newton's ring.

4.1. Experimental setup. The experiment consists of the following: a pressure-shear gas gun for producing the compressive stress pulses; Mn-Cu stress gauge units for directly measuring the compressive stress-time profiles [Ma 1998]; a soft recovery apparatus [Raiser et al. 1990]; two electrical circuits, one for measuring the projectile impact velocities and another for examining the misalignment angles between the impacting planes.

The pressure-shear gas gun has a launch tube 60 mm in diameter and 6 m long. A keyway runs along the tube's length to prevent the projectile from rotating during firing. The main part of the projectile is a

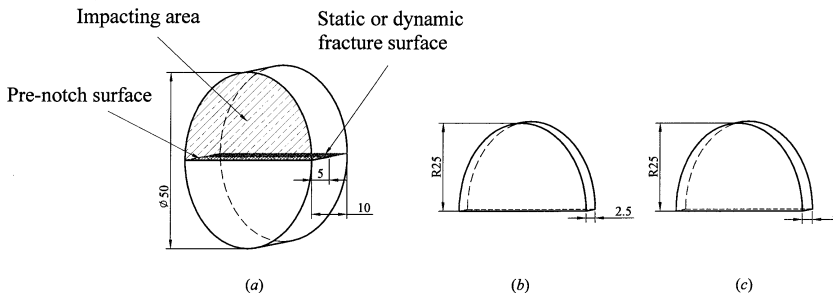


Figure 4. The configurations and geometries of the crashing components used in this study, including the specimen (a), transmission plate and flyer (b), and momentum plate (c).

high-density plastic foam column 58 mm in diameter and 0.25 m long. Its front face is bonded to the flyer and its rear end is connected an aluminum tail that holds two sealing O-rings and a key fit to the keyway. Because the plastic foam has much lower impedance than the flyer, it can be taken for granted that the compressive stress pulse is reflected into the tensile unloading pulse at the bond interface between the flyer and the plastic projectile.

Figure 5 shows the experimental configuration schematically. The target assembly consists of an inner ring supporting the specimens and an outer tapped ring connected to a holder. The holder system is designed so that it can be accurately adjusted with small translations along the three axial directions and small rotations in the three angle coordinates. (See the inset in Figure 5). Thus, the relative position and orientation of the flyer and the specimen can be precisely fixed before the impact tests. A heavy steel anvil is placed ahead of the momentum trap to reduce the influence of the projectile's impulse. During impact, the projectile momentum consists of two parts: one from the fast moving flyer and another from its aluminum tail. In first collision stage, that is, when the flyer hits the transmission plate, the flyer imparts its momentum to the momentum trap, causing stress wave propagation, but is then taken away after it separates from the specimen. In this way, we prevent the tensile unloading pulse from again loading the specimen and ensure that it is only loaded with a single pulse. In the later stage of impact,

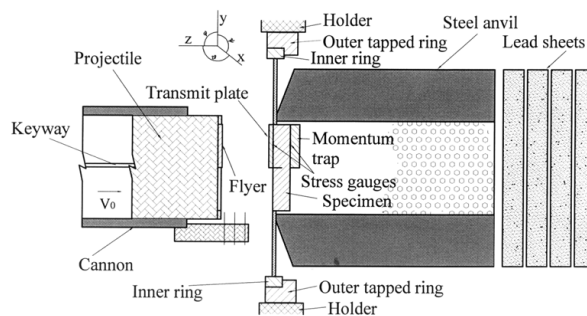


Figure 5. The schematic of the target assembly.

the aluminum tail hits the steel anvil and transfers its momentum to the steel anvil. Energy is further dissipated through the plastic deformation of lead sheets located in the other end of pressure chamber; see Figure 5. The steel anvil then contains specimens which can be easily seen and recovered intact for the postmortem microscopic analysis.

4.2. Experimental procedure. The impact test takes place in a pressure chamber which can sustain a gas pressure up to 16 MPa. Prior to the test, it is evacuated to a pressure of $2\text{--}3 \times 10^{-6}$ Pa, and, during the test, its internal pressure remains at $2\text{--}5 \times 10^{-5}$ Pa. The inclination pitch between the flyer's impacting planes and the target plate is measured using a tilt system consisting of three pairs of pins and an amplifying circuit. The measurements show that the inclination pitches are well controlled on the order of $2\text{--}4 \times 10^{-5}$ radians. The impinging velocities of the flyer are initialized by the method described in [Fowles et al. 1970]; the largest measured relative difference among the impact velocities is less than 2 percent. The Mn-Cu stress gauge technique [Ma 1998] is used to measure how the compressive stress varies with time at impact. Gauges are embedded at two interfaces of the collision system; one is in front of the specimen and another is behind it (see Figure 5). For each shot, a TPM3323 oscilloscope records two sets of compressive stress-time data. We use the data for analyzing the experimental results in the following section.

5. Experimental results and discussion

In the impact experiment, we conducted nine shots with the asymmetrical plate impact technique. We observed two different types of failure mechanisms when the impact velocity increased from 150 m/s to 210 m/s. At velocities less than 180 m/s, only crack fracture occurs. As the impact velocity is increased into the range of 190–210 m/s, a complex failure takes place involving both crack fracture and microcavity damage in the crack tip field. The former catches our attention in this article, but we may consider the latter in the future. This result shows that the failure behaviors are closely related to the loading rates.

Figure 6 shows the compressive stress-time profiles of two shots at the impact velocities of 173 m/s and 204 m/s. It is clear that the stress pulses last for less than a microsecond and approach very nearly the theoretical value 830 ns. The pulse rise time is less than 200 ns. In this figure, the curve with the higher peak stress is the input stress pulse measured at the interface between the transmission plate and the specimen, and the curve with lower peak stress is the output stress pulse measured at the interface between the specimen and the momentum trap. The dissimilarity between the two stress pulse profiles *a* and *b* (see Figure 6) implies that more mechanical energy flows into the specimen than out of it. Therefore, some mechanical energy is dissipated as the internal structure changes through microcrack formation, crack growth, plastic flow and microcavity damage. Note from the figure that a larger difference of the amplitudes of stress pulses usually presents before the peak compressive stress is reached. This indicates that dissipation of mechanical energy and change of material microstructure has already taken place during the first half of the stress pulses. At low impact speed (see Figure 6a), the similarity between the curves suggests that the stress pulses induce an elastodynamic response and only uncomplicated failure mechanisms such as crack growth occur; at high impact speed (see Figure 6b), the differing curves indicate that more complex failure mechanisms occur, involving not only crack growth, but also plastic softening and material damage. Ma and Duan [2000] report related results in detail.

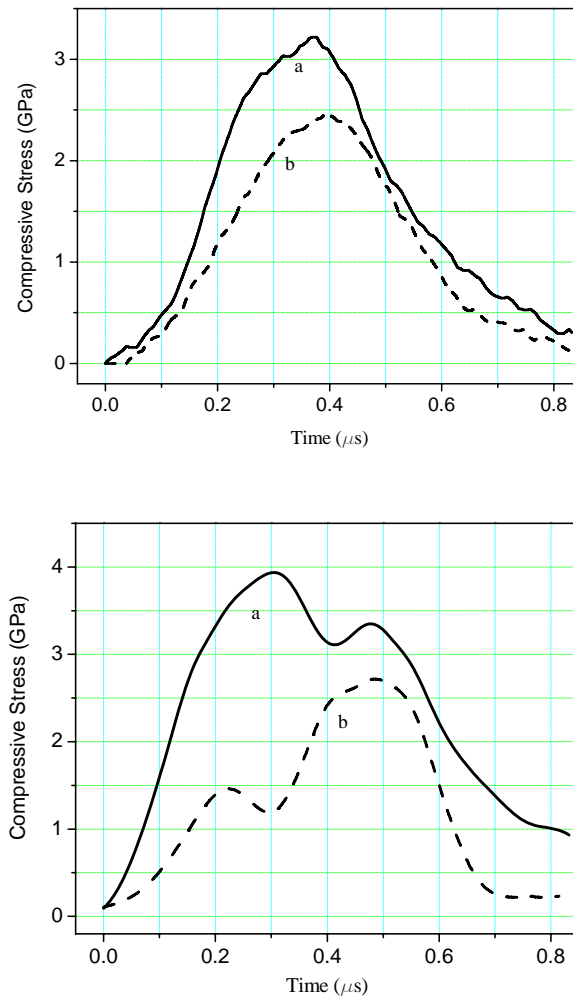


Figure 6. The compressive stress-time functions measured by Mn-Cu stress gauges, at impact velocities of 173 m/s (the first figure) and 204 m/s. The curve *a* represents the gauges embedded at the interface between the transmission plate and specimen, and the curve *b* is for gauges between the specimen and momentum plate.

Figure 7 shows the SEM images of the fracture surface when the impact speed was 173 m/s. The fracture surface consists of three distinct regions: a prenotched region, a dynamic fracture region, and a static fracture region. The uniform dynamic crack growth region suggests that a plane strain state at the extending crack tip prevails during impact. Figure 8 shows the corresponding SEM picture of the crack growth path, which has a straightforward interpretation as a discontinuous extension mechanism of moving cracks. Clearly, the crack grows in two stages. During the first, the crack begins to form at the notch tip on the impacting side and extends about 130 μm normal to the notch periphery before kinking. Because the loading rate is high enough, the stress intensity factor of the notch tip field reaches the material's fracture toughness and initiates a crack. Additionally, because the notch tip lacks surface

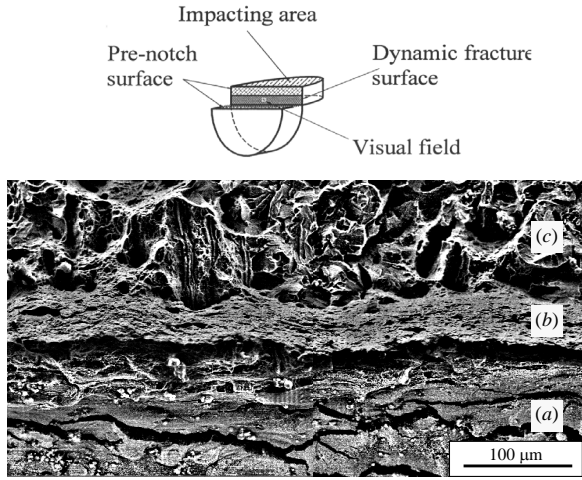


Figure 7. The SEM picture taken from the central region of the specimen fracture surface. The inset shows explicitly the fracture mechanism of the plane strain state at the crack tip.

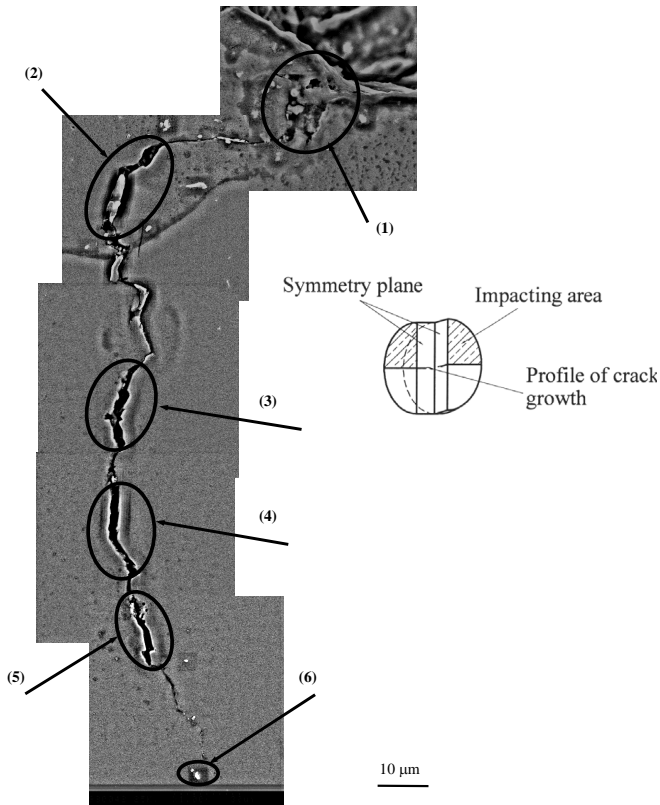


Figure 8. As seen under a microscope, the main crack interacting with the microcracks. The visual field is located in the sample's symmetry plane.

traction, the crack must be initiated by the hoop tensile stress, whose the intensity has gone beyond the yield limit, resulting in plastic softening. It seems clear that the cracks have started through the ductile initiation mechanism. This conclusion is also supported strongly by the residual opening displacement of the crack face indicated by the ellipse (1) in the figure. Moreover, in our prior impact experiments [Ma and Duan 2000], we have observed that the angle of crack initiation relative to the original prenotch line is approximately 55° , which does not deviate far from the location of crack initiation observed in [Ravi-Chandar 1995; Ravi-Chandar et al. 2000], nor from the point of maximum circumferential stress calculated by [Lee and Freund 1990]. Evidently, the geometry the notch tip and the mechanism of the plastic softening are responsible for the slight discrepancy. Furthermore, the crack extends approximately normally to the notch periphery. This suggests that the crack growth mechanism is dominated by mode I cracking at this time even though the intense compressive stress pulse generates a mixed-mode stress field at the crack tip. The first image in Figure 9 magnifies the fracture surface. Comparing the observed features with the static brittle features shown in Figure 3, we see that the crack growth behaviors exhibit obvious cleavage characteristics. Therefore, in this stage, the mode I crack begins and grows by different mechanisms, that is, by ductile initiation and brittle growth. The maximum hoop stress criterion [Ravichandran and Clifton 1989] causes these to mechanisms occur.

In the second stage, the growing crack changes its extension orientation from perpendicular to the notch periphery to compressive stress pulse propagation. That is, the crack grows along the original crack line on which shear stress is maximal. Hence, the maximum shear stress criterion now governs the

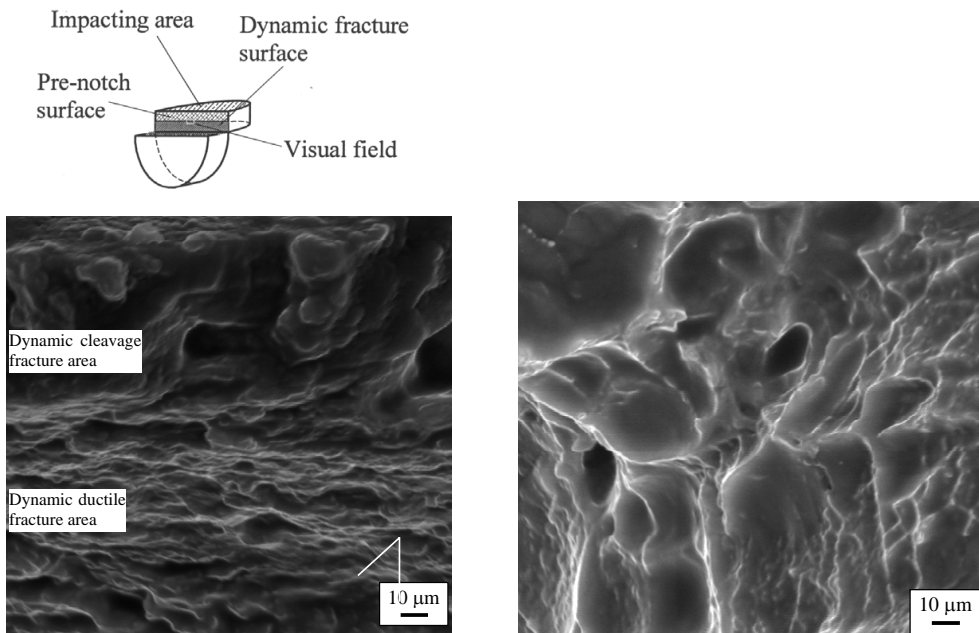


Figure 9. Microscopic image of the dynamic fracture surface after mode I cracking illustrates ductile cracking under asymmetrical impact conditions; the view field is above. The second image illustrates the same, but with mode II cracking.

crack extension. Microscopic images of the dynamic fracture surface (see the second image in Figure 9) show extensive dimpling and drawing, implying that ductile fracture has become the dominant failure mechanism. Actually, it is the large shear stress on the crack line that induces the heating and plastic softening. From the discussion above, we conclude that the crack fracture extension mode has undergone a transition from mode I to mode II, and the failure mode has also experienced a complex change from ductile initiation, to brittle growth, and back again to ductile growth, after the dominant stress driving the crack growth changes from the maximum hoop tensile stress at the crack tip to maximum shear stress along the crack line.

From the experimental results obtained above, we have seen that two crucial mechanisms of the crack growth need further attention. The first is the kinking phenomenon along a curved path. It should be noted from Figure 8 that the crack kinking occurs at the point where the mode I crack growth ends and the mode II crack growth starts, as indicated by the ellipse marked (2). On the one hand, the asymmetrical impact loading produces an elastic, perhaps following plastic, compressive stress pulse that propagates as a plane pulse in the impacted side of the specimen. When the pulse reaches the notch tip, an unloading tensile pulse is generated due to the dispersion the stress wave. Because the impact speed is high, the consequent tensile pulse is strong enough to induce mode I crack initiation and growth. As the energy dissipation needed for crack growth increases, the intensity of the hoop tensile stress decreases rapidly; in contrast, the shear stress intensity increases quickly. As the hoop stress becomes weaker than the shear stress, shear stress effects begin to dominate the crack growth. On the other hand, inherent flaws in the material, such as those marked by ellipse (2) Figure 8, can also potentially cause the crack to kink. At very least, these flaws favor crack kinking. Evidently, both the local mechanical field and the internal structure of the material can cause crack kinking.

The second crack growth mechanism is one of discontinuous extension. During the impact process, the precursor of the compressive stress pulse first makes the material flaws nucleate, grow, and develop into a number of microcracks. Then, the shear stress acting along crack line initiates and extends microcracks ahead of main crack. Finally, these microcracks develop into a series of macroscopic subcracks. Subsequently, the interaction and coalescence of these subcracks result in an unsteady advance of the main crack. This extension mechanism can be clearly seen from the crack growth path illustrated in Figure 8. Material flaws are marked by six ellipses numbered (1)–(6). These nuclei develop later into microcracks. At the bottom, mark (6) denotes a microcavity, near which the crack has arrested but not yet coalesced. This demonstrates that several mechanisms are active as the unsteady crack extends. For instance, when the main crack interacts with mature microcracks near the crack tip and coalesces with them, the remaining microcracks a bit farther from the crack tip simultaneously nucleate and grow due to the shear stress, and then the subsequent interaction and coalescence of the cracks result in the discontinuous crack growth. In the present example, the high intensity stress pulses have caused five subcracks to nucleate and grow, exhibiting the entire process of unsteady crack extension. In the low speed shots of our experimental study [Ma and Duan 2000] and other previous studies [Ravi-Chandar and Knauss 1984], authors observed and investigated theoretically [Abraham and Gao 2000; Needleman 1999] only the interaction between the main crack and one subcrack ahead of the crack tip. However, it is worthwhile to investigate the mechanisms of multiple subcrack nucleation and growth. We hope that more interesting mechanisms of crack growth will be revealed which would probably not be found when only studying the interaction between a main crack and a single subcrack.

6. Discontinuous transient crack growth model

During an asymmetrical impact of an edge crack plate specimen, the flyer’s kinetic energy is transformed into the total impact energy of the collision system in such a way that compressive stress pulses enter the specimen at the face hit by the flyer and exit from other face into the momentum trap (see Figure 5). This implies that both positive and negative work have been done on the specimen body during the impact. Precisely, the former is equal to the kinetic energy of flyer and the latter is the kinetic energy of the momentum trap. Clearly, the net work adds to the internal energy of the material and dissipates through mechanisms such as crack growth, plastic deformation, and material damage. The energy equilibrium condition for the process [Freund 1990] is

$$\int_{t_1}^{t_2} \int_{S_1} \sigma_{ij}^{(1)} n_j \frac{\partial u_i^{(1)}}{\partial \tau} dS_1 d\tau - \int_{t_1}^{t_2} \int_{S_2} \sigma_{ij}^{(2)} n_j \frac{\partial u_i^{(2)}}{\partial \tau} dS_2 d\tau = \int_{t_1}^{t_2} F_C d\tau, \tag{6-1}$$

where S_i ($i = 1, 2$) are the plane curves around the areas affected by the compressive stress pulses $\sigma^{(i)}$. $\Delta t = t_2 - t_1$ is the pulse time interval. The two terms on the left side of the equal sign in Equation (6-1) represent the positive and negative work done by the stress pulse in the interval, and therefore, the right side becomes the net work and is equal to the total energy dissipated in the specimen as the material responds to the dynamic loading. If we are only considering the crack growth mechanism and neglecting other energy dissipation mechanisms such as plastic deformation and material heating, the integrated function F_C is the instantaneous rate of energy flow toward the crack tip contour C through a small contour around it. The energy dissipation rates can be determined from the energy equilibrium relation Equation (6-1) and the compressive stress-time curves (see Figure 6). They are shown in Figure 10. The figure shows that the energy dissipates in four stages. The first corresponds to rapid energy dissipation (O–A in Figure 10), which suggests that not only the first subcrack initiates and grows but that other subcracks, such as the second and third, also initiate and advance, one after the other. Hence,

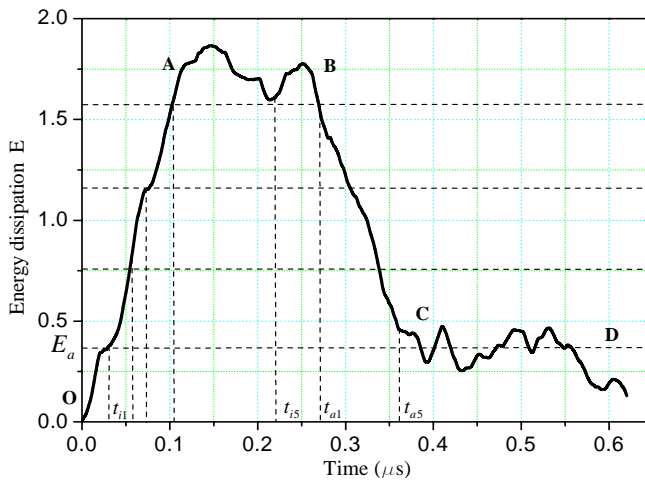


Figure 10. The energy dissipation rates are obtained from the measured stress pulse time series.

a great quantity of energy dissipates through the crack forces. In the second stage (A–B in Figure 10), the energy dissipation becomes much more stable, implying either that no new subcracks form or that some do but arrest immediately. In the third stage (B–C in Figure 10), an abrupt decrease in energy dissipation implies that the subcracks have coalesced and the main crack has stalled in the specimen. In the last stage (C–D in Figure 10), energy dissipates at a constant low level, suggesting the process of crack growth has stopped. The energy put into crack initiation and growth is mainly associated with the first three stages of the energy dissipation process.

The main, rapidly propagating crack consists of five subcracks with lengths l_k ($k = 1, 2, \dots, 5$) (see Table 1). For simplicity, we assume that the subcracks grow at constant velocity after they form and dissipate energy each in proportion to its length. Thus, each subcrack grows steadily, but the main crack advances unsteadily with nonuniform velocities due to the different initial time and growth rate of each subcrack. Each subcrack dissipates energy G_k :

$$G_k = C_k \int_{t_k^i}^{t_k^a} [E(t) - E_a] dt, \quad C_k = l_k/l, \tag{6-2}$$

where $E(t)$ is the current rate of energy dissipation of crack growth. E_a and l are the rate of energy dissipation of the crack arrest and the length of the main crack. If the critical energy release rates for crack initiation are assumed to be equal to those of the crack arrest fracture energy, then the initiation times t_k^i ($k = 1, 2, \dots, 4$) of the first four subcracks can be determined from the energy dissipation in Figure 10, and the corresponding ending times of subcrack growth, t_k^a ($k = 1, 2, \dots, 4$), can be determined by integrating the equations for dynamic crack tip motion Equation (2–1) and using the relation (6–2) as

$$\frac{1 - \mu^2}{E} \int_{t_k^i}^{t_k^a} [A_I(v)K_I^2 + A_{II}(v)K_{II}^2]v dt = \Gamma_k, \tag{6-3}$$

Experimental results in this study		Results based on the dynamic fracture theory [†]			Results obtained from the elastodynamic problem ^{††}		
No. (k)	l_k (mm)	V_k^a (mm/ μ s)	t_k^i (ns)	Δt_k (ns)	V_k^a (mm/ μ s)	t_k^i (ns)	Δt (ns)
1	0.132	1.34	168	98.51	1.59	168	83.02
2	0.128	1.47	198	87.10	1.77	198	72.32
3	0.048	2.82	220	17.02	2.49	220	18.28
4	0.068	2.73	245	24.91	2.21	245	30.77
5	0.076	2.54	352	29.92	1.97	337	38.58

Table 1. Characteristic parameters of each subcrack. Here the l_k ($k = 1, 2, \dots, 5$) are the lengths of five subcracks. t_k^i , V_k^a , and Δt_k are the initial time, average velocities, and interval of time for growth of each subcrack. [†][Freund 1990]; ^{††}[Lee and Freund 1990].

for $k = 1, 2, \dots, 5$, where $\Gamma_k = G_k/l_k$ is the mechanical energy flowing into the subcrack tip per unit crack advance length. For the last subcrack, the arrest time t_5^a can be determined directly from Figure 10, and its initiation time t_5^i can be obtained from (6–3). Table 1 shows the results.

Figure 11 shows the lengths of the subcracks and the positions of the main crack tip at times, t_k^i , ($k = 1, 2, \dots, 5$). The first shows results of the dynamic fracture theory [Freund 1990], and the second shows analytic results of the idealized elastodynamic problem [Lee and Freund 1990]. As the first subcrack is advancing (with an average velocity of V_1^a), the compressive stress pulses propagating at the longitudinal wave speed 6020 m/s arrive at the initial location of the second subcrack, causing it to initiate at time t_2^i . This implies that, on the macroscopic scale, the main crack grows suddenly longer and

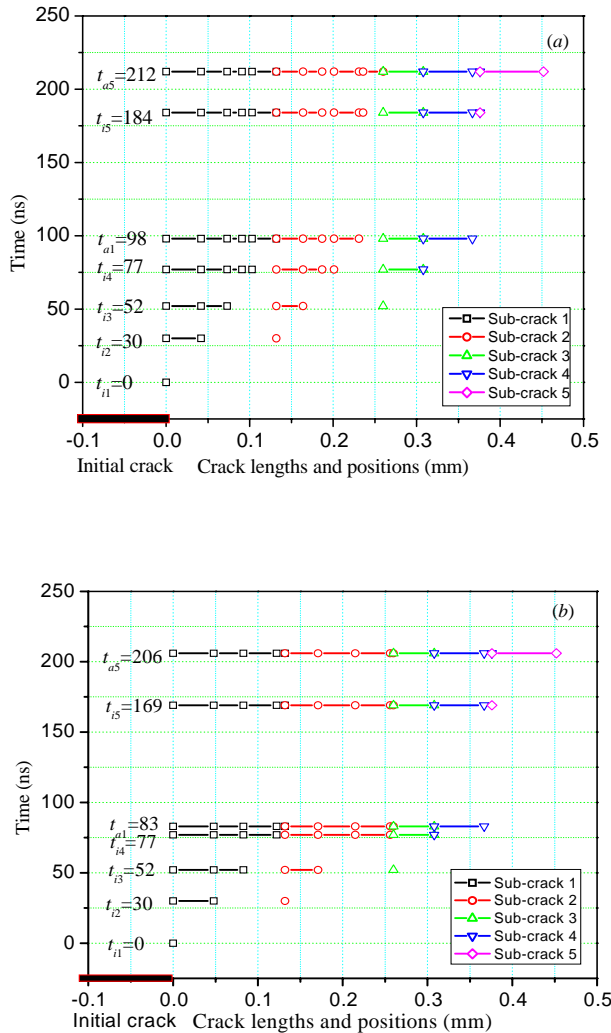


Figure 11. The lengths of the subcracks and the site of the main crack tip at characteristic times. (a) displays the analytic results from classical dynamic fracture theory and (b) is that of Lee and Freund [1990].

the growth velocities jump discontinuously from slow to fast. Note that, at this time, the second subcrack tip replaces the first subcrack tip to become the main crack tip. In the same way, subsequent initiation and growth of other subcracks induce crack growth velocity jumps. By assuming that the behavior of each subcrack follows from the elastodynamic theory of continuum mechanics, we explain the unsteady growth of the main crack by some interesting features in the history of the extension velocities.

By fitting results in Figure 11 to curves, we can obtain crack tip positions as a function of time. By differentiating, we find speed versus time, illustrated in Figure 12. At t_1^i , crack growth begins. Only the first subcrack has started. Its uniform speed V_1^a completely determines the overall growth rate and the initiation of the main crack. Then, as other subcracks begin to form and grow, the main crack grows faster and more erratically: its speed goes from constant subsonic speeds less than Rayleigh wave speed c_R to nonuniform intersonic speeds higher than shear wave speed c_s . After that, some of the subcracks stop growing, but a few that extend continuously into the main crack continue to grow steadily for about 100 ns at an intersonic speed near $\sqrt{2}c_s$. Finally, when the first several subcracks stop advancing and coalesce, the main crack growth is completely governed by the last, unsteadily growing, subcrack. The extending speed quickly decreases to subsonic levels, and the cracking ceases.

The theoretical and numerical simulation studies [Needleman 1999; Rosakis et al. 1999; 2000; Abraham and Gao 2000; Geubelle and Kubair 2001] have shown two key characteristics of intersonic crack growth: (i) if crack growth speed is between c_R and c_s , the energy release rate of the moving crack tip is negative, and elastodynamic fracture energy theory cannot describe the mechanisms of unsteady intersonic crack growth; (ii) the steady growth speed of a mode II crack should be either subsonic (that is, lower than c_R) or intersonic (higher than the c_s), but stable intersonic growth speed will consistently come close to a constant speed of about $\sqrt{2}c_s$. Based on the discontinuous crack growth model, we can conclude that the initial compressive stress pulses control the subcrack initiation. Actually, whether the subcrack can initiate under asymmetrical impact loading depends completely on the energy flux toward the crack tip, that is, the intensity of the stress pulse. The initial time is closely related to the propagation speed of the stress pulse. Here, the compressive stress pulse propagates at the longitudinal wave speed,

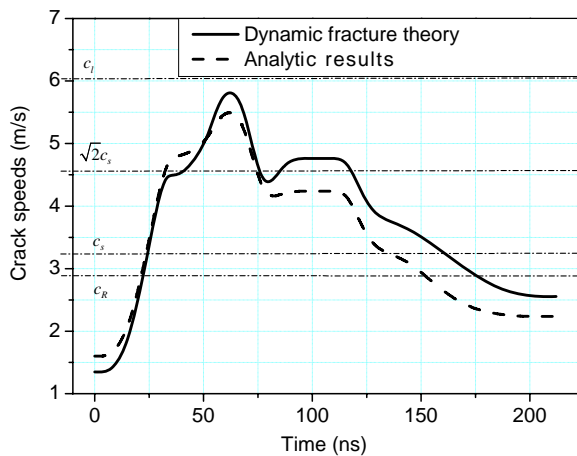


Figure 12. The speed-time profiles of the main crack growth from the interacting transient cracking model.

which in all probability makes the subcracks initiate continuously in short time intervals competing with the arrival of the longitudinal wave. Hence, the continuous initiation and growth mechanisms of several subcracks ahead of the crack tip lead to an extremely rapid increase of the crack growth speed, which is responsible for the transition from subsonic to intersonic.

Generally, the theory of continuum mechanics can effectively predict the growth of a single crack; however, it is too limited to explain the simultaneous initiation and growth of several cracks. This is possibly the source of the nonsensical negative energy release rate. However, using the discontinuous crack growth model put forward here, this nonsense is straightforwardly and reasonably interpreted. Moreover, we have seen that the successive growth and coalescence among the subcracks make the main crack grow steadily at intersonic speeds of about $\sqrt{2}c_s$, but the reason for this specific speed cannot yet be understood clearly through qualitative analysis based on the discontinuous crack growth model. Quantitative understanding of intersonic crack growth will require more delicate and profound theoretical analysis and numeral simulation. In conclusion, the discontinuous transient crack growth model can explain very well why the crack growth speed quickly increases from subsonic to intersonic and can at least qualitatively describe the various features of the intersonic crack growth.

7. Conclusion and remarks

We summarize as follows:

- (1) We developed a recoverable plate impact experiment with loading rate of $10^8 \text{ MPa m}^{1/2}\text{s}^{-1}$ for studying the mechanisms of the shear dominated crack extension. Using this technique, we can generate a single compressive stress pulse of submicrosecond duration and produce a plane strain deformation field at a mode II crack tip in the edge crack plate specimen.
- (2) The dynamic fracture testing results of Hard-C 60[#] steel indicate that the stress pulse can induce several microcracks ahead of the crack tip to nucleate and grow simultaneously and to finally develop into macroscopic subcracks. The interaction and coalescence of these subcracks is responsible for unsteady extension of the shear dominated cracks. We inferred failure mode transitions, both from a mode I to mode II crack and from cleavage to ductile fracture.
- (3) We established a discontinuous transient crack growth model and analyzed the unstable extension of the shear dominated cracks with discontinuously varying extension speeds. The model describes qualitatively the main characteristics of the intersonic crack extension, such as the forbidden speed region between c_R and c_s , and the steady limit speed $\sqrt{2}c_s$ when the crack growth rates increase from subsonic to intersonic. The results show that transient mechanisms such as the nucleation, interaction and coalescence among the subcracks cause the main crack extension speed to rapidly exceed the forbidden speed and that subsequent stable growth of subcracks cause the intersonic growth of the main crack.

Acknowledgements

We extend our gratitude for many helpful discussions and guidance on English writing to Professor Keren Wang and Professor Lanhong Dai of the Institute of Mechanics in the Chinese Academy of Sciences.

References

- [Abraham and Gao 2000] F. F. Abraham and H. Gao, "How fast can crack propagate?", *Phys. Rev. Lett.* **84**:14 (2000), 3113–3116.
- [Achenbach 1973] J. D. Achenbach, *Wave propagation in elastic solids*, North-Holland, Amsterdam, 1973.
- [Cox et al. 2005] B. N. Cox, H. Gao, D. Gross, and D. Ritted, "Modern topics and challenges in dynamic fracture", *J. Mech. Phys. Solids* **53**:3 (2005), 565–596.
- [Erdogan and Sih 1963] F. Erdogan and G. C. Sih, "On the crack extension in plates under plane loading and transverse shear", *J. Basic Eng. (Trans. ASME)* **85**:4 (1963), 519–527.
- [Fowles et al. 1970] G. R. Fowles, G. E. Duvall, J. Asay, P. Bellamy, F. Feismann, D. Grady, T. Michaels, and R. Mitchell, "Gas gun for impact studies", *Rev. Sci. Instrum.* **41**:7 (1970), 984–996.
- [Freund 1990] L. B. Freund, *Dynamic fracture mechanics*, Cambridge University Press, Cambridge, NY, 1990.
- [Geubelle and Kubair 2001] P. H. Geubelle and D. V. Kubair, "Intersonic crack propagation in homogeneous media under shear-dominated loading: numerical analysis", *J. Mech. Phys. Solids* **49**:3 (2001), 571–587.
- [Kalthoff 1987] J. F. Kalthoff, "Shadow optical analysis of dynamic shear fracture", pp. 16–21 in *Proc. int. conf. on photo-mechanics and speckle metrology*, San Diego, CA, Aug. 1987.
- [Kalthoff 1988] J. F. Kalthoff, "Shadow optical analysis of dynamic shear fracture", *Opt. Eng.* **27** (1988), 835–840.
- [Kalthoff 1990] J. F. Kalthoff, "Transition in the failure behavior of dynamically shear loading cracks", *Appl. Mech. Rev.* **43**:5 (1990), S247–S250. Part. 2.
- [Lee and Freund 1990] Y. J. Lee and L. B. Freund, "Fracture initiation due to asymmetric impact loading of an edge cracked plate", *J. Appl. Mech. (Trans. ASME)* **57** (1990), 104–111.
- [Ma 1998] W. Ma, *Experimental and theoretical studies on the dynamic fracture toughness of materials under pressure-shear combined stress waves*, PhD thesis, Institute of Mechanics of CAS, 1998.
- [Ma and Duan 2000] W. Ma and Z. Duan, "The investigation on dynamic fracture behavior of materials under compressive-shear combined stress waves", *Acta Mech. Sin.* **16**:4 (2000), 335–346.
- [Needleman 1999] A. Needleman, "An analysis of intersonic crack growth under shear loading", *J. Appl. Mech. (Trans. ASME)* **66**:4 (1999), 847–857.
- [Prakash and Clifton 1992] V. Prakash and R. J. Clifton, "Experiment and analytical investigation of dynamic fracture under conditions of plane strain", pp. 412–444 in *Fracture mechanics: twenty-second symposium*, edited by H. A. Ernst et al., ASTM STP 1131, Philadelphia, 1992.
- [Raiser et al. 1990] G. Raiser, R. J. Clifton, and M. Ortiz, "A soft-recovery plate impact experiment for studying microcracking in ceramics", *Mech. Mater.* **10**:1-2 (1990), 43–58.
- [Ravi-Chandar 1995] K. Ravi-Chandar, "On the failure mode transitions in polycarbonate under dynamic mixed-mode loading", *Int. J. Solids Struct.* **32**:6/7 (1995), 925–938.
- [Ravi-Chandar and Knauss 1984] K. Ravi-Chandar and W. G. Knauss, "An experimental investigation into dynamic fracture, I: crack initiation and arrest", *Int. J. Fracture* **25**:4 (1984), 247–262.
- [Ravi-Chandar et al. 2000] K. Ravi-Chandar, J. Lu, B. Yang, and Z. Zhu, "Failure mode transitions in polymers under high strain rate loading", *Int. J. Fracture* **101**:1-2 (2000), 33–72.
- [Ravichandran and Clifton 1989] G. Ravichandran and R. J. Clifton, "Dynamic fracture under plane wave loading", *Int. J. Fracture* **40**:3 (1989), 157–201.
- [Rosakis et al. 1999] A. J. Rosakis, O. Samudrala, and D. Coker, "Crack faster than the shear wave speed", *Science* **284**:5418 (1999), 1337–1340.
- [Rosakis et al. 2000] A. J. Rosakis, O. Samudrala, and D. Coker, "Intersonic shear crack growth along weak planes", *Mater. Res. Innov.* **3**:4 (2000), 236–243.
- [Samudrala et al. 2002] O. Samudrala, H. Huang, and A. J. Rosakis, "Subsonic and intersonic mode, II: crack propagation with a rate-dependent cohesive zone", *J. Mech. Phys. Solids* **50**:6 (2002), 1231–1268.

[Zhou et al. 1996] M. Zhou, A. J. Rosakis, and G. Ravichandran, “Dynamically propagating shear bands in impact-loaded prenotched plates, I: Experimental investigations of temperature signatures and propagation speed”, *J. Mech. Phys. Solids* **44:6** (1996), 981–1006.

Received 19 Jun 2006. Revised 30 May 2007. Accepted 31 May 2007.

WEI MA: watwm@imech.ac.cn

Institute of Mechanics, Chinese Academy of Sciences, 15 Beisihuanxi Road, Beijing 100080, China

ZHUPING DUAN: zpduan@imech.ac.cn.

Institute of Mechanics, Chinese Academy of Sciences, 15 Beisihuanxi Road, Beijing 100080, China

ANISOTROPIC STRESS STATE AROUND INTERNALLY PRESSURIZED MICROCHANNELS

YONG XUE GAN

This work derives internal pressure induced stresses in material imbedded with square-shaped microchannels. The first part provides background on microchanneled materials at micro and nanoscale to motivate investigating the stress and deformation states. The second part develops a simplified model to characterize the plastic flow and/or motion of dislocations within crystalline, microchanneled materials. The model helps identify slip bands around the channels under plane strain deformation conditions. The third part derives solutions to the stress states around the microchannels, obtaining closed form solutions which hold for regions containing and away from the channel boundary. Figures depict the stress solutions in both physical and stress space. The results predict nonuniform deformation states around the channels and also reveal the yield conditions associated with the plastic flow along different slip bands. The work concludes with case studies on the stress states of microneedles containing square microchannels for applications such as fluid injection, nanofiber growth, and cell registration.

1. Introduction

Microchannels and arrays of channels function as important components in many microscale and nanoscale systems [Allen 2005]. For example, microchannels and their arrays can be fabricated for molecular sieves, particle filters, capillary pores, or nutrient delivery units. Microchannels have also been used for chemical reaction flow beds, nanoimprinting molds, ink jets, and templates for synthesis of nanofibers. Fabrication technology for microfluidic channels has been extensively studied [Franssila 2004]. To make a microchannel, it is very common to sandwich a sacrificial photoresist layer between two layers. Supporting posts may be added into the photoresist to allow larger embedded features, as shown by Hwang and Song [2007]. After photolithography, microchannels form from selective dissolution of the photoresist [Senturia 2001].

Many publications explore new technology for fabricating microchannels. A three dimensional manufacturing process has been developed to make embedded microchannels using scanning laser systems, as shown by Lee et al. [2003], Li et al. [2004], Yu et al. [2004], Yu et al. [2006a], and Yu et al. [2006b]. The authors discussed potential ways to manipulate and position cells using suction forces. Recently, Ziegler et al. [2006] fabricated neural probes with built-in microfluidic channels by micromolding and thermal bonding of Parylene without using a photoresist. The probes containing the fluidic channels were tested for delivering small amounts of drugs into biological tissue as well as for neural recording.

Keywords: microchannel, anisotropic deformation, stress field, plastic flow, nanocrystalline material.

This work is supported by The Durbin Faculty Development Grant from The Cooper Union for the Advancement of Science and Art.

One issue confronting microchannels is mechanical deformation. Engineers must ensure that the channels maintain a constant size, even as they are put through the rigors of their various applications. For microchannels used for inkjet printing, biofluid printing, fuel injection, drug delivery, or integrated circuits (IC), dimensional stability requires good cooling. A constant size is also required to successfully register a single cell in a microwell or channel. And, when using microchannels for bioparticle registration [Zhe et al. 2007] or microinjection [Lu et al. 2007], controlling their size is necessary for accurate counting or medicine delivery.

Microchannels in devices such as microfluid droplet injectors are typically under under both thermal and internal compressive loads, as addressed by Tseng et al. [2002a] and Tseng et al. [2002b]. These loads can cause single channels to deform in a way the could significantly influence the performance of the entire channel array structure, in view of hydraulic cross-talk, flow resistance and fluid accumulation. In microfluidic devices, the stresses around the microchannels come from other sources, such as fluid pressure, electric potential, van der Waals, and capillary forces. Sidewall contact friction, as described by Timpe and Komvopoulos [2006], may also cause the stresses to redistribute around the microchannels. Predicting the deformation state around a microchannel requires determining the stress field.

The problem of microcavities in isotropic plastic materials has caught much attention because of their importance in fracture mechanics. For example, Tvergaard and Hutchinson [2002] analyzed numerically a two-dimensional plane strain model with multiple discrete cavities and found that cavity interaction determines the threshold for crack initiation and their resistance to growth. Lubarda et al. [2004] studied how cavities grow by emitting dislocations and proposed an onset criterion for such events at the surface of a cavity under remote tension. They also calculated, for any initial cavity size, the critical stress for emitting a single dislocation or a dislocation pair. They found that the critical stress decreases with increasing cavity size and also found that dislocations with a wider core are more likely to be emitted than ones with a narrow core.

Many factors influence the growth of cavities in elastic-plastic crystalline solids, for example, plastic anisotropy [O'Regan et al. 1997] and crystallographic orientation [Schacht et al. 2003]. The length-scale effect in plastic deformation has also been found in the growth of microcavities [Fleck et al. 1994]; the nonlocal elastic-plastic material model reveals that the rate of cavity growth decreases significantly when the cavities are shrunk to sizes approaching the characteristic length of the material [Tvergaard and Niordson 2004]. The cavity size distribution also affects the crack growth rate [Needleman and Tvergaard 1991]. Huang et al. [1991] and Tvergaard [1991] have addressed cavitation instabilities in elastic-plastic solids.

Using the formalism of anisotropic slip line theory, Kysar et al. [2005] derived the stress state in a cylindrical void due to far-field external compression. In recent work [Gan and Kysar 2007], we presented the solutions to the stresses from both internal pressure and far-field loading. In addition, we obtained experimental and simulation results to validate the theory predicting the deformed state in materials containing microcavities [Gan et al. 2006]. In fabricating microelectromechanical systems (MEMS) and nanoelectromechanical systems (NEMS) in single crystalline materials such as Si, Cu, Ni, Ag, Au, and Pd, sharp-cornered channels may form because of anisotropic etching [Senturia 2001]. Understanding the deformation of materials containing such channels — which will entail studying the anisotropic stress states around them — will be helpful for MEMS and NEMS design.

This work uses a simplified plastic flow model to derive stresses near square-shaped microchannels. We determine slip bands around the channels in materials under plane strain deformation conditions and establish different stress zones associated with the active slip of two systems. We derive closed-form solutions in stress zones that either contain or are away from the channel inner boundary. The stress solutions are plotted in both physical space and stress space. The results will be used to analyze the deformation state around the microchannels. Finally, we give stress maps of microneedles containing square shaped microchannels.

2. Plasticity analysis

2.1. Slip model. If the matrix material containing microchannels has a well defined yield point, the plastic flow analysis of Nadai [1950] will determine the stress state in the infinitesimal control volume containing the boundary point O shown in Figure 1a. Define x - y coordinates so that the x -axis is parallel to the internal pressure. Also define local ξ - η coordinates so the ξ -axis follows the plastic flow. The ξ - η coordinates define the principal stresses of the problem. The maximum normal stress σ_m is parallel to the η -axis, and the maximum shear stress τ_m is along the ξ -axis.

Assuming that the angle between x and ξ is ϕ , the principal stress components are

$$\sigma_m = -\frac{p}{2} [1 - \cos(2\phi)], \quad \tau_m = -\frac{p}{2} \sin(2\phi).$$

Define $-\epsilon_{xx}$ as the compressive plastic strain in the η direction. Assuming incompressibility, the materials expands in all other directions, and the magnitude of strain due to the expansion must be $\epsilon_{xx}/2$. If the pressure along the entire boundary NT is uniform, as shown in Figure 1b, the normal strain along the

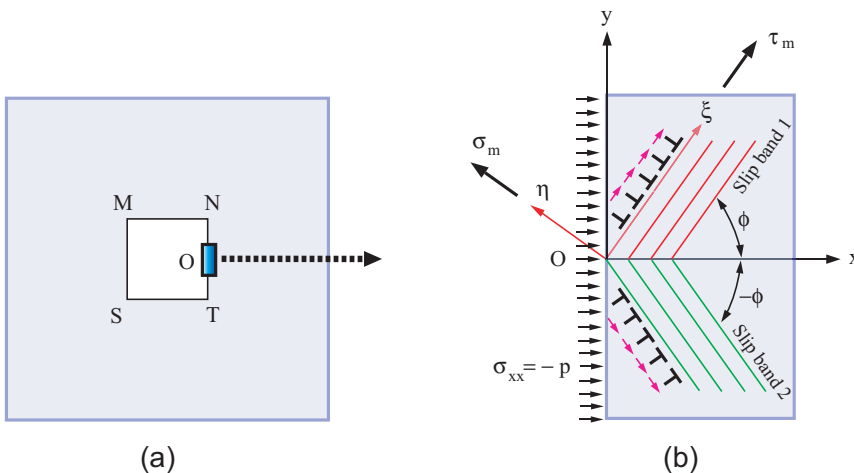


Figure 1. Schematic of a microchannel and the deformation state: (a) square microchannel, (b) magnified region around point O showing the slip in the material under internal pressure.

η -axis, ϵ_m , and the shear strain along the ξ -axis, γ_m , are

$$\epsilon_m = \frac{\epsilon_{xx}}{4} [1 + 3 \cos(2\phi)], \quad \gamma_m = \frac{3\epsilon_{xx}}{4} \sin(2\phi).$$

In this problem, we consider slip to be the major plastic deformation mechanism. The plastic flow along the ξ -axis results in vanishing net normal strain, that is

$$\epsilon_m = \frac{\epsilon_{xx}}{4} [1 + 3 \cos(2\phi)] = 0,$$

from which $\cos(2\phi) = -1/3$ and $\phi = 54.7^\circ$. By symmetry, another solution $\phi = -54.7^\circ$ holds in the quadrant with $y < 0$ and $x > 0$, as schematically shown in Figure 1b. Also by symmetry, we obtain the distribution of all the slip bands around the microchannel, as shown in Figure 2. From Figure 2, only one slip band exists in each half-quadrant, that is, only one slip system is active. For example, in the angular region $0 \leq \theta \leq \pi/4$, slip system 1 is active, while in $\pi/4 \leq \theta \leq \pi/2$, only slip system 2 is active, and so forth. According to Rice [1973], if the single slip condition holds, the two families of slip lines form mutually orthogonal nets. Slip lines parallel to the slip direction are defined as α -lines; and those normal to the slip plane are called β -lines. In this case, the α -lines are along the ξ -axis, while the β -lines are along the η -axis.

2.2. Yield surface. Schmid’s Law for a single split system describes the state just before it yields:

$$\mathbf{n} \cdot \boldsymbol{\Sigma} \cdot \mathbf{s} = \pm \tau, \tag{1}$$

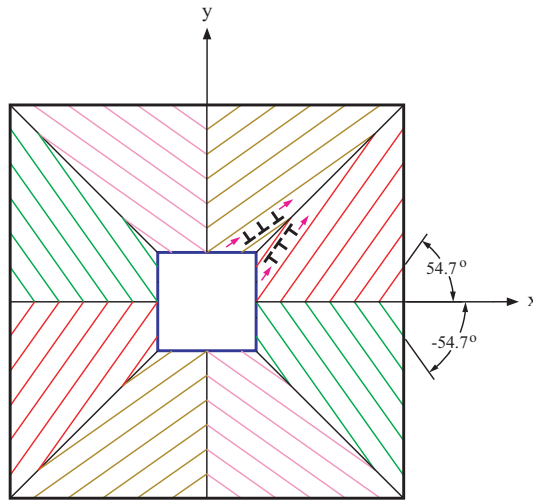


Figure 2. Illustration of the slip bands around the microchannel.

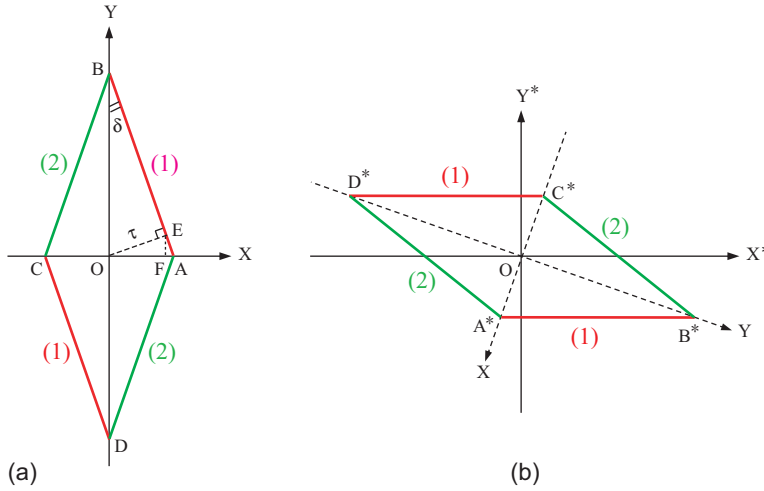


Figure 3. Yield surface associated with the two active slip systems: (a) yield surface without rotation, (b) rotated yield surface.

where τ is the shear strength, \mathbf{n} is the surface normal of the slip plane, \mathbf{s} is a unit vector along the slip direction, and Σ is the stress tensor given in rectangular coordinates as

$$\Sigma = \begin{pmatrix} \sigma_{xx} & \sigma_{xy} & \sigma_{xz} \\ \sigma_{yx} & \sigma_{yy} & \sigma_{yz} \\ \sigma_{zx} & \sigma_{zy} & \sigma_{zz} \end{pmatrix}. \quad (2)$$

We denote the rectangular components of \mathbf{n} and \mathbf{s} by (s_x, s_y, s_z) and (n_x, n_y, n_z) . Because we consider here deformation under the plane strain conditions, the slip occurs within the x - y plane, and $s_z = 0$. For the plane strain state, $\sigma_{xz} = \sigma_{zx} = 0$ and $\sigma_{yz} = \sigma_{zy} = 0$. Also, because the stress tensor is symmetric, $\sigma_{xy} = \sigma_{yx}$.

Fully written out in components, Equation (1) reads

$$n_x \sigma_{xx} s_x + n_y \sigma_{yx} s_x + n_x \sigma_{xy} s_y + n_y \sigma_{yy} s_y = \pm \tau,$$

or, rearranging,

$$n_x s_x \sigma_{xx} + n_y s_y \sigma_{yy} s + (n_x s_y + n_y s_x) \sigma_{yx} = \pm \tau.$$

The components of \mathbf{s} and \mathbf{n} are expressed in the slip angle ϕ as

$$\begin{aligned} s_x &= \cos \phi, & s_y &= \sin \phi, \\ n_x &= -s_y = -\sin \phi, & n_y &= s_x = \cos \phi, \end{aligned}$$

and the yield condition becomes either of

$$\sin(2\phi) \frac{\sigma_{xx} - \sigma_{yy}}{2} + \cos(2\phi) \sigma_{xy} = \pm \tau \quad \text{or} \quad \sigma_{xy} = \tan(2\phi) \frac{\sigma_{xx} - \sigma_{yy}}{2} \pm \frac{\tau}{\cos(2\phi)}. \quad (3)$$

Let $X = (\sigma_{xx} - \sigma_{yy})/2$ and $Y = \sigma_{xy}$. The yield functions as defined by Equation (3) can be plotted in the stress space or Π -plane with X as the abscissa and Y as the axis. The function can be used to

Vertex	A	B	C	D
$X \left(\frac{\sigma_{xx} - \sigma_{yy}}{2\tau} \right)$	$\frac{3\sqrt{2}}{4}$	0	$-\frac{3\sqrt{2}}{4}$	0
$Y \left(\frac{\sigma_{xy}}{\tau} \right)$	0	3	0	-3

Table 1. Yield surface vertices on (left) X - Y plane and (right) the X^* - Y^* plane.

define a yield surface shown in Figure 3a and derived as follows. Obviously, two parallel lines define the yield condition for the active slip of slip system 1 with the angle ϕ . The slope of the two lines is $\tan(2\phi)$, and the two lines intercept the Y -axis at $\pm\tau / \cos(2\phi)$. Similarly, for the slip system with the slip angle $-\phi$, slip system 2, the yield surfaces are represented by another two lines with slope $-\tan(2\phi)$ and intercepting the Y -axis at $\pm\tau / \cos(2\phi)$. Altogether, these four lines draw the diamond shape shown in the figure. Table 1 lists the coordinates of the diamond’s vertices.

In a local ξ - η coordinate system with the ξ -axis along the slip direction \mathbf{s} and the η -axis along the slip plane normal \mathbf{n} , the yield surface is obtained by rotating clockwise by 2ϕ the original yield surface in the Π -plane. Figure 3b shows the rotated yield surface plotted on the Π^* -plane with X^* as the abscissa and Y^* as the axis. Table 2 lists the vertices.

We will use these results from the analysis of yielding for solving the stresses in Section 3.

3. Stress field solution

3.1. Boundary condition. Because the inner surface of the microchannel is under compression, we have at point O that $\sigma_{xx} = -p$, where p is the internal pressure. As an approximation, we assume that this boundary condition propagates into the inner vertical wall of the channel. We assume that $\sigma_{xy} = 0$ on the inner wall because the free surface condition holds. However, σ_{yy} needs to be determined from the yield conditions. We note that the sign before τ in the right hand sides of Equation (3) should be positive because the compressive state inside the channel implies $(\sigma_{xx} - \sigma_{yy})/2 < 0$. Thus, the stress state at point O in the x - y physical space corresponds to point C in the X - Y stress space.

Vertex	A*	B*	C*	D*
$X^* \left(\frac{\sigma_{xx} - \sigma_{yy}}{2\tau} \right)$	$-\frac{1}{2\sqrt{2}}$	$2\sqrt{2}$	$\frac{1}{2\sqrt{2}}$	$-2\sqrt{2}$
$Y^* \left(\frac{\sigma_{xy}}{\tau} \right)$	-1	-1	1	1

Table 2. Yield surface vertices on the X^* - Y^* plane.

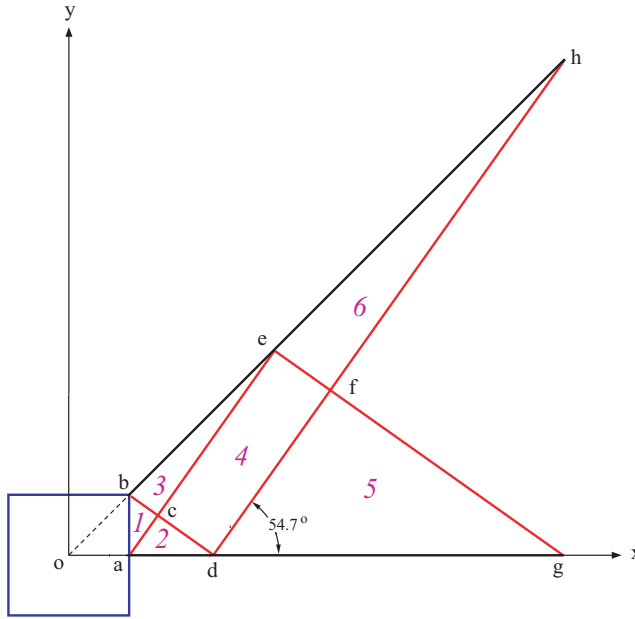


Figure 4. Typical stress zones in the angular region $0 \leq \theta \leq \pi/4$.

Once the sign before τ in Equation (3) is known, the stress component σ_{yy} can be found from a simplified yield condition, that is,

$$\sigma_{xy} = \tan(2\phi) \frac{\sigma_{xx} - \sigma_{yy}}{2} + \frac{\tau}{\cos(2\phi)}.$$

Substituting σ_{xx} and σ_{xy} into this equation and solving for σ_{yy} yields

$$\sigma_{yy} = \frac{\tau}{\sin(2\phi)} - p.$$

Therefore, the boundary conditions can be expressed as

$$\sigma_{xx} = -p, \quad \sigma_{yy} = \frac{\tau}{\sin(2\phi)} - p, \quad \sigma_{xy} = 0.$$

In polar coordinates, the stress components on the boundary are

$$\sigma_{rr} = \sigma_{xx} \cos^2 \theta + \sigma_{yy} \sin^2 \theta + \sigma_{xy} \sin(2\theta) = \frac{2\tau \sin^2 \theta}{\sin(2\phi)} - p,$$

$$\sigma_{\theta\theta} = \sigma_{xx} \sin^2 \theta + \sigma_{yy} \cos^2 \theta - \sigma_{xy} \sin(2\theta) = \frac{2\tau \cos^2 \theta}{\sin(2\phi)} - p,$$

$$\sigma_{r\theta} = -\frac{1}{2}(\sigma_{xx} - \sigma_{yy}) \sin(2\theta) + \sigma_{xy} \cos(2\theta) = \frac{\tau \sin(2\theta)}{\sin(2\phi)}.$$

Vertex	x -position	y -position
a	1	0
b	1	1
c	$1 + \sqrt{2}/3$	$2/3$
d	$1 + \sqrt{2}$	0
e	$2 + \sqrt{2}$	$2 + \sqrt{2}$
f	$2 + 5\sqrt{2}/3$	$4/3 + \sqrt{2}$
g	$4 + 3\sqrt{2}$	0

Table 3. Stress zone vertices.

3.2. Stress zones. The analysis of plastic flow and slip band in Section 2.1 implies the region around the microchannel can be divided into discrete zones as shown in Figure 4. In each zone, the stresses show similar properties. For example, in stress zone 1, the stresses are influenced by the boundary conditions given in Section 3.1. Stress zone 2 is adjacent to stress zone 1, and all the points in the two zones share the same β -line. Stress zone 3 is also adjacent to stress zone 1, but all the points in these two zones share the same α -line. Stress zone 4 is bounded by two α -lines (ce and df) and two β -lines (cd and ef). Additional stress zones such as stress zone 5 and stress zone 6 can be defined, as illustrated in Figure 4. For convenience, Table 3 lists the vertex coordinates in these stress zones.

3.3. Stress zone 1. Suppose that R_1 is an arbitrary point within stress zone 1. The α -line passing through R_1 intercepts the inner boundary of the microchannel at point P_1 , while the β -line intercepts the inner

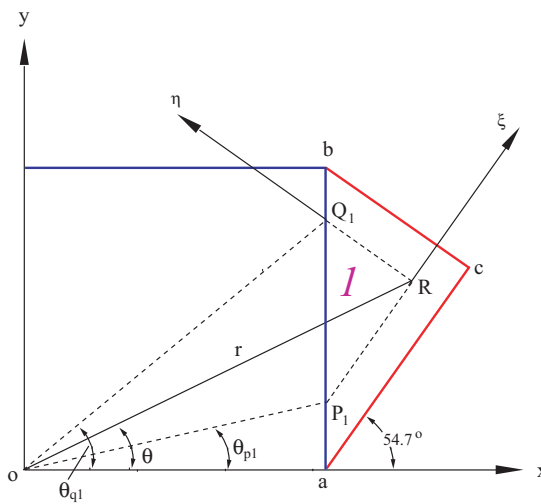


Figure 5. Drawing for finding stress in stress zone 1.

boundary at point Q_1 , as shown in Figure 5. At the boundary points P_1 and Q_2 , the stress states are

$$\text{at } P_1 : \begin{cases} \sigma_{rr} = \frac{2\tau \sin^2 \theta_{p1}}{\sin(2\phi)} - p, \\ \sigma_{\theta\theta} = \frac{2\tau \cos^2 \theta_{p1}}{\sin(2\phi)} - p, \\ \sigma_{r\theta} = \frac{\tau \sin(2\theta_{p1})}{\sin(2\phi)}, \end{cases} \quad \text{at } Q_1 : \begin{cases} \sigma_{rr} = \frac{2\tau \sin^2 \theta_{q1}}{\sin(2\phi)} - p, \\ \sigma_{\theta\theta} = \frac{2\tau \cos^2 \theta_{q1}}{\sin(2\phi)} - p, \\ \sigma_{r\theta} = \frac{\tau \sin(2\theta_{q1})}{\sin(2\phi)}, \end{cases}$$

where θ_{p1} and θ_{q1} are defined as in Figure 5.

Now define a local ξ - η coordinate system with its ξ -axis along the α -line and the η -axis along the β -line for the split system with slip angle $\phi = 54.7^\circ$. By applying the slip line theory as developed by Hill [1998] and Rice and Tracey [1969], the stress component $\sigma_{\xi\xi}$ in these coordinates is, at point R_1 , the same as at point P_1 , while $\sigma_{\eta\eta}$ at point R_1 equals that at Q_1 . This is because the equilibrium equations are satisfied just before yielding. If there is no body force, the equilibrium conditions in the two dimensional Cartesian coordinate x - y system are

$$\frac{\partial \sigma_{xx}}{\partial x} + \frac{\partial \sigma_{xy}}{\partial y} = 0, \quad \frac{\partial \sigma_{yx}}{\partial x} + \frac{\partial \sigma_{yy}}{\partial y} = 0.$$

Because the equilibrium must be satisfied for the entire stress zone, it is possible to seek a solution along the characteristics that are the anisotropic slip line traces, as mentioned before. Therefore, we are ready to determine the relationship among stress components along the α -line or β -line. If a new ξ - η coordinate system is chosen so that ξ and η coincide with the α -line and the β -line, $\sigma_{\xi\eta} = \sigma_{\eta\xi} = \tau$ holds in the initial stage of yielding, with τ being the critical shear stress for the active slip system. This ignores any strain hardening effect. The equilibrium conditions in the local ξ - η coordinate system are

$$\frac{\partial \sigma_{\xi\xi}}{\partial \xi} = 0, \quad \frac{\partial \sigma_{\eta\eta}}{\partial \eta} = 0.$$

The solutions of characteristics are

$$\begin{aligned} \sigma_{\xi\xi} = \sigma_{\xi\xi}(\xi_1, \eta_1) \quad \text{along the } \alpha\text{-line: } \frac{dy}{dx} &= \tan \phi, \\ \sigma_{\eta\eta} = \sigma_{\eta\eta}(\xi_2, \eta_2) \quad \text{along the } \beta\text{-line: } \frac{dy}{dx} &= -\cot \phi, \\ \sigma_{\xi\eta} = \sigma_{\eta\xi} = \tau \quad \text{along both the } \alpha\text{- and } \beta\text{-lines,} \end{aligned} \quad (4)$$

where ϕ is the slip angle, (ξ_1, η_1) and (ξ_2, η_2) are boundary points, and P_1 and Q_1 are associated with the α -line and β -line, respectively. Using this, the yield conditions, and the related boundary conditions, the stress state in stress zone 1 at the initial stage of plastic deformation can be fully determined.

At point P_1 , the value of $\sigma_{\xi\xi}$ is found from the polar stress components, that is,

$$\sigma_{\xi\xi} = \frac{\sigma_{rr} + \sigma_{\theta\theta}}{2} + \frac{\sigma_{rr} - \sigma_{\theta\theta}}{2} \cos [2(\phi - \theta)] + \sigma_{r\theta} \sin [2(\phi - \theta)].$$

Substituting the values of polar stresses at point P_1 from Section 3.3 yields

$$\sigma_{\xi\xi} = -p + \frac{\tau}{\sin(2\phi)} - \frac{\tau \cos(2\theta_{p1})}{\sin(2\phi)} \cos[2(\phi - \theta)] + \frac{\tau \sin(2\theta_{p1})}{\sin(2\phi)} \sin[2(\phi - \theta)], \quad (5)$$

where θ_{p1} , which is related to the position of $R_1(r, \theta)$, can be expressed as

$$\theta_{p1} = \arctan \left[r(\sin \theta - \sqrt{2} \cos \theta) + \sqrt{2} \right].$$

Similarly, at point Q_1 , the value of $\sigma_{\eta\eta}$ can be expressed as

$$\sigma_{\eta\eta} = \frac{\sigma_{rr} + \sigma_{\theta\theta}}{2} + \frac{\sigma_{rr} - \sigma_{\theta\theta}}{2} \cos[2(\phi - \theta)] - \sigma_{r\theta} \sin[2(\phi - \theta)].$$

Substituting the polar stresses at point Q_1 from Section 3.3 gives

$$\sigma_{\eta\eta} = -p + \frac{\tau}{\sin(2\phi)} + \frac{\tau \cos(2\theta_{q1})}{\sin(2\phi)} \cos[2(\phi - \theta)] - \frac{\tau \sin(2\theta_{q1})}{\sin(2\phi)} \sin[2(\phi - \theta)], \quad (6)$$

where

$$\theta_{q1} = \arctan \left[r \left(\sin \theta + \frac{\cos \theta}{\sqrt{2}} \right) - \frac{1}{\sqrt{2}} \right]. \quad (7)$$

If the yield condition holds in stress zone 1, the stress component $\sigma_{\xi\eta} = \tau$.

3.4. Stress zone 2. This stress zone shares its β -line with stress zone 1, as illustrated in Figure 6. According to the slip line theory, the stress component $\sigma_{\eta\eta}$ in the two zones takes the same form, that is, Equation (6). To find $\sigma_{\xi\xi}$ in stress zone 2, we use the yield condition along line $\theta = 0^+$ because the α -line intercepts the abscissa.

The boundary line $\theta = 0^+$ in physical space maps to the rotated stress space point C^* . From the rotated yield surface as shown in Figure 6, the relationship between $\sigma_{\xi\xi}$ and $\sigma_{\eta\eta}$ at any boundary point, P_2 is

$$\frac{\sigma_{\xi\xi}(r^*, 0^+) - \sigma_{\eta\eta}(r^*, 0^+)}{2\tau} = \frac{1}{2\sqrt{2}}. \quad (8)$$

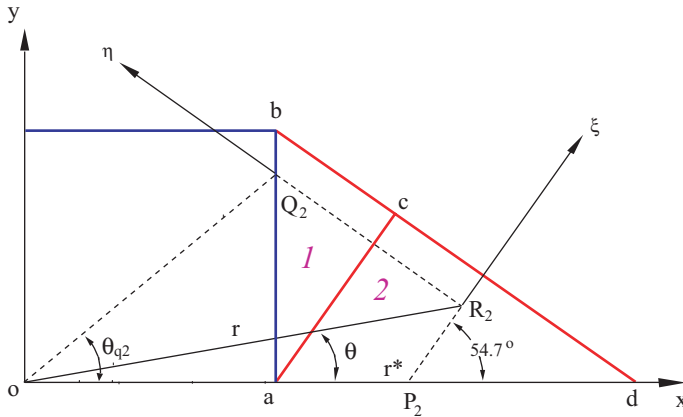


Figure 6. Drawing for finding stress in stress zone 2.

Rearranging this yields

$$\sigma_{\xi\xi}(r^*, 0^+) = \sigma_{\eta\eta}(r^*, 0^+) + \frac{\tau}{\sqrt{2}}. \quad (9)$$

$\sigma_{\eta\eta}(r^*, 0^+)$ can be found from Equation (6) by setting $\theta = 0^+$ and replacing θ_{q1} by $\theta_{q2} = \theta_{q1}(r^*, 0^+)$:

$$\sigma_{\eta\eta}(r^*, 0^+) = -p + \frac{\tau}{\sin(2\phi)} + \tau \cot(2\phi) \cos(2\theta_{q2}) - \tau \sin(2\theta_{q2}), \quad (10)$$

where θ_{q2} is related to r^* , which can be determined from Equation (7) as

$$\theta_{q2} = \arctan \left[\frac{1}{\sqrt{2}}(r^* - 1) \right]. \quad (11)$$

Substituting Equation (10) into Equation (9) yields

$$\sigma_{\xi\xi}(r^*, 0^+) = -p + \frac{\tau}{\sin(2\phi)} + \tau \cot(2\phi) \cos(2\theta_{q2}) - \tau \sin(2\theta_{q2}) + \frac{\tau}{\sqrt{2}}.$$

To find the stress state inside the entire region defined as stress zone 2, we apply the variation method. This is done by expressing r^* and θ_{q2} as functions of r and θ . With respect to Figure 6, if the boundary point $P_2(r^*, 0^+)$ goes into stress zone 2, the law of sines requires

$$r^* = r \frac{\sin(\phi - \theta)}{\sin \phi} = \frac{\sqrt{3}r}{\sqrt{2}} \sin(\phi - \theta). \quad (12)$$

The general form of θ_{q2} follows from Equation (11) and Equation (12), that is,

$$\theta_{q2} = \arctan \left[\frac{\sqrt{3}r}{2} \sin(\phi - \theta) - \frac{1}{\sqrt{2}} \right].$$

Therefore, the stress state in stress zone 2 is

$$\begin{aligned} \sigma_{\xi\xi} &= -p + \frac{\tau}{\sin(2\phi)} + \tau \cot(2\phi) \cos(2\theta_{q2}) - \tau \sin(2\theta_{q2}) + \frac{\tau}{\sqrt{2}}, \\ \sigma_{\eta\eta} &= -p + \frac{\tau}{\sin(2\phi)} + \frac{\tau \cos(2\theta_{q1})}{\sin(2\phi)} \cos[2(\phi - \theta)] - \frac{\tau \sin(2\theta_{q1})}{\sin(2\phi)} \sin[2(\phi - \theta)], \\ \sigma_{\xi\eta} &= \tau. \end{aligned}$$

3.5. Stress zone (3). According to Figure 7, stress zone 3 and stress zone 1 share the same α -line and also the stress component $\sigma_{\xi\xi}$. To find the stress component $\sigma_{\eta\eta}$, we use the yield condition along the boundary line $\theta = \pi/4$. The yield condition is mapped from the point D^* on the rotated yield surface and can be expressed as

$$\frac{\sigma_{\xi}(r^{**}, \pi/4) - \sigma_{\eta\eta}(r^{**}, \pi/4)}{2\tau} = -2\sqrt{2}.$$

From this and Equation (5), $\sigma_{\eta\eta}(r^{**}, \pi/4)$ can be found by setting $\theta = \pi/4$ and $\theta_{p1} = \theta_{p3}$ as

$$\sigma_{\eta\eta}(r^{**}, \frac{\pi}{4}) = -p + \frac{\tau}{\sin(2\phi)} - \frac{\tau \cos(2\theta_{p3})}{\sin(2\phi)} \cos \left[2\left(\phi - \frac{\pi}{4}\right) \right] + \frac{\tau \sin(2\theta_{p3})}{\sin(2\phi)} \sin \left[2\left(\phi - \frac{\pi}{4}\right) \right] + 4\sqrt{2}\tau, \quad (13)$$

where θ_{p3} is θ_{p1} at $r = r^{**}$ and $\theta = \pi/4$, that is,

$$\theta_{p3} = \arctan \left[r^{**} \left(\frac{1}{\sqrt{2}} - 1 \right) + \sqrt{2} \right]. \tag{14}$$

Noting that $\phi = 54.7^\circ$, Equation (13) simplifies to

$$\sigma_{\eta\eta}(r^{**}, \frac{\pi}{4}) = -p + \frac{\tau}{\sin(2\phi)} - \frac{2\sqrt{2}\tau \cos(2\theta_{p3})}{3 \sin(2\phi)} + \frac{\tau \sin(2\theta_{p3})}{3 \sin(2\phi)} + 4\sqrt{2}\tau.$$

To extend the stress solutions to the entire stress zone 3, r^{**} , as a function of r and θ , becomes, by the law of sines,

$$r^{**} = \frac{\sqrt{2}r}{1 + \sqrt{2}} (\cos \theta + \sqrt{2} \sin \theta). \tag{15}$$

Therefore, the stress state in stress zone 3 is

$$\begin{aligned} \sigma_{\xi\xi} &= -p + \frac{\tau}{\sin(2\phi)} - \frac{\tau \cos(2\theta_{p1})}{\sin(2\phi)} \cos [2(\phi - \theta)] + \frac{\tau \sin(2\theta_{p1})}{\sin(2\phi)} \sin [2(\phi - \theta)], \\ \sigma_{\eta\eta} &= -p + \frac{\tau}{\sin(2\phi)} - \frac{2\sqrt{2}\tau \cos(2\theta_{p3})}{3 \sin(2\phi)} + \frac{\tau \sin(2\theta_{p3})}{3 \sin(2\phi)} + 4\sqrt{2}\tau, \\ \sigma_{\xi\eta} &= \tau. \end{aligned}$$

The general form of θ_{p3} follows from substituting r^{**} in (15) into (14):

$$\theta_{p3} = \arctan \left[\sqrt{2} - r(\cos \theta + \sqrt{2} \sin \theta)(3 - 2\sqrt{2}) \right].$$

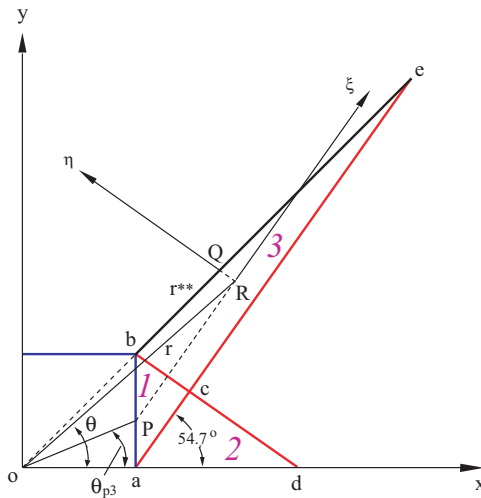


Figure 7. Drawing for finding stress in stress zone 3.

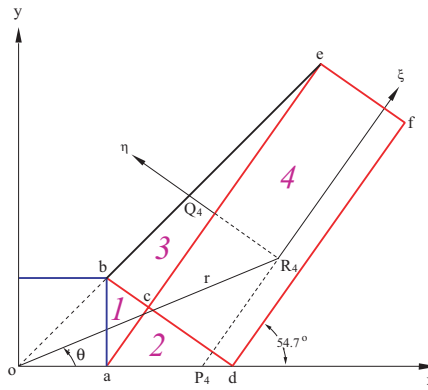


Figure 8. Drawing for finding stress in stress zone 4.

3.6. Stress zone 4. The analysis of this zone (and the next) is very much like that of stress zone 3. According to Figure 8, stress zone 4 and stress zone 2 share the same α -line and $\sigma_{\xi\xi}$. Also, stress zone 4 and stress zone 3 share the same β -line, and thus $\sigma_{\eta\eta}$ as well. Therefore, the stress state in stress zone 4 can be obtained as

$$\begin{aligned}
 \sigma_{\xi\xi} &= -p + \frac{\tau}{\sin(2\phi)} + \tau \cot(2\phi) \cos(2\theta_{q2}) - \tau \sin(2\theta_{q2}) + \frac{\tau}{\sqrt{2}}, \\
 \sigma_{\eta\eta} &= -p + \frac{\tau}{\sin(2\phi)} - \frac{2\sqrt{2}\tau \cos(2\theta_{p3})}{3 \sin(2\phi)} + \frac{\tau \sin(2\theta_{p3})}{3 \sin(2\phi)} + 4\sqrt{2}\tau, \\
 \sigma_{\xi\eta} &= \tau.
 \end{aligned}
 \tag{16}$$

3.7. Stress zone 5. From Figure 9, stress zone 5 and stress zone 4 share a β -line and $\sigma_{\eta\eta}$ in the form given by Equation (16). To find $\sigma_{\xi\xi}$ in stress zone 5, we use the same method as used for finding $\sigma_{\xi\xi}$ in stress zone 2. We apply the yield condition along line $\theta = 0^+$, as shown in Equation (8), for establishing the relationship between $\sigma_{\xi\xi}$ and $\sigma_{\eta\eta}$ at any point on this boundary.

We define a new parameter $\theta_{p5} = \theta_{p3}(r^*, 0^+)$ for deriving $\sigma_{\xi\xi}$ in this zone, that is,

$$\theta_{p5} = \arctan \left[\sqrt{2} - r^*(3 - 2\sqrt{2}) \right].$$

A more general form of θ_{p5} for points inside the stress zone is

$$\theta_{p5} = \arctan \left[\sqrt{2} - \frac{3 - 2\sqrt{2}}{\sqrt{2}} r (\sqrt{2} \cos \theta - \sin \theta) \right].$$

The stress state in stress zone 5 is

$$\begin{aligned} \sigma_{\xi\xi} &= -p + \frac{\tau}{\sin(2\phi)} - \frac{2\sqrt{2}\tau}{3\sin(2\phi)} \cos(2\theta_{p5}) + \frac{\tau \sin(2\theta_{p5})}{\sin(2\phi)} + \frac{\tau}{\sqrt{2}} + 4\sqrt{2}\tau, \\ \sigma_{\eta\eta} &= -p + \frac{\tau}{\sin(2\phi)} - \frac{2\sqrt{2}\tau \cos(2\theta_{p3})}{3\sin(2\phi)} + \frac{\tau \sin(2\theta_{p3})}{3\sin(2\phi)} + 4\sqrt{2}\tau, \\ \sigma_{\xi\eta} &= \tau. \end{aligned}$$

3.8. Stress zone 6. The procedures for finding the stresses in stress zone 6 are the same those for stress zone 3. Stress zone 6 and stress zone 4 share the an α -line and $\sigma_{\xi\xi}$. The stress component $\sigma_{\eta\eta}$ is found from the yield condition along the boundary line $\theta = \pi/4$, which is shown in Section 3.5.

For the points on the boundary $\theta = \pi/4$, we define θ_{q6} , a function of r^{**} , as

$$\theta_{q6} = \arctan \left(\frac{\sqrt{2}-1}{2} r^{**} - \frac{1}{\sqrt{2}} \right).$$

For the points within stress zone 6, θ_{q6} is a function of r and θ , that is,

$$\theta_{q6} = \arctan \left(\frac{3\sqrt{2}-4}{2} r (\cos \theta + \sqrt{2} \sin \theta) - \frac{1}{\sqrt{2}} \right).$$

Therefore, the stress state in stress zone 6 is given by

$$\begin{aligned} \sigma_{\xi\xi} &= -p + \frac{\tau}{\sin(2\phi)} + \tau \cot(2\phi) \cos(2\theta_{q2}) - \tau \sin(2\theta_{q2}) + \frac{\tau}{\sqrt{2}}, \\ \sigma_{\eta\eta} &= -p + \frac{\tau}{\sin(2\phi)} + \tau \cot(2\phi) \cos(2\theta_{q6}) - \tau \sin(2\theta_{q6}) + \frac{\tau}{\sqrt{2}} + 4\sqrt{2}\tau, \\ \sigma_{\xi\eta} &= \tau. \end{aligned}$$

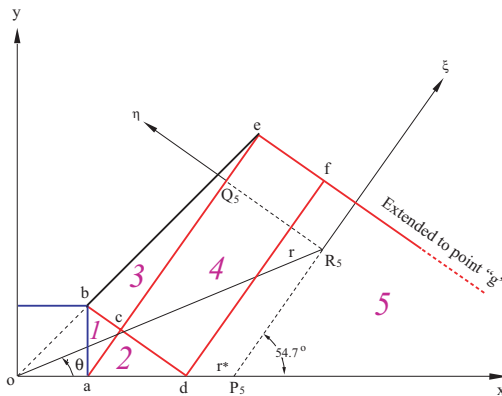


Figure 9. Drawing for finding stress in stress zone 5.

4. Results and discussion

4.1. Stress along circumferential paths. The analytical solutions in the region $0 \leq \theta \leq 45^\circ$, as presented in Sections 3.3 to Section 3.8, provide for obtaining the stress field around the microchannel through a series of mapping operations along special symmetrical lines. The first mapping is that the solutions in $0 \leq \theta \leq 45^\circ$ can be reflected over the line $\theta = 45^\circ$ to get the solutions in $45^\circ \leq \theta \leq 90^\circ$. The solution from $0 \leq \theta \leq 90^\circ$ can be translated 90° for solving in $90^\circ \leq \theta \leq 180^\circ$. Once we know the stress around the upper half of the channel, the values in lower half plane follow from reflection across x -axis.

In the following discussion, the half width of the microchannel is defined as w_o . To show the stress solutions quantitatively and for simplicity, we set to unity the half width of the channel. We also set τ to unity, and the internal pressure becomes

$$p = \frac{\tau}{\sin \phi \cos \phi} = \frac{3}{\sqrt{2}},$$

which is the critical value for initiation yielding at the boundary point O of Figure 1.

Figure 10 and Figure 11 show the stress state along circumferential paths in the angular range $0 \leq \theta \leq 180^\circ$. Figure 10 depicts the stresses along the path $r/w_o = r_b/w_o = \sqrt{2}$. There, the stresses are normalized by the critical shear strength τ . Figure 10a shows the stress components in the local ξ - η coordinate system. The normal stresses $\sigma_{\xi\xi}$ and $\sigma_{\eta\eta}$ show jump abruptly $\theta = 45^\circ$ and $\theta = 135^\circ$. Nevertheless, the most rapid change in the shear stress $\sigma_{\xi\eta}$ occurs at $\theta = 90^\circ$.

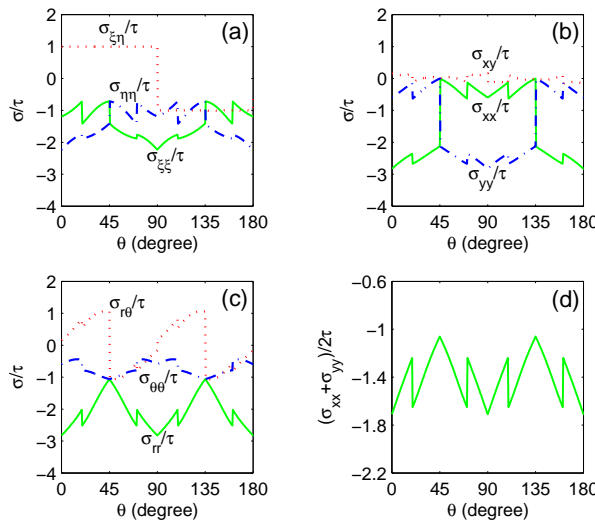


Figure 10. Stress state around the circumferential path $r/w_o = r_b/w_o = \sqrt{2}$: (a) normalized stress components in the local ξ - η coordinates, (b) normalized stress components in x - y Cartesian coordinates, (c) normalized stress components in r - θ polar coordinates, (d) the normalized out-of-plane stress component.

Figure 10b shows the stresses in the x - y Cartesian coordinates. The shear stress σ_{xy} is almost equal to zero, which is reasonable because the circumferential path is very close to the inner wall of the microchannel. On the inner wall of the channel, the nonshear boundary condition holds. By the same logic, the numerical values of normal stresses σ_{xx} and σ_{yy} also recover the boundary conditions. For example, in the angular ranges $0 \leq \theta \leq 45^\circ$ and $135^\circ \leq \theta \leq 180^\circ$, $\sigma_{xx} \approx -p = -3/\sqrt{2}$, and $\sigma_{yy} \approx 0$, which means that material near the two vertical walls of the microchannels is under a horizontal pressure of about $-p$. Nevertheless, in the range $45^\circ \leq \theta \leq 135^\circ$, $\sigma_{xx} \approx 0$ and $\sigma_{yy} \approx -p = -3/\sqrt{2}$, indicating that material close to the top horizontal wall of the microchannel undergoes a vertical compressive pressure of about $-p$.

In polar coordinates, the shear stress $\sigma_{r\theta}$ changes abruptly at $\theta = 45^\circ$ and $\theta = 135^\circ$, as shown in Figure 10c. $\sigma_{r\theta}$ is a periodic function with period 90° . The radial and hoop stress components, σ_{rr} and $\sigma_{\theta\theta}$, are also 90° -periodic functions. In addition, they show mirror symmetry about the line $\theta = 90^\circ$. Figure 10d shows how the the trace of the stresses changes along the angular path. Under the assumed isochoric condition, the trace of the stresses is equal to the out-of-plane stress.

We also examine the stress solutions along another two circumferential paths,

$$r/w_o = (r_b + r_c)/(2w_o) \approx 1.52 \quad \text{and} \quad r/w_o = r_c/w_o = \sqrt{5 + 2\sqrt{2}}/\sqrt{3} \approx 1.62.$$

The stresses along these two constant-radius lines show the same trend, that is, the stress state is nonuniform, resulting in anisotropic deformation of material around the microchannel. Another common feature which can be seen from the results is that all stress components except for $\sigma_{\xi\eta}$ peak either along the lines

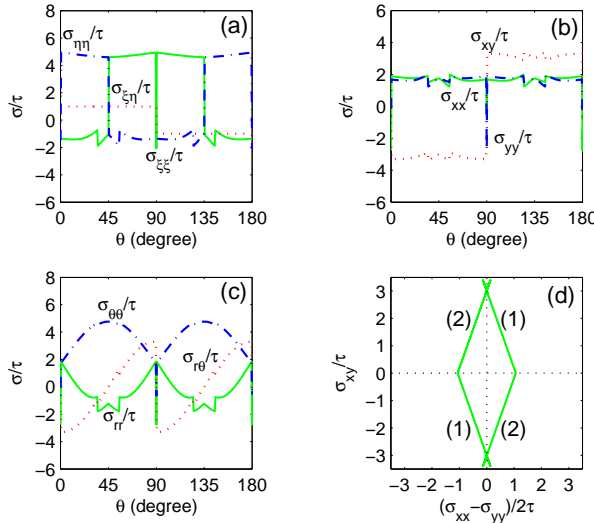


Figure 11. Stress state around the circumferential path $r/w_o = r_d/w_o = 1 + \sqrt{2}$: (a) normalized stress components in the local ξ - η coordinates, (b) normalized stress components in x - y Cartesian coordinates, (c) normalized stress components in r - θ polar coordinates, (d) yield surface.

$\theta = 45^\circ$ and $\theta = 135^\circ$ or close to these lines. Evidently, the regions containing the radial lines $\theta = 45^\circ$ and $\theta = 135^\circ$ experience higher loading than elsewhere, and we expect intense shear deformation along these two lines. This agrees with the slip model shown in Figure 1.

Figure 11 shows the stress state along the path, $r/w_o = r_d/w_o = 1 + \sqrt{2}$. The stress field is not uniform along this path, which indicates an anisotropic deformation state. Specifically, Figure 11d illustrates the yield surface along the path. The plastic deformation there comes from the active slip of the two slip systems marked (1) and (2). Obviously, Figure 11d recovers well the yield conditions from the analytical model of plasticity in Section 2.2 and shown in Figure 3b. We note that the line $\theta = 45^\circ$ is the boundary for slip system 1 and slip system 2. Similarly, $\theta = 135^\circ$ is also a slip sector boundary. These are the places where stress concentrates before yielding due to the corner effect. Material on these boundaries can flow along either slip system 1 or slip system 2. Thus, the yield surface bifurcates at the intercept points on the vertical axis in Figure 11d.

4.2. Stress maps. In this section, we present the stress maps of microneedles containing square microchannels. These have potential applications for cell registration, fluid injection, and nanofiber synthesis. As a case study, we choose a cylindrical microneedle with radius $r/w_o = r_e/w_o = 2 + 2\sqrt{2} \approx 4.83$. w_o is the microchannel half-width, as defined in Section 4.1. The channel itself is centered in the cylindrical needle. We assume here that internal pressure controls the deformation. Thus, the boundary conditions for stresses on the inside wall propagate in material around the channel along the characteristics (slip-lines). The assumption is reasonable for cases such as confined growth of nanofibers within the channel, fluid injection from the channel, and cell registration under suction by internal pressure.

Figure 12 shows stress zones in the needle around the microchannel, which exhibit the expected four-fold symmetry. Figures 13–16 show stress maps in different coordinate systems and various other features, as discussed below.

Figure 13 maps the normalized radial stress σ_{rr}/τ ; the map reveals evenly distributed compressive regions near the inner wall of the channel. These compressive regions propagate along the slip sector

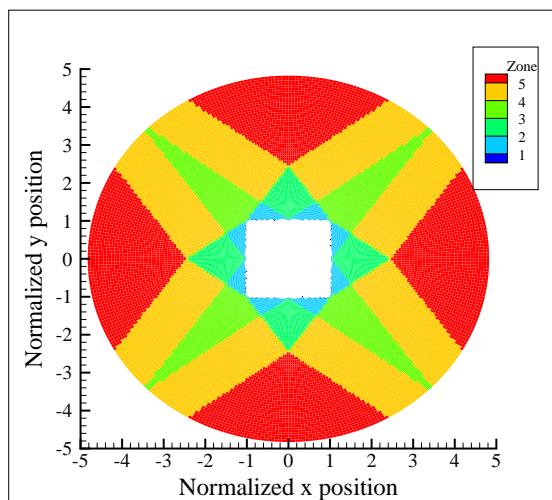


Figure 12. Contour plot showing the stress zones around the microchannel.

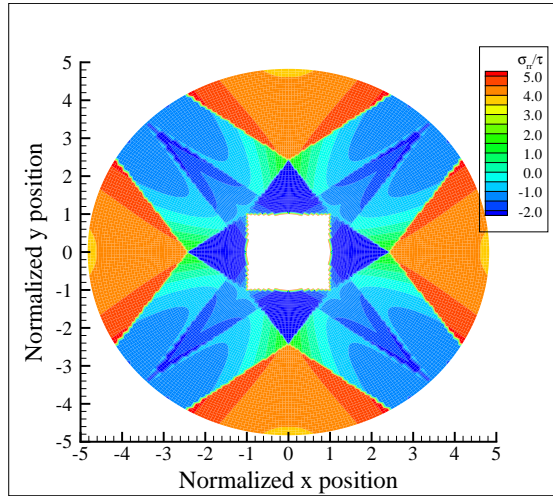


Figure 13. Contour map showing the normalized polar stress σ_{rr}/τ around the microchannel.

boundaries, that is, along multiples of $\theta = \pi/4$. The compressed regions are separate from the regions under intense tension away from the channel. The normalized hoop stress $\sigma_{\theta\theta}/\tau$, shown in Figure 14, shows a similar compressed region near the channel’s inner wall. However, close to the outer boundary of the microneedle, the $\sigma_{\theta\theta}/\tau$ implies a tension state. On the map of normalized polar shear stress ($\sigma_{r\theta}/\tau$ in Figure 15), we see neutral zones around the channel. Away from the channel and along circumferential paths — for example, at $r/w_o = 1 + \sqrt{2}$ — the stress state alternates between compression and tension.

We can also examine in the x - y global Cartesian coordinate system the stress maps for σ_{xx}/τ and σ_{yy}/τ . They exhibit discrete tension and compression zones. The inner boundary conditions propagate in the stress zones adjacent to the inner wall. For example, we find $\sigma_{xx} = -p$ in $0 \leq \theta \leq 45^\circ$ within the

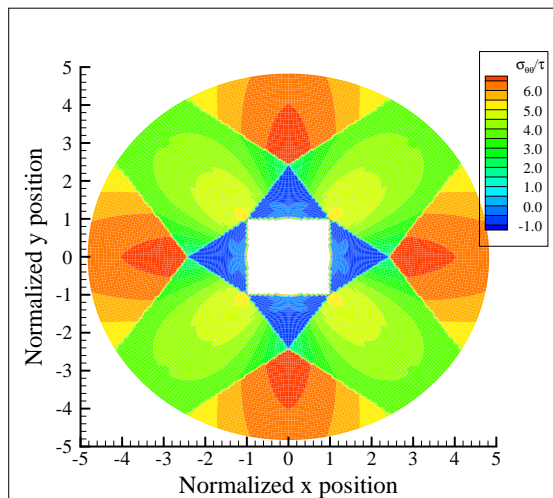


Figure 14. Contour map showing the normalized polar stress $\sigma_{\theta\theta}/\tau$ around the microchannel.

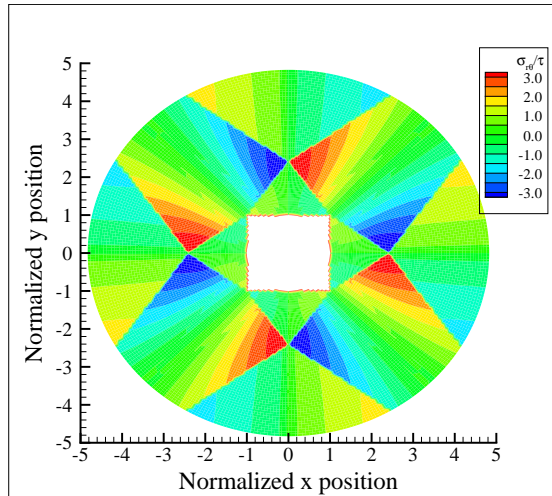


Figure 15. Contour map showing the normalized polar stress $\sigma_{r\theta}/\tau$ around the microchannel.

zone containing the channel's vertical wall, while $\sigma_{yy} = -p$ in $45^\circ \leq \theta \leq 90^\circ$ within the zone horizontal wall. Tension stress states occupy the region near to the outer boundary of the microneedle. We note that the map σ_{yy}/τ is just σ_{xx}/τ rotated by $\pi/2$. On the map for normalized shear stress σ_{xy}/τ , the inner wall satisfies the nonshear condition. The nonshear zones are located along both the x - and y -axis. The shear zones appear at multiples of $\theta = \pi/4$.

Figure 16 shows, in the ξ - η local Cartesian coordinate system, the stress maps for $\sigma_{\xi\xi}/\tau$. Obviously, the $\sigma_{\eta\eta}/\tau$ map can be obtained by rotating the figure by $\pi/2$. In this map, the normalized stress $\sigma_{\xi\xi}/\tau$ is constant along the characteristics, or α -lines. Similarly, $\sigma_{\eta\eta}/\tau$ is constant along β -lines. This agrees with the predictions of slip line theory. In the local coordinate system, the normalized shear stress $\sigma_{\xi\eta}/\tau$ stays

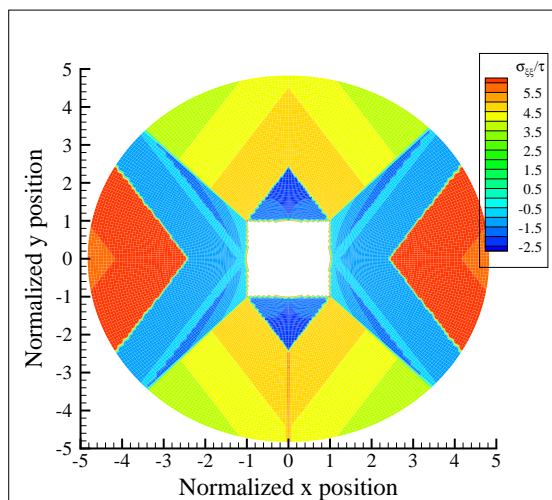


Figure 16. Contour map showing the normalized stress $\sigma_{\xi\xi}/\tau$ in the local ξ - η Cartesian coordinates.

constant in each quadrant, revealing the anisotropic plasticity of the material. The results also indicate the deformation behavior of global yielding without any strain hardening.

We can also look at the trace of the stresses. In the plane, the trace is related to pressure; out of the plane, it represents stress under isochoric conditions. The trace results show the nonuniform distributions in the in-plane pressure and the out-of-plane stress. Finally, we examine the normalized in-plane stress difference $(\sigma_{xx} - \sigma_{yy})/(2\tau)$, which is the stress measure on the stress space abscissa. This difference shows symmetrically distributed zones. The stress maps of Figures 12–16 reveal the nonuniform stress states to be as predicted by the analytical solutions in Section 3, namely, that materials containing microchannels under internal pressure exhibit anisotropic plastic deformation.

We stress that the model here is an idealized and simplified one which provides some preliminary results. For more sophisticated material models, it is difficult to obtain closed form solutions, and only numerical solutions may be available. Thus, subsequent finite element simulations should be implemented to treat real world problems with different strain hardening laws. Because analytical solutions can only be obtained from simplified models that assume an ideally rigid plastic solid, this work may be considered as a good starting point for tackling more complicated cases. Already underway are systematic finite element simulations of microchannels with different geometrical configurations shaped like as squares, circles, cylinders, and ellipses; these are based on material models with a prescribed elastic-plastic constitutive relation. Using the preliminary results presented in this work, it may be possible to compare the analytical predictions with numerical ones.

Another issue facing the practical applications is the stress concentration problem. Typically, stress concentrates at sharp corners and cracks. In this model, stress will concentrate at the four microchannel corners with $\theta = \pi/4, 3\pi/4, 5\pi/4, \text{ and } 7\pi/4$. Stress concentrations cause the material to yield at a lower overall stress level. Thus, the yield surface will contract and the points B and D shown in Figure 3a will move towards the origin. Consequently, the yield surface will change from a diamond to a more complex shape. The stress zones would need to be redefined and the processes for seeking the analytical solutions to the stresses would be more complicated. In the end, finite element simulations may be the proper way to deal with the stress concentration issue.

5. Conclusions

From our studies of the stress states around microchannels under internal compressive loading, the following conclusions can be made.

First, the simplified yielding model can be used to characterize the plastic flow in materials containing microchannels. When the material is under strain deformation conditions, the model allows identification of slip bands around the channels.

Second, we can obtain closed form solutions to stress fields around the microchannels. The solutions hold in both the zones containing and those away from the inner boundary. The stress distributions are nonuniform. The results predict anisotropic deformation states around the channels.

Third, we determine the yield conditions associated with the plastic flow along different slip bands. From the yield surface along circumferential paths, it is found that, at the corner of the square-shaped microchannel, two slip systems have the same chance of being activated.

Finally, the stress maps of microneedles containing square microchannels reveal discrete isostress zones and predict anisotropic plastic deformation of the material around the channels.

References

- [Allen 2005] J. J. Allen, *Micro electro mechanical system design*, Taylor and Francis, Boca Raton, FL, 2005.
- [Fleck et al. 1994] N. A. Fleck, G. M. Muller, M. F. Ashby, and J. W. Hutchinson, “Strain gradient plasticity: theory and experiment”, *Acta Metall. Mater.* **42**:2 (1994), 475–487.
- [Franssila 2004] S. Franssila, *Introduction to microfabrication*, J. Wiley, New York, 2004.
- [Gan and Kysar 2007] Y. X. Gan and J. W. Kysar, “Cylindrical void in a rigid-ideally plastic single crystal, III: hexagonal close-packed crystal”, *Int. J. Plasticity* **23**:4 (2007), 592–619.
- [Gan et al. 2006] Y. X. Gan, J. W. Kysar, and T. L. Morse, “Cylindrical void in a rigid-ideally plastic single crystal, II: experiments and simulations”, *Int. J. Plasticity* **22**:1 (2006), 39–72.
- [Hill 1998] R. Hill, *The mathematical theory of plasticity*, Oxford University Press, New York, 1998.
- [Huang et al. 1991] Y. Huang, J. W. Hutchinson, and V. Tvergaard, “Cavitation instabilities in elastic-plastic solids”, *J. Mech. Phys. Solids* **39**:2 (1991), 223–241.
- [Hwang and Song 2007] H.-S. Hwang and J.-T. Song, “An effective method to prevent stiction problems using a photoresist sacrificial layer”, *J. Micromech. Microeng.* **17**:2 (2007), 245–249.
- [Kysar et al. 2005] J. W. Kysar, Y. X. Gan, and G. Mendez-Arzuza, “Cylindrical void in a rigid-ideally plastic single crystal, I: anisotropic slip line theory solution for face-centered cubic crystals”, *Int. J. Plasticity* **21**:8 (2005), 1481–1520.
- [Lee et al. 2003] N. K. S. Lee, G. H. Yu, J. Y. Chen, and A. Joneja, “Effect of mechanical alignment system on assembly accuracy”, *J. Manuf. Sci. Eng. (Trans. ASME)* **125**:3 (2003), 595–608.
- [Li et al. 2004] B. Li, H. Yu, A. Sharon, and X. Zhang, “Rapid three-dimensional manufacturing of microfluidic structures using a scanning laser system”, *Appl. Phys. Lett.* **85**:12 (2004), 2426–2428.
- [Lu et al. 2007] Z. Lu, P. C. Y. Chen, J. Nam, R. Ge, and W. Lin, “A micromanipulation system with dynamic force-feedback for automatic batch microinjection”, *J. Micromech. Microeng.* **17**:2 (2007), 314–321.
- [Lubarda et al. 2004] V. A. Lubarda, M. S. Schneider, D. H. Kalantar, B. A. Remington, and M. A. Meyers, “Void growth by dislocation emission”, *Acta Mater.* **52**:6 (2004), 1397–1408.
- [Nadai 1950] A. Nadai, *Theory of flow and fracture of solids*, McGraw-Hill, New York, 1950.
- [Needleman and Tvergaard 1991] A. Needleman and V. Tvergaard, “A numerical study of void distribution effects on dynamic, ductile crack growth”, *Eng. Fract. Mech.* **38**:2-3 (1991), 157–173.
- [O’Regan et al. 1997] T. L. O’Regan, D. F. Quinn, M. A. Howe, and P. E. McHugh, “Void growth simulations in single crystals”, *Comput. Mech.* **20**:1-2 (1997), 115–121.
- [Rice 1973] J. R. Rice, “Plane strain slip line theory for anisotropic rigid/plastic materials”, *J. Mech. Phys. Solids* **21**:2 (1973), 63–74.
- [Rice and Tracey 1969] J. R. Rice and D. M. Tracey, “On the ductile enlargement of voids in triaxial stress fields”, *J. Mech. Phys. Solids* **17**:3 (1969), 201–217.
- [Schacht et al. 2003] T. Schacht, N. Untermann, and E. Steck, “The influence of crystallographic orientation on the deformation behavior of single crystals containing microvoids”, *Int. J. Plasticity* **19**:10 (2003), 1605–1626.
- [Senturia 2001] S. D. Senturia, *Microsystem design*, Kluwer Academic, Boston, 2001.
- [Timpe and Komvopoulos 2006] S. J. Timpe and K. Komvopoulos, “The effect of adhesion on the static friction properties of sidewall contact interfaces of microelectromechanical devices”, *J. Microelectromech. S.* **15**:6 (2006), 1612–1621.
- [Tseng et al. 2002a] F.-G. Tseng, C.-J. Kim, and C.-M. Ho, “A high-resolution high-frequency monolithic top-shooting microinjector free of satellite drops “CPart I: Concept, design, and model”, *J. Microelectromech. S.* **11**:5 (2002), 427–436.
- [Tseng et al. 2002b] F.-G. Tseng, C.-J. Kim, and C.-M. Ho, “A high-resolution high-frequency monolithic top-shooting microinjector free of satellite drops “CPart II: Fabrication, implementation, and characterization”, *J. Microelectromech. S.* **11**:5 (2002), 437–447.

- [Tvergaard 1991] V. Tvergaard, “Failure by ductile cavity growth at a metal-ceramic interface”, *Acta Metall. Mater.* **39**:3 (1991), 419–426.
- [Tvergaard and Hutchinson 2002] V. Tvergaard and J. W. Hutchinson, “Two mechanisms of ductile fracture: void by void growth versus multiple void interaction”, *Int. J. Solids Struct.* **39**:13-14 (2002), 3581–3597.
- [Tvergaard and Niordson 2004] V. Tvergaard and C. Niordson, “Nonlocal plasticity effects on interaction of different size voids”, *Int. J. Plasticity* **20**:1 (2004), 107–120.
- [Yu et al. 2004] H. Yu, O. Balogun, B. Li, T. W. Murray, and X. Zhang, “Building embedded microchannels using a single layered SU-8 and determining Young’s modulus using a laser acoustic technique”, *J. Micromech. Microeng.* **14**:11 (2004), 1576–1584.
- [Yu et al. 2006a] H. Yu, O. Balogun, B. Li, T. W. Murray, and X. Zhang, “Fabrication of three-dimensional microstructures based on single-layered SU-8 for lab-on-chip applications”, *Sensor. Actuat. A Phys.* **127**:2 (2006), 228–234.
- [Yu et al. 2006b] H. Yu, B. Li, and X. Zhang, “Flexible fabrication of three-dimensional multi-layered microstructures using a scanning laser system”, *Sensor. Actuat. A Phys.* **125**:2 (2006), 553–564.
- [Zhe et al. 2007] J. Zhe, A. Jagtiani, P. Dutta, J. Hu, and J. Carletta, “A micromachined high throughput Coulter counter for bioparticle detection and counting”, *J. Micromech. Microeng.* **17**:2 (2007), 304–313.
- [Ziegler et al. 2006] D. Ziegler, T. Suzuki, and S. Takeuchi, “Fabrication of flexible neural probes with built-in microfluidic channels by thermal bonding of parylene”, *J. Microelectromech. S.* **15**:6 (2006), 1477–1482.

Received 2 Apr 2007. Accepted 11 Jun 2007.

YONG XUE GAN: yong.gan@utoledo.edu

Department of Mechanical, Industrial and Manufacturing Engineering College of Engineering, University of Toledo, Toledo, OH 43606, United States

DYNAMIC RIGID-PLASTIC DEFORMATION OF ARBITRARILY SHAPED PLATES

TATIANA PAVLOVNA ROMANOVA AND YURI VLADIMIROVICH NEMIROVSKY

A rigid, perfectly-plastic model of solids is applied to study the dynamic behavior of simply supported or clamped, arbitrarily shaped plates on visco-elastic foundation. The role of membrane forces and transverse shear forces in the yield condition and the influence of geometry changes are neglected. The plate is subjected to explosive loads uniformly distributed over the surface. Several mechanisms of dynamic deformation of the plate are considered. For each mechanism, equations of the dynamic behavior are obtained. Operating conditions of these mechanisms are analyzed. Analytical expressions for the limit and high loads and for the maximum final deflections are obtained. Detailed analyses are given for an astroid-shaped plate, for a plate with a contour consisting of two arcs and for a plate with an internal free hole or a rigid insert.

1. Introduction

The issues involved in calculating structural deformation under the action of intensive short-time loads are important in modern solid mechanics. To solve such problems, the model of a rigid-plastic body is widely used [Komarov and Nemirovsky 1984]. The model is based on the assumption that the body starts deforming if the stress reaches the limiting value and plastic deformations become possible. Elastic deformations are neglected. For thin-walled elements of structures, this simplification allows solving numerous important practical problems. Nevertheless, all well-known solutions concern only axisymmetric and rectangular plates.

The method proposed in the present work allows, on the basis of the theory of a rigid, perfectly-plastic body, calculating any supported plates of an arbitrary piecewise smooth curvilinear contour, subjected to short-time intensive dynamic loads. The method can be useful in engineering practice.

Notation

P	intensity of load
P_{\max}	maximum value of load
P_0, \bar{P}_0	limit loads
P_1	load defining high loads
p_0, p_1, P_m	dimensionless loads
t, t_0	current and initial times
K_1, K_2	factors of elastic and viscous resistance

Keywords: rigid-plastic plate, arbitrarily shaped plate, dynamic load, limit load, final deflection.

This work was supported by the Russian Foundation for Basic Research (grant no. 05-01-00161-a).

Z_1, Z_2, S_p	regions in plate
l	contour of plate
dl	element of contour l
l_1, l_2	plastic hinge curves
$(x, y), (x_1, y_1),$ $(x_2, y_2), (x_h, y_h)$	Cartesian coordinates
φ, φ_h	parameters
$\varphi_i, \varphi_j, \varphi_D, \varphi_{hi}, \varphi^b, \varphi_h^b$	boundary values of parameter φ
φ_0	initial value of parameter φ_D
$D_h, D_{\min}, D_{\max}, D,$ D_0, D_a, d_i, d_1, d_2	distances
K, A, N	powers of inertial, external and internal forces
S	area of plate
ds	element of area
u, w_c	deflections
w_{\max}	maximum of final deflection
ρ, ρ_a	surface density of plate material and insert material
l_m	lines of discontinuity of angular velocity
m	quantity of lines of discontinuity of angular velocities
$[\partial\theta_m/\partial t]$	discontinuity of angular velocities on l_m
dl_m	element of line l_m
κ_1, κ_2	main curvatures of surface of deflection rate of plate
$\dot{\alpha}$	rate of change of angle of rotation
*	index denoting admissible velocities
M_m	bending moment on l_m
M_0	limit bending moment
n	normal to the contour l
AB, AC	normals to the contour l
η	parameter of supported contour
β	parameter of internal contour
i, j	indexes
(v_1, v_2)	curvilinear orthogonal coordinates
v_{2h}	parameter corresponding to v_2
v_{2j}	boundary value of parameter v_2
a_1, b_1	semiaxes of semiellipse
a	parameter of astroid-shaped plate
L	function designated in Equation (2)
L_h	function designated in Equation (15)
$\Sigma_1, \Sigma_2, \Sigma_3, \Sigma_4, \Sigma_5, \Sigma_6, G, G_1, F$	factors
T	time of removing of load
t_1	time of end of first phase of deformation
t_f	time of stop of plate

R, γ	radius and half of central corner of arc of circle
I, I_*	integral characteristics of load
\bar{l}, \bar{l}_2	polygonal contours
δ, δ_0	dimensionless functions
r	radius of curvature of curve l
r_1	radius
ξ, ς	coordinates of center of curvature of curve l
ρ_1, ρ_2	radiuses of curvature
N_1, N_2, N_3, N_4	components of power of internal forces in plate
l_3	tangent to curve l_1
ABE, BED_1, AED_1, AD_2E	planes
$\psi_1, \psi_2, \beta_1, \beta_2$	angles in Figure 3

2. Model, assumptions and equations of motion

We consider a thin rigid perfectly-plastic simply supported or clamped plate of an arbitrary piecewise smooth curvilinear contour l (Figure 1). The plate is subjected to a uniformly distributed short-time intensive dynamic load of high intensity $P(t)$. We consider explosive load characterized by the instantaneous reaching of the maximum value $P_{\max} = P(t_0)$ at the initial time t_0 with the subsequent rapid decrease. The plate rests on a viscoelastic foundation (K_1 and K_2 are the coefficients of elastic and viscous resistance). The deflections are small. The role of membrane forces and transverse shear forces in the yield condition and the influence of geometry changes are ignored.

Let the equations for the contour l of the plate be written in a parametric form

$$x = x_1(\varphi), \quad y = y_1(\varphi), \quad \text{with } 0 \leq \varphi \leq 2\pi.$$

Except for singular points, the radius of curvature of the contour l is equal to

$$r(\varphi) = \frac{L^3}{x_1' y_1'' - y_1' x_1''}, \quad (1)$$

$$L(\varphi) = \sqrt{x_1'^2(\varphi) + y_1'^2(\varphi)}, \quad (\cdot)' = \partial(\cdot)/\partial\varphi. \quad (2)$$

To be specific, we assume that the x -size of the plate is not smaller than its geometric size along the y axis. We have two assumptions about the shape of the deformable plate.

Assumption 1. Under the loads slightly higher than the limit load P_0 , a plastic hinge line l_1 is formed in the internal area of the plate (Figure 1). As a result, the plate is deformed into parts of certain ruled surfaces. The normal bending moment on the line l_1 is equal to the limit bending moment M_0 . The line l_1 can consist of several parts (Figure 1 bottom) or degenerate into a point (for a circular plate). The parts of the plastic hinge line l_1 can be either rectilinear or curvilinear. If there are singular points on the contour l then the line l_1 intersects them (the top left and bottom of Figure 1).

We assume that the rate of variation of the angle of plate-surface rotation with respect to the horizontal plane at the contour l is independent of the parameter φ and that the position of the line l_1 is determined

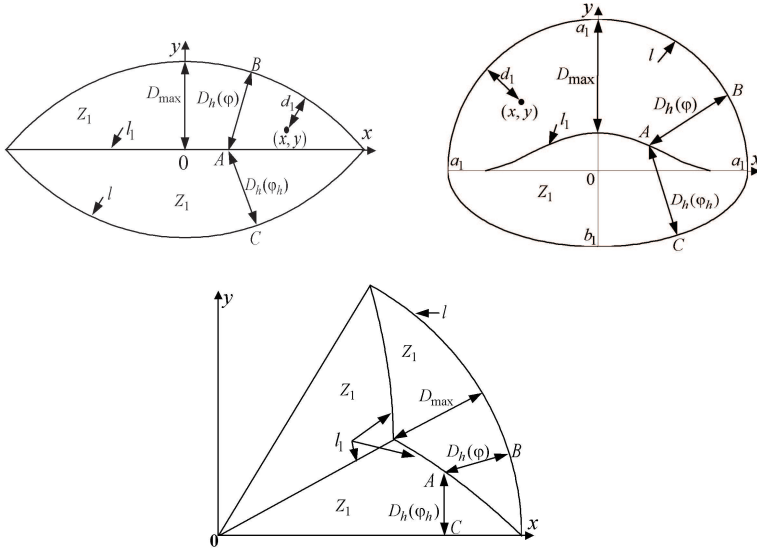


Figure 1. Mechanism 1 for the plates of different shapes.

from the condition of equality of the distances measured along the normal to the external contour l from the line l_1 to the contour l . This assumption is substantiated for a sector plate by Nemirovsky and Romanova [2004], based on the condition of minimum of the limit load. This assumption is obviously valid for a circular plate [Hopkins and Prager 1953].

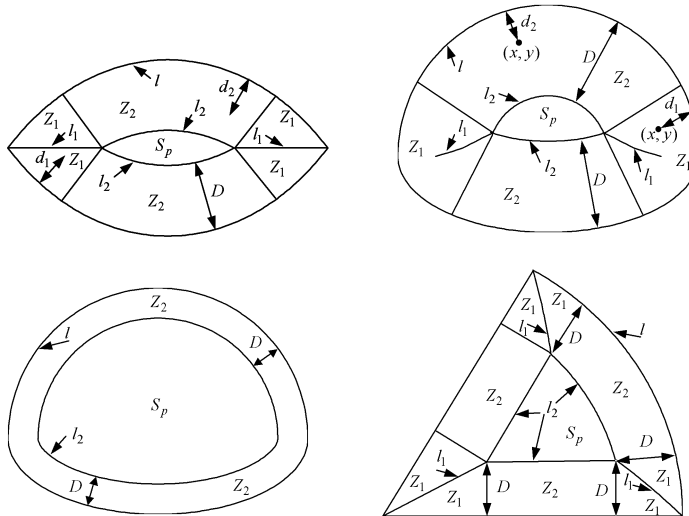


Figure 2. Mechanism 2 and 3 for the plates of different shapes (the positions of the coordinate axes are the same as those in Figure 1).

Assumption 2. Under rather high loads, a region S_p of an intense plastic deformation is formed in the internal area of the plate (Figure 2). The region S_p moves translationally. The contour of the region S_p is the plastic hinge line l_2 , and the normal bending moment on the line l_2 is equal to M_0 .

Let the equations for the line l_1 have the form $x = x_h(\varphi)$, $y = y_h(\varphi)$. The distance D_h measured along the normal to the contour l from the line l to l_1 is

$$D_h(\varphi) = \sqrt{[x_1(\varphi) - x_h(\varphi)]^2 + [y_1(\varphi) - y_h(\varphi)]^2}. \quad (3)$$

From the Assumption 1, it follows that the line l_1 is defined by the system of equations

$$\begin{aligned} x'_1(\varphi)[x_h(\varphi) - x_1(\varphi)] + y'_1(\varphi)[y_h(\varphi) - y_1(\varphi)] &= 0, \\ x'_1(\varphi_h)[x_h(\varphi) - x_1(\varphi_h)] + y'_1(\varphi_h)[y_h(\varphi) - y_1(\varphi_h)] &= 0, \\ D_h(\varphi) = D_h(\varphi_h), \quad x_h(\varphi) = x_h(\varphi_h), \quad y_h(\varphi) = y_h(\varphi_h). \end{aligned} \quad (4)$$

Here φ_h corresponds to φ parameter of the contour l , for which the relation $|AB| = |AC|$ holds (AB , AC are the perpendiculars to the contour l in Figure 1). The plates of different shapes and the positions of the lines l_1 in the plates are presented in Figure 1.

The normal to the contour curve l directed inward the region occupied by the plate gets either on the line l_1 , or on the line l_2 : $x = x_2(\varphi)$, $y = y_2(\varphi)$. We denote by Z_i the region of the plate that does not involve the region S_p in which the normal from any point to the contour l gets on the line l_i for $i = 1, 2$ (Figures 1–2). The number of the regions Z_i depends on the shape of the support counter l of the plate. In Appendix A, it is shown that the normal to the curve l_2 is also the normal to the contour l . In Appendix B, it is shown that, in any smooth part of the contour l , the distance between curves l_2 and l is independent of the parameter φ and the equation for the curve l_2 looks like Equation (B.5) if the region S_p is nonsingular. From the definition of the line l_1 , it follows that at the boundaries of the regions Z_1 and Z_2 the relations $D(t) = D_h(\varphi^b(t)) = D_h(\varphi_h^b(t))$ where φ^b , φ_h^b are the parameters of the boundaries of the regions Z_1 and Z_2 . Consequently, the distance between curves l_2 and l in all regions Z_2 is the same and is equal to $D(t)$ (Figure 2).

Depending on the value of P_{\max} , three mechanisms of deformation are possible in the dynamics of a rigid-plastic plate. Under the loads lower than the limit load (low loads, $0 < P_{\max} \leq P_0$), the plate remains at rest. For the loads slightly higher than the limit load (moderate loads, $P_0 < P_{\max} \leq P_1$) as in the cases of a bending of beams [Mazalov and Nemirovsky 1975; Komarov and Nemirovsky 1984], circular and annular plates [Hopkins and Prager 1953; 1954; Perzyna 1958; Florence 1965; 1966; Youngdahl 1971], rectangular and polygonal plates [Jones et al. 1970; Virma 1972; Mazalov and Nemirovsky 1975; Nemirovsky and Romanova 1987; 1988], the plastic hinge line l_1 is formed in the internal area of the plate (see Assumption 1). Let us call this mechanism of deformation *mechanism 1* (Figure 1). For the values of P_{\max} ($P_{\max} > P_1$) high enough, the dynamics of the plate as the dynamics of all above-listed structures yields the emergence of the intense plastic deformation region S_p that moves translationally (see Assumption 2). Thus, two situations are possible: that the line l_1 is present (*mechanism 2* is presented in the top left, top right and the bottom right of Figure 2 for high loads) and that the line l_1 does not present (*mechanism 3* is presented in the bottom left of Figure 2 for super high loads).

Let us denote

$$\max_{\varphi} D_h(\varphi) = D_{\max} \quad \text{and} \quad \min_{\varphi} D_h(\varphi) = D_{\min}.$$

For the curve l_2 that has no mutually intersected segments, the following conditions must be satisfied.

$$D < D_{\max} \quad \text{and} \quad y_2(\varphi) \geq y_h(\varphi), \quad y_2(\varphi_h) \leq y_h(\varphi_h),$$

(see the plates presented in the top left and top right of Figure 2 for example). Therefore, the curve l_2 presented in (B.5) is not determined for all values of φ . The case $D \geq D_{\max}$ corresponds to mechanism 1 that the region S_p and the curve l_2 are absent (Figure 1); the case $D_{\min} \leq D < D_{\max}$ corresponds to mechanism 2 (top left, top right and the bottom right of Figure 2); the case $D < D_{\min}$ corresponds to mechanism 3. For the plates with singular points on the supporting contour l , equality $D_{\min} = 0$ carries out. Therefore, such plates are not deformed according to mechanism 3 (Figure 2, top left and bottom right) and they have plastic hinge line l_1 present in deformation with any action of the loads exceeding the the limit load. Mechanism 3 is realized only for plates with a smooth contour l (Figure 2, bottom left).

Mechanism 2 corresponds to a general case of deformation of the plate. In the absence of the region S_p , it corresponds to mechanism 1. If the line l_1 is absent then it corresponds to mechanism 3. Let us consider mechanism 2 in detail.

According to mechanism 2, the equations of motion of the plate, that we obtain from the virtual power principle and d’Alembert principle [Erkhov 1978], are

$$K = A - N, \tag{5}$$

$$K = \iint_S \rho \frac{\partial^2 u}{\partial t^2} \frac{\partial u^*}{\partial t} ds, \quad A = \iint_S \left[P(t) - K_1 u - K_2 \frac{\partial u}{\partial t} \right] \frac{\partial u^*}{\partial t} ds, \tag{6}$$

$$N = \sum_m \int_{l_m} M_m \left[\frac{\partial \theta^*}{\partial t} \right]_{l_m} dl_m + M_0 \iint_S (|\kappa_1^*| + |\kappa_2^*|) ds. \tag{7}$$

Here K , A , N are the powers of inertial, external and internal forces in the plate, respectively; S is the area of the plate; u is the deflection; ρ is the surface density of the plate material; t is the current time; ds is the element of area of the plate; m is the index of the lines of discontinuity of angular velocity; l_m are the lines of discontinuity in angular velocity including the contour of the plate; $[\partial \theta / \partial t]_{l_m}$ is the discontinuity in angular velocity on l_m ; M_m is the bending moment on l_m ; dl_m is the element of line for l_m ; κ_1 and κ_2 are the main curvatures of surface of deflection rate of plate. The upper index “*” denotes the admissible velocities. If there is no resistance foundation, Equation (5) coincides with the equation of motion of [Jones 1971a], the axial forces being assumed to equal zero, which means that geometrical changes are ignored. Note that Jones [1971a] suggests using this equation for plates of an arbitrary contour and arbitrary edge conditions; however, it has been used in the literature up to now for circular and rectangular plates only [Jones 1971b; Jones and Shen 1993; Jones 1973; Zhu et al. 1994].

Let us denote the deflection and the velocity of the deflection in the region S_p by $w_c(t)$ and $\dot{w}_c(t)$, where $\dot{f} = \partial f / \partial t$ for function f . Let us denote the angle of rotation of the region Z_2 from the horizontal plane at the supported contour by α . Because of the continuity of velocities at the boundaries of the regions S_p and Z_2 , the rate of variation of this angle α is independent of the parameter φ . Taking into

account of the continuity of velocities at the boundary of the regions Z_1 and Z_2 and Assumption 1, we obtain that the rate of variation of the angle of rotation of the region Z_1 at the supported contour is equal to $\dot{\alpha}(t)$. The deflection rate in the different regions of the plate is given by

$$\begin{aligned} (x, y) \in Z_i : \quad \dot{u}(x, y, t) &= \dot{\alpha}(t)d_i(x, y), \quad i = 1, 2, \\ (x, y) \in S_p : \quad \dot{u}(x, y, t) &= \dot{w}_c(t), \end{aligned} \tag{8}$$

where $d_i(x, y)$ is the distance from a point (x, y) to the supported contour of the region Z_i (Figure 1–2).

We introduce the curvilinear orthogonal coordinate system (v_1, v_2) related to the Cartesian coordinate system by the relations

$$x = x_1(v_2) - v_1 \frac{y'_1(v_2)}{L(v_2)}, \quad y = y_1(v_2) + v_1 \frac{x'_1(v_2)}{L(v_2)}. \tag{9}$$

The curves $v_1 = \text{const}$ are at the distance v_1 from the contour l and have the radius of the curvature $\rho_1 = r(v_2) - v_1$. The straight lines $v_2 = \text{const}$ are the perpendiculars to the external contour l of the plate. Their radius of the curvature is $\rho_2 = \infty$. The element of area is $ds = L(1 - v_1/r)dv_1dv_2$. Then the equation of the supported contour l has the form $v_1 = 0$ for $0 \leq v_2 \leq 2\pi$. If the line l_1 consists of one part then its equation has the form $v_1 = D_h(v_2)$ for $0 \leq v_2 \leq \varphi_1$, $\varphi_2 \leq v_2 \leq \pi$. The equation of the line l_2 has the form $v_1 = D(t)$ for $\varphi_1 \leq v_2 \leq \varphi_2$, $\varphi_{h2} \leq v_2 \leq \varphi_{h1}$ where, for $i = 1, 2$, φ_i, φ_{hi} are boundary values.

Then the deflection rate of the plate (8) is given by:

$$\begin{aligned} (x, y) \in Z_i : \quad \dot{u}(v_1, v_2, t) &= \dot{\alpha}(t)v_1, \quad i = 1, 2, \\ (x, y) \in S_p : \quad \dot{u}(v_1, v_2, t) &= \dot{w}_c(t). \end{aligned} \tag{10}$$

With the introduced denotations and (10) taken into account, the expressions (6) become

$$\begin{aligned} K &= \rho \left[\dot{\alpha}^* \ddot{\alpha} \sum_{i=1}^2 \iint_{Z_i} v_1^2 ds + \dot{w}_c^* \ddot{w}_c \iint_{S_p} ds \right], \\ A &= \dot{\alpha}^* \sum_{i=1}^2 \iint_{Z_i} [P(t) - K_1 \alpha v_1 - K_2 \dot{\alpha} v_1] v_1 ds + \dot{w}_c^* \iint_{S_p} [P(t) - K_1 w_c - K_2 \dot{w}_c] ds. \end{aligned} \tag{11}$$

We represent the expression (7) for the power of internal forces in the plate in the form

$$N = \sum_{i=1}^4 N_i \tag{12}$$

where N_1, N_2, N_3, N_4 are the powers of internal forces on the contour l , in the regions Z_1 and Z_2 , on the line l_2 and on the line l_1 , respectively:

$$\begin{aligned} N_1 &= (1 - \eta)M_0 \oint_l [\dot{\theta}^*]_l dl, & N_2 &= M_0 \iint_{Z_1 \cup Z_2} (|\kappa_1^*| + |\kappa_2^*|) ds, \\ N_3 &= M_0 \oint_{l_2} [\dot{\theta}^*]_{l_2} dl_2, & N_4 &= M_0 \int_{l_1} [\dot{\theta}^*]_{l_1} dl_1. \end{aligned} \tag{13}$$

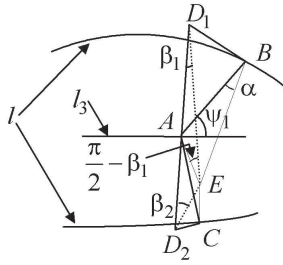


Figure 3. Supplementary construction for the calculation of the discontinuity of angular velocity on l_1 .

Here $\eta = 0$ for the clamped contour l and $\eta = 1$ for the simply supported contour.

From (10) and the normal to the line l_2 is the normal to the contour l , it follows that

$$[\dot{\theta}^*]_l = [\dot{\theta}^*]_{l_2} = \dot{\alpha}, \quad \kappa_1 = \frac{\partial^2 \dot{u}}{\partial v_1^2} = 0, \quad \kappa_2 = \frac{1}{\rho_1} \frac{\partial \dot{u}}{\partial v_1} = \frac{\dot{\alpha}(t)}{r - v_1}.$$

Then we have

$$N_1 = (1 - \eta) M_0 \dot{\alpha}^* \int_0^{2\pi} L dv_2,$$

$$N_2 = M_0 \dot{\alpha}^* \iint_{Z_1 \cup Z_2} \frac{1}{r - v_1} ds$$

$$= M_0 \dot{\alpha}^* \left[\int_0^{\varphi_1} \frac{L D_h}{r} dv_2 + \left(\int_{\varphi_1}^{\varphi_2} \frac{L}{r} dv_2 \right) D(t) + \int_{\varphi_2}^{\varphi_{h2}} \frac{L D_h}{r} dv_2 + \left(\int_{2\pi - \varphi_{h2}}^{2\pi - \varphi_{h1}} \frac{L}{r} dv_2 \right) D(t) + \int_{\varphi_{h1}}^{2\pi} \frac{L D_h}{r} dv_2 \right], \tag{14}$$

$$N_3 = M_0 \dot{\alpha}^* \oint_{l_2} dl_2 = M_0 \dot{\alpha}^* \left\{ \int_{\varphi_1}^{\varphi_2} L \left[1 - \frac{D(t)}{r} \right] dv_2 + \int_{\varphi_{h2}}^{\varphi_{h1}} L \left[1 - \frac{D(t)}{r} \right] dv_2 \right\}.$$

To calculate N_4 in (13), we have

$$dl_1 = L_h dv_2, \quad \text{where } L_h = \sqrt{x_h'^2 + y_h'^2}. \tag{15}$$

We consider a case where the line l_1 consists of one part. For the calculation of $[\dot{\theta}^*]_{l_1}$ with $v_2 \in [0, \varphi_1]$ at point $A = (D_h(v_2), v_2) \in l_1$ of the undeformed plate, we draw the perpendiculars AB and AC that they intersect the contour l at $B = (0, v_2)$ and $C = (0, v_{2h})$ so $AB \perp l$, $AC \perp l$, $|AB| = |AC| = D_h(v_2)$ (Figure 1, 3). At point A , we draw the line l_3 which is tangent to the line l_1 . Through the segment AB , we draw the plane ABE which is perpendicular to an initial surface of the plate, where $AE \perp AB$ (Figure 3). We draw the plane BED_1 which is tangent to the deformed surface of the plate along the straight line BE . Then we have $\angle ABE = \alpha$. Through point B , we draw the plane AED_1 which is perpendicular to the line l_3 . Let us denote $\angle AD_1E = \beta_1$. With the similar constructions for point C , we obtain point

D_2 such that the equality $\angle AD_2E = \beta_2$ holds. Then we have $[\dot{\theta}^*]_{l_1}(v_2) = \dot{\beta}_1 + \dot{\beta}_2$. From $|AE| = |AB|\alpha$, $|AE| = |AD_1|\beta_1$ and $AB \perp BD_1$, it follows that

$$\dot{\beta}_1 = \dot{\alpha} \sin \psi_1, \tag{16}$$

where ψ_1 is the minimum angle between the segment AB and the line l_3 such that

$$\sin \psi_1 = \frac{y'_1 y'_h + x'_1 x'_h}{LL_h}. \tag{17}$$

In a similar manner, $\dot{\beta}_2 = \dot{\alpha} \sin \psi_2$ where ψ_2 is the minimum angle between the segment AC and the line l_3 . From (15)–(17), it follows that

$$\dot{\beta}_1 dl_1 = \dot{\alpha} \frac{y'_1 y'_h + x'_1 x'_h}{L} dv_2.$$

From (1), (3), (4), it follows that

$$\frac{y'_1 y'_h + x'_1 x'_h}{L} = L \left[1 - \frac{D_h(v_2)}{r} \right];$$

then we have

$$\dot{\beta}_1 dl_1 = \dot{\alpha} L \left[1 - \frac{D_h(v_2)}{r} \right] dv_2 \quad \text{for } v_2 \in [0, \varphi_1].$$

In a like manner, we obtain

$$\dot{\beta}_2 dl_1 = \dot{\alpha} L \left[1 - \frac{D_h(v_2)}{r} \right] dv_2 \quad \text{for } v_2 \in [\varphi_{h1}, 2\pi].$$

We have similar expression for $v_2 \in [\varphi_2, \pi]$ and $v_2 \in [\pi, \varphi_{h2}]$. Then the expression (13) for N_4 looks like

$$N_4 = M_0 \dot{\alpha}^* \left[\int_0^{\varphi_1} L \left(1 - \frac{D_h}{r} \right) dv_2 + \int_{\varphi_2}^{\varphi_{h2}} L \left(1 - \frac{D_h}{r} \right) dv_2 + \int_{\varphi_{h1}}^{2\pi} L \left(1 - \frac{D_h}{r} \right) dv_2 \right]. \tag{18}$$

Substituting the expressions (14), (18) into (12), we get the power of internal forces in the plate

$$N = M_0(2 - \eta) \dot{\alpha}^* \int_l dl. \tag{19}$$

The expression (19) for the cases of smooth or pyramidal shape of the deformable plate coincides with the result obtained by Rzhantsyn [1982]. It is possible to show that the expression (7) for the power of internal forces has the form (19) also in the case that the line l_1 consists of several parts.

Substituting equalities (11), (19) into (5) and taking into account that $\dot{w}_c^*(t)$ and $\dot{\alpha}^*(t)$ are independent, we obtain the following equations of motion

$$(\rho \ddot{\alpha} + K_2 \dot{\alpha} + K_1 \alpha) \sum_i \iint_{Z_i} v_1^2 ds = P(t) \sum_i \iint_{Z_i} v_1 ds - M_0(2 - \eta) \int_l dl, \quad (i = 1, 2) \tag{20}$$

$$\rho \ddot{w}_c + K_2 \dot{w}_c + K_1 w_c = P(t). \tag{21}$$

The condition of the continuity of velocities at the boundaries of the regions S_p and Z_2 yields the equality

$$\dot{\alpha}D = \dot{w}_c. \quad (22)$$

At the boundaries of the regions Z_1 and Z_2 , we have the following relations

$$D = D_h(v_{2j}) \quad (23)$$

where $j = 1, \dots$ and $v_{2j}(t)$ are the parameters of the boundaries of the regions Z_1 and Z_2 .

At the initial time, the plate is at rest and undeformed as

$$\alpha(t_0) = \dot{\alpha}(t_0) = w_c(t_0) = \dot{w}_c(t_0) = 0. \quad (24)$$

The initial value $D_0 = D(t_0)$ depends on the value of P_{\max} . This is shown below for some special cases.

The system of Equations (20)–(23), for $i = 1, 2$ describes the plate motion according to mechanism 2. In the case of deformation according to mechanism 1, the regions S_p and Z_2 are absent and the plate motion is described by Equation (20) for $i = 1$. In the case of deformation according to mechanism 3, the region Z_1 does not present and the behavior of the plate is governed by Equations (20)–(22) for $i = 2$.

The method described in the present work is used to study the dynamic behavior of the following plates in the absence of resistance foundation: elliptical plates [Nemirovsky and Romanova 2002a], a plate with a contour consisting of a semicircle of radius a_1 and a semiellipse with semiaxes a_1 and b_1 with $b_1 \leq a_1$ (the top right of Figure 1, the top right, bottom left of Figure 2) [Nemirovsky and Romanova 2002b], a plate with a contour consisting of straight-line and arbitrary smooth curvilinear parts [Nemirovsky and Romanova 2002c], a plate with a contour consisting of two semicircles and two straight-line segments [Nemirovsky and Romanova 2001b], sector plates [Nemirovsky and Romanova 2004] (the bottom of Figure 1 and the bottom right of Figure 2).

Below we consider the examples of the dynamic behavior of plates of an arbitrary contour in the absent of visco-elastic foundation. The method proposed in the present work allows to take into account resistance foundation. The influence of visco-elastic foundation on final deflections and the opportunity of the optimization of the process of pulsed forming of metal plates of sophisticated contour were discussed by Nemirovsky and Romanova [1991; 2001a].

3. Dynamic behavior of a rigid-plastic astroid-shaped plate

We consider the dynamic behavior of the plates of an arbitrary contour by an example of the astroid-shaped plate whose contour is written in a parametric form $x_1 = a \cos^3 \varphi$ and $y_1 = a \sin^3 \varphi$ with $0 \leq \varphi \leq 2\pi$ (Figure 4 left). For this plate, we have

$$L(\varphi) = 3a|\sin \varphi \cos \varphi|, \quad D_h(\varphi) = a|\sin^3 \varphi / \cos \varphi|, \quad D_{\max} = D_h(\pi/4) = a/2.$$

Depending on the value of P_{\max} , two mechanisms of deformation are possible for the plate being considered. Under moderate loads, the plate is deformed into four parts of a ruled surface with the formation of four rectilinear plastic hinge lines located on the coordinate axes (mechanism 1 is presented in Figure 4, left). Under high loads, the region S_p is formed in the central part of the plate. The region S_p moves translationally (mechanism 2 is presented in Figure 4, right). Equation (B.5) for the contour of S_p

becomes

$$x_2 = a \cos^3 \varphi - D \sin \varphi \operatorname{sign}(\sin 2\varphi), \quad y_2 = a \sin^3 \varphi - D \cos \varphi \operatorname{sign}(\sin 2\varphi)$$

where

$$\begin{aligned} \varphi_D \leq \varphi \leq \pi/2 - \varphi_D, \quad \pi/2 + \varphi_D \leq \varphi \leq \pi - \varphi_D, \\ \pi + \varphi_D \leq \varphi \leq 3\pi/2 - \varphi_D, \quad 3\pi/2 + \varphi_D \leq \varphi \leq 2\pi - \varphi_D. \end{aligned}$$

$\varphi_D(t)$ is the parameter determining the size of the region S_p and $0 < \varphi_D \leq \pi/4$. The regions S_p and Z_2 are not present if $\varphi_D = \pi/4$.

Equations (20), (21), (23) for mechanism 2 of the astroid-shaped plate in the absence of resistance foundation look like

$$\rho \ddot{\alpha}(\Sigma_1 + \Sigma_2) = P(t)(\Sigma_3 + \Sigma_4) - M_0(2 - \eta)\Sigma_5, \tag{25}$$

$$\rho(\dot{\alpha}D)' = P(t), \tag{26}$$

$$D = \Sigma_6. \tag{27}$$

Here

$$\begin{aligned} \Sigma_1(\varphi_D) &= \iint_{Z_1} v_1^2 ds = 8 \int_0^{\varphi_D} \left[\int_0^{D_h(v_2)} v_1^2 F(v_1, v_2) dv_1 \right] dv_2 \\ &= \frac{2a^4}{3} \left(\frac{\sin^{11} \varphi_D}{\cos^3 \varphi_D} + \frac{\sin^9 \varphi_D}{\cos \varphi_D} + \frac{9}{8} \sin^7 \varphi_D \cos \varphi_D + \frac{63}{48} \sin^5 \varphi_D \cos \varphi_D \right. \\ &\quad \left. + \frac{315}{192} \sin^3 \varphi_D \cos \varphi_D - \frac{315}{128} (\varphi_D - \sin \varphi_D \cos \varphi_D) \right), \end{aligned}$$

$$\Sigma_2(\varphi_D) = \iint_{Z_2} v_1^2 ds = 8 \int_{\varphi_D}^{\pi/4} \left[\int_0^D v_1^2 F(v_1, v_2) dv_1 \right] dv_2$$

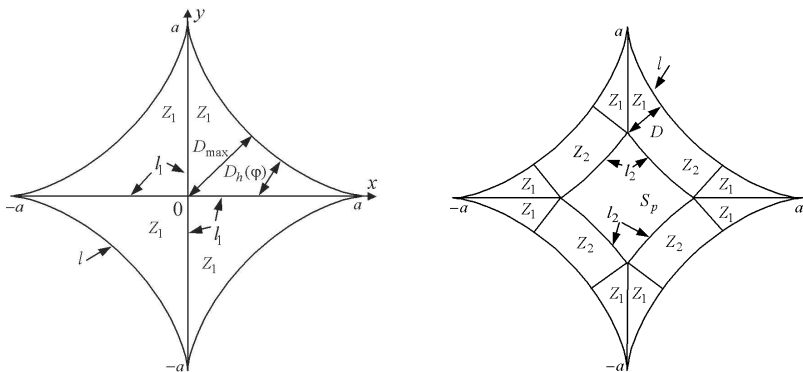


Figure 4. Mechanism 1 (left) and 2 (right) for astroid-shaped plate (the positions of the coordinate axes on the right are the same as those on the left).

$$= \frac{2a^4 \sin^9 \varphi_D}{\cos^3 \varphi_D} \left[\frac{\sin^3 \varphi_D}{\cos \varphi_D} (\pi/4 - \varphi_D) + 1 - 2 \sin^2 \varphi_D \right],$$

$$\begin{aligned} \Sigma_3(\varphi_D) &= \iint_{Z_1} v_1 ds = 8 \int_0^{\varphi_D} \left[\int_0^{D_h(v_2)} v_1 F(v_1, v_2) dv_1 \right] dv_2 \\ &= \frac{4a^3}{3} \left(\frac{\sin^{10} \varphi_D}{\cos^2 \varphi_D} + \sin^8 \varphi_D - \frac{\sin^6 \varphi_D}{6} - \frac{\sin^4 \varphi_D}{4} - \frac{\sin^2 \varphi_D}{2} - \ln \cos \varphi_D \right), \end{aligned}$$

$$\begin{aligned} \Sigma_4(\varphi_D) &= \iint_{Z_2} v_1 ds = 8 \int_{\varphi_D}^{\pi/4} \left[\int_0^D v_1 F(v_1, v_2) dv_1 \right] dv_2 \\ &= \frac{2a^3 \sin^6 \varphi_D}{3 \cos^2 \varphi_D} \left[\frac{4 \sin^3 \varphi_D}{\cos \varphi_D} (\pi/4 - \varphi_D) + 9 \left(\frac{1}{2} - \sin^2 \varphi_D \right) \right], \end{aligned}$$

$$\Sigma_5 = \int_l dl = 8 \int_0^{\pi/4} L(\varphi) d\varphi = 6a,$$

$$\Sigma_6(\varphi_D) = a \sin^3 \varphi_D / \cos \varphi_D,$$

where $F(v_1, v_2) = v_1 + 3a \sin v_2 \cos v_2$.

If $0 < P_{\max} \leq P_0$ (low loads), the plate remains undeformed. We determine the limit load P_0 from Equation (25) at the moment t_0 of the beginning of the deformation (24) and from the condition $\ddot{\alpha}(t_0) = 0$,

$$P_0 = \min_{0 < \varphi_D \leq \pi/4} \frac{M_0(2 - \eta) \Sigma_5}{\Sigma_3 + \Sigma_4} = \frac{M_0(2 - \eta) \Sigma_5}{\Sigma_3(\pi/4)} \approx 32.55 \frac{M_0(2 - \eta)}{a^2}.$$

Thus the region S_p degenerates into a point which is the center of the coordinates.

If $P_0 < P_{\max} \leq P_1$ (moderate loads), where P_1 is the load under which the region S_p appears, the plate is deformed in accordance with mechanism 1. We determine the load P_1 as follows. From (25), (26) we eliminate $\ddot{\alpha}$. As a result, we have

$$-\frac{\rho \dot{\alpha} \dot{D}}{D} (\Sigma_1 + \Sigma_2) = P(t) \left[\Sigma_3 + \Sigma_4 - \frac{\Sigma_1 + \Sigma_2}{D} \right] - M_0(2 - \eta) \Sigma_5. \tag{28}$$

Taking into account that the relations

$$\dot{\alpha}(t_0) = 0, \quad P_1 = P(t_0), \quad \varphi_D(t_0) = \pi/4, \quad D(t_0) = a/2$$

hold if the region S_p appears at the initial time t_0 whereas the regions S_p and Z_2 are absent, we obtain from (28) that

$$P_1 = \frac{M_0(2 - \eta) \Sigma_5}{\Sigma_3(\pi/4) - \frac{2}{a} \Sigma_1(\pi/4)} \approx 63.33 \frac{M_0(2 - \eta)}{a^2}.$$

For moderate loads, the plate motion is governed by the Equation (25) for $\varphi_D = \pi/4$, which becomes

$$\ddot{\alpha}(t) = G[P(t) - P_0] \tag{29}$$

where $G = \Sigma_3(\pi/4)/[\rho\Sigma_1(\pi/4)]$. The initial conditions have the form (24). The load is removed at the time $t = T$, and the plate moves inertially for certain time.

For $t_0 \leq t \leq T$, integrating Equation (29), we have

$$\dot{\alpha}(t) = G \left[\int_{t_0}^t P(\tau) d\tau - P_0(t - t_0) \right], \quad \alpha(t) = G \left[\int_{t_0}^t \int_{t_0}^m P(\tau) d\tau dm - P_0 \frac{(t - t_0)^2}{2} \right].$$

At $T < t \leq t_f$, the motion of the plate occurs due to inertia until the plate stops at the time t_f and it is governed by the equation $\ddot{\alpha}(t) = -GP_0$ with the initial conditions $\dot{\alpha}(T), \alpha(T)$. The moment t_f is determined by the condition

$$\dot{\alpha}(t_f) = 0. \tag{30}$$

Integrating the equation of motion, we obtain

$$\begin{aligned} \dot{\alpha}(t) &= \dot{\alpha}(T) - GP_0(t - T), \\ \alpha(t) &= \alpha(T) + \dot{\alpha}(T)(t - T) - GP_0(t - T)^2/2. \end{aligned} \tag{31}$$

It follows Equations (30), (31) that

$$t_f = t_0 + \int_{t_0}^T P(t) dt / P_0. \tag{32}$$

The deflections are calculated from (8) or (10). The maximum final deflection is in the center of the plate and it is

$$w_{\max} = D_{\max} G \left[\left(\int_{t_0}^T P(t) dt \right)^2 / (2P_0) - \int_{t_0}^T (t - t_0) P(t) dt \right]. \tag{33}$$

If $P_{\max} > P_1$ (high loads), the plate motion begins with the developed region S_p and $\varphi_0 = \varphi_D(t_0)$ which is less than $\pi/4$. The initial value φ_0 is determined by Equation (28) with the equality $\dot{\alpha}(t_0) = 0$ and the relation (27):

$$P_{\max} \left[\Sigma_3(\varphi_0) + \Sigma_4(\varphi_0) - \frac{\Sigma_1(\varphi_0) + \Sigma_2(\varphi_0)}{\Sigma_6(\varphi_0)} \right] = M_0(2 - \eta)\Sigma_5. \tag{34}$$

In the first phase ($t_0 < t \leq t_1$) of deformation, the plate motion occurs according to mechanism 2 and is described by Equations (22), (25)–(27) with the initial conditions (24) and (34). In this phase, the region S_p decreases by the law described by Equation (28). The time t_1 corresponding to the disappearance of the region S_p is determined by the equality $\varphi_D(t_1) = \pi/4$. At the end of this phase, the values of $\dot{\alpha}(t_1)$ and $\alpha(t_1)$ are determined.

The second phase ($t_1 < t \leq t_f$) of the plate motion occurs according to mechanism 1 until the stop at the time t_f . The deformation is governed by Equation (29) subject to the initial conditions determined at the end of the first phase. The time t_f is determined by (30). All deflections in the plate are calculated from (8) or (10) and (22) with allowance for all phases of motion.

In the case of high load represented by a rectangular pulse ($P(t) = P_{\max}$ for $t_0 \leq t \leq T$ and $P(t) = 0$ for $t > T$), the motion occurs with the constant region S_p during the action of the load ($t_0 \leq t \leq T$) and is described by Equations (22), (25)–(27) for $\varphi_D = \varphi_0$ determined from (34) with the initial conditions (24). After removal of the load, the second and the third phases of motion ($T < t \leq t_1$ and $t_1 < t \leq t_f$) occur.

They are described by the same equations in the first and second phases of motion of the plate under explosive loading but for the condition $P(t) = 0$.

The results of the deflections $w = ua^2\rho/(M_0T^2)$ of the simply supported astroid-shaped plate in the cross section $y = x$ are shown in Figure 5. Curves 1–3 correspond to the deflections of the plate under a high load of a rectangular pulse with $P_{\max} = 135.27M_0/a^2$ at the times $t = T$, $t = t_1 = 2.14T$, $t = t_f = 4.16T$, respectively. Curves 4–6 refer to the deflections of the plate under a high load with a linear decreasing ramp time ($P(t) = 310.28(T - t)M_0/a^2$ for $0 \leq t \leq T$ and $P(t) = 0$ for $t > T$) at the times $t = T$, $t = t_1 = 2.5T$, $t = t_f = 4.77T$, respectively. The numerical calculations show that

$$t_1 = I/P_1, \quad t_f = I/P_0, \tag{35}$$

where $I = \int_0^T P(t)dt$ is the full pulse of the load.

4. Dynamic behavior of a plate whose contour consists of two arcs of circle

As another example, we consider the dynamic behavior of the plate with a contour consisting of two arcs of circle of the radius R and the central corner 2γ (Figure 1, top left; Figure 6). For this plate, $v_1 = R - r_1$, $v_2 = \phi$ where (r_1, ϕ) is the polar coordinate system with the pole located in the point $x = 0, y = -R \cos \gamma$. We have

$$D_h(\varphi) = R[1 - \cos \varphi / \cos(\gamma - \varphi)], \quad D_{\max} = D_h(\gamma) = R(1 - \cos \gamma)$$

with $0 \leq \varphi \leq \gamma$ and $0 < \gamma \leq \pi/2$. Depending on the value of P_{\max} , two mechanisms of deformation are possible for this plate. Under moderate loads, the plate is deformed into two parts of a cone surface with the formation of the rectilinear plastic hinge line locating on the x -axis (mechanism 1 is presented in Figure 1, top left). Under high loads, the region S_p is formed in the central part of the plate. The region S_p moves translationally (mechanism 2 is presented in Figure 6). The contour of the region S_p consists of two arcs of circle of the radius $R - D$ and the central corner $2(\gamma - \varphi_D)$, where $\varphi_D(t)$ is the parameter determining the size of the region S_p ($0 < \varphi_D \leq \gamma$). At $\varphi_D = \gamma$, the regions S_p and Z_2 are not present.

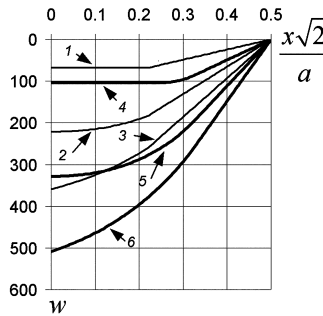


Figure 5. Deflections of a simply supported astroid-shaped plate in the cross section $x = y$.

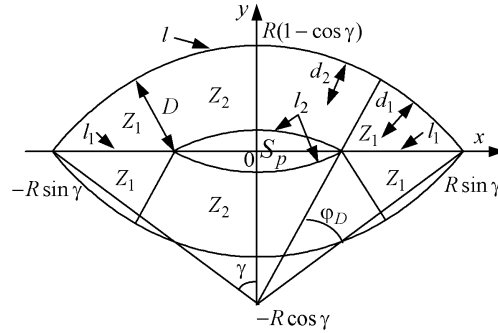


Figure 6. Mechanism 2 for the plate with a contour consisting of two arcs of a circle.

The equations of motion (20)–(23) for mechanism 2 of the plate being considered in the absence of resistance foundation look like (22), (25)–(27) where

$$\begin{aligned} \Sigma_1(\varphi_D) &= \iint_{Z_1} d_1^2 ds = 4 \int_0^{\varphi_D} \left[\int_{\frac{R \cos \gamma}{\cos(\gamma - \varphi)}}^R r_1 (R - r_1)^2 dr_1 \right] d\varphi \\ &= \frac{R^4}{3} \left\{ \varphi_D - 2 \cos^2 \gamma (3 + \cos^2 \gamma) [\operatorname{tg} \gamma - \operatorname{tg}(\gamma - \varphi_D)] \right. \\ &\quad \left. + 4 \cos^3 \gamma \left[\frac{\operatorname{tg} \gamma}{\cos \gamma} - \frac{\operatorname{tg}(\gamma - \varphi_D)}{\cos(\gamma - \varphi_D)} + \ln \frac{\cos \gamma [1 - \sin(\gamma - \varphi_D)]}{\cos(\gamma - \varphi_D)(1 - \sin \gamma)} \right] + \cos^4 \gamma \left[\frac{\sin(\gamma - \varphi_D)}{\cos^3(\gamma - \varphi_D)} - \frac{\sin \gamma}{\cos^3 \gamma} \right] \right\}, \\ \Sigma_2(\varphi_D) &= \iint_{Z_2} d_2^2 ds = 4 \int_0^{\gamma - \varphi_D} \left[\int_{R-D}^R r_1 (R - r_1)^2 dr_1 \right] d\varphi \\ &= \frac{(\gamma - \varphi_D) R^4}{3} \left[1 - \frac{\cos \gamma}{\cos(\gamma - \varphi_D)} \right]^3 \left[1 + \frac{3 \cos \gamma}{\cos(\gamma - \varphi_D)} \right], \\ \Sigma_3(\varphi_D) &= \iint_{Z_1} d_1 ds = 4 \int_0^{\varphi_D} \left[\int_{\frac{R \cos \gamma}{\cos(\gamma - \varphi)}}^R r_1 (R - r_1) dr_1 \right] d\varphi = \frac{2R^3}{3} \left\{ \varphi_D - \cos^2 \gamma [2 \operatorname{tg} \gamma - 3 \operatorname{tg}(\gamma - \varphi_D)] \right. \\ &\quad \left. + \cos^3 \gamma \left[\ln \frac{\cos \gamma [1 - \sin(\gamma - \varphi_D)]}{\cos(\gamma - \varphi_D)(1 - \sin \gamma)} - \frac{\operatorname{tg}(\gamma - \varphi_D)}{\cos(\gamma - \varphi_D)} \right] \right\}, \\ \Sigma_4(\varphi_D) &= \iint_{Z_2} d_2 ds = 4 \int_0^{\gamma - \varphi_D} \left[\int_{R-D}^R r_1 (R - r_1) dr_1 \right] d\varphi \\ &= \frac{2(\gamma - \varphi_D) R^3}{3} \left[1 - \frac{\cos \gamma}{\cos(\gamma - \varphi_D)} \right]^2 \left[1 + \frac{2 \cos \gamma}{\cos(\gamma - \varphi_D)} \right], \end{aligned}$$

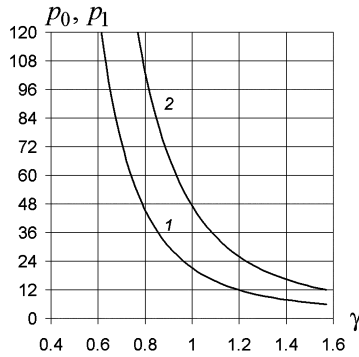


Figure 7. Dimensionless loads p_0 (curve 1) and p_1 (curve 2) for plate with a contour consisting of two arcs of a circle.

$$\Sigma_5 = \int_l dl = 4\gamma R,$$

$$\Sigma_6(\varphi_D) = R[1 - \cos \gamma / \cos(\gamma - \varphi_D)].$$

The analysis of the dynamic behavior of the plate being considered is similar to the analysis performed above for the astroid-shaped plate. We present some results. The limit load is calculated by the formula

$$\begin{aligned} P_0 &= \min_{0 < \varphi_D \leq \gamma} \frac{M_0(2 - \eta)\Sigma_5}{\Sigma_3 + \Sigma_4} = \frac{M_0(2 - \eta)\Sigma_5}{\Sigma_3(\gamma)} \\ &= \frac{M_0(2 - \eta)}{R^2} \frac{6\gamma}{\gamma - \sin 2\gamma + \cos^3 \gamma \ln[\cos \gamma / (1 - \sin \gamma)]}. \end{aligned} \tag{36}$$

The load P_1 under which the region S_p appears is found by the formula

$$\begin{aligned} P_1 &= \frac{M_0(2 - \eta)\Sigma_5}{\Sigma_3(\gamma) - \Sigma_1(\gamma)/D_{\max}} \\ &= \frac{12M_0(2 - \eta)\gamma}{R^2} \left/ \left[2 \left(\gamma - \sin 2\gamma + \cos^3 \gamma \ln \frac{\cos \gamma}{1 - \sin \gamma} \right) \right. \right. \\ &\quad \left. \left. - \frac{\gamma - 3 \sin \gamma \cos \gamma + 2 \cos^3 \gamma \left(2 \ln \frac{\cos \gamma}{1 - \sin \gamma} - \sin \gamma \right)}{1 - \cos \gamma} \right] \right. \end{aligned} \tag{37}$$

For the central corner $\gamma = \pi/2$, the plate being considered becomes a circular plate of the radius R . The limit load for it from the formula (36) is $P_0 = 6M_0(2 - \eta)/R^2$. In the simply supported case, this value is equal to the exact value of the limit load \bar{P}_0 obtained by Hopkins and Prager [1954]. For the clamped contour, the limit load from the formula (36) is equal to $2\bar{P}_0$. In [Florence 1966], it is obtained as a result of the approached decision using the Tresca yield criterion and is equal to $1.875\bar{P}_0$. For a circular plate, the formula (37) gives $P_1 = 2P_0$. In the simply supported case, this result coincides with those obtained by Hopkins and Prager [1954] and Perzyna [1958]. In the clamped case, Florence [1966] obtained that $P_1 = 1.998 \times 1.875\bar{P}_0 = 3.746\bar{P}_0$. Figure 7 shows the dimensionless loads p_0 and p_1 versus

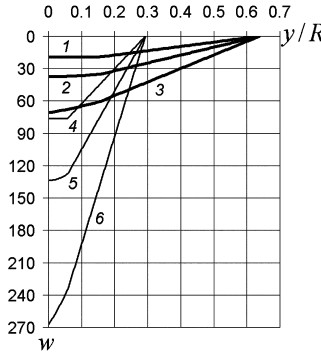


Figure 8. Deflections of a simply supported plate with a contour consisting of two arcs of a circle in the cross section $x = 0$.

the geometrical parameter γ ($p_i = P_i R^2 / [(2 - \eta) M_0]$, $i = 0, 1$). The curves 1, 2 correspond to the loads p_0, p_1 , respectively.

For moderate loads, the final deflection in the center of the plate being considered is calculated from the formula (33) $G = \Sigma_3(\gamma) / [\rho \Sigma_1(\gamma)]$.

The results of the deflections $w = u R^2 \rho / (M_0 T^2)$ of the simply supported plate being considered in the cross section $x = 0$ are in Figure 8. The plate is subjected to a high load represented by rectangular pulse $P(t) = P_m M_0 / R^2$ for $0 \leq t \leq T$ and $P(t) = 0$ for $t > T$. Curves 1–3 correspond to the deflections of the plate with $\gamma = 1, 2, D_{\max} = 0.638R$ and $P_m = 38.37$ at the times $t = T, t = t_1 = 1.48T, t = t_f = 3.22T$, respectively. Curves 4–6 correspond to the deflections of the plate with $\gamma = \pi/4, D_{\max} = 0.293R$ and $P_m = 152.22$ at the times $t = T, t = t_1 = 1.38T, t = t_f = 3.13T$, respectively. As in the case of the astroid plate, the numerical calculations show that the equalities (35) are valid.

For circular simply supported plate ($\gamma = \pi/2, \eta = 1$), the final deflection and the duration of response obtained by the offered method coincide with the result obtained by Perzyna [1958] and Youngdahl [1971].

By the method described in the present work, we analyzed an astroid-shaped plate and a plate with a contour consisting of two arches of circle under explosive loads represented by the various form of a pulse in the absence of resistance foundation. All calculations show that the equalities (35) are valid. In addition, it is established that the plates have the equal final deflections if different loads have two equal integral characteristics I and $I_* = \int_0^T t P(t) dt$. This property for the maximum final deflection is obtained analytically for rigid-plastic circular plates by Youngdahl [1971] and for regular polygonal plates by Nemirovsky and Romanova [1995].

5. Dynamic behavior of a plate with an internal free hole or a rigid insert

The previous result is easy to modify for the determination of the dynamic deformation of the plates of a smooth curvilinear convex contour l , having an internal hole l_2 which can be either free or clamped by an absolutely rigid insert, which is located at the identical distance D_a from the external contour. We assume that $D_a \leq D_{\min}$. The equation of the internal contour l_2 has the form (B.5) for $D = D_a$ (see Appendix B). We consider the following. By the action of the load $P(t)$, the plate is deformed into

a cone-shaped surface without the formation of the region of intense plastic deformation whereas the rigid insert and the points of the internal contour l_2 move translationally with the identical velocity $\dot{w}_c(t)$. Consequently, the angle of rotation of the plate surface around of the contour l is identical for all φ . Let us denote this angle by $\alpha(t)$.

Since, on the internal contour l_2 , the normal bending moment is equal to zero for the free contour and equal to M_0 for the case of a rigid insert, the power of internal forces is

$$N = \dot{\alpha}^* M_0 \left[(2 - \eta) \int_l dl - \beta \int_{l_2} dl \right], \tag{38}$$

where $\beta = 1$ for the case of a free hole and $\beta = 0$ for the plate with a rigid insert. We have

$$\int_l dl = \int_0^{2\pi} L(\varphi) d\varphi, \quad \int_{l_2} dl = \int_0^{2\pi} \sqrt{x'^2_2 + y'^2_2} d\varphi,$$

where $L(\varphi)$ is determined in (2). Taking into account the expression (B.5) for l_2 , we get

$$\int_{l_2} dl = \int_0^{2\pi} L(\varphi) d\varphi - D_a \int_0^{2\pi} \frac{L(\varphi)}{r(\varphi)} d\varphi.$$

Then the expression (38) for N becomes

$$N = \dot{\alpha}^* M_0 \left[(2 - \eta - \beta) \int_0^{2\pi} L(\varphi) d\varphi + D_a \beta \int_0^{2\pi} \frac{L(\varphi)}{r(\varphi)} d\varphi \right].$$

The expressions (6) look like

$$\begin{aligned} K &= \rho \dot{\alpha}^* \ddot{\alpha} \iint_{Z_2} v_1^2 ds + (1 - \beta) \rho_a \dot{w}_c^* \ddot{w}_c \iint_{S_p} ds, \\ A &= \dot{\alpha}^* \left[P(t) \iint_{Z_2} v_1 ds - (K_1 \alpha + K_2 \dot{\alpha}) \iint_{Z_2} v_1^2 ds \right] \\ &\quad + (1 - \beta) \dot{w}_c^* [P(t) - K_1 w_c - K_2 \dot{w}_2] \iint_{S_p} ds, \end{aligned}$$

where ρ_a is the surface density of the insert material. Substituting the expressions K, A, N into (5) and taking into account the condition (22) of continuity of the velocities at the contour l_2 for $D = D_a$, we obtain the equation of motion of the plate under consideration:

$$\begin{aligned} &(\rho \ddot{\alpha} + K_1 \alpha + K_2 \dot{\alpha}) \iint_{Z_2} v_1^2 ds + (1 - \beta) D_a^2 (\rho_a \ddot{\alpha} + K_1 \alpha + K_2 \dot{\alpha}) \iint_{S_p} ds \\ &= P(t) \left[\iint_{Z_2} v_1 ds + (1 - \beta) D_a \iint_{S_p} ds \right] - M_0 \left[(2 - \eta - \beta) \int_0^{2\pi} L(\varphi) d\varphi + D_a \beta \int_0^{2\pi} \frac{L(\varphi)}{r(\varphi)} d\varphi \right]. \end{aligned} \tag{39}$$

The initial conditions look like (24).

We determine the limit load P_0 from (39), (24) and $\ddot{\alpha}(t_0) = 0$. Then, we have

$$P_0 = M_0 \left[(2 - \eta - \beta) \int_0^{2\pi} L(\varphi) d\varphi + D_a \beta \int_0^{2\pi} \frac{L(\varphi)}{r(\varphi)} d\varphi \right] / \left[\iint_{Z_2} v_1 ds + (1 - \beta) D_a \iint_{S_p} ds \right].$$

In the case of an annular plate of radius R with a free internal contour ($\beta = 1$), the limit load is

$$P_0 = \frac{6M_0(1 - \eta + D_a/R)}{D_a^2(3 - 2D_a/R)}.$$

For the simply supported external contour, this result coincides with that obtained by Grigoriev [1953]. For the clamped external contour, this limit load for various D_a/R exceeds the result calculated by Grigoriev [1953] by approximately 7%.

Equation (39) is an ordinary differential equation of 2-nd order with constant coefficients and a variable right part. Methods of solution of the Cauchy problem for such equations are well-known.

We determine the solution of the problem in the case of a free internal hole ($\beta = 1$) and in the absence of resistance foundation ($K_1 = K_2 = 0$). Then Equation (39) becomes (29) for $G = G_1$ where

$$G_1 = \iint_{Z_2} v_1 ds / \left(\rho \iint_{Z_2} v_1^2 ds \right).$$

Therefore, the analysis of the behavior of the plate being considered is similar to the analysis of the behavior of the plate under a moderate load, which is performed above in the part 3, for $G = G_1$ and $D_{\max} = D_a$. The moment that the plate comes to rest is determined by (32). The final deflection on the contour l_2 is calculated from (33). For an annular plate with the simply supported external contour, this result coincides with that obtained by Mroz [1958] for a moderate load.

6. Conclusions

A rigid-plastic model is applied to study the dynamic behavior of simply supported or clamped plates of arbitrary piecewise smooth curvilinear contour under uniformly distributed short-time intensive loads on visco-elastic foundation. Several mechanisms of the dynamic deformation of the plates are considered. For each mechanism, equations of the dynamic deformation are derived. Operating conditions of these mechanisms are analyzed. The equations for the plastic hinge lines in the plate are obtained. A curvilinear orthogonal coordinate system in which double integrals in the equations of motion can be conveniently calculated is proposed. Analytical expressions for the limit and high loads and the maximum final deflections are obtained. Detailed analyses are given for an astroid-shaped plate and for the plate with a contour consisting of two arcs of circle. The calculations show that the fact that different explosive loads having two equal integral characteristics I and I_* is responsible for the identical final deflections of the plates. The governing equations for the behavior of a plate with an internal free hole or a rigid insert are obtained on analytically solvable form and details of the behavior are studied.

Appendix A

We show that the line normal to the curve l_2 is also the normal to the contour l . We approximate the curvilinear contour l by polygonal contour \bar{l} . For the polygonal plate obtained, the contour of the internal region which moves translationally becomes a polygonal contour \bar{l}_2 . Nemirovsky and Romanova [1987; 1988] showed that segments of the internal contour \bar{l}_2 are parallel to the corresponding segments of an external contour \bar{l} and line normal to any segments of \bar{l}_2 is also normal to corresponding side of \bar{l} . Hence, as the number of segments of the polygonal contour \bar{l} tends to be infinity, the contour \bar{l}_2 comes closer and closer to l_2 , and the normal to the curve l_2 at any point of l_2 is also a normal to the contour l .

Appendix B

Let us consider any smooth part of the contour l . We draw the normal to the curve l_2 from point $(x_2, y_2) \in l_2$ so that it intersects l at point $(x_1, y_1) \in l$. The distance between curves l and l_2 is written as $D = \delta r$, where $r(\varphi)$ is the radius of curvature of the curve l and $\delta = \delta(\varphi, t) \geq 0$ is a dimensionless function. The equation for the curve l_2 has the form

$$x_2 = x_1 - \delta(x_1 - \xi), \quad y_2 = y_1 - \delta(y_1 - \varsigma).$$

Here ξ, ς are the coordinates of the center of curvature of the curve l :

$$\xi = x_1 - \frac{y_1' L^2}{x_1' y_1'' - y_1' x_1''}, \quad \varsigma = y_1 + \frac{x_1' L^2}{x_1' y_1'' - y_1' x_1''},$$

where $L(\varphi)$ is given in (2)

Then the equations for the curve l_2 look like

$$x_2 = x_1 - \delta \frac{y_1' L^2}{x_1' y_1'' - y_1' x_1''}, \quad y_2 = y_1 + \delta \frac{x_1' L^2}{x_1' y_1'' - y_1' x_1''}. \tag{B.1}$$

As the normal to the contour l is also the normal to l_2 (Appendix A), we obtain

$$x_2'(x_2 - x_1) + y_2'(y_2 - y_1) = 0, \quad x_1'(x_1 - x_2) + y_1'(y_1 - y_2) = 0.$$

These relations yield

$$x_2' y_1' = y_2' x_1'. \tag{B.2}$$

Differentiating (B.1) and substituting the resulting relations into (B.2), we arrive at the differential equation for the function $\delta(\varphi, t)$

$$\delta' \frac{L^4}{x_1' y_1'' - y_1' x_1''} + \delta \left\{ x_1' \left[\frac{x_1' L^2}{x_1' y_1'' - y_1' x_1''} \right]' + y_1' \left[\frac{y_1' L^2}{x_1' y_1'' - y_1' x_1''} \right]' \right\} = 0.$$

Taking into account the following relations

$$\begin{aligned} x_1' \left[\frac{x_1' L^2}{x_1' y_1'' - y_1' x_1''} \right]' + y_1' \left[\frac{y_1' L^2}{x_1' y_1'' - y_1' x_1''} \right]' &= (x_1' x_1'' + y_1' y_1'') \frac{L^2}{x_1' y_1'' - y_1' x_1''} + (x_1'^2 + y_1'^2) \left[\frac{L^2}{x_1' y_1'' - y_1' x_1''} \right]' \\ &= L L' \frac{L^2}{x_1' y_1'' - y_1' x_1''} + L^2 \left[\frac{L^2}{x_1' y_1'' - y_1' x_1''} \right]' \\ &= L \left[\frac{L^3}{x_1' y_1'' - y_1' x_1''} \right]', \end{aligned}$$

we obtain the solution of the equation for the function $\delta(\varphi, t)$:

$$\delta = \delta_0(x_1' y_1'' - y_1' x_1'')/L^3, \quad \delta_0 = \delta_0(t) \geq 0. \quad (\text{B.3})$$

The radius of curvature $r(\varphi)$ of the curve l has the form (1); then, it follows (B.3) that

$$D = \delta(\varphi, t)r(\varphi) = \delta_0(t). \quad (\text{B.4})$$

Consequently, the distance D between the curves l and l_2 is independent of the parameter φ . With (B.3), (B.4), (B.1) for l_2 becomes

$$x_2 = x_1 - D y_1' / L, \quad y_2 = y_1 + D x_1' / L. \quad (\text{B.5})$$

References

- [Erkhov 1978] M. I. Erkhov, *Theory of ideal plastic solids and structures*, Nauka, Moscow, 1978. (in Russian).
- [Florence 1965] A. L. Florence, "Annular plate loaded by a transverse linear pulse", *AIAA J.* **3**:9 (1965), 1726–1733.
- [Florence 1966] A. L. Florence, "Behavior of a clamped circular rigid-plastic plate under explosive pressure", *Trans ASME (Ser. E, J. Appl. Mech.)* **33**:2 (1966), 11–17.
- [Grigoriev 1953] A. S. Grigoriev, "On the load-carrying capacities of the annular plates", *Ingen. Sbornik* **16** (1953), 177–182. (in Russian).
- [Hopkins and Prager 1953] H. G. Hopkins and W. Prager, "The load-carrying capacities of circular plates", *J. Mech. Phys. Solids* **2**:1 (1953), 1–13.
- [Hopkins and Prager 1954] H. G. Hopkins and W. Prager, "On the dynamics of plastic circular plates", *Z. Angew. Math. Phys.* **5** (1954), 317–330.
- [Jones 1971a] N. Jones, "A theoretical study of the dynamic plastic behavior of beams and plates with finite-deflections", *Int. J. Solids Struct.* **7** (1971a), 1007–1029.
- [Jones 1971b] N. Jones, "Large deflection of rectangular plates", *J. Ship Res.* **15**:2 (1971b), 164–171.
- [Jones 1973] N. Jones, "Slamming damage", *J. Ship Res.* **17**:2 (1973), 80–86.
- [Jones and Shen 1993] N. Jones and W. Q. Shen, "Dynamic response and failure of fully clamped circular plates under impulsive loading", *Int. J. Impact Eng.* **13**:2 (1993), 259–278.
- [Jones et al. 1970] N. Jones, T. O. Uran, and S. A. Tekin, "The dynamic plastic behavior of fully clamped rectangular plates", *Int. J. Solids Struct.* **6**:2 (1970), 1499–1512.
- [Komarov and Nemirovsky 1984] K. L. Komarov and Y. V. Nemirovsky, *Dynamics of rigid-plastic structural elements*, Nauka, Novosibirsk, 1984. (in Russian).
- [Mazalov and Nemirovsky 1975] V. N. Mazalov and Y. V. Nemirovsky, "Dynamics of thin-walled plastic structures", pp. 155–247 in *Dynamic Problems of Plastic Media (ser. Mech.)*, vol. 5, 1975.
- [Mroz 1958] Z. Mroz, "Plastic deformations of annular plates under dynamic loads", *Arch. Mech. Stos.* **10** (1958), 499–516.

- [Nemirovsky and Romanova 1987] Y. V. Nemirovsky and T. P. Romanova, “Dynamic behavior of doubly connected polygonal plastic plates”, *Int. Appl. Mech.* **23**:5 (1987), 458–464.
- [Nemirovsky and Romanova 1988] Y. V. Nemirovsky and T. P. Romanova, “Dynamic bending of polygonal plastic slabs”, *J. Appl. Mech. Tech. Phys.* **29**:4 (1988), 591–597.
- [Nemirovsky and Romanova 1991] Y. V. Nemirovsky and T. P. Romanova, “Dynamics of polygonal plastic plates with rounded corners”, *Strength Mater. (Ukraine)* **32**:9 (1991), 62–66.
- [Nemirovsky and Romanova 1995] Y. V. Nemirovsky and T. P. Romanova, “Effect pulsed load form on final deformations of rigid-plastic plates of a complex form”, *J. Appl. Mech. Tech. Phys.* **36**:6 (1995), 113–121.
- [Nemirovsky and Romanova 2001a] Y. V. Nemirovsky and T. P. Romanova, “Dynamic plastic deformation of curvilinear plates”, *Int. Appl. Mech.* **37**:12 (2001a), 1568–1578.
- [Nemirovsky and Romanova 2001b] Y. V. Nemirovsky and T. P. Romanova, “Optimization of dynamic plastic deformation of plates with a complex contour”, *J. Appl. Mech. Tech. Phys.* **42**:1 (2001b), 152–159.
- [Nemirovsky and Romanova 2002a] Y. V. Nemirovsky and T. P. Romanova, “Dynamic plastic damage of simply and doubly connected elliptic plates”, *J. Appl. Mech. Tech. Phys.* **43**:2 (2002a), 291–301.
- [Nemirovsky and Romanova 2002b] Y. V. Nemirovsky and T. P. Romanova, “Modeling and analysis of pressing of thing-walled structures of smooth convex contours”, pp. 231–239 in *Mechanics of shells and plates, proc. XX int. conf. on theory of shells and plates*, Nizhnii Novgorod State University, 2002b. (in Russian).
- [Nemirovsky and Romanova 2002c] Y. V. Nemirovsky and T. P. Romanova, “Damage of plane barriers of nonconcave contours under explosive loads”, *Nauch. vestnik* **2** (2002c), 77–85. Novosibirsk State Technical University (in Russian).
- [Nemirovsky and Romanova 2004] Y. V. Nemirovsky and T. P. Romanova, “Dynamic behavior of rigid-plastic sector plates”, *Int. Appl. Mech.* **40**:4 (2004), 440–447.
- [Perzyna 1958] P. Perzyna, “Dynamic load carrying capacity of circular plate”, *Arch. Mech. Stos.* **10**:5 (1958), 635–647.
- [Rzhanitsyn 1982] A. R. Rzhanitsyn, *Structural mechanics*, Vysshaya Shkola, Moscow, 1982. (in Russian).
- [Virma 1972] E. Virma, “Dynamics of plastic rectangular plates”, *Uch. Zap. Tart. Univ.* **305** (1972), 289–299.
- [Youngdahl 1971] C. K. Youngdahl, “Influence of pulse on the final plastic deformation of a circular plate”, *Int. J. Solids Struct.* **7**:9 (1971), 1127–1142.
- [Zhu et al. 1994] L. Zhu, D. Faulkner, and A. D. Atkins, “The impact of rectangular plates made from strain-rate sensitive material”, *Int. J. Impact Eng.* **15**:3 (1994), 243–255.

Received 17 Apr 2006. Revised 11 May 2006. Accepted 3 Jul 2007.

TATIANA PAVLOVNA ROMANOVA: shulgin@itam.nsc.ru
Institute of Theoretical and Applied Mechanics of the Siberian Branch of the Russian Academy of Science,
Institutskaya str., 4/1, Novosibirsk, 630090, Russia

YURI VLADIMIROVICH NEMIROVSKY: nemirov@itam.nsc.ru
Institute of Theoretical and Applied Mechanics of the Siberian Branch of the Russian Academy of Science,
Institutskaya str., 4/1, Novosibirsk, 630090, Russia

INTERACTION OF A DISLOCATION WITH COLLINEAR RIGID LINES AT THE INTERFACE OF PIEZOELECTRIC MEDIA

ZHONGMIN XIAO, HONGXIA ZHANG AND BINGJIN CHEN

This paper investigates the electroelastic interaction between a dislocation and collinear interfacial rigid lines in two dissimilar piezoelectric materials subjected to remote loadings. Both conducting and dielectric rigid lines are considered. The general solutions for the field variables are obtained based on the Stroh formalism and analytical function theory. The stress and electric displacement fields at the tips of rigid conducting lines are present as either a square root singularity or a combination of any two of the three kinds of singularities: square root singularity, nonsquare root singularity and oscillatory singularity. The stress and electric displacement fields at the tips of rigid dielectric lines exhibit either a square root singularity or a combination of square root and oscillatory singularities. Singularities depend on the electroelastic properties of the two piezoelectric materials. The rigid line extension force is expressed in terms of the strain and electric field intensity factors which are analogous to the stress and electric displacement intensity factors defined for interfacial cracks. The exact field solutions for the case of a single interfacial rigid line are presented. The tangential and radial components of the image force on the dislocation are calculated. Numerical examples are presented to demonstrate the effects of some important parameters on the image force.

1. Introduction

Piezoelectric materials are widely used as sensors, actuators, and electromechanical devices due to their inherent electromechanical coupling behavior. However, defects such as dislocations, cracks, cavities, and inclusions can adversely influence the performance of such piezoelectric devices. Therefore it is of great importance to investigate the behaviors of various defects in electroelastic fields in order to understand the fracture behaviors of these materials and predict the integrity of these devices.

Many efforts have been devoted to the crack models in piezoelectric materials [Pak 1990a; Sosa and Pak 1990; Suo et al. 1992]. Suo et al. [1992] analyzed the generalized two dimensional problem of an interfacial impermeable crack in piezoelectric bimetals. They discovered that the crack tip fields show the type of singularities of order $r^{-1/2 \pm i\varepsilon}$ and $r^{-1/2 \mp \kappa}$. Ou and Wu [2003] further proved that either ε or κ is equal to zero for the problem of an interfacial impermeable crack in a transversely isotropic piezoelectric bimaterial system. Beom [2003] and Hausler et al. [2004] examined a permeable crack at the interface of two piezoelectric media and identified an oscillatory singularity for the fields. Beom and Atluri [2002] derived two pairs of oscillatory singularities for the fields around an interfacial conducting crack tip in piezoelectric bimetals. Ru [2000] studied a conducting crack between electrode layers and piezoelectric ceramics. He identified a square root singularity for the tip tensile stress and a nonsquare root singularity for the shear stress. Wang and Shen [2002] gave a general treatment on various interfacial

Keywords: piezoelectric, bimetals, dislocation, rigid lines, interface, energy release rate, image force.

defects in piezoelectric media. Xiao and Zhao [2004] analyzed a Zener–Stroh crack at the interface of metal/piezoelectric bimetals by means of Green’s function. Contributions have also been made to study the dislocation-inclusion/interface/crack interaction in piezoelectric materials, for example [Meguid and Deng 1998; Xiao et al. 2004; Fang et al. 2005; Chen et al. 2005a; Chen et al. 2005b] and [Gao et al. 2005].

Rigid line problems also attract researchers’ attention. Some solutions for the problems of rigid lines in purely elastic materials under mechanical loading were obtained by Li and Ting [1989], Jiang [1991], Ballarini [1990], Wu [1990], Jiang and Liu [1992], and Asundi and Deng [1995]. The stresses possess a pronounced oscillatory character at the tip of interfacial rigid lines. Deng and Meguid [1998] analyzed all the possible singularities of the field variables at an interfacial rigid conducting line tip in piezoelectric materials loaded at infinity. Recently, the interactions of a screw dislocation with interfacial rigid lines in piezoelectric solids have been studied by Liu et al. [2004] and Xiao et al. [2007]. Chen et al. [2007] examined the interaction of a dislocation with collinear rigid lines in a piezoelectric solid. To our knowledge, however, no attempt has been made to investigate the generalized two-dimensional interaction between a dislocation and interfacial rigid lines in piezoelectric media.

The current work presents the interactive solution for a dislocation and collinear rigid lines at the interface of two piezoelectric materials. Rigid conducting and dielectric lines are modeled. The field solutions and the near-tip singularities are discussed in detail in Section 4 and Section 5. The generalized strain intensity factors are introduced to characterize the near-tip fields and rigid line extension forces are obtained. In Section 6, the exact solutions for a special case of a single interfacial rigid line are given. The image force on the dislocation is calculated in Section 7. In Section 8, the influences of some important parameters, such as the Burgers vector and dislocation position, on the image force are analyzed. A conclusion is given in Section 9.

2. Stroh formalism

Consider a linear piezoelectric solid in a Cartesian coordinate system (x_1, x_2, x_3) . For a two-dimensional problem where all the field variables depend on x_1 and x_2 only, a general solution can be expressed as

$$\mathbf{u} = \mathbf{A}\mathbf{f}(z) + \overline{\mathbf{A}}\overline{\mathbf{f}(\overline{z})}, \quad \mathbf{\Phi} = \mathbf{B}\mathbf{f}(z) + \overline{\mathbf{B}}\overline{\mathbf{f}(\overline{z})},$$

with

$$\mathbf{u} = [u_1, u_2, u_3, u_4]^T, \quad \mathbf{\Phi} = [\phi_1, \phi_2, \phi_3, \phi_4]^T,$$

$$\mathbf{f}(z) = [f_1(z), f_2(z), f_3(z), f_4(z)]^T.$$

In the above equations, \mathbf{u} and $\mathbf{\Phi}$ denote the generalized displacement and stress function vectors, respectively, \mathbf{A} and \mathbf{B} are the 4×4 matrices determined from material constants, and $\mathbf{f}(z)$ is a function vector to be found. For simplicity, each component of $\mathbf{f}(z)$ is considered to be a function of one complex variable z instead of $z_\alpha = x_1 + p_\alpha x_2$ ($\alpha = 1, 2, 3, 4$) [Suo et al. 1992], where p_α is a complex eigenvalue with positive imaginary part. Thus, the generalized strains (strain and electric field) and the generalized

stresses (stress and electric displacement) are given by

$$\mathbf{u}_{,1} = [u_{j,1}, -E_1]^T = \mathbf{A}\mathbf{f}(z) + \overline{\mathbf{A}\mathbf{F}(z)}, \tag{1}$$

$$\Phi_{,1} = [\sigma_{2j}, D_2]^T = \mathbf{B}\mathbf{F}(z) + \overline{\mathbf{B}\mathbf{F}(z)}, \tag{2}$$

$$\Phi_{,2} = [\sigma_{1j}, D_1]^T = \mathbf{B}\langle p_\alpha \rangle \mathbf{F}(z) + \overline{\mathbf{B}\langle p_\alpha \rangle \mathbf{F}(z)}, \tag{3}$$

respectively, where a comma denotes partial differentiation and $\mathbf{F}(z) = d\mathbf{f}(z)/dz$. when calculating the field variables, z should be replaced by z_α for the α th component function.

The matrices \mathbf{A} and \mathbf{B} , when properly normalized, satisfy the orthogonality relation:

$$\begin{bmatrix} \mathbf{B}^T & \mathbf{A}^T \\ \overline{\mathbf{B}}^T & \overline{\mathbf{A}}^T \end{bmatrix} \begin{bmatrix} \mathbf{A} & \overline{\mathbf{A}} \\ \mathbf{B} & \overline{\mathbf{B}} \end{bmatrix} = \begin{bmatrix} \mathbf{I} & \mathbf{0} \\ \mathbf{0} & \mathbf{I} \end{bmatrix}, \tag{4}$$

where \mathbf{I} is a 4×4 identity matrix. The three matrices \mathbf{S} , \mathbf{H} , and \mathbf{L} are defined by

$$\mathbf{H} = i2\mathbf{A}\mathbf{A}^T, \quad \mathbf{L} = i2\mathbf{B}\mathbf{B}^T, \quad \mathbf{S} = i(\mathbf{A}\mathbf{B}^T - \mathbf{I}),$$

respectively. In addition, Hermitian matrix \mathbf{M} , which appears in the analysis, is defined by

$$\mathbf{M} = -i\mathbf{B}\mathbf{A}^{-1} = \mathbf{H}^{-1} + i\mathbf{H}^{-1}\mathbf{S}.$$

For convenience, a Hermitian matrix \mathbf{Y} involving bimaterial properties is defined as

$$\mathbf{Y} = \mathbf{M}_1 + \overline{\mathbf{M}}_2,$$

where the subscripts 1 and 2 attached to matrices and vectors distinguish the two materials. The elements of \mathbf{Y} are represented by Y_{ij} . We introduce a 3×3 bimaterial matrix $\hat{\mathbf{Y}}$ with the elements \hat{Y}_{ij} given by

$$\hat{Y}_{ij} = Y_{ij} - \frac{1}{Y_{44}}Y_{i4}Y_{4j}. \tag{5}$$

It is easily shown from Equation (5) that

$$\hat{Y}_{ij}^{-1} = Y_{ij}^{-1}, \quad i, j = 1, 2, 3, \tag{6}$$

where \hat{Y}_{ij}^{-1} and Y_{ij}^{-1} denotes the elements of matrices $\hat{\mathbf{Y}}^{-1}$ and \mathbf{Y}^{-1} , respectively. It can be shown that $\hat{\mathbf{Y}}$ is a positive definite Hermitian matrix by using the properties of \mathbf{Y} .

3. Statement of the problem

Consider a piezoelectric dislocation with Burgers vector $\mathbf{b} = [b_1, b_2, b_3, b_\varphi]^T$ located at $z_d = x_{1d} + ix_{2d}$ in the upper half-infinite plane s_1 , as shown in Figure 1. The dislocation core is subjected to a line load $\mathbf{f} = [-p_1, -p_2, -p_3, q]^T$. Suppose there are collinear rigid lines l_k ($k = 1, 2, \dots, n$) with end points a_k and b_k at the interface of s_1 and the lower half-infinite plane s_2 , with the plane subjected to the uniform loading at infinity. Let L_l and L_b denote the unions of rigid lines and perfectly bonded parts along the x_1 axis, respectively.

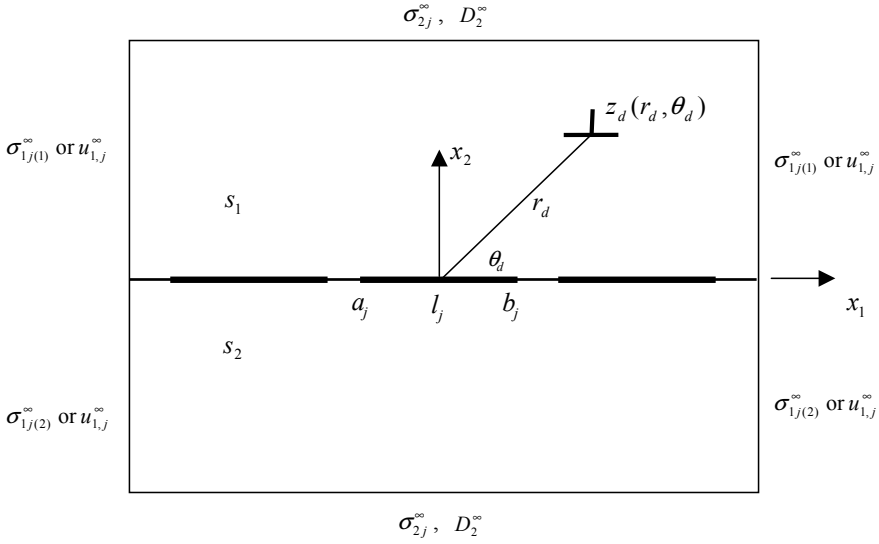


Figure 1. A piezoelectric dislocation near collinear rigid line inclusions at the interface of two dissimilar piezoelectric media.

The mechanical boundary and equilibrium conditions of interfacial rigid lines are

$$u_{j,1}^+(x_1) = u_{j,1}^-(x_1) = \delta_{j2}\omega_k, \quad j = 1, 2, 3, \quad k = 1, 2, \dots, n, \quad \text{on } L_l, \quad (7)$$

$$\int_{L_l} (\sigma_{2j}^+(x_1) - \sigma_{2j}^-(x_1)) dx_1 = 0, \quad j = 1, 2, 3, \quad \text{on } L_l, \quad (8)$$

$$\int_{L_l} (\sigma_{22}^+(x_1) - \sigma_{22}^-(x_1)) x_1 dx_1 = 0, \quad \text{on } L_l, \quad (9)$$

where ω_k are unknown constants which represent the rotation of the k th rigid line, and the superscripts + and - refer to the boundary values from s_1 and s_2 , respectively.

Assuming zero thickness of rigid lines, the electric boundary conditions are described as

$$E_1^+(x_1) = E_1^-(x_1) = 0, \quad \text{on } L_l, \quad (10)$$

$$\int_{L_l} (D_2^+(x_1) - D_2^-(x_1)) dx_1 = 0, \quad \text{on } L_l, \quad (11)$$

for the conducting case, and

$$E_1^+(x_1) = E_1^-(x_1), \quad \text{on } L_l, \quad (12)$$

$$D_2^+(x_1) = D_2^-(x_1), \quad \text{on } L_l \quad (13)$$

for the dielectric case.

The boundary conditions along perfectly bonded parts are

$$u_j^+(x_1) = u_j^-(x_1), \quad j = 1, 2, 3, 4, \quad \text{on } L_b, \tag{14}$$

$$\sigma_{2j}^+(x_1) = \sigma_{2j}^-(x_1), \quad D_2^+(x_1) = D_2^-(x_1), \quad j = 1, 2, 3, \quad \text{on } L_b. \tag{15}$$

4. Formulation and solution

Let $F_1(z)$ and $F_2(z)$ be the complex potentials in s_1 and s_2 , respectively. Based on the superposition principle, we can express

$$F_k(z) = F_k^\infty + F_{ka}(z) + F_{kb}(z), \quad k = 1, 2, \tag{16}$$

where constant vectors F_k^∞ are determined by the uniform loading at infinity in the absence of rigid lines, $F_{ka}(z)$ are the complex potentials due to the interaction of a dislocation with a perfectly bonded interface. The complex potentials $F_{kb}(z)$ correspond to the perturbed field due to collinear interfacial rigid lines. $F_{ka}(z)$ and $F_{kb}(z)$ vanish at infinity.

We begin with the perfectly bonded interface problem in the absence of rigid lines. Such loadings $\Phi_{,1}^\infty = [\sigma_{21}^\infty, \sigma_{22}^\infty, \sigma_{23}^\infty, D_2^\infty]^T$ and $u_{,1}^\infty = [\varepsilon_{11}^\infty, \varepsilon_{12}^\infty + \omega^\infty, 2\varepsilon_{13}^\infty, -E_1^\infty]^T$ are applied that the continuous conditions on tractions and displacements at the interface are satisfied. Thus, from Equation (1) and (2), we have

$$A_k F_k^\infty + \bar{A}_k \bar{F}_k^\infty = u_{,1}^\infty, \quad B_k F_k^\infty + \bar{B}_k \bar{F}_k^\infty = \Phi_{,1}^\infty, \quad k = 1, 2, \quad -\infty < x_1 < \infty. \tag{17}$$

In view of Equation (4) and (17), one has

$$F_k^\infty = A_k^T \Phi_{,1}^\infty + B_k^T u_{,1}^\infty, \quad k = 1, 2.$$

Tractions and displacements are continuous along the entire x_1 axis, so that

$$u_{a,1}^+(x_1) = u_{a,1}^-(x_1), \quad \Phi_{a,1}^+(x_1) = \Phi_{a,1}^-(x_1), \quad -\infty < x_1 < \infty, \tag{18}$$

where $u_{a,1}$ and $\Phi_{a,1}$ denote the generalized strains and stresses due to the dislocation at z_d , respectively. For this subproblem, the solution can be given by

$$F_a(z) = \begin{cases} F_{1d}(z) + F_{10}(z), & z \in s_1, \\ F_{20}(z), & z \in s_2, \end{cases} \tag{19}$$

where $F_{1d}(z)$ is the solution for a dislocation at z_d in an infinite plane given by

$$F_{1d}(z) = \frac{1}{2\pi i} \left\langle \frac{1}{z - z_{d\alpha}} \right\rangle (B_1^T b + A_1^T f). \tag{20}$$

The above bracket $\langle \rangle$ denotes a diagonal matrix. With the arguments of [Suo et al. 1992], one finds

$$F_{10}(z) = A_1^{-1} Y^{-1} (\bar{M}_1 - \bar{M}_2) \bar{A}_1 \bar{F}_{1d}(z), \tag{21}$$

$$F_{20}(z) = 2A_2^{-1} \bar{Y}^{-1} H_1^{-1} A_1 F_{1d}(z). \tag{22}$$

The substitution of the above equations into Equation (19) gives the complete solution.

Consider the rigid lines disturbed subproblem. From Equations (7), (10) or (12), and (14), the displacement continuities along the x_1 axis, along with Equations (1), (16), (17) and (18), give

$$A_1 F_{1b}^+(x_1) + \bar{A}_1 \bar{F}_{1b}^-(x_1) = A_2 F_{2b}^-(x_1) + \bar{A}_2 \bar{F}_{2b}^+(x_1), \quad -\infty < x_1 < \infty. \tag{23}$$

By the analytic continuity argument, it follows that

$$\begin{cases} A_1 F_{1b}(z) = \bar{A}_2 \bar{F}_{2b}(z), & z \in s_1, \\ A_2 F_{2b}(z) = \bar{A}_1 \bar{F}_{1b}(z), & z \in s_2. \end{cases} \tag{24}$$

With such representations, the generalized stress jumps across rigid lines are obtained as

$$\Delta \Phi_{,1}(x_1) = iY [I^+(x_1) - I^-(x_1)], \tag{25}$$

where

$$I(z) = \begin{cases} A_1 F_{1b}(z), & z \in s_1, \\ Y^{-1} \bar{Y} A_2 F_{2b}(z), & z \in s_2. \end{cases} \tag{26}$$

Since $\Delta \Phi_{,1}(x_1) = 0$ on L_b from Equation (15), (25) shows that

$$I(z) = [I_1(z), I_2(z), I_3(z), I_4(z)]^T$$

is analytic in the entire plane except at the rigid lines.

Substituting Equation (16) into (1) with (17) gives

$$u_{,1}(x_1) = u_{,1}^\infty + u_{a,1}(x_1) + I^+(x_1) + \bar{Y}^{-1} Y I^-(x_1), \tag{27}$$

where

$$u_{a,1}(x_1) = \frac{2}{\pi} \text{Im} \left[N \left\langle \frac{1}{x - z_{d\alpha}} \right\rangle d \right]. \tag{28}$$

In the above equation, $N = \bar{Y}^{-1} H_1^{-1} A_1$ and $d = B_1^T b + A_1^T f$, which are defined for simplicity. The elements of matrix N and vector d are represented by N_{ij} ($i, j = 1, 2, 3, 4$) and d_i ($i = 1, 2, 3, 4$), respectively. Once $I(z)$ is found, so is the full field.

The solution is simple if Y is real. When the collinear rigid lines are in a homogeneous material, Y is indeed real. Y can be real for bimetals having sufficient symmetry. In the following, real Y is assumed in Sections 4.1 and 4.2, and the case that Y is complex is examined in Sections 4.3 and 4.4.

4.1. Rigid conducting lines: the fields of a square root singularity. With real Y , from Equations (7), (10) and (27), one has

$$I^+(x_1) + I^-(x_1) = \Omega - u_{,1}^\infty - u_{a,1}(x_1), \quad \text{on } L_l, \tag{29}$$

where

$$\Omega = \begin{cases} [0, \omega_1, 0, 0]^T, & \text{on } l_1, \\ \dots\dots\dots \\ [0, \omega_n, 0, 0]^T, & \text{on } l_n. \end{cases} \tag{30}$$

The general solution can be obtained from the method of [Muskhelishvili 1975] as

$$\begin{aligned}
 \mathbf{I}(z) = \frac{1}{2} X(z) \left\{ \oint_{\eta} \frac{\boldsymbol{\Omega}}{X(\xi)(\xi - z)} d\xi - \mathbf{u}_{,1}^{\infty} \left[\frac{1}{X(z)} - x(\infty) \right] \right. \\
 \left. - \frac{1}{\pi i} \mathbf{N} \left\langle \frac{1}{(z_{\alpha} - z_{d\alpha}) X(z_{\alpha})} - 1 - \frac{1}{(z_{\alpha} - z_{d\alpha}) X(z_{d\alpha})} \right\rangle \mathbf{d} \right. \\
 \left. + \frac{1}{\pi i} \bar{\mathbf{N}} \left\langle \frac{1}{(z_{\alpha} - \bar{z}_{d\alpha}) X(z_{\alpha})} - \frac{1}{(z_{\alpha} - \bar{z}_{d\alpha}) X(\bar{z}_{d\alpha})} - 1 \right\rangle \bar{\mathbf{d}} + \mathbf{P}^a(z) \right\}, \quad (31)
 \end{aligned}$$

where

$$\mathbf{P}^a(z) = \mathbf{c}_{n-1}^a z^{n-1} + \dots + \mathbf{c}_0^a, \quad (32)$$

$$X(z) = \prod_{j=1}^n (z - a_j)^{-1/2} (z - b_j)^{-1/2}, \quad (33)$$

$$x(\infty) = \prod_{j=1}^n [z - (a_j + b_j)/2], \quad (34)$$

in which η is the union of the n contours η_1, \dots, η_n , surrounding the rigid lines L_1, \dots, L_n in clockwise direction.

From Equations (8), (11) and (25), we can obtain the closed path integral

$$\oint_{\eta_j} \mathbf{I}(z) dz = \mathbf{0}, \quad j = 1, 2, \dots, n. \quad (35)$$

One has from Equations (9) and (25) the closed path integral

$$\mathbf{Y}^{(2)} \oint_{\eta_j} \mathbf{I}(z) dz = 0, \quad j = 1, 2, \dots, n. \quad (36)$$

The n vectors \mathbf{c}_{j-1}^a and n constants ω_j ($j = 1, 2, \dots, n$) can be obtained by substituting Equation (31) into Equations (35) and (36) with Equations (32)–(34). $\mathbf{F}_{kb}(z)$ can be found by using Equation (26).

4.2. Rigid dielectric lines: the fields of a square root singularity. The condition, Equation (13), along the rigid dielectric lines leads to

$$\mathbf{Y}^{(4)} \mathbf{I}(z) = 0. \quad (37)$$

One has from Equation (37) that

$$I_4(z) = -\frac{Y_{4j}}{Y_{44}} I_j(z), \quad j = 1, 2, 3. \quad (38)$$

Thus we have

$$\mathbf{I}(z) = (\hat{\mathbf{I}} - \mathbf{E}) \hat{\mathbf{I}}(z), \quad (39)$$

where $\hat{\mathbf{I}}(z) = [I_1(z), I_2(z), I_3(z)]^T$, $\hat{\mathbf{I}}$ is obtained by deleting the fourth column from a 4×4 identity matrix, and $\mathbf{E} = [\mathbf{E}_1, \mathbf{E}_2, \mathbf{E}_3]$ with $\mathbf{E}_i = [0, 0, 0, Y_{4i}/Y_{44}]^T$. The relations in Equations (37)–(39) are valid for real and complex Y .

With real Y , Equations (5), (6), (7), (27) and (39) lead to

$$\hat{\mathbf{I}}^+(x_1) + \hat{\mathbf{I}}^-(x_1) = \hat{\mathbf{\Omega}} - \hat{\mathbf{u}}_{,1}^\infty - \hat{\mathbf{u}}_{a,1}(x_1), \tag{40}$$

where

$$\hat{\mathbf{\Omega}} = \begin{cases} [0, \omega_1, 0]^T, & \text{on } l_1, \\ \dots\dots\dots \\ [0, \omega_n, 0]^T, & \text{on } l_n, \end{cases} \tag{41}$$

$$\hat{\mathbf{u}}_{,1}^\infty = [u_{1,1}^\infty, u_{2,1}^\infty, u_{3,1}^\infty]^T, \quad \hat{\mathbf{u}}_{a,1} = [u_{1,1}^a, u_{2,1}^a, u_{3,1}^a]^T.$$

The general solution to Equation (40) is given by

$$\begin{aligned} \hat{\mathbf{I}}(z) = \frac{1}{2}X(z) \left\{ \oint_{\eta} \frac{\hat{\mathbf{\Omega}}}{X(\xi)(\xi - z)} d\xi - \hat{\mathbf{u}}_{,1}^\infty \left[\frac{1}{X(z)} - x(\infty) \right] \right. \\ \left. - \frac{1}{\pi i} \hat{N} \left\langle \frac{1}{(z_\alpha - z_{d\alpha})X(z_\alpha)} - 1 - \frac{1}{(z_\alpha - z_{d\alpha})X(z_{d\alpha})} \right\rangle d \right. \\ \left. + \frac{1}{\pi i} \tilde{N} \left\langle \frac{1}{(z_\alpha - \bar{z}_{d\alpha})X(z_\alpha)} - \frac{1}{(z_\alpha - \bar{z}_{d\alpha})X(\bar{z}_{d\alpha})} - 1 \right\rangle \bar{d} + \mathbf{P}^b(z) \right\}, \tag{42} \end{aligned}$$

where \hat{N} is a 3×4 matrix obtained by deleting the fourth row of matrix N and

$$\mathbf{P}^b(z) = \mathbf{c}_{n-1}^b z^{n-1} + \dots + \mathbf{c}_0^b. \tag{43}$$

Using Equations (8), (25) and (39), we can obtain the closed path integral

$$\oint_{\eta_j} \hat{\mathbf{I}}(z) dz = \mathbf{0}, \quad j = 1, 2, \dots, n. \tag{44}$$

From Equations (5), (9), (25), and (39), one has the closed path integral

$$\hat{\mathbf{Y}}^{(2)} \oint_{\eta_j} \hat{\mathbf{I}}(z) z dz = 0, \quad j = 1, 2, \dots, n, \tag{45}$$

where $\hat{\mathbf{Y}}^{(2)} = [\hat{Y}_{21}, \hat{Y}_{22}, \hat{Y}_{23}]$. Substituting Equation (42) into Equations (44) and (45), with Equations (33), (34), and (43), we have the n vectors \mathbf{c}_{j-1}^b and the n constants ω_j ($j = 1, 2, \dots, n$). Then, we can find $\mathbf{F}_{kb}(z)$ by using Equation (26).

For both conducting and dielectric cases, we can evaluate the generalized strain and stress intensity factors at the right tip of the j th rigid line as

$$\mathbf{k} = [k_1, k_2, k_3, k_4]^T = \lim_{x \rightarrow b_j} \sqrt{2\pi(x - b_j)}(\mathbf{I}(x) + \bar{\mathbf{I}}(x)), \quad (46)$$

$$\mathbf{K} = [K_{II}, K_I, K_{III}, K_D]^T = \lim_{x \rightarrow b_j} \sqrt{2\pi(x - b_j)}[i\mathbf{M}_1\mathbf{I}(x) - i\bar{\mathbf{M}}_1\bar{\mathbf{I}}(x)], \quad (47)$$

respectively. For the dielectric case, Equation (46), in view of (39), can be rewritten as

$$\mathbf{k} = (\hat{\mathbf{I}} - \mathbf{E})\hat{\mathbf{k}}, \quad (48)$$

where

$$\hat{\mathbf{k}} = [k_1, k_2, k_3]^T = \lim_{x \rightarrow b_j} \sqrt{2\pi(x - b_j)}[\hat{\mathbf{I}}(x) + \bar{\hat{\mathbf{I}}}(x)]. \quad (49)$$

Thus, the generalized strains at the interface a distance r ahead of the tip, and the generalized stress jumps a distance r behind the tip, of the j th rigid line, are given by

$$\mathbf{u}(r) = (2r/\pi)^{1/2}\mathbf{k}, \quad (50)$$

$$\Delta\Phi_{,1}(r) = (1/2\pi r)^{1/2}\mathbf{Y}\mathbf{k}, \quad (51)$$

respectively. For the dielectric case, Equation (51) can be further rewritten as

$$[\Delta\sigma_{21}(r), \Delta\sigma_{22}(r), \Delta\sigma_{23}(r)]^T = (1/2\pi r)^{1/2}\hat{\mathbf{Y}}\hat{\mathbf{k}}, \quad \Delta D_2(r) = 0. \quad (52)$$

In view of Equation (47), the generalized stresses at the interface a distance r ahead of the j th rigid line tip are given by

$$[\sigma_{2j}(r), D_2(r)]^T = (2\pi r)^{-1/2}\mathbf{K}. \quad (53)$$

It is interesting to note that Equation (50) has the same structure as the expression of the generalized stresses ahead of an impermeable crack tip and (51) has the same structure as that of the generalized displacements behind the crack tip [Suo et al. 1992].

Furthermore, the rigid line extension force can be calculated by the closure integral

$$G = \lim_{\delta \rightarrow 0} -\frac{1}{2\delta} \int_0^\delta \Delta\Phi_{,1}^T(r)\mathbf{u}(\delta - r)dr. \quad (54)$$

Substituting Equations (50) and (51) into (54) leads to

$$G = -\frac{1}{4}\mathbf{k}^T\mathbf{Y}\mathbf{k}. \quad (55)$$

For the dielectric case, Equation (55) can be further rewritten as

$$G = -\frac{1}{4}\hat{\mathbf{k}}^T\hat{\mathbf{Y}}\hat{\mathbf{k}}. \quad (56)$$

It should be pointed out that all the results in Section 4.1 and Section 4.2 are applied to the corresponding problems of collinear rigid conducting and dielectric lines in a homogeneous piezoelectric material, where $\mathbf{M}_1 = \mathbf{M}_2$ and $\mathbf{Y} = 2\mathbf{H}_1^{-1}$.

4.3. Rigid conducting lines: the fields of square root, nonsquare root and oscillatory singularities.

For complex Y , Equations (7), (10), and (27) lead to

$$I^+(x_1) + \bar{Y}^{-1}YI^-(x_1) = \Omega - u_{,1}^\infty - u_{a,1}(x_1), \quad \text{on } L_l. \tag{57}$$

Assuming that the eigenvalues of $\bar{Y}^{-1}Y$ take the form $-e^{2\pi i\delta_\alpha}$ with $\delta_\alpha = -1/2 + i\varepsilon_\alpha$, we have

$$\varepsilon_{1,2} = \pm\varepsilon, \quad \varepsilon_{3,4} = \mp i\kappa, \tag{58}$$

where

$$\begin{aligned} \varepsilon &= \tanh^{-1}(\beta_1)/\pi, & \kappa &= \tan^{-1}(-i\beta_2)/\pi, \\ \beta_1 &= [(b^2 - c)^{1/2} - b]^{1/2}, & \beta_2 &= i[(b^2 - c)^{1/2} + b]^{1/2}, \\ b &= \text{tr}[(D^{-1}U)^2]/4, & c &= ||D^{-1}U||, \\ D &= \text{Re}[Y], & U &= \text{Im}[Y]. \end{aligned}$$

Let Λ_α be the eigenvector of $\bar{Y}^{-1}Y$ corresponding to the eigenvalue $-e^{2\pi i\delta_\alpha}$. Suo et al. [1992] assumed that both values of ε and κ are nonzero and four linearly independent eigenvectors would be obtained for impermeable cracks in a piezoelectric bimaterial system. Here, three combinations of ε and κ are considered:

- case 1:** $\varepsilon \neq 0$ ($b \neq 0$), $\kappa \neq 0$ ($c \neq 0$),
- case 2:** $\varepsilon \neq 0$ ($b < 0$), $\kappa = 0$ ($c = 0$),
- case 3:** $\varepsilon = 0$ ($b > 0$), $\kappa \neq 0$ ($c = 0$).

It can be identified that the eigenvectors Λ_1 and Λ_2 are complex conjugates, that is, $\Lambda_2 = \bar{\Lambda}_1$, and Λ_3 and Λ_4 are real for cases 1 and 2, and all of them are real for case 3 [Deng and Meguid 1998]. Ou and Wu [2003] confirmed that cases 2 and 3 apply to the problem of an impermeable interfacial crack in a transversely isotropic piezoelectric bimaterial system. Four linearly independent eigenvectors can be obtained for the three cases. For simplicity, we define

$$\Lambda_A = [\Lambda_1, \Lambda_2, \Lambda_3, \Lambda_4], \quad \Lambda_B = \begin{cases} [\bar{\Lambda}_1, \Lambda_1, \Lambda_4, \Lambda_3], & \text{for case 1,} \\ [\bar{\Lambda}_1, \Lambda_1, \Lambda_3, \Lambda_4], & \text{for case 2,} \\ [\Lambda_1, \Lambda_2, \Lambda_4, \Lambda_3], & \text{for case 3,} \end{cases} \tag{59}$$

which satisfy

$$\Lambda_B^T D \Lambda_A = \langle v_1, v_2, v_3, v_4 \rangle, \quad \begin{cases} v_1 = v_2, v_3 = v_4, & \text{for case 1,} \\ v_1 = v_2, & \text{for case 2,} \\ v_3 = v_4, & \text{for case 3.} \end{cases} \tag{60}$$

In the above three cases, the general solution to Equation (57) can be given as

$$I(z) = \sum_{\alpha=1}^4 \lambda_\alpha(z) \Lambda_\alpha, \tag{61}$$

with

$$\lambda_\alpha(x_1) = \frac{e^{-\pi\varepsilon_\alpha} k'_\alpha X_\alpha(x_1)}{2\sqrt{2\pi} \cos(i\pi\varepsilon_\alpha)}. \tag{62}$$

In the above equation, for cases 1 and 2, the factors k'_1 and k'_2 are complex conjugates (that is, $k'_2 = \bar{k}'_1$), and k'_3 and k'_4 are real. For case 3, $k'_1, k'_2, k'_3,$ and k'_4 are real. $X_\alpha(z)$ is given by

$$X_\alpha(z) = \prod_{j=1}^n (z - a_j)^{-1/2+i\varepsilon_\alpha} (z - b_j)^{-1/2-i\varepsilon_\alpha}. \tag{63}$$

The arrangement of k'_i ensures that the strain and electric field are real (see Equation (69) below). Multiplying the two sides of (57) by $\mathbf{W} = \mathbf{\Lambda}_B^T \mathbf{D}$ with the elements $W_{\alpha j}$, with the aid of (61), we obtain:

$$[\lambda_\alpha(x_1)]^+ + e^{2\pi\varepsilon_\alpha} [\lambda_\alpha(x_1)]^- = \mathbf{W}^\alpha \mathbf{I}^0(x_1)/v_\alpha, \quad \alpha = 1, 2, 3, 4, \tag{64}$$

where

$$\mathbf{I}^0(x_1) = \mathbf{\Omega} - \mathbf{u}_{,1}^\infty - \mathbf{u}_{a,1}(x_1), \tag{65}$$

and $\mathbf{W}^\alpha = [W_{\alpha 1}, W_{\alpha 2}, W_{\alpha 3}, W_{\alpha 4}]$. The solution to Equation (64) is given as

$$\begin{aligned} \lambda_\alpha(z) = & \frac{X_\alpha(z)}{(1 + e^{2\pi\varepsilon_\alpha})v_\alpha} \left\{ \oint_\eta \frac{\mathbf{W}^\alpha \mathbf{\Omega}}{X_\alpha(\xi)(\xi - z)} d\xi - \mathbf{W}^\alpha \mathbf{u}_{,1}^\infty \left[\frac{1}{X_\alpha(z)} - x_\alpha(\infty) \right] \right. \\ & - \frac{1}{i\pi} \sum_{j=1}^4 W_{\alpha j} \sum_{k=1}^4 N_{jk} d_k \left[\frac{1}{(z - z_{dk})X_\alpha(z)} - \frac{1}{(z - z_{dk})X_\alpha(z_{dk})} - 1 \right] \\ & \left. + \frac{1}{i\pi} \sum_{j=1}^4 W_{\alpha j} \sum_{k=1}^4 \bar{N}_{jk} \bar{d}_k \left[\frac{1}{(z - \bar{z}_{dk})X_\alpha(z)} - \frac{1}{(z - \bar{z}_{dk})X_\alpha(\bar{z}_{dk})} - 1 \right] + P_\alpha^c(z) \right\}, \tag{66} \end{aligned}$$

where

$$P_\alpha^c(z) = c_{\alpha n-1}^c z^{n-1} + \dots + c_{\alpha 0}^c, \tag{67}$$

$$x_\alpha(\infty) = \prod_{j=1}^n [z - (a_j + b_j)/2 - i\varepsilon_\alpha(b_j - a_j)]. \tag{68}$$

The $4n$ constants $c_{\alpha k}^c$ ($\alpha = 1, 2, 3, 4, k = 0, 1, \dots, n - 1$) and n constants ω_j ($j = 1, 2, \dots, n$) are obtained by substituting Equation (61) into Equations (35) and (36) with Equations (63) and (66)–(68). As a result, $\mathbf{F}_{kb}(z)$ can be found by using (26).

The generalized strains along the interface can be written as

$$\mathbf{u}_{,1}(x_1) = \frac{1}{\sqrt{2\pi}} [k'_1 X_1(x_1) \mathbf{\Lambda}_1 + k'_2 X_2(x_1) \mathbf{\Lambda}_2 + k'_3 X_3(x_1) \mathbf{\Lambda}_3 + k'_4 X_4(x_1) \mathbf{\Lambda}_4]. \tag{69}$$

The components $k'_1 X_1(x_1)$ and $k'_2 X_2(x_1)$ present the singularities of $r^{-1/2 \mp i\varepsilon_\alpha}$, and $k'_3 X_3(x_1)$ and $k'_4 X_4(x_1)$ exhibit the singularities of $r^{-1/2 \pm \kappa}$, at the interface a distance r ahead of the rigid conducting line tip. In cases 1 and 2, $k'_1 X_1(x_1)$ and $k'_2 X_2(x_1)$ are in the plane spanned by $\text{Re}[\mathbf{\Lambda}_1]$ and $\text{Im}[\mathbf{\Lambda}_1]$, and $k'_3 X_3(x_1)$

and $k'_4 X_4(x_1)$ are along the Λ_3 and Λ_4 directions, respectively. In case 3, $k'_i X_i(x_1)$ ($i = 1, 2, 3, 4$) are along the Λ_i directions. In case 1, the components are analogous to the corresponding tractions and charge for an impermeable interfacial crack in piezoelectric media, where $\varepsilon \neq 0$ and $\kappa \neq 0$ are assumed [Suo et al. 1992].

At the interface, the generalized stresses disturbed by rigid conducting lines are given by

$$[\sigma_{2j}(x_1), D_2(x_1)]^T = 2 \operatorname{Re} \left[\sum_{\alpha=1}^4 \lambda_\alpha(x_1) \mathbf{B}_1 \mathbf{A}_1^{-1} \Lambda_\alpha \right]. \tag{70}$$

At the tips of rigid conducting lines, the generalized stresses present oscillatory and nonsquare root singularities in case 1, oscillatory and square root singularities in case 2, and square root and nonsquare root singularities in case 3.

The generalized strain intensity factors at the right tip of the j th rigid conducting line are defined as

$$\begin{aligned} \tilde{k}_\alpha &= \lim_{x_1 \rightarrow b_j} k'_\alpha \prod_{i=1}^n (x_1 - a_i)^{-1/2+i\varepsilon_\alpha} \prod_{i=1, i \neq j}^n (x_1 - b_i)^{-1/2-i\varepsilon_\alpha} \\ &= \lim_{x_1 \rightarrow b_j} 2\sqrt{2\pi} \cos(i\pi\varepsilon_\alpha) e^{\pi\varepsilon_\alpha} (x_1 - b_j)^{1/2+i\varepsilon_\alpha} \lambda_\alpha(x_1), \end{aligned} \tag{71}$$

where \tilde{k}_1 and \tilde{k}_2 are complex conjugates, and \tilde{k}_3 and \tilde{k}_4 are real for cases 1 and 2. All \tilde{k}_i are real for case 3.

At the interface a distance r ahead of the j th rigid conducting line tip, the generalized displacements are

$$\mathbf{u}(r) = \sqrt{\frac{r}{2\pi}} \sum_{\alpha=1}^4 \frac{2}{1-i2\varepsilon_\alpha} \tilde{k}_\alpha r^{-i\varepsilon_\alpha} \Lambda_\alpha. \tag{72}$$

The generalized stress jumps at the interface a distance r behind the j th rigid conducting line tip are

$$\Delta \Phi_{,1}(r) = \mathbf{D} \sqrt{\frac{1}{2\pi r}} \sum_{\alpha=1}^4 \frac{1}{\cos(i\pi\varepsilon_\alpha)} \tilde{k}_\alpha r^{-i\varepsilon_\alpha} \Lambda_\alpha. \tag{73}$$

It is worth noting that the structure of the generalized displacements in Equation (72) is the same as that of the generalized stresses ahead of an impermeable crack tip, and the structure of the generalized stress jumps in Equation (73) is the same as that of the generalized displacement jumps behind the crack tip [Suo et al. 1992].

By substituting Equations (72) and (73) into (54), the j th rigid line extension force is obtained as

$$G = \begin{cases} -\frac{v_1}{2 \cosh^2 \pi \varepsilon} |\tilde{k}_1|^2 - \frac{v_3}{2 \cos^2 \pi \kappa} \tilde{k}_3 \tilde{k}_4, & \text{for case 1,} \\ -\frac{v_1}{2 \cosh^2 \pi \varepsilon} |\tilde{k}_1|^2 - \frac{v_3}{4} \tilde{k}_3^2 - \frac{v_4}{4} \tilde{k}_4^2, & \text{for case 2,} \\ -\frac{v_1}{4} \tilde{k}_1^2 - \frac{v_2}{4} \tilde{k}_2^2 - \frac{v_3}{2 \cos^2 \pi \kappa} \tilde{k}_3 \tilde{k}_4, & \text{for case 3.} \end{cases} \tag{74}$$

4.4. Rigid dielectric lines: the fields of oscillatory and square root singularities. For complex Y , Equations (5), (6), (7), (27), and (39) lead to

$$\hat{\mathbf{I}}^+(x_1) + \bar{\hat{\mathbf{A}}}^{-1} \hat{\mathbf{Y}} \hat{\mathbf{I}}^-(x_1) = \hat{\mathbf{\Omega}} - \hat{\mathbf{u}}_{,1}^\infty - \hat{\mathbf{u}}_{a,1}(x_1). \tag{75}$$

Similarly, the eigenvalues of $\bar{\hat{\mathbf{A}}}^{-1} \hat{\mathbf{Y}}$ are assumed to be the form $e^{2\pi\varepsilon_\alpha}$. One has

$$\varepsilon_{1,2} = \pm\varepsilon, \quad \varepsilon_3 = 0, \tag{76}$$

where

$$\varepsilon = \frac{1}{2\pi} \ln \frac{1+\eta}{1-\eta}, \quad \eta = \sqrt{-\frac{1}{2} \text{tr}[(\hat{\mathbf{D}}^{-1} \hat{\mathbf{U}})^2]}, \quad \hat{\mathbf{D}} = \text{Re}[\hat{\mathbf{Y}}], \quad \hat{\mathbf{U}} = \text{Im}[\hat{\mathbf{Y}}]. \tag{77}$$

The associated eigenvectors $\mathbf{\Lambda}_1$ and $\mathbf{\Lambda}_2$ are complex conjugates, that is, $\mathbf{\Lambda}_2 = \bar{\mathbf{\Lambda}}_1$, and $\mathbf{\Lambda}_3$ is real. We define

$$\mathbf{\Lambda}_A = [\mathbf{\Lambda}_1, \bar{\mathbf{\Lambda}}_1, \mathbf{\Lambda}_3], \quad \mathbf{\Lambda}_B = [\bar{\mathbf{\Lambda}}_1, \mathbf{\Lambda}_1, \mathbf{\Lambda}_3], \tag{78}$$

which satisfy

$$\mathbf{\Lambda}_B^T \hat{\mathbf{D}} \mathbf{\Lambda}_A = \langle v_1, v_2, v_3 \rangle, \quad v_1 = v_2. \tag{79}$$

The general solution of Equation (75) can be given as

$$\hat{\mathbf{I}}(z) = \sum_{\alpha=1}^3 \lambda_\alpha(z) \mathbf{\Lambda}_\alpha, \tag{80}$$

where $\lambda_\alpha(z)$ is evaluated by Equation (62), with the factors k'_1 and k'_2 being complex conjugates, and k'_3 being real. A similar procedure to that adopted in the preceding section permits us to obtain

$$\begin{aligned} \lambda_\alpha(z) = & \frac{X_\alpha(z)}{(1 + e^{2\pi\varepsilon_\alpha})v_\alpha} \left\{ \oint_{\eta} \frac{\hat{\mathbf{W}}^\alpha \hat{\mathbf{\Omega}}}{X_\alpha(\xi)(\xi - z)} d\xi - \hat{\mathbf{W}}^\alpha \hat{\mathbf{u}}_{,1}^\infty \left[\frac{1}{X_\alpha(z)} - x_\alpha(\infty) \right] \right. \\ & - \frac{1}{i\pi} \sum_{j=1}^3 \hat{\mathbf{W}}_{\alpha j} \sum_{k=1}^4 N_{jk} d_k \left[\frac{1}{(z - z_{dk})X_\alpha(z)} - \frac{1}{(z - z_{dk})X_\alpha(z_{dk})} - 1 \right] \\ & \left. + \frac{1}{i\pi} \sum_{j=1}^3 \hat{\mathbf{W}}_{\alpha j} \sum_{k=1}^4 \bar{N}_{jk} \bar{d}_k \left[\frac{1}{(z - \bar{z}_{dk})X_\alpha(z)} - \frac{1}{(z - \bar{z}_{dk})X_\alpha(\bar{z}_{dk})} - 1 \right] + P_\alpha^d(z) \right\}, \tag{81} \end{aligned}$$

where $\hat{\mathbf{W}}^\alpha$ denotes the first (α) row of the matrix $\hat{\mathbf{W}} = \hat{\mathbf{\Lambda}}_B^T \hat{\mathbf{D}}$ with the elements \hat{W}_{ij} , and

$$P_\alpha^d(z) = c_{\alpha n-1}^d z^{n-1} + \dots + c_{\alpha 0}^d. \tag{82}$$

Substituting Equation (80) into (44) and (45), with Equations (63), (68), (81), and (82), we find the $3n$ constants $c_{\alpha k}^d$ ($\alpha = 1, 2, 3, k = 0, 1, \dots, n-1$) and the n constants ω_j ($j = 1, 2, \dots, n$). The functions $F_{kb}(z)$ are obtained through (26).

The strains along the interface can be written as

$$\hat{\mathbf{u}}_{,1}(x_1) = \frac{1}{\sqrt{2\pi}} [k'_1 X_1(x_1) \mathbf{\Lambda}_1 + \bar{k}'_1 \bar{X}_1(x_1) \bar{\mathbf{\Lambda}}_1 + k'_3 X_3(x_1) \mathbf{\Lambda}_3]. \tag{83}$$

It is noted that the strains can be decomposed into two components: one is in the plane spanned by $\text{Re}[\mathbf{\Lambda}_1]$ and $\text{Im}[\mathbf{\Lambda}_1]$, and the other is along the $\mathbf{\Lambda}_3$ direction, in analogy to the tractions for a crack in anisotropic elastic media [Suo 1990]. At the j th rigid dielectric line tip, the strains present oscillatory and square root singularities. The strain intensity factors \tilde{k}_α ($\alpha = 1, 2, 3$) defined in Equation (71) for the conducting case are used here to characterize these singularities together with (81). The electric field at the bonded interface is given by

$$E_1(x_1) = 2 \text{Re} [\mathbf{e}^T \hat{\mathbf{I}}(x)], \tag{84}$$

where $\mathbf{e} = [-Y_{41}/Y_{44}, -Y_{42}/Y_{44}, -Y_{43}/Y_{44}]^T$. Equation (84) implies that the tip electric field also exhibits oscillatory and square root singularities.

Along the interface, the generalized stresses disturbed by the rigid dielectric lines are obtained as

$$[\sigma_{2j}(x_1), D_2(x_1)]^T = 2 \text{Re} \left[\mathbf{B}_1 \mathbf{A}_1^{-1} (\hat{\mathbf{I}} - \mathbf{E}) \sum_{\alpha=1}^3 \lambda_\alpha(x_1) \mathbf{\Lambda}_\alpha \right]. \tag{85}$$

It should be noted that the near-tip stress and electric displacement fields present oscillatory and square root singularities, similar to the fields near the tips of a permeable interfacial crack in piezoelectric media [Beom 2003].

At a distance r ahead of the j th rigid dielectric line tip, the displacements are

$$\hat{\mathbf{u}}(r) = \sqrt{\frac{r}{2\pi}} \sum_{\alpha=1}^3 \frac{2}{1 - i2\varepsilon_\alpha} \tilde{k}_\alpha r^{-i\varepsilon_\alpha} \mathbf{\Lambda}_\alpha. \tag{86}$$

The stress jumps at a distance r behind the j th rigid dielectric line tip are

$$[\Delta\sigma_{21}(r), \Delta\sigma_{22}(r), \Delta\sigma_{23}(r)]^T = \hat{\mathbf{D}} \sqrt{\frac{1}{2\pi r}} \sum_{\alpha=1}^3 \frac{1}{\cos(i\pi\varepsilon_\alpha)} \tilde{k}_\alpha r^{-i\varepsilon_\alpha} \mathbf{\Lambda}_\alpha. \tag{87}$$

By substituting Equations (86) and (87) into Equation (54), the j th rigid line extension force is obtained as

$$G = -\frac{v_1}{2 \cosh^2 \pi \varepsilon} |\tilde{k}_1|^2 - \frac{v_3}{4} \tilde{k}_3^2. \tag{88}$$

5. Near tip fields around a single rigid line with a real \mathbf{Y}

In this section we consider a single interfacial rigid line of length $2a$ centered along the x_1 axis for the case that \mathbf{Y} is real. The rotation of the rigid line is assumed to be ω . One has

$$\mathbf{\Omega} = [0, \omega, 0, 0]^T, \tag{89}$$

$$\hat{\mathbf{\Omega}} = [0, \omega, 0]^T, \tag{90}$$

$$X(z) = (z + a)^{-1/2}(z - a)^{-1/2}, \quad x(\infty) = z.$$

5.1. A single rigid conducting line: the fields of a square root singularity. In this case, Equation (31) becomes

$$\begin{aligned} \mathbf{I}(z) = \frac{1}{2}(\boldsymbol{\Omega} - \mathbf{u}_{,1}^\infty) \left[1 - \frac{z}{\sqrt{z^2 - a^2}} \right] - \frac{1}{2\pi i} \mathbf{N} \left\langle \frac{1}{z_\alpha - z_{d\alpha}} \left(1 - \sqrt{\frac{z_{d\alpha}^2 - a^2}{z_\alpha^2 - a^2}} \right) - \frac{1}{\sqrt{z_\alpha^2 - a^2}} \right\rangle \mathbf{d} \\ + \frac{1}{2\pi i} \bar{\mathbf{N}} \left\langle \frac{1}{z_\alpha - z_{d\alpha}} \left(1 - \sqrt{\frac{z_{d\alpha}^2 - a^2}{z_\alpha^2 - a^2}} \right) - \frac{1}{\sqrt{z_\alpha^2 - a^2}} \right\rangle \bar{\mathbf{d}} + \frac{z}{2\sqrt{z^2 - a^2}} \mathbf{c}_0^a(z). \end{aligned} \quad (91)$$

Substituting Equation (91) into (35) and (36), and applying the residue theorem, we have

$$\mathbf{c}_0^a = 0, \quad (92)$$

$$\omega = \frac{1}{Y_{22}} \left\{ \mathbf{Y}^{(2)} \mathbf{u}_{,1}^\infty + \frac{4}{\pi a^2} \text{Im} \left[\mathbf{Y}^{(2)} \mathbf{N} \left\langle \sqrt{z_{d\alpha}^2 - a^2} - z_{d\alpha} \right\rangle \mathbf{d} \right] \right\}. \quad (93)$$

Substituting Equation (91) into (26) with Equations (92) and (93), using Equations (19)–(22), and neglecting constants, one has

$$\begin{aligned} \mathbf{F}_1(z) = \frac{1}{2\pi i} \mathbf{A}_1^{-1} \left\{ \mathbf{A}_1 \left\langle \frac{1}{z_\alpha - z_{d\alpha}} \right\rangle \mathbf{d} - \mathbf{N} \left\langle \frac{1}{z_\alpha - z_{d\alpha}} \left[1 - \sqrt{\frac{z_{d\alpha}^2 - a^2}{z_\alpha^2 - a^2}} \right] - \frac{1}{\sqrt{z_\alpha^2 - a^2}} \right\rangle \mathbf{d} \right. \\ \left. + \bar{\mathbf{A}}_1 \left\langle \frac{1}{z_\alpha - \bar{z}_{d\alpha}} \right\rangle \bar{\mathbf{d}} - \bar{\mathbf{N}} \left\langle \frac{1}{z_\alpha - \bar{z}_{d\alpha}} \left[1 + \sqrt{\frac{\bar{z}_{d\alpha}^2 - a^2}{z_\alpha^2 - a^2}} \right] + \frac{1}{\sqrt{z_\alpha^2 - a^2}} \right\rangle \bar{\mathbf{d}} + (\mathbf{u}_{,1}^\infty - \boldsymbol{\Omega}) \frac{i\pi z}{\sqrt{z^2 - a^2}} \right\}, \end{aligned} \quad (94)$$

$$\begin{aligned} \mathbf{F}_2(z) = \frac{1}{2\pi i} \mathbf{A}_2^{-1} \left\{ \mathbf{N} \left\langle \frac{1}{z_\alpha - z_{d\alpha}} \left[1 + \sqrt{\frac{z_{d\alpha}^2 - a^2}{z_\alpha^2 - a^2}} \right] + \frac{1}{\sqrt{z_\alpha^2 - a^2}} \right\rangle \mathbf{d} \right. \\ \left. + \bar{\mathbf{N}} \left\langle \frac{1}{z_\alpha - \bar{z}_{d\alpha}} \left[1 - \sqrt{\frac{\bar{z}_{d\alpha}^2 - a^2}{z_\alpha^2 - a^2}} \right] - \frac{1}{\sqrt{z_\alpha^2 - a^2}} \right\rangle \bar{\mathbf{d}} + (\mathbf{u}_{,1}^\infty - \boldsymbol{\Omega}) \frac{i\pi z}{\sqrt{z^2 - a^2}} \right\}. \end{aligned} \quad (95)$$

Substitution of Equations (94) and (95) into (2) yields the complete stress and electric displacement field solutions in s_1 and s_2 , respectively.

By substituting Equation (91) into Equations (46) with (93), the generalized strain intensity factors at the right tip of the rigid conducting line are obtained as

$$\mathbf{k} = \sqrt{\pi a} (\mathbf{u}_{,1}^\infty - \boldsymbol{\Omega}) + \frac{2}{\sqrt{\pi a}} \text{Im} \left[\mathbf{N} \left\langle 1 - \sqrt{\frac{z_{d\alpha} + a}{z_{d\alpha} - a}} \right\rangle \mathbf{d} \right]. \quad (96)$$

Substituting Equation (91) into (47), one has the generalized stress intensity factors at the right tip of the rigid conducting line $\mathbf{K} = \mathbf{S}_1^T \mathbf{H}_1^{-1} \mathbf{k} = \mathbf{S}_2^T \mathbf{H}_2^{-1} \mathbf{k}$, where $\mathbf{S}_1^T \mathbf{H}_1^{-1} = \mathbf{S}_2^T \mathbf{H}_2^{-1}$ for real Y .

Substituting Equation (96) into (55) yields

$$G = -\frac{\pi a}{4}(\mathbf{u}_{,1}^\infty - \mathbf{\Omega})^T \mathbf{Y}(\mathbf{\Omega} - \mathbf{u}_{,1}^\infty) - (\mathbf{u}_{,1}^\infty - \mathbf{\Omega})^T \mathbf{Y} \operatorname{Im} \left[N \left\langle 1 - \sqrt{\frac{z_{d\alpha} + a}{z_{d\alpha} - a}} \right\rangle \mathbf{d} \right] - \frac{1}{\pi a} \operatorname{Im} \left[\mathbf{d}^T \left\langle 1 - \sqrt{\frac{z_{d\alpha} + a}{z_{d\alpha} - a}} \right\rangle N^T \right] \mathbf{Y} \operatorname{Im} \left[N \left\langle 1 - \sqrt{\frac{z_{d\alpha} + a}{z_{d\alpha} - a}} \right\rangle \mathbf{d} \right]. \quad (97)$$

5.2. A single rigid dielectric line: the fields of a square root singularity. In this case, Equation (42) reads

$$\hat{\mathbf{I}}(z) = (\hat{\mathbf{\Omega}} - \hat{\mathbf{u}}_{,1}^\infty) \left[\frac{1}{2} - \frac{z}{2\sqrt{z^2 - a^2}} \right] - \frac{1}{2\pi i} \hat{N} \left\langle \frac{1}{z_\alpha - z_{d\alpha}} \left[1 - \sqrt{\frac{z_{d\alpha}^2 - a^2}{z_\alpha^2 - a^2}} \right] - \frac{1}{\sqrt{z_\alpha^2 - a^2}} \right\rangle \mathbf{d} + \frac{1}{2\pi i} \bar{\hat{N}} \left\langle \frac{1}{z_\alpha - \bar{z}_{d\alpha}} \left[1 - \sqrt{\frac{\bar{z}_{d\alpha}^2 - a^2}{z_\alpha^2 - a^2}} \right] - \frac{1}{\sqrt{z_\alpha^2 - a^2}} \right\rangle \bar{\mathbf{d}} + \frac{z}{2\sqrt{z^2 - a^2}} \mathbf{c}_0^b. \quad (98)$$

Substituting Equation (98) into Equations (44) and (45), and applying the residue theorem, we obtain

$$\mathbf{c}_0^b = \mathbf{0}, \quad (99)$$

$$\omega = \frac{1}{\hat{Y}_{2j}} \left\{ \sum_{j=1}^3 \hat{Y}_{2j} u_{j,1}^\infty + \frac{4}{\pi a^2} \operatorname{Im} \left[\hat{Y} \hat{N} \left\langle \sqrt{z_{d\alpha}^2 - a^2} - z_{d\alpha} \right\rangle \mathbf{d} \right] \right\}. \quad (100)$$

Substituting Equation (98) into (39), using Equations (19)–(22), and (26), and neglecting constants, we have

$$\mathbf{F}_1(z) = \mathbf{A}_1^{-1} \left\{ \frac{1}{2\pi i} \mathbf{A}_1 \left\langle \frac{1}{z_\alpha - z_{d\alpha}} \right\rangle \mathbf{d} - \frac{1}{2\pi i} (2\bar{N} - \bar{\mathbf{A}}_1) \left\langle \frac{1}{z_\alpha - \bar{z}_{d\alpha}} \right\rangle \bar{\mathbf{d}} \right\} - \frac{1}{2\pi i} \mathbf{A}_1^{-1} (\hat{\mathbf{I}} - \mathbf{E}) \left\{ \hat{N} \left\langle \frac{1}{z_\alpha - z_{d\alpha}} \left[1 - \sqrt{\frac{z_{d\alpha}^2 - a^2}{z_\alpha^2 - a^2}} \right] - \frac{1}{\sqrt{z_\alpha^2 - a^2}} \right\rangle \mathbf{d} - \bar{\hat{N}} \left\langle \frac{1}{z_\alpha - \bar{z}_{d\alpha}} \left[1 - \sqrt{\frac{\bar{z}_{d\alpha}^2 - a^2}{z_\alpha^2 - a^2}} \right] - \frac{1}{\sqrt{z_\alpha^2 - a^2}} \right\rangle \bar{\mathbf{d}} + (\hat{\mathbf{\Omega}} - \hat{\mathbf{u}}_{,1}^\infty) \frac{i\pi z}{\sqrt{z^2 - a^2}} \right\}, \quad (101)$$

$$\mathbf{F}_2(z) = \mathbf{A}_2^{-1} \left\{ \frac{1}{2\pi i} N \left\langle \frac{2}{z_\alpha - z_{d\alpha}} \right\rangle \mathbf{d} + (\hat{\mathbf{I}} - \mathbf{E}) \left[-\frac{1}{2\pi i} \hat{N} \left\langle \frac{1}{z_\alpha - z_{d\alpha}} \left[1 - \sqrt{\frac{z_{d\alpha}^2 - a^2}{z_\alpha^2 - a^2}} \right] - \frac{1}{\sqrt{z_\alpha^2 - a^2}} \right\rangle \mathbf{d} + \frac{1}{2\pi i} \bar{\hat{N}} \left\langle \frac{1}{z_\alpha - \bar{z}_{d\alpha}} \left[1 - \sqrt{\frac{\bar{z}_{d\alpha}^2 - a^2}{z_\alpha^2 - a^2}} \right] - \frac{1}{\sqrt{z_\alpha^2 - a^2}} \right\rangle \bar{\mathbf{d}} - (\hat{\mathbf{\Omega}} - \hat{\mathbf{u}}_{,1}^\infty) \frac{z}{2\sqrt{z^2 - a^2}} \right] \right\}. \quad (102)$$

Substituting Equations (101) and (102) into (2) leads to the complete stress and electric displacement field solutions in s_1 and s_2 , respectively.

Substituting Equation (98) into (49) with (100), and using Equation (48), we obtain the generalized strain intensity factors at the right tip of the rigid dielectric line as

$$\mathbf{k} = \sqrt{\pi a}(\hat{\mathbf{I}} - \mathbf{E})(\hat{\mathbf{u}}_{,1}^{\infty} - \hat{\mathbf{\Omega}}) + \frac{2}{\sqrt{\pi a}}(\hat{\mathbf{I}} - \mathbf{E}) \operatorname{Im} \left[\hat{\mathbf{N}} \left\langle 1 - \sqrt{\frac{z_{d\alpha} + a}{z_{d\alpha} - a}} \right\rangle \mathbf{d} \right]. \quad (103)$$

Substituting Equation (98) into (47) with (100), one finds the generalized stress intensity factors at the right tip of the rigid dielectric line as

$$\mathbf{K} = \mathbf{S}_1^T \mathbf{H}_1^{-1} \mathbf{k} = \mathbf{S}_2^T \mathbf{H}_2^{-1} \mathbf{k}. \quad (104)$$

Substituting Equation (103) into (56) leads to

$$\begin{aligned} G = & -\frac{\pi a}{4}(\hat{\mathbf{u}}_{,1}^{\infty} - \hat{\mathbf{\Omega}})^T \hat{\mathbf{Y}}(\hat{\mathbf{u}}_{,1}^{\infty} - \hat{\mathbf{\Omega}}) - (\hat{\mathbf{u}}_{,1}^{\infty} - \hat{\mathbf{\Omega}})^T \hat{\mathbf{Y}} \operatorname{Im} \left[\hat{\mathbf{N}} \left\langle 1 - \sqrt{\frac{z_{d\alpha} + a}{z_{d\alpha} - a}} \right\rangle \mathbf{d} \right] \\ & - \frac{1}{\pi a} \operatorname{Im} \left[\mathbf{d}^T \left\langle 1 - \sqrt{\frac{z_{d\alpha} + a}{z_{d\alpha} - a}} \right\rangle \hat{\mathbf{N}}^T \right] \hat{\mathbf{Y}} \operatorname{Im} \left[\hat{\mathbf{N}} \left\langle 1 - \sqrt{\frac{z_{d\alpha} + a}{z_{d\alpha} - a}} \right\rangle \mathbf{d} \right]. \end{aligned} \quad (105)$$

It is observed that the electric field applied at infinity cannot induce the rotation of the interfacial rigid dielectric line, and makes no contribution to the singularities of the stress and electric displacement fields at the tips of the interfacial rigid dielectric line in the two half-infinite planes.

6. Near-tip fields around a single rigid line with a complex Y

In this section, let us consider a rigid line of length $2a$ centered along the x_1 axis, when Y is complex. The rotation of the rigid line is assumed to be ω . Equations (30) and (41) become Equations (89) and (90), respectively. Equations (63) and (68) become

$$X_{\alpha}(z) = (z + a)^{-1/2+i\varepsilon_{\alpha}}(z - a)^{-1/2-i\varepsilon_{\alpha}}, \quad (106)$$

$$x_{\alpha}(\infty) = z - i2a\varepsilon_{\alpha}, \quad (107)$$

respectively. For convenience, we define

$$q_1(z, \alpha) = \frac{z - i2a\varepsilon_{\alpha}}{\sqrt{z^2 - a^2}} \left[\frac{z + a}{z - a} \right]^{i\varepsilon_{\alpha}}, \quad (108)$$

$$q_2(z, z_{d\beta}, \alpha) = \frac{1}{z - z_{d\beta}} \left\{ 1 - \sqrt{\frac{z_{d\beta}^2 - a^2}{z^2 - a^2}} \left[\frac{z + a}{z - a} \right]^{i\varepsilon_{\alpha}} \left[\frac{z_{d\beta} - a}{z_{d\beta} + a} \right]^{i\varepsilon_{\alpha}} \right\} - \frac{1}{\sqrt{z^2 - a^2}} \left[\frac{z + a}{z - a} \right]^{i\varepsilon_{\alpha}}. \quad (109)$$

6.1. A single rigid conducting line: the fields of square root, nonsquare root and oscillatory singularities. Substituting Equation (66) into Equations (35), and (36), with Equations (67) ($n = 1$), (89), (106),

and (107), and applying the residue theorem, we have

$$\lambda_\alpha(z) = (\mathbf{W}^\alpha \mathbf{u}_{,1}^\infty - W_{\alpha 2} \omega) q_1(z, \alpha) - \frac{1}{i\pi} \sum_{j=1}^4 W_{\alpha j} \left[\sum_{\beta=1}^4 N_{j\beta} d_\beta q_2(z, z_{d\beta}, \alpha) - \sum_{k=1}^4 \bar{N}_{j\beta} \bar{d}_\beta q_2(z, \bar{z}_{d\beta}, \alpha) \right], \quad (110)$$

$$\omega = \rho_1 \sum_{k=1}^4 v_k \left\{ \sum_{j=1}^4 \frac{1}{i\pi a^2} W_{kj} \left[\sum_{r=1}^4 N_{jr} d_r [i2a\varepsilon_k - z_{dr} + (z_{dr} + a)^{1/2-i\varepsilon_k} (z_{dr} - a)^{1/2+i\varepsilon_k}] - \sum_{r=1}^4 \bar{N}_{jr} \bar{d}_r [i2a\varepsilon_k - \bar{z}_{dr} + (\bar{z}_{dr} + a)^{1/2-i\varepsilon_k} (\bar{z}_{dr} - a)^{1/2+i\varepsilon_k}] \right] + \mathbf{W}^k \mathbf{u}_{j,1}^\infty (1/2 + 2\varepsilon_k^2) \right\}, \quad (111)$$

where

$$\rho_1 = 1 / \sum_{k=1}^4 v_k W_{k2} (1/2 + 2\varepsilon_k^2), \quad v_k = \frac{\Xi_k}{(1 + e^{2\pi\varepsilon_k}) v_k}, \quad (112)$$

with Ξ_k being the elements of the 1×4 matrix $\Xi = \mathbf{Y}^{(2)} \mathbf{\Lambda}_A$.

Substituting Equation (110) into (61) with (111), and using Equations (19)–(22), and (26), we find

$$\mathbf{F}_1(z) = \frac{1}{2\pi i} \left[\left\langle \frac{1}{z_\alpha - z_{d\alpha}} \right\rangle \mathbf{d} - \mathbf{A}_1^{-1} (2\bar{\mathbf{N}} - \bar{\mathbf{A}}_1) \left\langle \frac{1}{z_\alpha - \bar{z}_{d\alpha}} \right\rangle \bar{\mathbf{d}} \right] + \mathbf{A}_1^{-1} \sum_{\alpha=1}^4 \frac{\lambda_\alpha \mathbf{\Lambda}_\alpha}{(1 + e^{2\pi\varepsilon_\alpha}) v_\alpha}, \quad (113)$$

$$\mathbf{F}_2(z) = \frac{1}{\pi i} \mathbf{A}_2^{-1} \mathbf{N} \left\langle \frac{1}{z_\alpha - z_{d\alpha}} \right\rangle \mathbf{d} + \mathbf{A}_2^{-1} \bar{\mathbf{Y}}^{-1} \mathbf{Y} \sum_{\alpha=1}^4 \frac{\lambda_\alpha \mathbf{\Lambda}_\alpha}{(1 + e^{2\pi\varepsilon_\alpha}) v_\alpha}. \quad (114)$$

Substitution of the above equations into Equation (2) yields the complete stress and electric displacement field solutions in s_1 and s_2 .

By substituting Equation (110) into (71), the generalized strain intensity factors at the right tip of the rigid conducting line are obtained as

$$\tilde{k}_\alpha = \frac{(2a)^{i\varepsilon_\alpha}}{v_\alpha} \left\{ \frac{1}{i\sqrt{\pi a}} \sum_{j=1}^4 W_{\alpha j} \left[\sum_{k=1}^4 N_{jk} d_k \left[1 - \sqrt{\frac{z_{dk} + a}{z_{dk} - a}} \left(\frac{z_{dk} - a}{z_{dk} + a} \right)^{i\varepsilon_\alpha} \right] - \sum_{k=1}^4 \bar{N}_{jk} \bar{d}_k \left[1 - \sqrt{\frac{\bar{z}_{dk} + a}{\bar{z}_{dk} - a}} \left(\frac{\bar{z}_{dk} - a}{\bar{z}_{dk} + a} \right)^{i\varepsilon_\alpha} \right] \right] + \sqrt{\pi a} \mathbf{W}^\alpha (\mathbf{u}_{,1}^\infty - \mathbf{\Omega}) (1 - i2\varepsilon_\alpha) \right\}. \quad (115)$$

The rigid line extension force can be obtained by substituting Equation (115) into (74). This solution procedure is not given in detail here.

6.2. A single rigid dielectric line: the fields of square root and oscillatory singularities. Substituting Equation (80) into (44), and (45) with Equations (81) ($n = 1$), (90), (106), and (107), and applying the

residue theorem, we have

$$\lambda_\alpha(z) = (\hat{W}^\alpha \hat{u}_{,1}^\infty - \hat{W}_{\alpha 2} \omega) q_1(z, \alpha) - \frac{1}{i\pi} \sum_{j=1}^3 \hat{W}_{\alpha j} \left[\sum_{\beta=1}^4 N_{j\beta} d_\beta q_2(z, z_{d\beta}, \alpha) - \sum_{k=1}^4 \bar{N}_{j\beta} \bar{d}_\beta q_2(z, \bar{z}_{d\beta}, \alpha) \right], \quad (116)$$

$$\omega = \rho_2 \sum_{k=1}^3 \vartheta_k \left\{ \frac{1}{i\pi a^2} \sum_{j=1}^3 \hat{W}_{kj} \left\{ \sum_{r=1}^4 N_{jr} d_r [i2a\varepsilon_k - z_{dr} + (z_{dr} + a)^{1/2-i\varepsilon_k} (z_{dr} - a)^{1/2+i\varepsilon_k}] - \sum_{r=1}^4 \bar{N}_{jr} \bar{d}_r [i2a\varepsilon_k - \bar{z}_{dr} + (\bar{z}_{dr} + a)^{1/2-i\varepsilon_k} (\bar{z}_{dr} - a)^{1/2+i\varepsilon_k}] \right\} + \sum_{j=1}^3 \hat{W}_{kj} \hat{u}_{j,1}^\infty (1/2 + 2\varepsilon_k^2) \right\}, \quad (117)$$

where

$$\rho_2 = \frac{1}{\sum_{k=1}^3 \vartheta_k \hat{W}_{k2} (1/2 + 2\varepsilon_k^2)}, \quad \vartheta_k = \frac{Q_k}{(1 + e^{2\pi\varepsilon_k}) v_k}, \quad (118)$$

with Q_k being the elements of the 1×3 matrix $\mathbf{Q} = \hat{Y}^{(2)} \mathbf{\Lambda}_A$.

Substituting Equation (116) into (80) with (117), and using Equations (19)–(22), (26), and (39), we find

$$F_1(z) = \frac{1}{2\pi i} \left[\left\langle \frac{1}{z_\alpha - z_{d\alpha}} \right\rangle \mathbf{d} - \mathbf{A}_1^{-1} (2\bar{\mathbf{N}} - \bar{\mathbf{A}}_1) \left\langle \frac{1}{z_\alpha - \bar{z}_{d\alpha}} \right\rangle \bar{\mathbf{d}} \right] + \mathbf{A}_1^{-1} (\hat{\mathbf{I}} - \mathbf{E}) \sum_{\alpha=1}^3 \frac{\lambda_\alpha \mathbf{\Lambda}_\alpha}{(1 + e^{2\pi\varepsilon_\alpha}) v_\alpha}, \quad (119)$$

$$F_2(z) = \frac{1}{\pi i} \mathbf{A}_2^{-1} \mathbf{N} \left\langle \frac{1}{z_\alpha - z_{d\alpha}} \right\rangle \mathbf{d} + \mathbf{A}_2^{-1} \bar{\mathbf{Y}}^{-1} \mathbf{Y} (\hat{\mathbf{I}} - \mathbf{E}) \sum_{\alpha=1}^3 \frac{\lambda_\alpha \mathbf{\Lambda}_\alpha}{(1 + e^{2\pi\varepsilon_\alpha}) v_\alpha}. \quad (120)$$

Substitution of the above equations into Equation (2) yields the complete stress and electric displacement field solution in s_1 and s_2 .

By substituting Equation (116) into (71), the strain intensity factors at the right tip of the rigid dielectric line are obtained as

$$\tilde{k}_\alpha = \frac{(2a)^{i\varepsilon_\alpha}}{v_\alpha} \left\{ \frac{1}{i\sqrt{\pi a}} \sum_{j=1}^3 \hat{W}_{\alpha j} \left\{ \sum_{k=1}^4 N_{jk} d_k \left[1 - \sqrt{\frac{z_{dk} + a}{z_{dk} - a}} \left(\frac{z_{dk} - a}{z_{dk} + a} \right)^{i\varepsilon_\alpha} \right] - \sum_{k=1}^4 \bar{N}_{jk} \bar{d}_k \left[1 - \sqrt{\frac{\bar{z}_{dk} + a}{\bar{z}_{dk} - a}} \left(\frac{\bar{z}_{dk} - a}{\bar{z}_{dk} + a} \right)^{i\varepsilon_\alpha} \right] + \sqrt{\pi a} \hat{W}^\alpha (\hat{u}_{,1}^\infty - \hat{\mathbf{\Omega}}) (1 - i2\varepsilon_\alpha) \right\} \right\}, \quad (121)$$

for $\alpha = 1, 2, 3$. The rigid line extension force can be obtained by substituting Equation (121) into (88).

Similar to the case in which Y is real, the electric field applied at infinity does not affect either the rotation of the single interfacial rigid dielectric line, or the stress and electric displacement fields in the two half-infinite planes with the single interfacial rigid dielectric line.

7. Image force on the piezoelectric dislocation

The image forces in the x and y directions on the piezoelectric dislocation are obtained from the generalized Peach–Koehler formula [Pak 1990b] as

$$F_x = \sigma_{i2}^d b_i = \mathbf{b}^T \Phi_{,1}^d, \quad F_y = -\sigma_{i1}^d b_i = \mathbf{b}^T \Phi_{,2}^d,$$

where σ_{i2}^d (or $\Phi_{,1}^d$) and σ_{i1}^d (or $-\Phi_{,2}^d$) are the generalized stresses obtained by subtracting the fields generated by the piezoelectric dislocation with $z \rightarrow z_d$. Here we consider the case of a single rigid line of length $2a$ centered along the interface of two piezoelectric media in the absence of far-field loads.

7.1. A single rigid conducting line. For the case in which Y is real, we obtain, from Equations (2), (3), and (94):

$$\begin{aligned} \Phi_{,1}^d &= \frac{1}{\pi} \operatorname{Im} \left[\mathbf{B}_1 \mathbf{A}_1^{-1} \bar{\mathbf{A}}_1 \langle g_1(z_{d\alpha}) \rangle \bar{\mathbf{B}}_1^T \mathbf{b} - \mathbf{B}_1 \mathbf{A}_1^{-1} N \langle g_2(z_{d\alpha}) \rangle \mathbf{B}_1^T \mathbf{b} \right. \\ &\quad \left. - \mathbf{B}_1 \mathbf{A}_1^{-1} \bar{N} \langle g_3(z_{d\alpha}) \rangle \bar{\mathbf{B}}_1^T \mathbf{b} \right] - \operatorname{Re} [\mathbf{B}_1 \mathbf{A}_1^{-1} \boldsymbol{\Omega} g_4(z_d)], \\ \Phi_{,2}^d &= \frac{1}{\pi} \operatorname{Im} \left[\mathbf{B}_1 \mathbf{A}_1^{-1} \bar{\mathbf{A}}_1 \langle p_\alpha g_1(z_{d\alpha}) \rangle \bar{\mathbf{B}}_1^T \mathbf{b} - \mathbf{B}_1 \mathbf{A}_1^{-1} N \langle p_\alpha g_2(z_{d\alpha}) \rangle \mathbf{B}_1^T \mathbf{b} \right. \\ &\quad \left. - \mathbf{B}_1 \mathbf{A}_1^{-1} \bar{N} \langle p_\alpha g_3(z_{d\alpha}) \rangle \bar{\mathbf{B}}_1^T \mathbf{b} \right] - \operatorname{Re} [\mathbf{B}_1 \langle p_\alpha \rangle \mathbf{A}_1^{-1} \boldsymbol{\Omega} g_4(z_d)], \end{aligned}$$

where

$$\begin{aligned} g_1(z_{d\alpha}) &= \frac{1}{z_{d\alpha} - \bar{z}_{d\alpha}}, & g_2(z_{d\alpha}) &= \frac{z_{d\alpha} - \sqrt{z_{d\alpha}^2 - a^2}}{z_{d\alpha}^2 - a^2}, \\ g_3(z_{d\alpha}) &= \frac{z_{d\alpha} - \bar{z}_{d\alpha} + \sqrt{z_{d\alpha}^2 - a^2} + \sqrt{\bar{z}_{d\alpha}^2 - a^2}}{(z_{d\alpha} - \bar{z}_{d\alpha})\sqrt{z_{d\alpha}^2 - a^2}}, & g_4(z_d) &= \frac{z_d}{\sqrt{z_d^2 - a^2}}, \end{aligned}$$

and the nonzero component ω of $\boldsymbol{\Omega}$ is obtained from Equation (93) by deleting the first term due to the remote loads.

For the case in which Y is complex, from Equations (2), (3), and (113), one has

$$\begin{aligned} \Phi_{,1}^d &= \frac{1}{\pi} \operatorname{Im} \left[\mathbf{B}_1 \mathbf{A}_1^{-1} (\bar{\mathbf{A}}_1 - 2\bar{N}) \langle g_1(z_{d\alpha}) \rangle \bar{\mathbf{B}}_1^T \mathbf{b} \right] + 2 \operatorname{Re} \left[\mathbf{B}_1 \mathbf{A}_1^{-1} \sum_{\alpha=1}^4 \frac{\lambda_\alpha^d(z_d) \boldsymbol{\Lambda}_\alpha}{(1 + e^{2\pi \varepsilon_\alpha}) v_\alpha} \right], \\ \Phi_{,2}^d &= \frac{1}{\pi} \operatorname{Im} \left[\mathbf{B}_1 \mathbf{A}_1^{-1} (\bar{\mathbf{A}}_1 - 2\bar{N}) \langle p_\alpha g_1(z_{d\alpha}) \rangle \bar{\mathbf{B}}_1^T \mathbf{b} \right] + 2 \operatorname{Re} \left[\mathbf{B}_1 \langle p_\alpha \rangle \mathbf{A}_1^{-1} \sum_{\alpha=1}^4 \frac{\lambda_\alpha^d(z_d) \boldsymbol{\Lambda}_\alpha}{(1 + e^{2\pi \varepsilon_\alpha}) v_\alpha} \right], \end{aligned}$$

where the nonzero component ω of $\boldsymbol{\Omega}$ is obtained from Equation (111) by deleting the last term due to the remote loads and $\lambda_\alpha^d(z_d)$ can be found from (110) by letting $z \rightarrow z_d$.

7.2. A single rigid dielectric line. For the case in which Y is real, from Equations (2), (3), and (101), one has

$$\begin{aligned} \Phi_{,1}^d &= \frac{1}{\pi} \operatorname{Im} \left[\mathbf{B}_1 \mathbf{A}_1^{-1} (\bar{\mathbf{A}}_1 - 2\bar{\mathbf{N}}) \langle g_1(z_{d\alpha}) \rangle \bar{\mathbf{B}}_1^T \mathbf{b} - \mathbf{B}_1 \mathbf{A}_1^{-1} (\hat{\mathbf{I}} - \mathbf{E}) \hat{\mathbf{N}} \langle g_2(z_{d\alpha}) \rangle \mathbf{B}_1^T \mathbf{b} \right. \\ &\quad \left. + \mathbf{B}_1 \mathbf{A}_1^{-1} (\hat{\mathbf{I}} - \mathbf{E}) \tilde{\mathbf{N}} \langle g_5(z_{d\alpha}) \rangle \bar{\mathbf{B}}_1^T \mathbf{b} \right] - \operatorname{Re} [\mathbf{B}_1 \mathbf{A}_1^{-1} (\hat{\mathbf{I}} - \mathbf{E}) \hat{\mathbf{\Omega}} g_4(z_d)], \\ \Phi_{,2}^d &= \frac{1}{\pi} \operatorname{Im} \left[\mathbf{B} \mathbf{A}_1^{-1} (\bar{\mathbf{A}}_1 - 2\bar{\mathbf{N}}) \langle p_\alpha g_1(z_{d\alpha}) \rangle \bar{\mathbf{B}}_1^T \mathbf{b} - \mathbf{B} \mathbf{A}_1^{-1} (\hat{\mathbf{I}} - \mathbf{E}) \hat{\mathbf{N}} \langle p_\alpha g_2(z_{d\alpha}) \rangle \mathbf{B}_1^T \mathbf{b} \right. \\ &\quad \left. + \mathbf{B} \mathbf{A}_1^{-1} (\hat{\mathbf{I}} - \mathbf{E}) \tilde{\mathbf{N}} \langle p_\alpha g_5(z_{d\alpha}) \rangle \bar{\mathbf{B}}_1^T \mathbf{b} \right] - \operatorname{Re} [\mathbf{B} \langle p_\alpha \rangle \mathbf{A}_1^{-1} (\hat{\mathbf{I}} - \mathbf{E}) \hat{\mathbf{\Omega}} g_4(z_d)], \end{aligned}$$

where

$$g_5(z_{d\alpha}) = \frac{z_{d\alpha} + \bar{z}_{d\alpha} - \sqrt{z_{d\alpha}^2 - a^2} - \sqrt{\bar{z}_{d\alpha}^2 - a^2}}{(\sqrt{z_{d\alpha}^2 - a^2} + \sqrt{\bar{z}_{d\alpha}^2 - a^2}) \sqrt{z_{d\alpha}^2 - a^2}},$$

and the nonzero component ω of $\hat{\mathbf{\Omega}}$ is obtained from Equation (100) by deleting the first term due to the remote loads.

For the case in which Y is complex, we have from Equations (2), (3), and (119)

$$\begin{aligned} \Phi_{,1}^d &= \frac{1}{\pi} \operatorname{Im} [\mathbf{B}_1 \mathbf{A}_1^{-1} (\bar{\mathbf{A}}_1 - 2\bar{\mathbf{N}}) \langle g_1(z_{d\alpha}) \rangle \bar{\mathbf{B}}_1^T \mathbf{b}] + 2 \operatorname{Re} \left[\mathbf{B}_1 \mathbf{A}_1^{-1} (\hat{\mathbf{I}} - \mathbf{E}) \sum_{\alpha=1}^3 \frac{\lambda_\alpha^d(z_d) \mathbf{\Lambda}_\alpha}{(1 + e^{2\pi\varepsilon_\alpha}) v_\alpha} \right], \\ \Phi_{,2}^d &= \frac{1}{\pi} \operatorname{Im} [\mathbf{B}_1 \mathbf{A}_1^{-1} (\bar{\mathbf{A}}_1 - 2\bar{\mathbf{N}}) \langle p_\alpha g_1(z_{d\alpha}) \rangle \bar{\mathbf{B}}_1^T \mathbf{b}] + 2 \operatorname{Re} \left[\mathbf{B}_1 \langle p_\alpha \rangle \mathbf{A}_1^{-1} (\hat{\mathbf{I}} - \mathbf{E}) \sum_{\alpha=1}^3 \frac{\lambda_\alpha^d(z_d) \mathbf{\Lambda}_\alpha}{(1 + e^{2\pi\varepsilon_\alpha}) v_\alpha} \right], \end{aligned}$$

where the nonzero component ω of $\hat{\mathbf{\Omega}}$ is obtained from Equation (117) by deleting the last term due to the remote loads, and $\lambda_\alpha^d(z_d)$ can be found from (116) by let $z \rightarrow z_d$.

8. Numerical examples and discussions

In this section, numerical examples are performed to show a) the singularity types of the near-tip stress and electric displacement field, as well as b) to examine the effects of such parameters as the position of the mixed dislocation, and the Burgers vector components b_1, b_2, b_φ , on the image force. As an example, BaTiO₃ is considered for s_1 and PZT-6B for s_2 , with material properties listed in Table 1 [Ou and Wu 2003]. Poling directions of the two materials are assumed to be along the x_2 axis. Based on the material constants given, we obtain

$$\begin{aligned} \varepsilon &= 0, & \kappa &= 0.03528, & (122) \\ \mathbf{\Lambda}_A &= \begin{bmatrix} 0 & 0 & 3.506 \times 10^{-10} & -3.506 \times 10^{-10} \\ 0 & -1.6807 \times 10^{-9} & -2.245 \times 10^{-10} & -2.245 \times 10^{-10} \\ 1 & 0 & 0 & 0 \\ 0 & 0.9999 & 0.9999 & 0.9999 \end{bmatrix} \end{aligned}$$

		PZT-6B	BaTiO ₃
c_{11}	GPa	168	150
c_{12}	GPa	60	66
c_{13}	GPa	60	66
c_{33}	GPa	163	146
c_{44}	GPa	27.1	44
e_{31}	C/m ²	-0.90	-4.35
e_{33}	C/m ²	7.10	17.5
e_{15}	C/m ²	4.60	11.4
ε_{11}	10 ⁻¹⁰ C/Vm	36.0	98.7
ε_{13}	10 ⁻¹⁰ C/Vm	34.0	112

Table 1. Material Properties for BaTiO₃ and PZT-6B. The poling direction is along the x_3 axis.

for the conducting case, and

$$\varepsilon = 0.02439, \quad (123)$$

$$\mathbf{\Lambda}_A = \begin{bmatrix} 0.7315 & 0.7315 & 0 \\ 0.6818i & -0.6818i & 0 \\ 0 & 0 & 1 \end{bmatrix}$$

for the dielectric case.

For BaTiO₃/PZT-6B bimaterial, it is found from Equations (58), (63), and (122) that the stress and electric displacement fields at the rigid conducting line tips present square root and nonsquare root singularities. It is also observed from Equations (76) and (123) that the stress and electric displacement fields at the rigid dielectric line tips have square root and oscillatory singularities, for BaTiO₃/PZT-6B and other piezoelectric materials.

Here, the tangential and radial components of the image force are analyzed, given by

$$F_t = -F_x \sin[\theta_d] + F_y \cos[\theta_d], \quad F_r = F_x \cos[\theta_d] + F_y \sin[\theta_d].$$

The normalizing factors are taken as

$$F_0(b_i) = \frac{1}{4\pi a} \mathbf{b}^T \mathbf{L}_1 \mathbf{b}, \quad i = 1, 2, 4,$$

for nonzero b_i . Thus the normalized tangential and radial components of the image force are given by

$$F_t^*(b_i) = F_t(b_i)/F_0(b_i), \quad F_r^*(b_i) = F_r(b_i)/F_0(b_i), \quad i = 1, 2, 4,$$

where a positive term contributes to the repulsive force and a negative term to the attractive force.

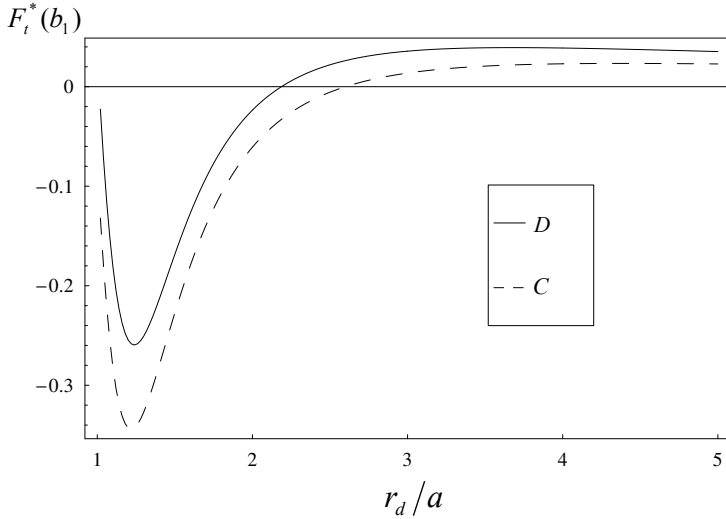


Figure 2. Normalized tangential force $F_t^*(b_1)$ versus r_d/a for $\theta_d = \pi/8$.

Normalized forces $F_t^*(b_1)$, $F_r^*(b_1)$, $F_t^*(b_2)$, $F_r^*(b_2)$, $F_t^*(b_\varphi)$ and $F_r^*(b_\varphi)$ versus r_d/a are depicted in Figures 2–7, respectively, for $\theta_d = \pi/8$. Normalized forces $F_t^*(b_1)$, $F_r^*(b_1)$, $F_t^*(b_2)$, $F_r^*(b_2)$, $F_t^*(b_\varphi)$ and $F_r^*(b_\varphi)$ versus θ_d , for $r_d = 1.5a$, are plotted in Figures 8–13, respectively. The symbols C and D in the figures stand for the conducting and dielectric cases, respectively.

In the tangential direction, it is seen from Figure 2 that the interface and the rigid dielectric lines attract the dislocation with b_1 at a point (r_d, θ_d) when $r_d/a < \hat{r}_1^*$, and repel the dislocation with b_1 at a point (r_d, θ_d) when $r_d/a > \hat{r}_1^*$. The same phenomenon can be observed if \hat{r}_1^* is replaced by \hat{r}_2^* ($\hat{r}_2^* > \hat{r}_1^*$) for the conducting case. It is also found that the attractive force is stronger and the repulsive force is weaker

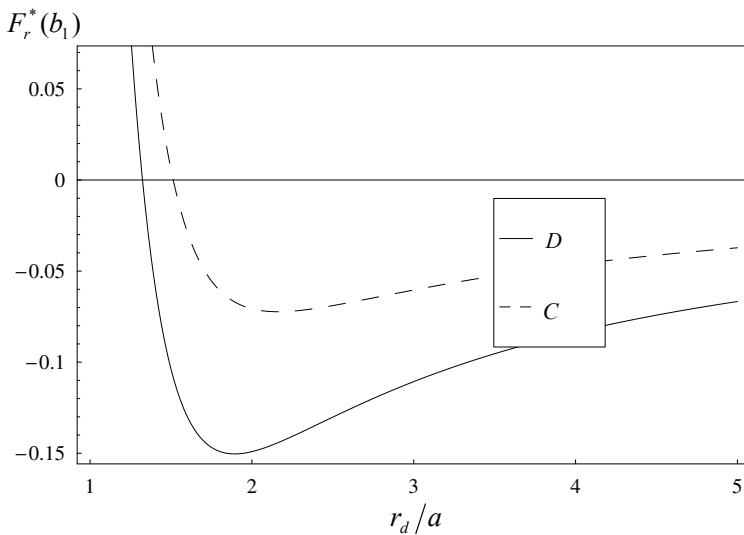


Figure 3. Normalized radial force $F_r^*(b_1)$ versus r_d/a for $\theta_d = \pi/8$.

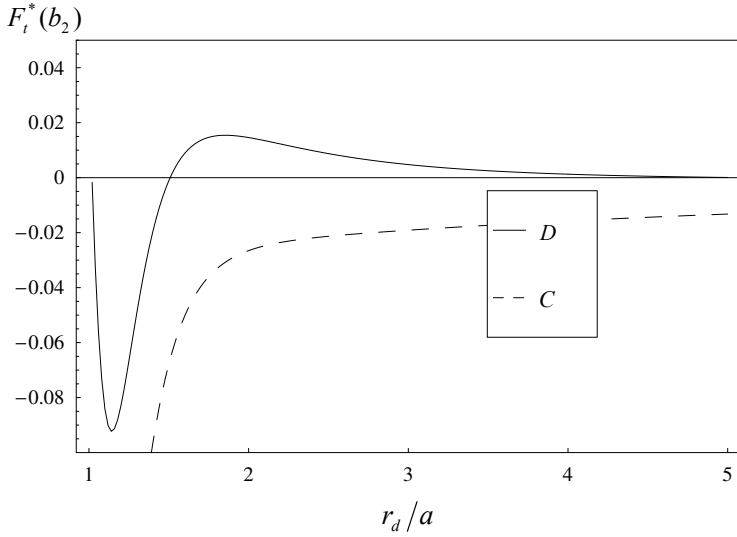


Figure 4. Normalized tangential force $F_t^*(b_2)$ versus r_d/a for $\theta_d = \pi/8$.

for the conducting case than for the dielectric case. The opposite phenomenon is observed from Figure 3 in the radial direction, where \hat{r}_1^* and \hat{r}_2^* are replaced by \hat{r}_3^* and \hat{r}_4^* ($\hat{r}_4^* > \hat{r}_3^*$), respectively.

As shown in Figure 4, in the tangential direction, the interface and the rigid conducting line always attract the dislocation with b_2 . However, the interface and the rigid dielectric line repel the dislocation with b_2 at a point (r_d, θ_d) when $r_d/a < \hat{r}_5^*$ or $r_d/a > \hat{r}_6^*$ ($\hat{r}_6^* > \hat{r}_5^*$), and attract the dislocation with b_2 at a point (r_d, θ_d) when $\hat{r}_5^* < r_d/a < \hat{r}_6^*$, in the tangential direction. Moreover from Figure 4, it should be noted that the attractive force on a dislocation with b_2 is stronger for the conducting case than for the dielectric case along the tangential direction. We can observe from Figure 5 that the interface and the

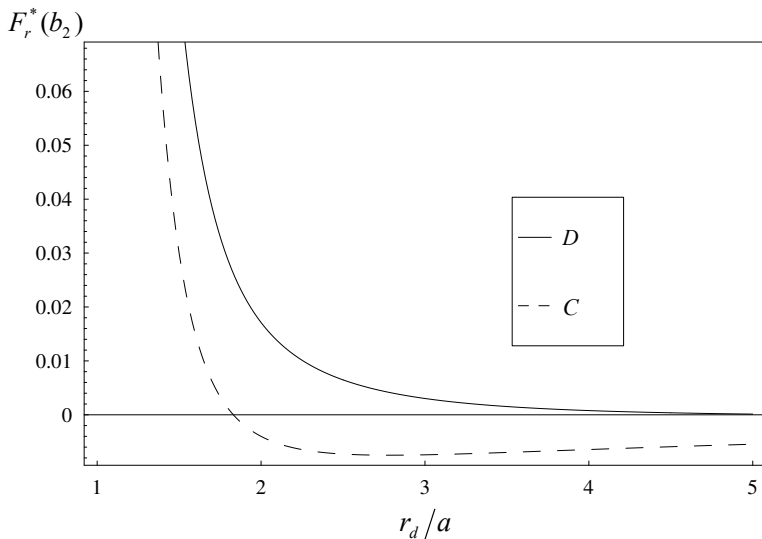


Figure 5. Normalized radial force $F_r^*(b_2)$ versus r_d/a for $\theta_d = \pi/8$.

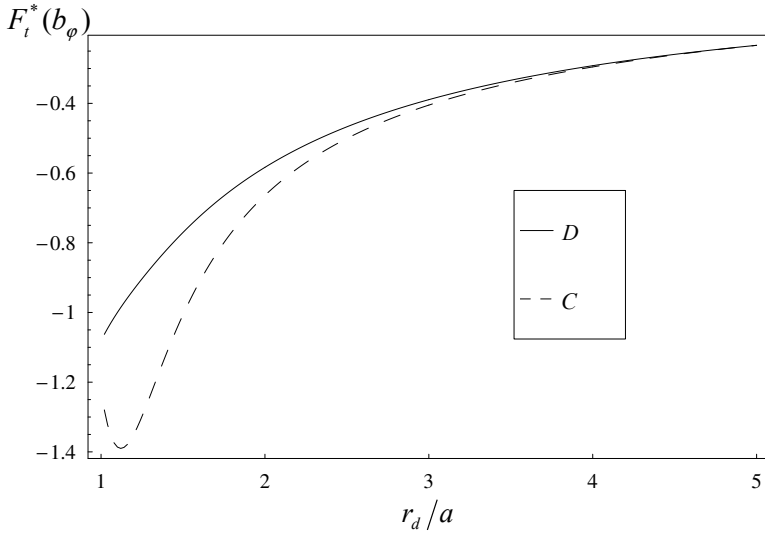


Figure 6. Normalized tangential force $F_t^*(b_\varphi)$ versus r_d/a for $\theta_d = \pi/8$.

rigid dielectric line always repel the dislocation with b_2 , in the radial direction. However, the interface and the rigid conducting line repel the dislocation with b_2 at a point (r_d, θ_d) when $r_d/a < \hat{r}_7^*$, and attract the dislocation with b_2 at a point (r_d, θ_d) when $r_d/a > \hat{r}_7^*$, in the radial direction. Also it can be observed that the rigid dielectric line repels the dislocation with b_2 more strongly than the rigid conducting line does.

In the tangential direction, it is clear from Figure 6 that the rigid conducting line induces a stronger attractive force on the dislocation with b_φ than does the rigid dielectric line. In the radial direction, it is observed from Figure 7 that the interface and the rigid dielectric line always attract the dislocation with

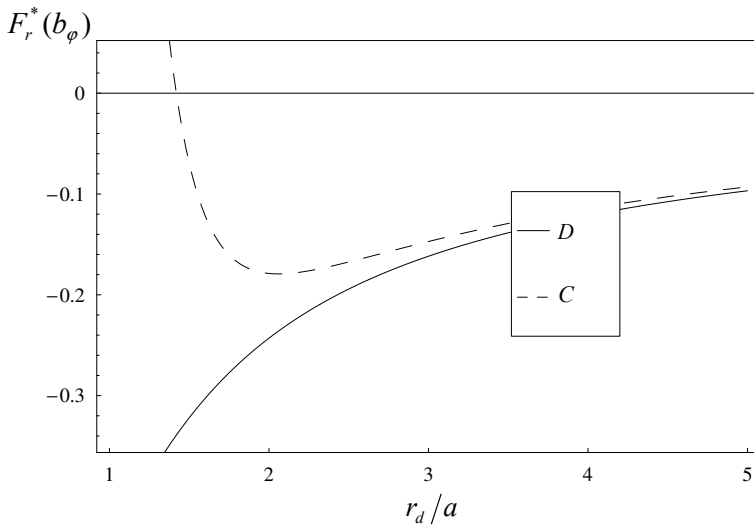


Figure 7. Normalized radial force $F_r^*(b_\varphi)$ versus r_d/a for $\theta_d = \pi/8$.

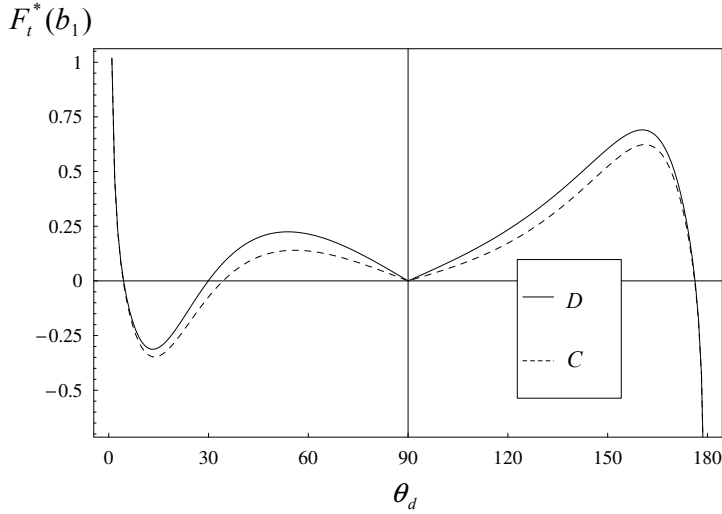


Figure 8. Normalized tangential force $F_t^*(b_1)$ versus θ_d for $r_d = 1.5a$.

b_φ . However, the interface and the rigid conducting line repel the dislocation with b_φ at a point (r_d, θ_d) when $r_d/a < \hat{r}_8^*$ and attract the dislocation with b_φ at a point (r_d, θ_d) when $r_d/a > \hat{r}_8^*$. Further, we observe from Figure 7 that the rigid dielectric line always attracts the dislocation with b_φ more strongly than does the rigid conducting line in the radial direction.

It is seen from Figure 8 that the value of the tangential force on a dislocation with b_1 away from the interface is always larger for the dielectric case than for the conducting case. This means that the effects on the forces due to the rigid dielectric line (the repulsive force is stronger and the attractive force is weaker) are stronger than the effects on the forces due to the rigid conducting line. From Figure 9, it can be observed that the value of the radial force on a dislocation with b_1 at a point (r_d, θ_d) , in which

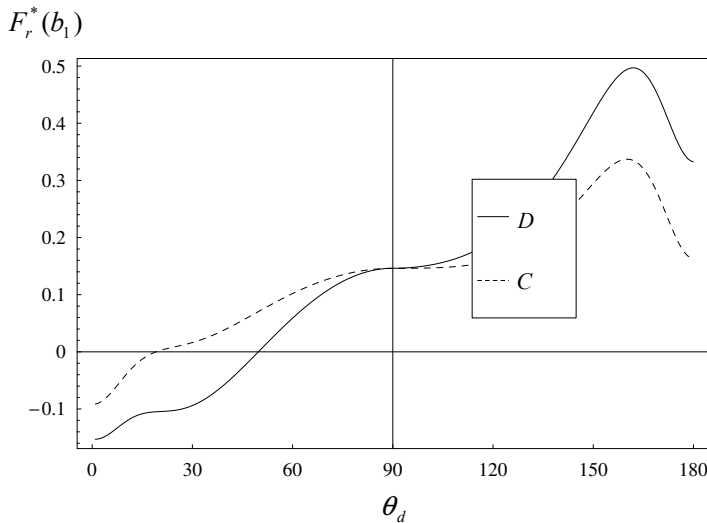


Figure 9. Normalized radial force $F_r^*(b_1)$ versus θ_d for $r_d = 1.5a$.

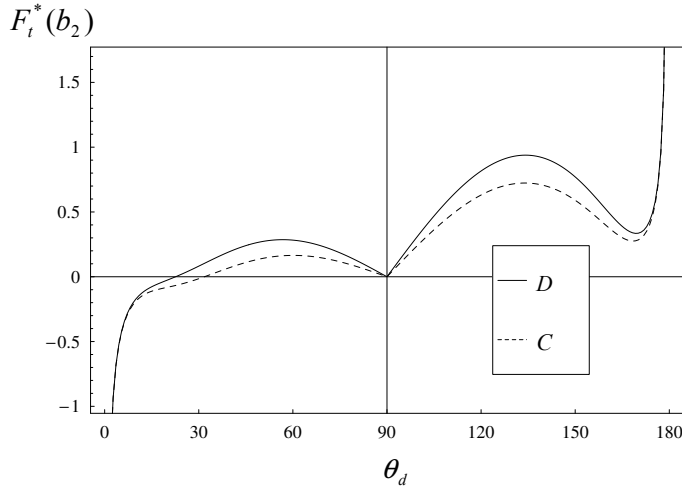


Figure 10. Normalized tangential force $F_t^*(b_2)$ versus θ_d for $r_d = 1.5a$.

$\theta_d < 90^\circ$, is always larger for the conducting case than for the dielectric case. However, the opposite phenomenon is observed when $90^\circ < \theta_d < 180^\circ$.

The force on a dislocation with b_2 , which repels the dislocation away from the interface (as is seen from Figure 10), is stronger due to a rigid dielectric line than the force due to a rigid conducting line in the tangential direction. The same phenomenon is observed from Figure 11 for the case $\theta_d < 90^\circ$ in the radial direction. It is also observed that the value of the radial force increases with increasing θ_d ($\theta_d < 90^\circ$ or $\theta_d > 90^\circ$).

It can be observed from Figure 12 that the attractive force on a dislocation with b_φ , at a point (r_d, θ_d) when $\theta_d < 90^\circ$, is always stronger for the rigid conducting line case than for the rigid dielectric line, in the tangential direction. Figure 12 also shows that the rigid dielectric line repels a dislocation with b_φ

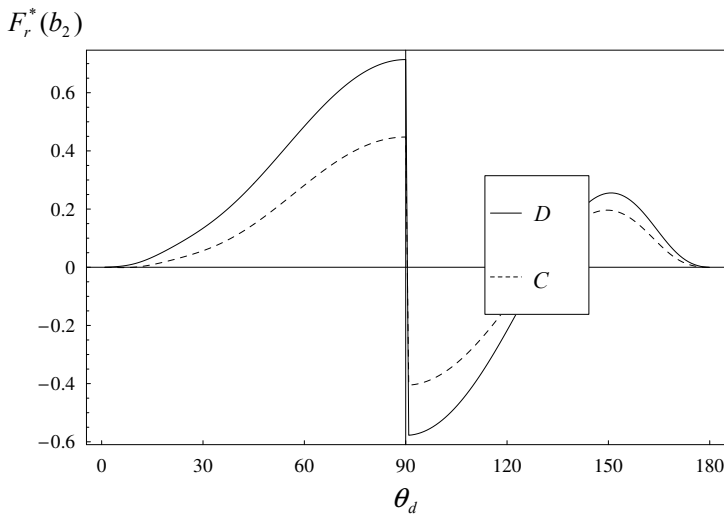


Figure 11. Normalized radial force $F_r^*(b_2)$ versus θ_d for $r_d = 1.5a$.

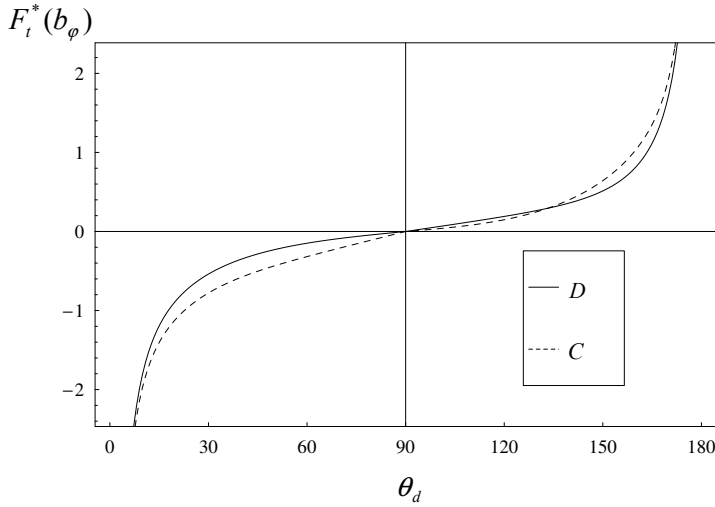


Figure 12. Normalized tangential force $F_t^*(b_\varphi)$ versus θ_d for $r_d = 1.5a$.

at a point (r_d, θ_d) more strongly than does the rigid conducting line, when $90^\circ < \theta_d < \theta_d^*$. The opposite phenomenon can be observed at a point (r_d, θ_d) , when $\theta_d^* < \theta_d < 180^\circ$. It is worth noting that the value of the tangential force increases with an increase in θ_d . Figure 13 clearly shows that the interface and the rigid dielectric line always attract a dislocation with b_φ in the radial direction, and the value of the radial force is always larger for the conducting case than for the dielectric case.

It is worth noting from Figures 2–7 that the image forces on the dislocation, which move it away from the interface along the radial direction, approach the same value gradually, and become zero ultimately for the two cases. This is due to the fact that the remarkable distance between the dislocation and the interface weakens the interaction between the dislocation and the rigid lines. It can be observed from

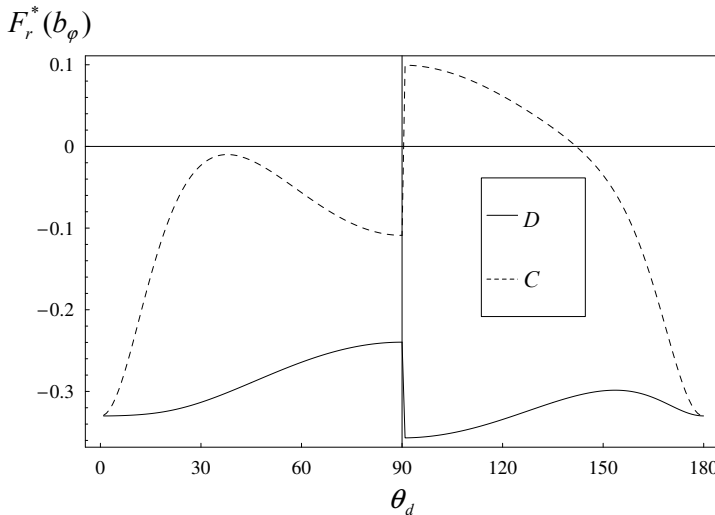


Figure 13. Normalized radial force $F_r^*(b_\varphi)$ versus θ_d for $r_d = 1.5a$.

Figures 8, 10, and 12 that the tangential forces on the dislocation near the interface approach the same value for the two cases, which indicates that the interaction between the dislocation and the interface is dominant. From Figures 11 and 13, a large change of the radial force acting on a dislocation near the point $z^*(1.5a, 90^\circ)$ is observed due to the electroelastic interaction. The dislocation with b_1 at $z^*(1.5a, 90^\circ)$ for the dielectric and conducting cases in equilibrium is also observed in the examples.

9. Conclusion

The Stroh formalism was employed to analyze the interaction between a piezoelectric dislocation and the collinear rigid lines, which are either conducting or dielectric, at the interface of two piezoelectric media. The general solutions for the field variables were obtained. A square root singularity was identified for the stress and electric displacement fields at the tips of interfacial rigid conducting/dielectric lines when the two piezoelectric media have sufficient symmetry so that the matrix \mathbf{Y} is real. It was further found that the stress and electric displacement fields at the tips of interfacial rigid conducting lines present either a combination of square root and oscillatory singularities or a combination of square root and nonsquare root singularities in transversely isotropic piezoelectric media where the matrix \mathbf{Y} is complex, or a combination of oscillatory and nonsquare root singularities in piezoelectric media whose material properties do not match suitably, so that the real numbers $\varepsilon \neq 0$ and $\kappa \neq 0$. The fields at the tips of rigid dielectric lines have square root and oscillatory singularities at the interface of a piezoelectric bimaterial system where the matrix \mathbf{Y} is complex. The strain and electric field intensity factors were introduced to characterize the near-tip field singularity. The expressions of the rigid line extension forces, based on the energy release rate and the mechanical energy release rate, were derived. The exact field solutions for the case of a single interfacial rigid line were presented. The effects of the Burgers vector and the dislocation position on the image force were analyzed in detail.

References

- [Asundi and Deng 1995] A. Asundi and W. Deng, "Rigid inclusions on the interface between dissimilar anisotropic media", *J. Mech. Phys. Solids* **43** (1995), 1045–1058.
- [Ballarini 1990] R. Ballarini, "A rigid line inclusion at a bimaterial interface", *Eng. Fract. Mech.* **37** (1990), 1–5.
- [Beom 2003] H. G. Beom, "Permeable cracks between two dissimilar piezoelectric materials", *Int. J. Solids Struct.* **40** (2003), 6669–6679.
- [Beom and Atluri 2002] H. G. Beom and S. N. Atluri, "Conducting cracks in dissimilar piezoelectric media", *Int. J. Fract.* **118** (2002), 285–301.
- [Chen et al. 2005a] B. J. Chen, K. M. Liew, and Z. M. Xiao, "A dislocation interacts with a finite crack in piezoelectric media", *Int. J. Eng. Sci.* **43** (2005a), 1206–1222.
- [Chen et al. 2005b] B. J. Chen, K. M. Liew, and Z. M. Xiao, "Unified electrical boundary conditions for a crack interacting with a dislocation in piezoelectric media", *Int. J. Solids Struct.* **42** (2005b), 5118–5128.
- [Chen et al. 2007] B. J. Chen, D. W. Shu, and Z. M. Xiao, "Dislocation interacting with collinear rigid lines in piezoelectric media", *Journal of Mechanics of Materials and Structures* **2:1** (2007), 23–42.
- [Deng and Meguid 1998] W. Deng and S. A. Meguid, "Analysis of conducting rigid inclusion at the interface of two dissimilar piezoelectric materials", *J. Appl. Mech. (Trans. ASME)* **65** (1998), 76–84.
- [Fang et al. 2005] Q. H. Fang, Y. W. Liu, and C. P. Jiang, "Electroelastic interaction between a piezoelectric screw dislocation and an elliptical inclusion with interfacial cracks", *Phys. Status Solidi (b)* **242** (2005), 2775–2794.
- [Gao et al. 2005] C.-F. Gao, P. Tong, and T.-Y. Zhang, "Interaction of a dipole with an interfacial crack in piezoelectric media", *Compos. Sci. Technol.* **65** (2005), 1354–1362.

- [Hausler et al. 2004] C. Hausler, C.-F. Gao, and H. Balke, “Collinear and periodic electrode-ceramic interfacial cracks in piezoelectric bimetals”, *J. Appl. Mech. (Trans. ASME)* **71** (2004), 486–492.
- [Jiang 1991] C.-P. Jiang, “The plane problem of collinear rigid lines under arbitrary loads”, *Eng. Fract. Mech.* **39** (1991), 299–308.
- [Jiang and Liu 1992] C. P. Jiang and C. T. Liu, “Stress distribution around a rigid line in dissimilar media”, *Eng. Fract. Mech.* **42** (1992), 27–32.
- [Li and Ting 1989] Q. Li and T. C. T. Ting, “Line inclusions in anisotropic elastic solids”, *J. Appl. Mech. (Trans. ASME)* **56** (1989), 556–563.
- [Liu et al. 2004] Y. W. Liu, Q. H. Fang, and C. P. Jiang, “A piezoelectric screw dislocation interacting with an interphase layer between a circular inclusion and the matrix”, *Int. J. Solids Struct.* **41** (2004), 3255–3274.
- [Meguid and Deng 1998] S. A. Meguid and W. Deng, “Electro-elastic interaction between a screw dislocation and an elliptical inhomogeneity in piezoelectric materials”, *Int. J. Solids Struct.* **35** (1998), 1467–1482.
- [Muskhelishvili 1975] N. I. Muskhelishvili, *Some basic problems of the mathematical theory of elasticity: fundamental equations plane theory of elasticity torsion and bending*, Fourth Edition ed., P. Noordhoff, Leyden, Holland, 1975.
- [Ou and Wu 2003] Z. C. Ou and X. Wu, “On the crack-tip stress singularity of interfacial cracks in transversely isotropic piezoelectric bimetals”, *Int. J. Solids Struct.* **40** (2003), 7499–7511.
- [Pak 1990a] Y. E. Pak, “Crack extension force in a piezoelectric material”, *J. Appl. Mech. (Trans. ASME)* **57** (1990a), 647–653.
- [Pak 1990b] Y. E. Pak, “Force on a piezoelectric screw dislocation”, *J. Appl. Mech. (Trans. ASME)* **57** (1990b), 863–869.
- [Ru 2000] C. Ru, “Electrode-ceramic interfacial cracks in piezoelectric multilayer materials”, *J. Appl. Mech. (Trans. ASME)* **67** (2000), 255–261.
- [Sosa and Pak 1990] H. A. Sosa and Y. E. Pak, “Three-dimensional eigenfunction analysis of a crack in a piezoelectric material”, *Int. J. Solids Struct.* **26** (1990), 1–15.
- [Suo 1990] Z. Suo, “Singularities, interfaces and cracks in dissimilar anisotropic media”, pp. 331–358 in *Proceedings of the Royal Society of London*, edited by 427, Series A, Mathematical and Physical Sciences, 1990.
- [Suo et al. 1992] Z. Suo, C.-M. Kuo, D. M. Barnett, and J. R. Willis, “Fracture mechanics for piezoelectric ceramics”, *J. Mech. Phys. Solids* **40** (1992), 739–765.
- [Wang and Shen 2002] X. Wang and Y.-p. Shen, “Exact solution for mixed boundary value problems at anisotropic piezoelectric bimaterial interface and unification of various interface defects”, *Int. J. Solids Struct.* **39** (2002), 1591–1619.
- [Wu 1990] K.-C. Wu, “Line inclusions at anisotropic bimaterial interface”, *Mech. Mater.* **10** (1990), 173–182.
- [Xiao and Zhao 2004] Z. M. Xiao and J. F. Zhao, “Electro-elastic stress analysis for a Zener-Stroh crack at the metal/piezoelectric bi-material interface”, *Int. J. Solids Struct.* **41** (2004), 2501–2519.
- [Xiao et al. 2004] Z. M. Xiao, J. Yan, and B. J. Chen, “Electro-elastic stress analysis for a screw dislocation interacting with a coated inclusion in piezoelectric solid”, *Acta Mech.* **172** (2004), 237–249.
- [Xiao et al. 2007] Z. M. Xiao, H. X. Zhang, and B. J. Chen, “A piezoelectric screw dislocation interacts with interfacial collinear rigid lines in piezoelectric bimetals”, *Int. J. Solids Struct.* **44** (2007), 255–271.

Received 8 Mar 2007. Accepted 17 Jul 2007.

ZHONGMIN XIAO: mzxiao@ntu.edu.sg

School of Mechanical and Aerospace Engineering, Nanyang Technological University, Nanyang Avenue, Singapore 639798

HONGXIA ZHANG: mhzhang@ntu.edu.sg

School of Mechanical and Aerospace Engineering, Nanyang Technological University, Nanyang Avenue, Singapore 639798

BINGJIN CHEN: mbchen@ntu.edu.sg

School of Mechanical and Aerospace Engineering, Nanyang Technological University, Nanyang Avenue, Singapore 639798

EXACT SOLUTION OF DOUBLE FILLED HOLE OF AN INFINITE PLATE

NAT KASAYAPANAND

The plane stress linear elastic solution to the problem of a circular disk embedded in a ring fitted into a uniaxially loaded infinite plate is solved using Airy stress functions. This exact solution is validated by reduction to the benchmark solutions: plate without hole, plate with a circular hole, plate with a circular inclusion, and plate with a ring inclusion. Numerical results of stress distribution are presented for changing material properties.

1. Introduction

It is well known that for a uniaxially loaded infinite plate with a hole a stress concentration of three occurs at the point where the load direction is tangent to the hole boundary [Love 1944; Sokolnikoff 1956; Timoshenko and Goodier 1970; Little 1973; Ugural and Fenster 1994]. Savin [1961] extensively examined the problem of stress concentrations in plates including those related to disk and ring inclusions. The analytical solution for tension applied in one direction in an orthotropic plate with circular filled center is conducted by Lekhnitskii [1968]. Recently, the current researches dealing with the elastic inclusions problem are obtained numerically by Parhi and Das [1972], Greengard and Helsing [1998], Liu et al. [2000], Fanzhong et al. [2002], and Wang et al. [2005]. However, there is no previous literature relating to the exact stress in the double filled hole of an infinite plate (that is, a circular elastic inclusion embedded into a reinforced hole in an elastic plane, and a reinforced ring is used) by different materials to reduce the stress concentration around the hole of plate. This configuration is useful for designing of the filled hole of plate systems in many engineering applications.

In this plane stress study, a linearly elastic disk embedded in an elastic ring is fitted into a hole of an infinite plate, all with the same thickness. All surfaces are seamlessly bonded between three materials that may be different. A proposed general solution without body forces is considered in terms of Airy stress functions so that stresses, strains, and displacements may be calculated. For convenience, rectangular Cartesian coordinates together with polar coordinates are used interchangeably.

Nomenclature

a	constant
A	constant
b	constant
c	constant
d	constant

Keywords: stress function, stress concentration, plane stress, circular hole, inclusion.

The author gratefully acknowledges the support provided by the Thailand Research Fund and Commission on Higher Education for carrying out this study.

D	domain
E	modulus of elasticity, N/m^2
r	radius coordinate, m
s	uniform uniaxial stress tension, N/m^2
u	component of displacement in radius direction, m
v	component of displacement in tangential direction, m
x	x -coordinate, m
y	y -coordinate, m

Greek symbols

ε	component of strain
Φ	stress function, N
ν	Poisson's ratio
θ	angle, degree
σ	component of stress, N/m^2

2. Theoretical formulation

Figure 1 shows the plane stress problem of an infinite plate subjected to the uniform uniaxial tension s . A disk (material 1) and a ring (material 2) having radius R_1 and R_2 , respectively, are seamlessly embedded into an infinite plate (material 3), all with the same thickness, and are assumed linear elastic, isotropic, and homogeneous.

Let u and v be components of displacements in the radial, r , and tangential, θ , directions. If the disk, ring, and plate, are labeled as 1, 2, and 3, respectively, then the regions in space occupied by them denoted by D_i ; $i = 1, 2$, and 3 are

$$\begin{aligned}
 D_1 &= ((r, \theta) : 0 \leq r \leq R_1, 0 \leq \theta \leq 2\pi), & D_2 &= ((r, \theta) : R_1 \leq r \leq R_2, 0 \leq \theta \leq 2\pi), \\
 D_3 &= ((r, \theta) : r \geq R_2, 0 \leq \theta \leq 2\pi). & & (1)
 \end{aligned}$$

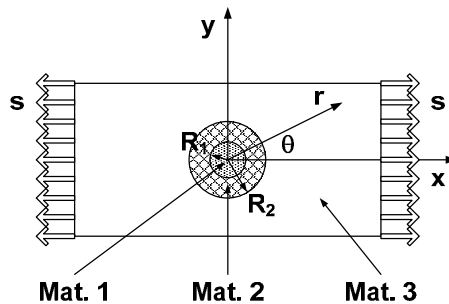


Figure 1. Boundary conditions of the double filled hole of plate.

The conditions at the interface of the disk, ring, and plate are

$$\begin{aligned} r = R_1; \quad u_1 = u_2, \quad v_1 = v_2, \quad \sigma_{rr1} = \sigma_{rr2}, \quad \sigma_{r\theta1} = \sigma_{r\theta2}, \\ r = R_2; \quad u_2 = u_3, \quad v_2 = v_3, \quad \sigma_{rr2} = \sigma_{rr3}, \quad \sigma_{r\theta2} = \sigma_{r\theta3}. \end{aligned} \quad (2)$$

The two-dimensional Cartesian to polar stress transform equations are

$$\begin{aligned} \sigma_{rr} = \sigma_{xx} \cos^2 \theta + \sigma_{yy} \sin^2 \theta + 2\sigma_{xy} \sin \theta \cos \theta, \quad \sigma_{\theta\theta} = \sigma_{xx} \sin^2 \theta + \sigma_{yy} \cos^2 \theta - 2\sigma_{xy} \sin \theta \cos \theta, \\ \sigma_{r\theta} = -(\sigma_{xx} - \sigma_{yy}) \sin \theta \cos \theta + \sigma_{xy}(\cos^2 \theta - \sin^2 \theta). \end{aligned} \quad (3)$$

With corresponding equations of equilibrium in polar coordinates

$$\frac{\partial \sigma_{rr}}{\partial r} + \frac{\sigma_{rr} - \sigma_{\theta\theta}}{r} + \frac{1}{r} \frac{\partial \sigma_{r\theta}}{\partial \theta} + F_r = 0, \quad \frac{\partial \sigma_{r\theta}}{\partial r} + \frac{2\sigma_{r\theta}}{r} + \frac{1}{r} \frac{\partial \sigma_{\theta\theta}}{\partial \theta} + F_\theta = 0. \quad (4)$$

The plane stress stress-strain relations are

$$\varepsilon_{rr} = \frac{1}{E}(\sigma_{rr} - \nu\sigma_{\theta\theta}), \quad \varepsilon_{\theta\theta} = \frac{1}{E}(\sigma_{\theta\theta} - \nu\sigma_{rr}), \quad \varepsilon_{r\theta} = \frac{\sigma_{r\theta}}{E}(1 + \nu), \quad (5)$$

where the linear strain-displacement relations are given by

$$\varepsilon_{rr} = \frac{\partial u}{\partial r}, \quad \varepsilon_{\theta\theta} = \frac{u}{r} + \frac{1}{r} \frac{\partial v}{\partial \theta}, \quad \varepsilon_{r\theta} = \frac{1}{2} \left(\frac{1}{r} \frac{\partial u}{\partial \theta} + \frac{\partial v}{\partial r} - \frac{v}{r} \right). \quad (6)$$

By following an Airy stress function (Φ) approach in which one assumes the body forces are negligible, the governing equations reduce to

$$\left(\frac{\partial^2}{\partial r^2} + \frac{1}{r} \frac{\partial}{\partial r} + \frac{1}{r^2} \frac{\partial^2}{\partial \theta^2} \right) \left(\frac{\partial^2 \Phi}{\partial r^2} + \frac{1}{r} \frac{\partial \Phi}{\partial r} + \frac{1}{r^2} \frac{\partial^2 \Phi}{\partial \theta^2} \right) = 0, \quad (7)$$

where the stress components are defined by

$$\sigma_{rr} = \frac{1}{r} \frac{\partial \Phi}{\partial r} + \frac{1}{r^2} \frac{\partial^2 \Phi}{\partial \theta^2}, \quad \sigma_{\theta\theta} = \frac{\partial^2 \Phi}{\partial r^2}, \quad \sigma_{r\theta} = -\frac{\partial}{\partial r} \left(\frac{1}{r} \frac{\partial \Phi}{\partial \theta} \right). \quad (8)$$

Consider the Airy's stress function in polar coordinates, written as

$$\Phi_i = a_{0i} + b_{0i} \ln r + c_{0i} r^2 + d_{0i} r^2 \ln r + (a_{2i} r^2 + b_{2i} r^4 + c_{2i} r^{-2} + d_{2i}) \cos(2\theta). \quad (9)$$

From Equations (5)–(9), the general expressions for stresses and displacements can be obtained as follows:

$$\begin{aligned}
 \sigma_{rri} &= 2c_{0i} + d_{0i} + b_{0i}r^{-2} + 2d_{0i} \ln r - (6c_{2i}r^{-4} + 4d_{2i}r^{-2} + 2a_{2i}) \cos(2\theta), \\
 \sigma_{\theta\theta i} &= 2c_{0i} + 3d_{0i} - b_{0i}r^{-2} + 2d_{0i} \ln r + (6c_{2i}r^{-4} + 2a_{2i} + 12b_{2i}r^2) \cos(2\theta), \\
 \sigma_{r\theta i} &= (-6c_{2i}r^{-4} - 2d_{2i}r^{-2} + 2a_{2i} + 6b_{2i}r^2) \sin(2\theta), \\
 u_i &= \frac{1}{E_i} \left(\left(-(1 + \nu_i)b_{0i}r^{-1} + 2(1 - \nu_i)c_{0i}r - (1 + \nu_i)d_{0i}r + 2(1 - \nu_i)d_{0i}r \ln r \right) \right. \\
 &\quad \left. + \left(2(1 + \nu_i)c_{2i}r^{-3} + 4d_{2i}r^{-1} - 2(1 + \nu_i)a_{2i}r - 4\nu_i b_{2i}r^3 \right) \cos(2\theta) \right) \\
 &\quad - A_{0i} \sin(\theta) + A_{1i} \cos(\theta), \\
 v_i &= \frac{1}{E_i} \left(4d_{0i}r\theta + \left(2(1 + \nu_i)c_{2i}r^{-3} - 2(1 - \nu_i)d_{2i}r^{-1} + 2(1 + \nu_i)a_{2i}r + 2(3 + \nu_i)b_{2i}r^3 \right) \sin(2\theta) \right) \\
 &\quad + A_{0i} \cos(\theta) + A_{1i} \sin(\theta) + r A_{2i}. \quad (10)
 \end{aligned}$$

The constants $a_{0i}, b_{0i}, c_{0i}, d_{0i}, a_{2i}, b_{2i}, c_{2i}$, and $d_{2i}; i = 1, 2, 3$ and $A_{0i}, A_{1i}, A_{2i}; i = 1, 2, 3$ are determined using the interface, boundary, and mathematical conditions in Equation (2).

3. Mathematical implementation

The constants in the Airy stress function are obtained by the following considerations: substitution of Equation (10) into Equation (6) reveals that all strain components are free from A_{0i}, A_{1i} , and A_{2i} , meaning that these constants are related to rigid body motion. It is assumed that the translation and rotational rigid body motions are zero, and that the origin of xy -coordinates is the reference point for zero displacements, so that A_{0i}, A_{1i} , and $A_{2i} = 0$. For the disk, the displacement at $r = 0$ must be finite, so we must set b_{01}, c_{21} , and $d_{21} = 0$. Because polar coordinates are used, it is a requirement that at any r stresses and displacements must be equal if θ is replaced by $\theta + 360^\circ$. Thus, d_{01}, d_{02} , and $d_{03} = 0$. Finally, the eighteen remaining constants: $a_{01}, c_{01}, a_{21}, b_{21}, a_{02}, b_{02}, c_{02}, a_{22}, b_{22}, c_{22}, d_{22}, a_{03}, b_{03}, c_{03}, a_{23}, b_{23}, c_{23}$, and d_{23} are determined by using the interface, boundary, and mathematical conditions.

The boundary conditions of the plate in polar coordinates are

$$\begin{aligned}
 \sigma_{rr3} &= \frac{s}{2}(1 + \cos(2\theta)), & \sigma_{\theta\theta3} &= \frac{s}{2}(1 - \cos(2\theta)), \\
 \sigma_{r\theta} &= -\frac{s}{2} \sin(2\theta).
 \end{aligned} \quad (11)$$

At the plate, taking the limit $r \rightarrow \infty$, the results are expressed as $c_{03} = \frac{s}{4}$, $a_{23} = -\frac{s}{4}$, $b_{23} = 0$.

Therefore, at this stage, the stress and displacement components are reduced to

$$\begin{aligned} \sigma_{rr1} &= 2c_{01} - 2a_{21} \cos(2\theta), & \sigma_{r\theta1} &= (2a_{21} + 6b_{21}r^2) \sin(2\theta), \\ \sigma_{rr1} &= 2c_{01} - 2a_{21} \cos(2\theta), & u_1 &= \frac{1}{E_1} \left(2(1 - \nu_1)c_{01}r - (2(1 + \nu_1)a_{21}r + 4\nu_1b_{21}r^3) \cos(2\theta) \right), \\ v_1 &= \frac{1}{E_1} (2(1 + \nu_1)a_{21}r + 2(3 + \nu_1)b_{21}r^3) \sin(2\theta), \\ \sigma_{rr2} &= 2c_{02} + b_{02}r^{-2} - (6c_{22}r^{-4} + 4d_{22}r^{-2} + 2a_{22}) \cos(2\theta), \\ \sigma_{r\theta2} &= (-6c_{22}r^{-4} - 2d_{22}r^{-2} + 2a_{22} + 6b_{22}r^2) \sin(2\theta), \\ u_2 &= \frac{1}{E_2} \left((-1 + \nu_2)b_{02}r^{-1} + 2(1 - \nu_2)c_{02}r \right. \\ &\quad \left. + (2(1 + \nu_2)c_{22}r^{-3} + 4d_{22}r^{-1} - 2(1 + \nu_2)a_{22}r - 4\nu_2b_{22}r^3) \cos(2\theta) \right), \\ v_2 &= \frac{1}{E_2} \left(2(1 + \nu_2)c_{22}r^{-3} - 2(1 - \nu_2)d_{22}r^{-1} + 2(1 + \nu_2)a_{22}r + 2(3 + \nu_2)b_{22}r^3 \right) \sin(2\theta), \\ \sigma_{rr3} &= \frac{s}{2} + b_{03}r^{-2} + \left(\frac{s}{2} - 6c_{23}r^{-4} - 4d_{23}r^{-2} \right) \cos(2\theta), \\ \sigma_{r\theta3} &= \left(-6c_{23}r^{-4} - 2d_{23}r^{-2} - \frac{s}{2} \right) \sin(2\theta), \\ u_3 &= \frac{1}{E_3} \left((-1 + \nu_3)b_{03}r^{-1} + (1 - \nu_3)\frac{s}{2}r \right) + \left(2(1 + \nu_3)c_{23}r^{-3} + 4d_{23}r^{-1} + (1 + \nu_3)\frac{s}{2}r \right) \cos(2\theta), \\ v_3 &= \frac{1}{E_3} \left(2(1 + \nu_3)c_{23}r^{-3} - 2(1 - \nu_3)d_{23}r^{-1} - (1 + \nu_3)\frac{s}{2}r \right) \sin(2\theta). \end{aligned} \tag{12}$$

Substitution of Equation (12) into the interface conditions (Equation (2)) yields

$$\begin{aligned} 2c_{01} &= 2c_{02} + b_{02}R_1^{-2}, \\ 2a_{21} &= 6c_{22}R_1^{-4} + 4d_{22}R_1^{-2} + 2a_{22}, \\ 2a_{21} + 6b_{21}R_1^2 &= -6c_{22}R_1^{-4} - 2d_{22}R_1^{-2} + 2a_{22} + 6b_{22}R_1^2, \\ \frac{1}{E_1} (2(1 - \nu_1)c_{01}R_1) &= \frac{1}{E_2} (-1 + \nu_2)b_{02}R_1^{-1} + 2(1 - \nu_2)c_{02}R_1, \\ \frac{1}{E_1} (2(1 + \nu_1)a_{21}R_1 + 4\nu_1b_{21}R_1^3) &= \frac{1}{E_2} \left(2(1 + \nu_2)c_{22}R_1^{-3} + 4d_{22}R_1^{-1} \right. \\ &\quad \left. - 2(1 + \nu_2)a_{22}R_1 - 4\nu_2b_{22}R_1^3 \right), \end{aligned}$$

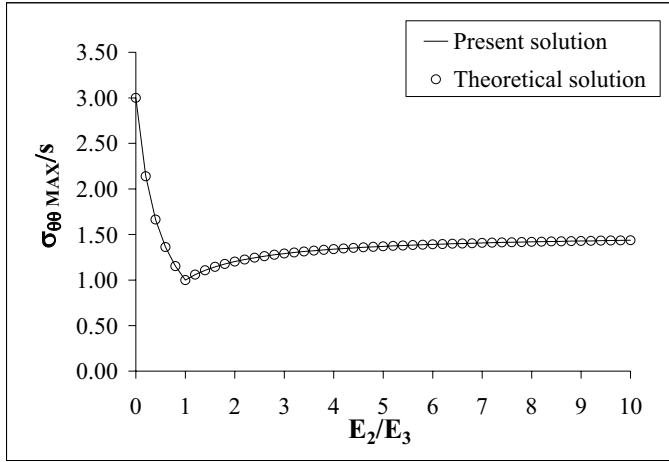


Figure 2. Stress concentration distribution for various modulus of elasticity ratios.

$$\frac{1}{E_1} (2(1 + \nu_1)a_{21}R_1 + 2(3 + \nu_1)b_{21}R_1^3) = \frac{1}{E_2} \left(2(1 + \nu_2)c_{22}R_1^{-3} - 2(1 - \nu_2)d_{22}R_1^{-1} + 2(1 + \nu_2)a_{22}R_1 + 2(3 + \nu_2)b_{2i}R_1^3 \right),$$

$$2c_{02} + b_{02}R_2^{-2} = \frac{s}{2} + b_{03}R_2^{-2},$$

$$-6c_{22}R_2^{-4} - 4d_{22}R_2^{-2} - 2a_{22} = \frac{s}{2} - 6c_{23}R_2^{-4} - 4d_{23}R_2^{-2},$$

$$-6c_{22}R_2^{-4} - 2d_{22}R_2^{-2} + 2a_{22} + 6b_{22}R_2^2 = -6c_{23}R_2^{-4} - 2d_{23}R_2^{-2} - \frac{s}{2},$$

$$\frac{1}{E_2} (-(1 + \nu_2)b_{02}R_2^{-1} + 2(1 - \nu_2)c_{02}R_2) = \frac{1}{E_3} \left(-(1 + \nu_3)b_{03}R_2^{-1} + (1 - \nu_3)\frac{s}{2}R_2 \right),$$

$$\frac{1}{E_2} \left(2(1 + \nu_2)c_{22}R_2^{-3} + 4d_{22}R_2^{-1} - 2(1 + \nu_2)a_{22}R_2 - 4\nu_2b_{22}R_2^3 \right) = \frac{1}{E_3} \left(2(1 + \nu_3)c_{23}R_2^{-3} + 4d_{23}R_2^{-1} + (1 + \nu_3)\frac{s}{2}R_2 \right),$$

$$\frac{1}{E_2} (2(1 + \nu_2)c_{22}R_2^{-3} - 2(1 - \nu_2)d_{22}R_2^{-1} + 2(1 + \nu_2)a_{22}R_2 + 2(3 + \nu_2)b_{2i}R_2^3) = \frac{1}{E_3} \left(2(1 + \nu_3)c_{23}R_2^{-3} - 2(1 - \nu_3)d_{23}R_2^{-1} - (1 + \nu_3)\frac{s}{2}R_2 \right).$$

There are three constants a_{01} , a_{02} , and a_{03} left undetermined. It is fortunate that these constants are not used in the expressions of stresses and displacements. Hence, the problem is solved mathematically. The appendix (available as an online supplement to this paper) details the values of all constants, and the stress equations in polar coordinates for all materials.

4. Validations

To confirm that the obtained stress functions are acceptable, benchmark solutions are examined.

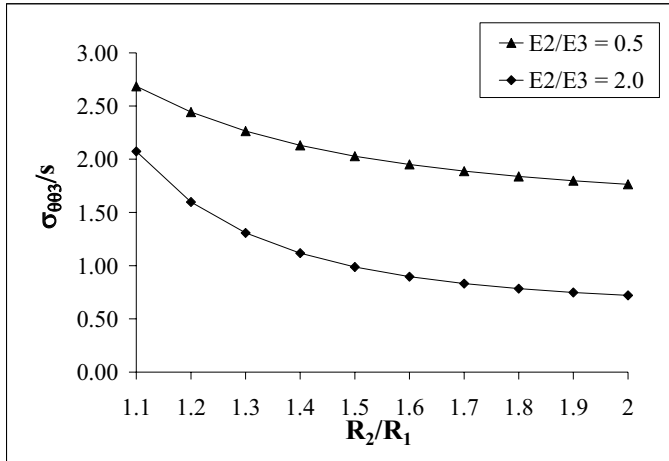


Figure 3. Circumferential stress at a hole in the function of radius ratio.

4.1. Plate without hole. For the case of a plate without a hole, the material properties of the disk, ring, and plate are set to the same values. For a uniaxial load in the x -direction the stress components are:

$$\begin{aligned} \sigma_{rr1} = \sigma_{rr2} = \sigma_{rr3} &= \frac{s}{2}(1 + \cos(2\theta)), & \sigma_{\theta\theta 1} = \sigma_{\theta\theta 2} = \sigma_{\theta\theta 3} &= \frac{s}{2}(1 - \cos(2\theta)), \\ \sigma_{r\theta 1} = \sigma_{r\theta 2} = \sigma_{r\theta 3} &= -\frac{s}{2} \sin(2\theta). \end{aligned} \tag{13}$$

They are exactly the same expressions as those for a linear elastic, homogeneous, isotropic plate loaded by a uniform normal traction in the x -direction.

4.2. Plate with a hole. To investigate the case of plate with a hole, the material properties of the disk and ring are set to zero. The problem becomes that of a plate with a hole of radius R_2 subjected to a uniform normal load in the x -direction. The stresses reduce to:

$$\begin{aligned} \sigma_{rr3} &= \frac{s}{2} \left(1 - \left(\frac{R_2}{r}\right)^2 + \left(1 - 4\left(\frac{R_2}{r}\right)^2 + 3\left(\frac{R_2}{r}\right)^4 \right) \cos(2\theta) \right), \\ \sigma_{\theta\theta 3} &= \frac{s}{2} \left(1 + \left(\frac{R_2}{r}\right)^2 - \left(1 + 3\left(\frac{R_2}{r}\right)^4 \right) \cos(2\theta) \right), \\ \sigma_{r\theta 3} &= \frac{s}{2} \left(-1 - 2\left(\frac{R_2}{r}\right)^2 + 3\left(\frac{R_2}{r}\right)^4 \right) \sin(2\theta), \\ \sigma_{rr1} = \sigma_{\theta\theta 1} = \sigma_{r\theta 1} &= 0, & \sigma_{rr2} = \sigma_{\theta\theta 2} = \sigma_{r\theta 2} &= 0. \end{aligned} \tag{14}$$

Again reproducing known results of a plate with a hole.

4.3. Plate with a circular inclusion. Considering a circular inclusion in an infinite plate, this result of doubly embedded elastic materials is reduced into the simple embedded composite material in a hole of an infinite plate by assuming that the material properties of the disk and ring are the same, but different from that of an infinite plate. Figure 2 shows the stress concentration factor distribution for various moduli of elasticity ratios of inclusion and matrix materials. The stress concentration factor decreases quickly with

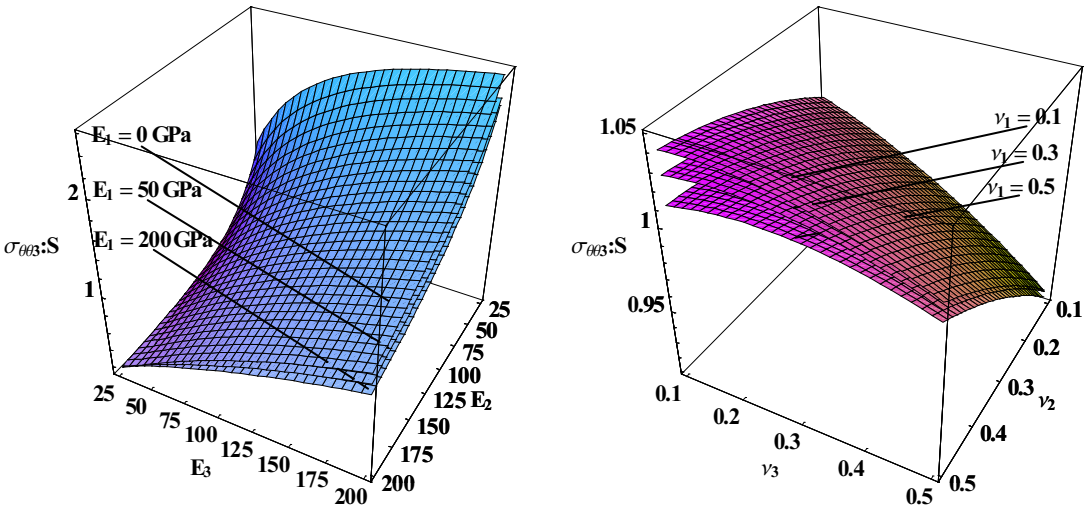


Figure 4. Left: effect of Poisson’s ratio on the circumferential stress of plate at the interface ($\theta = 90^\circ$, $R_2 = 2R_1$, $E_1 = E_2 = E_3 = 100$ GPa). Right: effect of modulus of elasticity on the circumferential stress of plate at the interface ($\theta = 90^\circ$, $R_2 = 2R_1$, $\nu_1 = \nu_2 = \nu_3 = 0.3$).

an increase in the inclusion-matrix modulus ratio when the inclusion is softer than the matrix. When the inclusion is harder than the matrix, the stress concentration factor increases again slowly. These results coincide with those published previously [Lekhnitskii 1968; Fanzhong et al. 2002; Wang et al. 2005].

4.4. Plate with a ring inclusion. Figure 3 shows the results for the case of plate with a ring inclusion. The circumferential stress at $\theta = 90^\circ$ is found to decrease slowly. This tendency compares well with the results by Savin [1961] (except that Savin examined a plate in plain strain), and a numerical study by Parhi and Das [1972].

5. Results and discussion

Some numerical results of the circumferential stress distributions in the plate (see Equation (A15) of the online supplement) at the interface $r = R_2$ due to different combinations of material properties are presented in Figure 4 for various values of E and ν , and for different materials. The results reveal that the stresses $\sigma_{\theta\theta 3}$ are very sensitive to the material properties of E_1 , E_2 , E_3 , ν_1 , ν_2 , and ν_3 . For example, to reduce of stress concentrations in bimaterial or trimaterial plates a compromise needs to be found between the material properties of the disk, ring, and plate. Moreover, the ratio between R_1 and R_2 should also be considered because the maximum circumferential stress is significantly depended on the radius ratio when the material properties are fixed.

6. Conclusion

The exact elastic solution of a circular disk embedded in a ring fitted in an infinite plate by different materials is conducted in this study. The plane stress problem in elasticity is considered for a plate

subjected to uniaxial uniform load. Boundary, interface, and mathematical conditions are analyzed to determine the solution of stress, strain, and displacement components. Thus, the Airy's stress functions are investigated for a disk, ring, and plate. Expressions in the solution are limited to the assumptions that the three materials are linearly elastic, isotropic, and homogeneous, and the problem is solved by the theory of infinitesimal linear elasticity.

References

- [Fanzhong et al. 2002] K. Fanzhong, Y. Zhenhans, and Z. Xiaoping, "BEM for simulation of a 2D elastic body with randomly distributed circular inclusions", *Acta Mech. Solida Sin.* **15** (2002), 81–88.
- [Greengard and Helsing 1998] L. Greengard and J. Helsing, "On the numerical evaluation of elastostatic fields in locally isotropic two-dimensional composites", *J. Mech. Phys. Solids* **46** (1998), 1441–1462.
- [Lekhnitskii 1968] S. G. Lekhnitskii, *Anisotropic plates*, Gordon and Breach, New York, 1968.
- [Little 1973] R. W. Little, *Elasticity*, Prentice-Hall, Englewood Cliffs New Jersey, 1973.
- [Liu et al. 2000] Y. J. Liu, N. Xu, and J. F. Luo, "Modeling of interphases in fiber-reinforced composites under transverse loading using the boundary element method", *J. Appl. Mech. (Trans. ASME)* **67** (2000), 143–150.
- [Love 1944] A. E. H. Love, *A treatise on the mathematical theory of elasticity*, Dover Publications, New York, 1944.
- [Parhi and Das 1972] K. K. Parhi and A. K. Das, "The effect of couple-stresses on stress concentration of a ring inclusion", *Acta Mech.* **14** (1972), 219–228.
- [Savin 1961] G. N. Savin, *Stress concentration around holes*, Pergamon Press, New York, 1961.
- [Sokolnikoff 1956] I. S. Sokolnikoff, *Mathematical theory of elasticity*, McGraw-Hill, New York, 1956.
- [Timoshenko and Goodier 1970] S. P. Timoshenko and J. N. Goodier, *Theory of elasticity*, McGraw-Hill, New York, 1970.
- [Ugural and Fenster 1994] A. C. Ugural and S. K. Fenster, *Advanced strength and applied elasticity*, Prentice Hall, Englewood Cliffs New Jersey, 1994.
- [Wang et al. 2005] J. Wang, S. G. Mogilevskaya, and S. L. Crouch, "An embedding method for modeling micromechanical behavior and macroscopic properties of composite materials", *Int. J. Solids Struct.* **42** (2005), 4588–4612.

Received 17 Apr 2007. Revised 18 Jul 2007. Accepted 23 Jul 2007.

NAT KASAYAPANAND: nat.kas@kmutt.ac.th

School of Energy, Environment, and Materials, King Mongkut's University of Technology Thonburi, 126 Pracha U-thit Rd., Bangmod, Thung-khru, Bangkok 10140, Thailand

TRANSIENT RESPONSE OF MAGNETO-ELECTRO-ELASTIC SIMPLY SUPPORTED CYLINDER USING FINITE ELEMENT

ATUL DAGA, NATRAJAN GANESAN AND KRISHNAPILLAI SHANKAR

The transient response of a simply supported layered cylinder made of a three-phase magneto-electro-elastic (MEE) composite, consisting of an elastic matrix reinforced with piezoelectric and piezomagnetic fiber has been studied by developing a semianalytical finite element method employing fourth-order Runge–Kutta method. Numerical results are presented for different volume fractions of piezomagnetic fiber in a three-phase MEE material with simply supported boundary conditions. A study of the transient responses of (PZT)-epoxy mixed component (PECP), (Terfenol-D)-epoxy mixed components (MSCP), barium titanate (BaTiO_3) and a two phase magneto-electro-elastic layered cylinder, under simply supported boundary conditions has also been presented. A comparison between the elastic and the coupled responses of the MEE cylinder is presented as well. Ansys 8.1 is used to validate the present code for the response of cylinder made of PECP and MSCP materials.

1. Introduction

The term magneto-electro-elastic solid has been used to refer to a class of materials exhibiting the coupling between mechanical, electric and magnetic fields. Composites made with piezoelectric and piezomagnetic phases not only have the original piezoelectric and piezomagnetic properties but also exhibit magneto-electric coupling effects which are not present in the constituents. Due to the ability of converting one form of energy to another, these materials have a number of applications such as sensors and actuators, in medical ultrasonic imaging, etc. A composite made of piezoelectric and piezomagnetic phases would be susceptible to brittle fracture because these materials are usually brittle ceramics. A three-phase magneto-electro-elastic composite consisting of piezoelectric and piezomagnetic phases separated by a polymer matrix would have greater ductility and formability [Jaesang et al. 2005]. One example of such a material is an elastic matrix made of epoxy reinforced with piezoelectric (BaTiO_3) and piezomagnetic fiber (CoFe_2O_4) fibers.

Due to the simple geometry and wide application, layered cylinder made of magneto-electro-elastic material has been of interest to various researchers. [Pan and Heyliger 2002] obtained the exact solution for three dimensional, linear, anisotropic magneto-electro-elastic and multilayered rectangular plates under simply supported edge conditions. Wang and Zhong [2003] studied the finitely long magneto-electro-elastic circular cylindrical shell under pressure and temperature changes using power series expansion method together with the Fourier series expansion method. Free vibrations studies of the magneto-electro-elastic cylindrical shell have been carried out by various authors [Buchanan 2003; Bhangale and Ganesan 2005; Annigeri et al. 2006]. The transient responses of the inelastic shells of revolution using finite difference solution techniques in time and space has been presented by Philip [1972]. Bhimaraddi

Keywords: magneto-electro-elastic, transient, finite element, Runge–Kutta.

[1987] studied the static and transient responses of composite cylindrical shell based on shear deformation theory using Newmark time integration method. Hou and Leung [2004] studied the transient response of a special nonhomogenous magneto-electro-elastic hollow cylinder using separation of variables and orthogonal expansion method. The plane strain problem is reduced to Volterra integrals, which are solved by means of interpolation method.

In this paper, the transient responses for different volume fractions of the piezomagnetic fiber in a three-phase magneto-electro-elastic layered cylinder under constant internal pressure with simply supported boundary conditions have been studied by developing the semianalytical finite element method using the constitutive equations of the piezomagnetic medium. The fourth-order Runge–Kutta method is employed to obtain the responses. The transient response for (PZT)–epoxy mixed component (PECP), (Terfenol-D)–epoxy mixed components (MSCP), barium titanate (BaTiO₃) and two phase magneto-electro-elastic (MEE) materials is also presented. A comparative study of the elastic and coupled responses of the three-phase MEE layered cylinder has also been done.

2. Constitutive equations

The constitutive equations for the magneto-electro-elastic medium relating stress σ_j , electric displacement D_j and magnetic induction B_j to strain S_k , electric field E_k and magnetic field H_k , exhibiting linear coupling between magnetic, electric and elastic field can be written as [Buchanan 2003]:

$$\sigma_j = C_{jk}S_k - e_{kj}E_k - q_{kj}H_k, \tag{1}$$

$$D_j = e_{jk}S_k + \varepsilon_{jk}E_k + m_{jk}H_k, \tag{2}$$

$$B_j = q_{jk}S_k + m_{jk}E_k + \mu_{jk}H_k, \tag{3}$$

where, C_{jk} , ε_{jk} and μ_{jk} are elastic, dielectric and magnetic permeability coefficients respectively and e_{kj} , q_{jk} and m_{jk} are the piezoelectric, piezomagnetic and magneto-electric material coefficients. The strain displacement, electric field-electric potential and magnetic field-magnetic potential used in finite

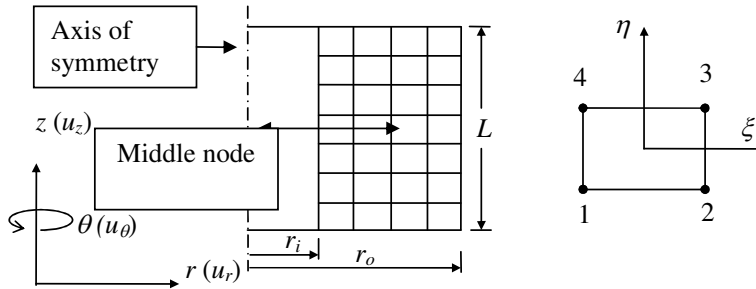


Figure 1. Cylinder discretization with four noded rectangular elements.

element method for the axisymmetric layered cylinder can be written as

$$\begin{aligned} S_{rr} = S_1 = \frac{\partial u}{\partial r}, \quad S_{\theta\theta} = S_2 = \frac{1}{r} \left(\frac{\partial v}{\partial \theta} + u \right), \\ S_{zz} = S_3 = \frac{\partial w}{\partial z}, \quad S_{rz} = S_5 = \frac{\partial w}{\partial r} + \frac{\partial u}{\partial z}, \end{aligned} \quad (4)$$

where u , v and w are the mechanical displacements in the r , θ and z directions. The electric field vector E_i is related to electric potential ϕ as

$$E_r = E_1 = -\frac{\partial \phi}{\partial r}, \quad E_z = E_3 = -\frac{\partial \phi}{\partial z}. \quad (5)$$

Similarly the magnetic field H_i is related to the magnetic potential ψ as

$$H_r = H_1 = -\frac{\partial \psi}{\partial r}, \quad H_z = H_3 = -\frac{\partial \psi}{\partial z}. \quad (6)$$

3. Finite element formulation

The finite element formulation for the axisymmetric layered cylinder with five degrees of freedom per node, u_r , u_z , u_θ , ϕ and ψ , is shown in Figure 1. Since the geometry and material properties of the layered cylinder do not vary along the circumferential θ direction, a simplified solution can be assumed by considering a function in the circumferential direction. The displacement, electric potential and magnetic potential can be written as trigonometric functions in the circumferential direction using the semianalytical finite element as

$$\begin{aligned} u_r = \sum u_r^n \cos n\theta, \quad u_\theta = \sum u_\theta^n \cos n\theta, \\ u_z = \sum u_z^n \cos n\theta, \quad \phi = \sum \phi^n \cos n\theta, \\ \psi = \sum \psi^n \cos n\theta, \end{aligned} \quad (7)$$

where $n = 0$ for axisymmetric case. Due to the orthogonal property of the trigonometric function, the solution becomes decoupled, a fact which leads to substantial saving in computational time. A four-noded rectangular element is used to model the layered cylinder structure.

The mechanical displacements, electrical, and magnetic potential can be expressed as $u = [N_i]\{u\}$, $\phi = [N_i]\{\phi\}$, $\psi = [N_i]\{\psi\}$, with $i = 1, 2, 3, 4$. The formulation for coupled field can be written in terms of the following stiffness matrices [Buchanan 2003]:

$$\begin{aligned} [[K_{uu}] - \omega^2[M]]\{U\} + [K_{u\phi}]\{\phi\} + [K_{u\psi}]\{\psi\} = F(t), \quad [K_{u\phi}]^T\{U\} - [K_{\phi\phi}]\{\phi\} - [K_{\phi\psi}]\{\psi\} = 0, \\ [K_{u\psi}]^T\{U\} - [K_{\phi\psi}]^T\{\phi\} - [K_{\psi\psi}]\{\psi\} = 0, \end{aligned} \quad (8)$$

where $F(t)$ is the constant pressure force as a function of time and

$$\begin{aligned}
 [K_{uu}] &= \int_v [B_u]^T [C] [B_u] dV, & [K_{u\phi}] &= \int_v [B_u]^T [e] [B_\phi] dV, \\
 [K_{u\psi}] &= \int_v [B_u]^T [q] [B_\psi] dV, & [K_{\phi\phi}] &= \int_v [B_\phi]^T [\varepsilon] [B_\phi] dV, \\
 [K_{\psi\psi}] &= \int_v [B_\psi]^T [\mu] [B_\psi] dV, & [K_{\phi\psi}] &= \int_v [B_\phi]^T [m] [B_\psi] dV, \\
 [M] &= \int_v [N]^T [\rho] [N] dV.
 \end{aligned} \tag{9}$$

$[B_u]$, $[B_\phi]$ and $[B_\psi]$ are shape function derivative matrices for strain displacement, electric field-electric potential and magnetic field-magnetic potential, respectively. Here $dV = 2\pi r dr dz$. Electric potential and magnetic potential can be removed from Equations (9) by condensation techniques resulting in

$$[M]\{\ddot{U}\} + [K_{eq}]\{U\} = F(t), \tag{10}$$

where

$$[K_{eq}] = [K_{uu}] + [K_{u\phi}][K_{II}]^{-1}[K_I] + [K_{u\psi}][K_V]^{-1}[K_{IV}]. \tag{11}$$

$[K_{eq}]$ is the equivalent stiffness matrix for magneto-electro-elastic material properties. The component matrices of Equation (11) are

$$\begin{aligned}
 [K_I] &= [K_{u\phi}]^T - [K_{\phi\psi}][K_{\psi\psi}]^{-1}[K_{u\psi}], & [K_{II}] &= [K_{\phi\phi}] - [K_{\phi\psi}][K_{\psi\psi}]^{-1}[K_{\phi\psi}]^T, \\
 [K_{IV}] &= [K_{u\psi}]^T - [K_{\phi\psi}]^T [K_{\phi\phi}]^{-1}[K_{u\phi}]^T, & [K_V] &= [K_{\psi\psi}] - [K_{\phi\psi}]^T [K_{\phi\phi}]^{-1}[K_{\phi\psi}].
 \end{aligned} \tag{12}$$

The eigen vectors corresponding to ϕ and ψ are given by

$$\phi = [K_{II}]^{-1}[K_I]\{U\}, \tag{13}$$

$$\psi = [K_V]^{-1}[K_{IV}]\{U\}. \tag{14}$$

To study the pure piezoelectric effect, the stiffness matrix can be derived as

$$[K_{\phi\phi,eq}] = [K_{uu}] + [K_{u\phi}][K_{\phi\phi}]^{-1}[K_{u\phi}]^T, \tag{15}$$

and to study the pure magnetic effect, the stiffness matrix can be derived as

$$[K_{\psi\psi,eq}] = [K_{uu}] + [K_{u\psi}][K_{\psi\psi}]^{-1}[K_{u\psi}]^T. \tag{16}$$

$[K_{\phi\phi,eq}]$, $[K_{\psi\psi,eq}]$ are the equivalent stiffness matrix considered for studying pure piezoelectric and piezomagnetic cylinder.

4. Results and discussions

4.1. Validation. Ansys 8.1 (www.ansys.com) has been used to validate the code developed for finding the transient response of a magneto-electro-elastic layered cylinder. Ansys cannot directly handle the magneto-electro-elastic material; hence the code has been validated with Ansys 8.1 for the response of

Materials	PECP	MSCP	MEE	BaTiO ₃
C_{11}	79.7	31.1	166	166
C_{12}	35.8	15.2	77	77
C_{13}	35.8	15.2	78	78
C_{33}	66.8	35.6	162	162
C_{44}	17.2	13.6	43	43
e_{15}	10.5	0	11.6	11.6
e_{31}	-5.9	0	-4.4	-4.4
e_{33}	15.2	0	18.6	18.6
ϵ_{11}	15.92	0	11.2	11.2
ϵ_{33}	15.92	0	12.6	12.6
μ_{11}	0	0.054	0.05	0.05
μ_{33}	0	0.054	0.1	0.1
q_{15}	0	-60.9	550	0
q_{31}	0	156.8	580.3	0
q_{33}	0	108.3	699.7	0
m_{11}	0	0	5	0
m_{33}	0	0	3	0

Table 1. Material properties for (PZT)-epoxy mixed component (PECP), (Terfenol-D)-epoxy mixed components (MSCP) barium titanate and two phase MEE material. Here C_{ij} is expressed in $10^9 N/m^2$; e_{ij} in C/m^2 ; ϵ_{ij} in $10^{-9} C/Vm$; q_{ij} in N/Am ; μ_{ij} in $10^{-4} Ns^2/C^2$ and m_{ij} in $10^{-12} Ns/VC$.

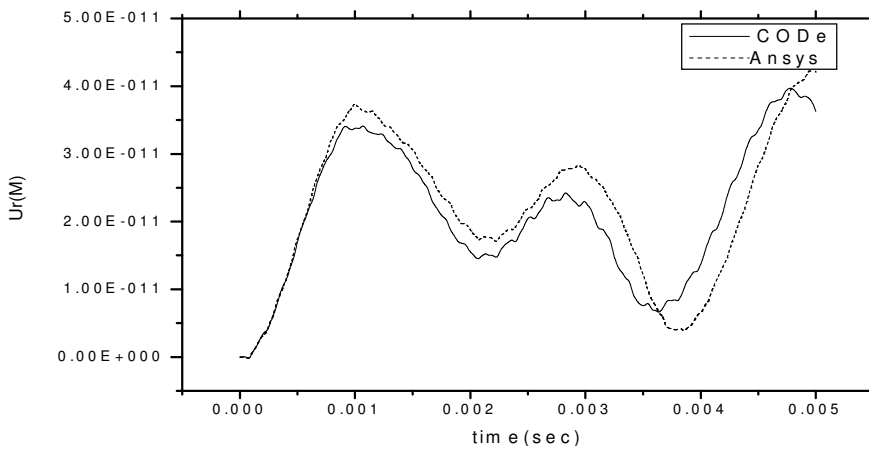


Figure 2. Comparison of U_r for PECP material.

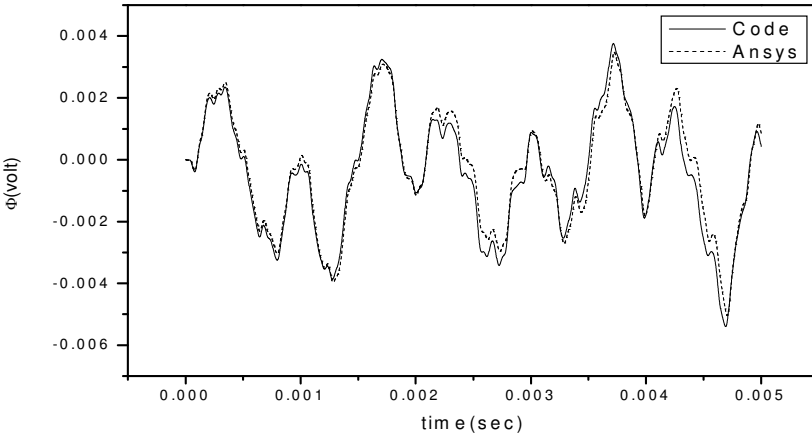


Figure 3. Comparison of ϕ for PECP material.

cylinder made of (PZT)-epoxy mixed component (PECP) and (Terfenol-D)-epoxy mixed components (MSCP) under simply supported boundary condition.

Ansys can directly solve the piezoelectric materials but the behavior of MSCP could not be computed directly with it. However, MSCP can be substituted by PECP; we note that the constitutive equations of both the materials are identical. The properties of the above material have been taken from [Liu et al. 2003]; see Table 1. The dimensions of the layered cylinder, length = 4 m, inner radius = 0.7 m and thickness = 0.6 m, are taken from [Wang and Zhong 2003]. The structure has been discretised with 6 elements in the radial direction and 40 elements in the axial direction. A constant internal pressure of 1 N/m^2 is applied. As is clear from Figures 2–5, the code results agree well with the Ansys results. The undulations in the curves of ϕ and ψ may be due to the presence of higher harmonics.

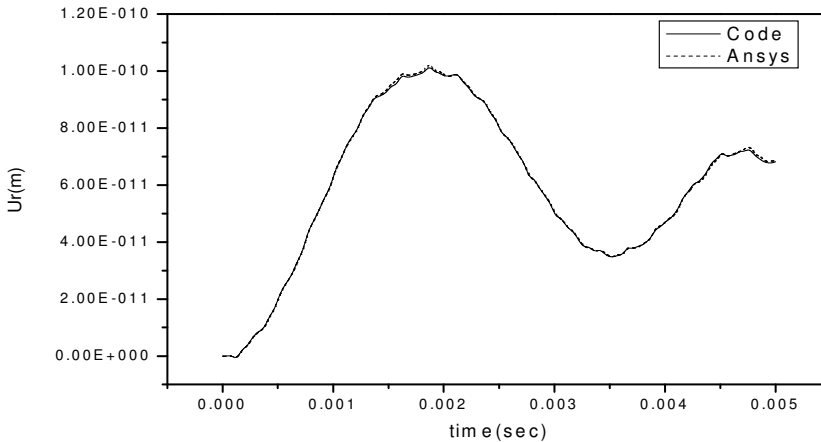


Figure 4. Comparison of U_r for MSCP Material.

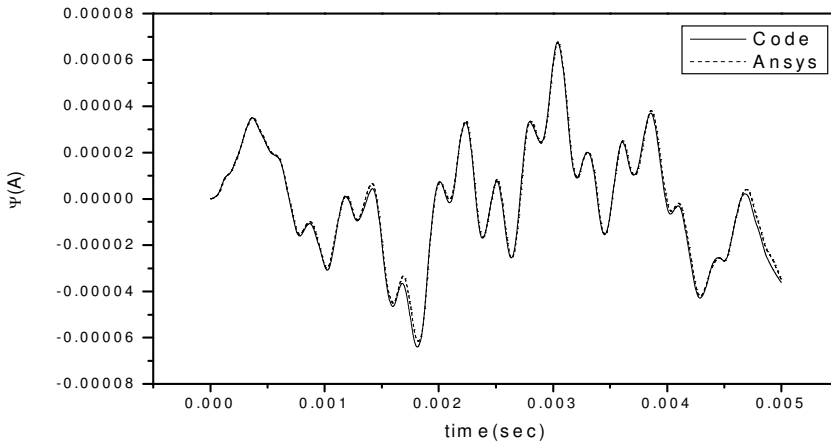


Figure 5. Comparison of ψ for MSCP Material.

Materials	$V_m - 0.1$	$V_m - 0.2$	$V_m - 0.3$	$V_m - 0.4$	$V_m - 0.5$
	$V_e - 0.5$	$V_e - 0.4$	$V_e - 0.3$	$V_e - 0.2$	$V_e - 0.1$
C_{11}	17.0	16.1	16.5	17.0	17.5
C_{12}	8.57	9.1	9.3	9.4	9.97
C_{13}	8.57	9.1	9.3	9.4	9.97
C_{33}	77.0	80.0	83.9	87.2	91.7
C_{44}	5.46	6.0	5.71	6.28	6.41
C_{66}	4.4	5.86	6.61	6.04	4.41
e_{15}	1.84	1.9	1.9	1.9	1.84
e_{31}	1.52	1.65	1.71	1.71	1.77
e_{33}	11.0	9.1	7.35	5.45	3.61
ϵ_{11}	0.394	0.294	0.264	0.235	0.205
ϵ_{33}	6.46	5.23	3.96	2.74	1.44
μ_{11}	2.92	3.15	2.92	3.14	3.37
μ_{33}	0.214	0.356	0.502	0.65	0.79
q_{15}	0.721	0.721	0.721	0.721	0.721
q_{31}	5.23	7.93	11.5	15.1	17.8
q_{33}	29.5	59.3	87.2	118.0	147.0
$m_{11}(\times 10^{14})$	0.171	0.254	0.265	0.218	0.126
$m_{33}(\times 10^{-10})$	0.658	1.03	1.18	1.03	0.652

Table 2. Material properties of the three-phase MEE materials for different volume fractions of the three-phase MEE material. Note that for all the materials the piezoelectric volume fraction (vf) is 0.4. Here V_m represents the piezomagnetic volume fraction and V_e represents the elastic matrix volume fraction. Also, C_{ij} is expressed in $10^9 N/m^2$; e_{ij} in C/m^2 ; ϵ_{ij} in $10^{-9} C/Vm$; q_{ij} in N/Am ; μ_{ij} in $10^{-4} Ns^2/C^2$ and m_{ij} in Ns/VC .

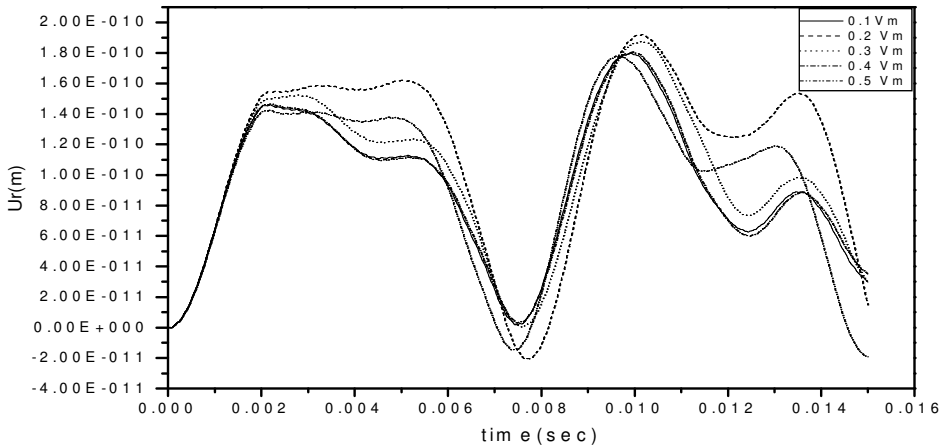


Figure 6. Comparison of U_r for different vf of MEE Material.

4.2. Response of the three-phase magneto-electro-elastic cylinder. The present computer code has been used to determine the response of three-phase magneto-electro-elastic layered cylinder under a constant internal pressure of 1 N/m^2 . The dimensions of the layered cylinder, length = 4 m, inner radius = 0.7 m and thickness = 0.6 m, are taken from [Wang and Zhong 2003]. The response has been studied at the middle node of the layered cylinder. The material properties are taken from [Jaesang et al. 2005] which are given in Table 2. In the MEE composite, the volume fraction of the fibrous piezoelectric phase is kept as constant 0.4 and the volume fraction of the piezomagnetic phase varies from 0.1–0.5; the remaining volume fraction is for the elastic material. The coupled response of the layered cylinder made of three phase magneto-electro-elastic material with a simply supported boundary condition has been plotted in Figures 10–13. The response has been plotted for a time period of 0.015 sec. In Figures 10–13, V_m represents the piezoelectric volume fraction.

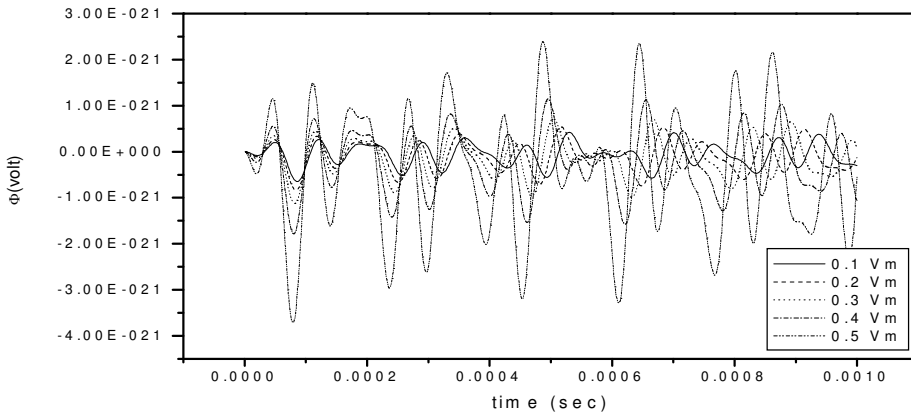


Figure 7. Comparison of ϕ for different vf of MEE material.

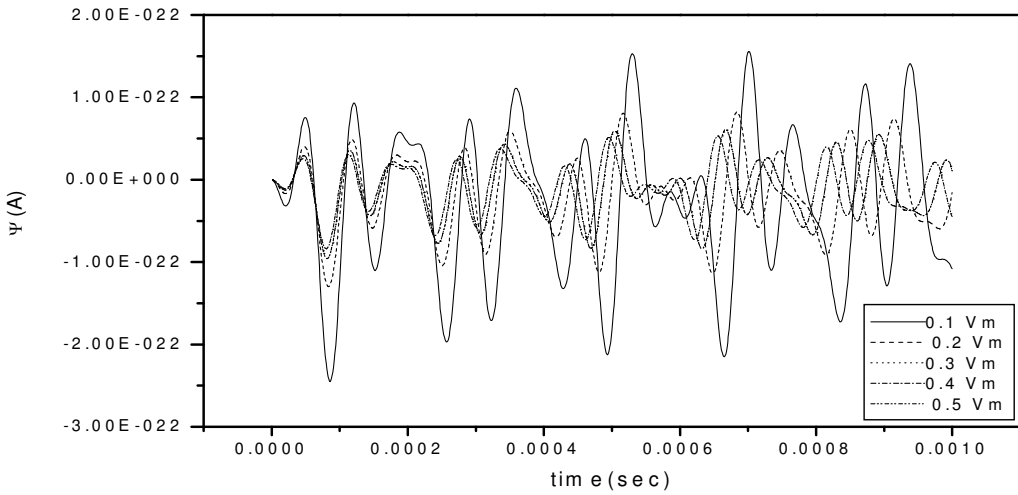


Figure 8. Comparison of ψ for different vf of MEE material.

Figure 6 shows the variation of radial displacement with respect to time. The variation of displacement for all the volume fraction more or less follows the same pattern. The peak value of the radial displacement occurs for the 0.2 volume fraction of the piezomagnetic fiber. The peak value of the displacement decreases with the increase in volume fraction of piezomagnetic phase in the MEE composite. This can be attributed to the fact that the stiffness of the cylinder increases with the increase in volume fraction of piezomagnetic phase as evident from the material properties given in Table 2.

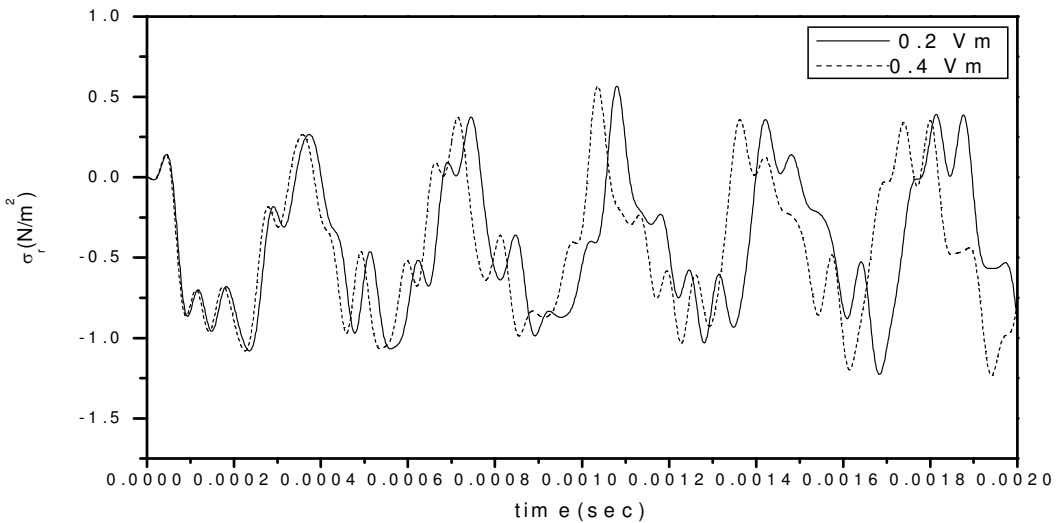


Figure 9. Comparison of σ_r for different vf of MEE material.

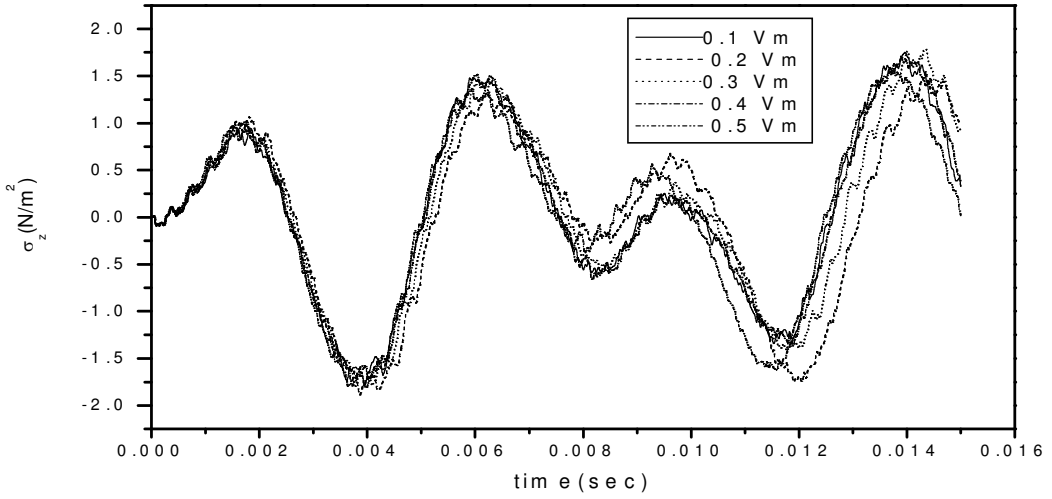


Figure 10. Comparison of σ_z for different vf of MEE material.

Figure 7 shows the magnified view of the variation of electric potential (ϕ) for different volume fractions for a time period of 0.001 sec. The distribution of ϕ shows the presence of higher harmonics. The value of ϕ reaches a maximum for the 0.5 volume fraction of the piezomagnetic fiber and it decreases with the decrease in volume fraction. The distribution of ϕ follows similar trend for all the materials.

Figure 8 shows the magnified view of the distribution of magnetic potential (ψ) for the different volume fractions of the piezomagnetic fiber for a time period of 0.001 sec. It is maximum for 0.1 volume fraction of the piezomagnetic fiber and goes on decreasing with the increase in volume fraction.

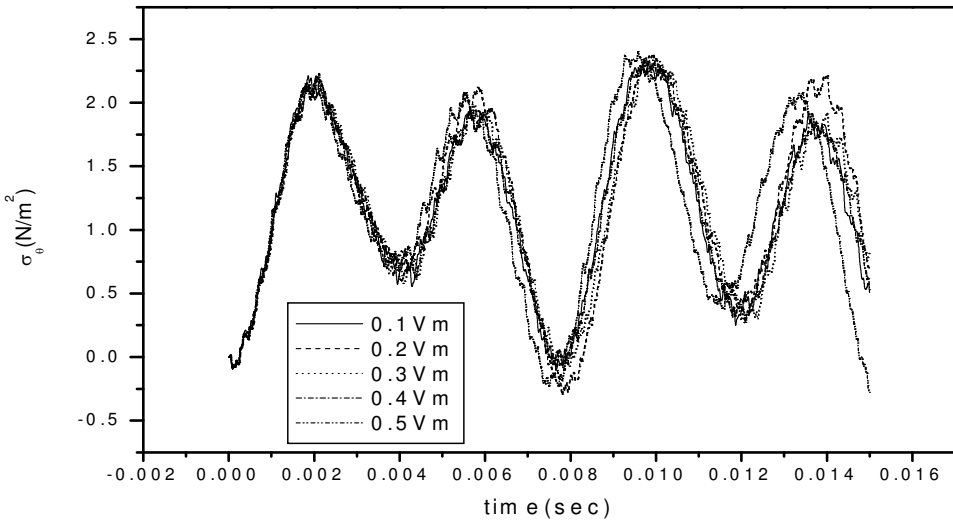


Figure 11. Comparison of σ_θ for different vf of MEE material.

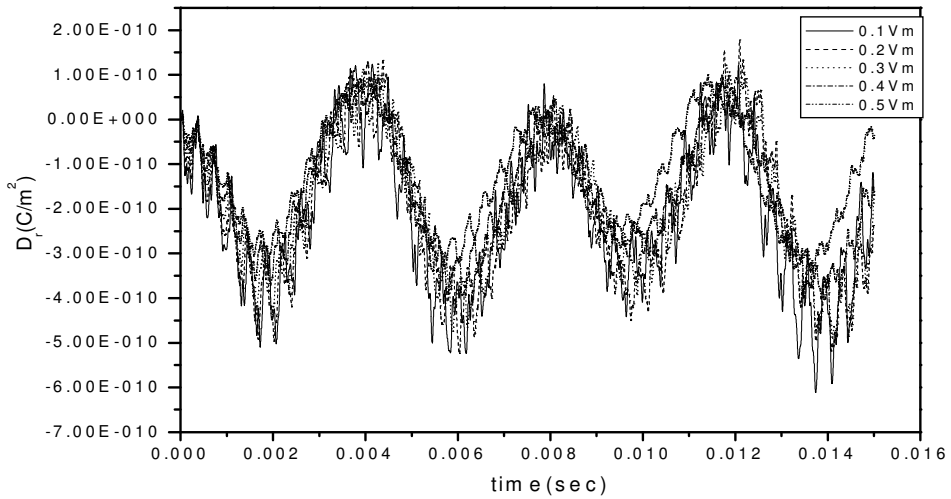


Figure 12. Comparison of D_r for different vf of MEE material.

Figures 9–11 show the distribution of stresses at the middle element of the layered cylinder. Figure 9 shows the magnified view of the distribution of radial stress (σ_r) for 0.2 and 0.4 volume fractions of the piezomagnetic fiber for a time period of 0.002 sec. The presence of higher harmonics can be seen from the stress distribution plots. The distribution of stress follows the same pattern for all volume fractions. The peak values of stresses are higher for σ_θ and σ_z compared to the other two, while σ_θ acts as a primary stress and its value is at a maximum for the 0.5 volume fraction of the piezomagnetic fiber.

Figure 12 shows the distribution of radial (D_r) electric displacement. The distribution pattern is similar for all the volume fractions of the MEE material. The value of the radial electric displacement

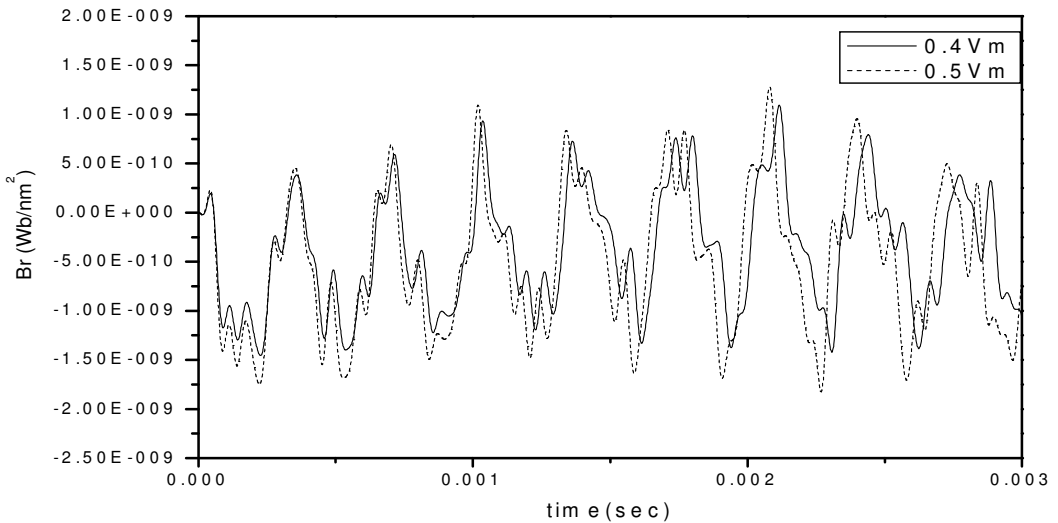


Figure 13. Comparison of B_r for different vf of MEE material.

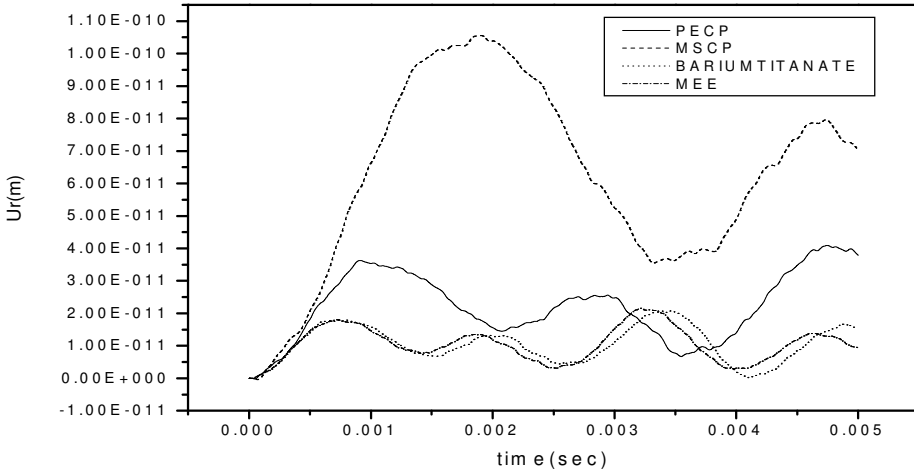


Figure 14. Comparison of U_r for simply supported layered cylinder.

is larger than that of the axial displacement. The peak value of D_r is for the 0.1 volume fraction of the piezomagnetic fiber and goes on decreasing with the increase in volume fraction. Figure 13 shows the magnified view of the distribution of radial magnetic induction (B_r) for the 0.4 and 0.5 volume fractions of the piezomagnetic fiber for a time period of 0.003 sec. The distribution pattern is similar for all the volume fractions of the piezomagnetic fiber in the MEE material. The value of the radial magnetic induction is larger than that of the axial magnetic induction. The peak value of B_r is for the 0.5 volume fraction of the piezomagnetic fiber and goes on decreasing with the decrease in volume fraction.

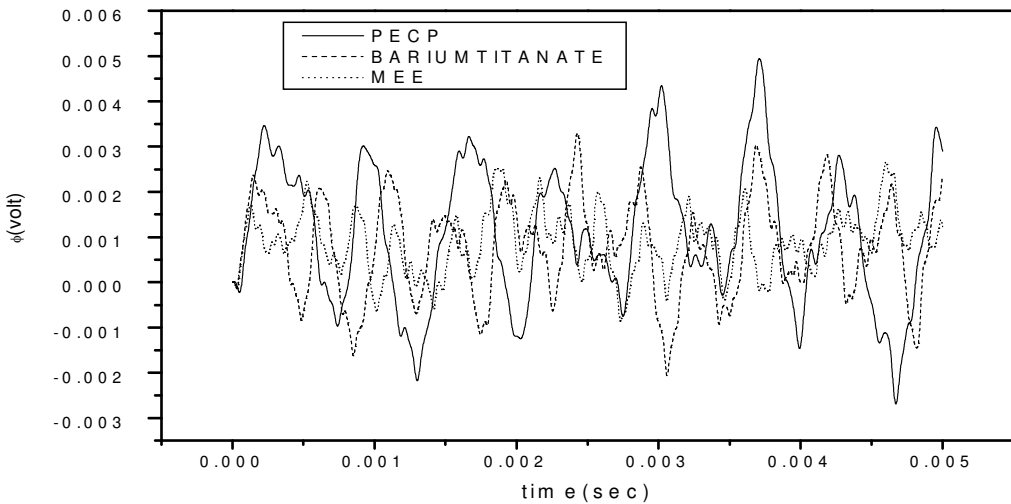


Figure 15. Comparison of ϕ for simply supported layered cylinder.

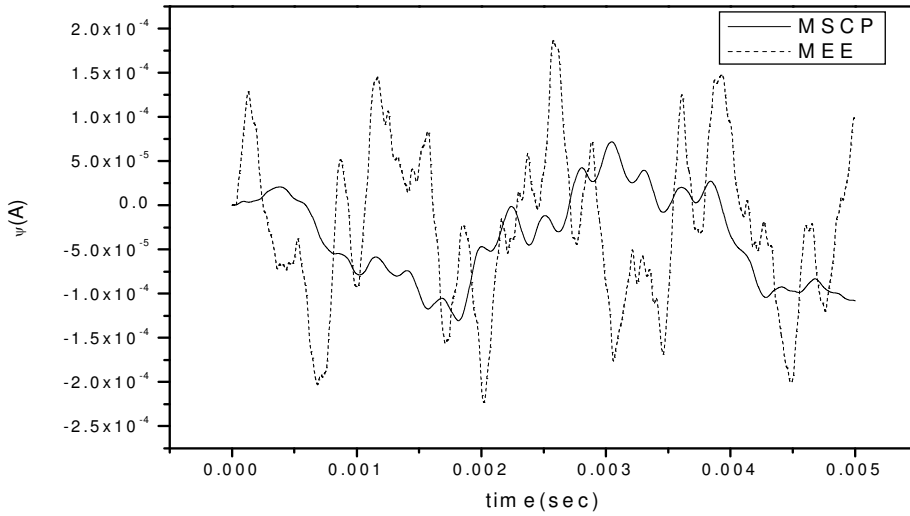


Figure 16. Comparison of ψ for simply supported layered cylinder.

4.3. Comparative studies of the responses of (PZT)-epoxy mixed component (PECP), (Terfenol-D)-epoxy mixed components (MSCP), barium titanate and a two phase MEE simply supported layered cylinder. The coupled response of the layered cylinder for different material with simply supported boundary conditions has been plotted in the Figures 14–16. The material properties for PECP and MSCP are taken from [Liu et al. 2003], barium titanate from [Aboudi 2001] and two phase MEE from [Jiang and Pan 2004]. The response at the middle node, that is, at the center of the layered cylinder, has been studied for a time lapse of 0.005 sec. Figure 14 shows that the peak value of the radial displacement U_r is maximum for the MSCP material and low for MEE material. This is due to the stiffening effect of the piezoelectric and piezomagnetic terms which increases the stiffness of the structure resulting from the generation of induced electric and magnetic fields in the MEE structures. It is clear from the displacement plot that the frequency is lowest for MSCP material and highest for MEE and BaTiO₃.

Figure 15 shows the variation of electric potential (ϕ) for the materials exhibiting piezoelectric characteristics. The value of electric potential (ϕ) is highest for PECP material and low for MEE material, which can be attributed to Equation (13) that the value of ϕ is directly proportional to displacement, which is also high for PECP material. The distribution of ϕ for all the materials follows the same pattern. Figure 16 shows the distribution of ψ for the materials exhibiting piezomagnetic characteristics. The value of ψ is larger for MEE material, and is due to the presence of high piezomagnetic coefficients compared to MSCP material given in Table 1.

The distribution of stresses at the middle element of the layered cylinder for all the materials is studied using the Equation (1). The peak values of σ_θ are high compared to other stresses. The value of stresses is maximum for MEE material. The stress distribution also reveals the presence of higher harmonics in the response. The distribution of the radial (D_r) and axial (D_z) electric displacement at the middle element of the layered cylinder for all the materials is studied using the Equation (2). The value of electric displacement in the radial direction is greater than that in the axial direction. The magnitude of

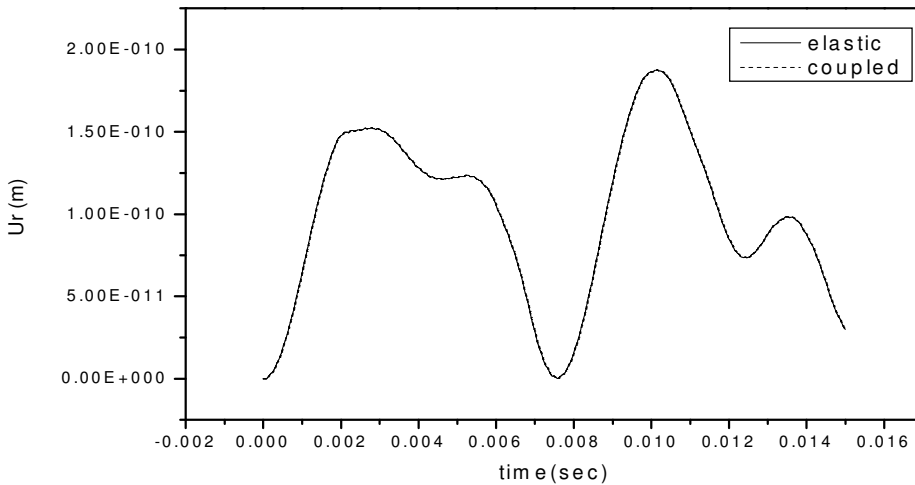


Figure 17. Comparison of U_r for elastic and coupled response for MEE material.

electric displacement is at its maximum for a cylinder made of PECP material, and is at a minimum for a cylinder made of MEE material—a fact which can be due to the presence of piezomagnetic coupling terms present in the MEE material. The distribution of radial (Br) and axial (Bz) magnetic induction at the middle element of the layered cylinder for all the materials is studied using the Equation (3). The value of magnetic induction in the radial direction is larger than that in the axial direction and is a maximum for MEE structures.

4.4. Comparison between the elastic and coupled responses of three phase magneto-electro-elastic simply supported layered cylinder. A comparison between the elastic and the coupled responses for the three phase magneto-electro-elastic simply supported layered cylinder has been plotted in Figure 17. The comparison of response is done for 0.3 vf of the piezomagnetic phase in the MEE composite. From the figure it is clear that the piezoelectric and piezomagnetic coupling terms do not play a part in the response of three phase magneto-electro-elastic structures. The contribution of coupling coefficients is negligible in the stiffness matrix of the structure. Hence the distribution of coupled ϕ and ψ is similar to that of uncoupled (elastic) ϕ and ψ .

5. Conclusion

The finite element method has been used to find the transient response of the three-phase magneto-electro-elastic simply supported layered cylinder under constant internal pressure. Numerical results have been presented for different volume fractions of the piezomagnetic phase in the composite. The responses of purely piezoelectric and piezomagnetic phases can also be calculated as special cases. A comparative study of the response of PECP, MSCP, barium titanate and two phase magneto-electro-elastic materials has been presented. A comparison between the coupled and the elastic responses of the 0.3 volume fraction of the three phase magneto-electro-elastic structure is also presented. It can be concluded from this study that (i) the magnitude of displacement is high for the three-phase MEE materials as compared with the other materials; (ii) the transient responses of the three-phase materials

show more complex characteristics compared with the other materials presented in the paper; (iii) the piezoelectric and piezomagnetic coupling terms do not play a role in the transient response of three-phase magneto-electro-elastic structures; and (iv) the magnitudes of electric potential and magnetic potential are low for the three-phase materials compared with the other materials which can be attributed to the low values of piezoelectric and piezomagnetic coefficients in the three-phase material.

References

- [Aboudi 2001] J. Aboudi, "Micromechanical analysis of fully coupled electro-magneto-thermo-elastic multiphase composites", *Smart Mater. Struct.* **10** (2001), 867–877.
- [Annigeri et al. 2006] A. R. Annigeri, N. Ganesan, and S. Swarnamani, "Free vibration of clamped clamped magneto-electro-elastic cylinder shell", *J. Sound Vib.* **292** (2006), 300–314.
- [Bhangale and Ganesan 2005] R. K. Bhangale and N. Ganesan, "Free vibration studies of simply supported non-homogeneous functionally graded magneto-electro-elastic finite cylindrical shells", *J. Sound Vib.* **288** (2005), 412–422.
- [Bhimaraddi 1987] A. Bhimaraddi, "Static and transient response of cylindrical shells", *Thin Walled Structures* **5** (1987), 157–179.
- [Buchanan 2003] G. R. Buchanan, "Free vibration of an infinite magneto-electro-elastic cylinder", *J. Sound Vib.* **268** (2003), 413–426.
- [Hou and Leung 2004] P. F. Hou and A. Y. T. Leung, "The transient responses of magneto-electro-elastic hollow cylinders", *Smart Mater. Struct.* **13** (2004), 762–776.
- [Jaesang et al. 2005] L. Jaesang, G. James, I. V. Boyd, and C. L. Dimitris, "Effective properties of three-phase electro-magneto-elastic composites", *Int. J. Eng. Sci.* **43** (2005), 790–825.
- [Jiang and Pan 2004] X. Jiang and E. Pan, "Exact solution of the 2D polynomoal inclusion problem in anisotropic magneto-electroelastic full-, half-, and bilateral-planes", *Int. J. Solids Struct.* **41**:16–17 (2004), 4361–4382.
- [Liu et al. 2003] Y. X. Liu, J. G. Wan, J. M. Liu, and C. W. Nan, "Effect of magnetic bias field on magnetoelectric coupling in magnetoelectric composites", *J. Appl. Phys.* **94** (2003), 5118–5122.
- [Pan and Heyliger 2002] E. Pan and P. R. Heyliger, "Free vibrations of simply supported and multilayered magneto-electro-elastic plates", *J. Sound Vib.* **252** (2002), 429–442.
- [Philip 1972] U. Philip, "Transient response of inelastic shells of revolution", *Comput. Struct.* **2** (1972), 975–989.
- [Wang and Zhong 2003] X. Wang and Z. Zhong, "A finitely long circular cylindrical shell of piezoelectric/piezomagnetic composite under pressuring and temperature change", *Int. J. Eng. Sci.* **41** (2003), 2429–2445.

Received 8 May 2007. Accepted 1 Aug 2007.

ATUL DAGA: atul_daga@rediffmail.com

Machine Design Section, Indian Institute of Technology Madras, Chennai 600 036, India

NATRAJAN GANESAN: nganesan@iitm.ac.in

Department of Mechanical Engineering, Indian Institute of Technology Madras, Chennai 600 036, India

KRISHNAPILLAI SHANKAR: skris@iitm.ac.in

Department of Mechanical Engineering, Indian Institute of Technology Madras, Chennai 600 036, India

SUBMISSION GUIDELINES

ORIGINALITY

Authors may submit manuscripts in PDF format on-line. Submission of a manuscript acknowledges that the manuscript is *original and has neither previously, nor simultaneously, in whole or in part, been submitted elsewhere*. Information regarding the preparation of manuscripts is provided below. Correspondence by email is requested for convenience and speed. For further information, write to:

Marie-Louise Steele
Division of Mechanics and Computation
Durand Building, Room 262
Stanford University
Stanford CA 94305

LANGUAGE

Manuscripts must be in English. A brief abstract of about 150 words or less must be included. The abstract should be self-contained and not make any reference to the bibliography. Also required are keywords and subject classification for the article, and, for each author, postal address, affiliation (if appropriate), and email address if available. A home-page URL is optional.

FORMAT

Authors are encouraged to use L^AT_EX and the standard article class, but submissions in other varieties of T_EX, and, exceptionally in other formats, are acceptable. Electronic submissions are strongly encouraged in PDF format only; after the refereeing process we will ask you to submit all source material.

REFERENCES

Bibliographical references should be listed alphabetically at the end of the paper and include the title of the article. All references in the bibliography should be cited in the text. The use of B^IB_T_EX is preferred but not required. Tags will be converted to the house format (see a current issue for examples), however, in the manuscript, the citation should be by first author's last name and year of publication, e.g. "as shown by Kramer, et al. (1994)". Links will be provided to all literature with known web locations and authors are encouraged to provide their own links on top of the ones provided by the editorial process.

FIGURES

Figures prepared electronically should be submitted in Encapsulated PostScript (EPS) or in a form that can be converted to EPS, such as GnuPlot, Maple, or Mathematica. Many drawing tools such as Adobe Illustrator and Aldus FreeHand can produce EPS output. Figures containing bitmaps should be generated at the highest possible resolution. If there is doubt whether a particular figure is in an acceptable format, the authors should check with production by sending an email to:

production@mathscipub.org

Each figure should be captioned and numbered so that it can float. Small figures occupying no more than three lines of vertical space can be kept in the text ("the curve looks like this:"). It is acceptable to submit a manuscript with all figures at the end, if their placement is specified in the text by means of comments such as "Place Figure 1 here". The same considerations apply to tables.

WHITE SPACE

Forced line breaks or page breaks should not be inserted in the document. There is no point in your trying to optimize line and page breaks in the original manuscript. The manuscript will be reformatted to use the journal's preferred fonts and layout.

PROOFS

Page proofs will be made available to authors (or to the designated corresponding author) at a web site in PDF format. Failure to acknowledge the receipt of proofs or to return corrections within the requested deadline may cause publication to be postponed.

Journal of Mechanics of Materials and Structures

Volume 3, N° 2 February 2008

Elastic constants and thermal expansion averages of a nontextured polycrystal	ROLAND DEWIT	195
Robustness analysis of structures based on plastic limit analysis with uncertain loads	YU MATSUDA AND YOSHIHIRO KANNO	213
Eulerian conjugate stress and strain	ANDREW N. NORRIS	243
Out-of-plane stress and displacement for through-the-thickness cracks in plates of finite thickness	JOHN CODRINGTON, ANDREI KOTOUSOV AND SOOK YING HO	261
Investigation of mode II crack growth following a very high speed impact	WEI MA AND ZHUPING DUAN	271
Anisotropic stress state around internally pressurized microchannels	YONG XUE GAN	291
Dynamic rigid-plastic deformation of arbitrarily shaped plates	TATIANA PAVLOVNA ROMANOVA AND YURI VLADIMIROVICH NEMIROVSKY	313
Interaction of a dislocation with collinear rigid lines at the interface of piezoelectric media	ZHONGMIN XIAO, HONGXIA ZHANG AND BINGJIN CHEN	335
Exact solution of double filled hole of an infinite plate	NAT KASAYAPANAND	365
Transient response of magneto-electro-elastic simply supported cylinder using finite element	ATUL DAGA, NATRAJAN GANESAN AND KRISHNAPILLAI SHANKAR	375



1559-3959(200802)3:2;1-B